

International Journal of Antennas and Propagation

Active Antennas for Space Applications

Guest Editors: Stefano Selleri and Giovanni Toso





Active Antennas for Space Applications

International Journal of Antennas and Propagation

Active Antennas for Space Applications

Guest Editors: Stefano Selleri and Giovanni Toso



Copyright © 2009 Hindawi Publishing Corporation. All rights reserved.

This is a special issue published in volume 2009 of “International Journal of Antennas and Propagation.” All articles are open access articles distributed under the Creative Commons Attribution License, which permits unrestricted use, distribution, and reproduction in any medium, provided the original work is properly cited.

Editorial Board

Mohammad Ali, USA
Charles Bunting, USA
Christophe Caloz, Canada
Dau-Chyrh Chang, Taiwan
Deb Chatterjee, USA
Zhi Ning Chen, Singapore
Christos Christodoulou, USA
Shyh-Jong Chung, Taiwan
Tayeb A. Denidni, Canada
Karu Esselle, Australia
Miguel Ferrando, Spain
Dejan Filipovic, USA
Lance Griffiths, USA
Yang Hao, UK

Wei Hong, China
Hon Tat Hui, Singapore
Tamer S. Ibrahim, USA
Shyh-Kang Jeng, Taiwan
Mandeep Jit Singh, Malaysia
Ahmed A. Kishk, USA
Ju-Hong Lee, Taiwan
Byungje Lee, South Korea
Le-Wei Li, Singapore
Yilong Lu, Singapore
Ananda S. Mohan, Australia
Pavel Nikitin, USA
Athanasios Panagopoulos, Greece
Matteo Pastorino, Italy

Sadasiva M. Rao, USA
Stefano Selleri, Italy
Krishnasamy T. Selvan, Malaysia
Zhongxiang Shen, Singapore
Seong-Youp Suh, USA
Parveen Wahid, USA
Yuanxun Ethan Wang, USA
Jeffrey Ward, USA
Quan Xue, Hong Kong
Tat Soon Yeo, Singapore
Wenhua Yu, USA
Lei Zhu, Singapore

Contents

Active Antennas for Space Applications, Stefano Selleri and Giovanni Toso
Volume 2009, Article ID 436565, 3 pages

Liquid Crystal-Reconfigurable Antenna Concepts for Space Applications at Microwave and Millimeter Waves, A. Gaebler, A. Moessinger, F. Goelden, A. Manabe, M. Goebel, R. Follmann, D. Koether, C. Modes, A. Kipka, M. Deckelmann, T. Rabe, B. Schulz, P. Kuchenbecker, A. Lapanik, S. Mueller, W. Haase, and R. Jakoby
Volume 2009, Article ID 876989, 7 pages

Active Reflectors: Possible Solutions Based on Reflectarrays and Fresnel Reflectors, Lorena Cabria, José Ángel García, Julio Gutiérrez-Ríos, Antonio Tazón, and Juan Vassallo
Volume 2009, Article ID 653952, 13 pages

An Iterative Technique for the Synthesis of Active Antenna Oscillator Arrays, Theodoros N. Kaifas and John N. Sahalos
Volume 2009, Article ID 208706, 11 pages

Cylindrical Dielectric Resonator Antennas with Harmonic Control as an Active Antenna Radiator, L. Lucci, G. Manara, P. Nepa, G. Pelosi, and S. Selleri
Volume 2009, Article ID 519850, 7 pages

Irregular Polyomino-Shaped Subarrays for Space-Based Active Arrays, R. J. Mailloux, S. G. Santarelli, T. M. Roberts, and D. Luu
Volume 2009, Article ID 956524, 9 pages

Sunflower Array Antenna with Adjustable Density Taper, Maria Carolina Viganó, Giovanni Toso, Gerard Caille, Cyril Mangenot, and Ioan E. Lager
Volume 2009, Article ID 624035, 10 pages

Active SAR Antennas: Design, Development, and Current Programs, P. Capece
Volume 2009, Article ID 796064, 11 pages

Performance Comparison of Reflector- and Planar-Antenna Based Digital Beam-Forming SAR, Marwan Younis, Sigurd Huber, Anton Patyuchenko, Federica Bordoni, and Gerhard Krieger
Volume 2009, Article ID 614931, 13 pages

Accurate Antenna Pattern Modeling for Phased Array Antennas in SAR Applications—Demonstration on TerraSAR-X, Markus Bachmann, Marco Schwerdt, and Benjamin Bräutigam
Volume 2009, Article ID 492505, 9 pages

Potential Benefits of Dynamic Beam Synthesis to Mobile Satellite Communication, Using the Inmarsat 4 Antenna Architecture as a Test Example, R. F. E. Guy
Volume 2009, Article ID 249602, 5 pages

Planar C-Band Antenna with Electronically Controllable Switched Beams, Mariano Barba, Juan E. Page, and Jose A. Encinar
Volume 2009, Article ID 625327, 7 pages



Ku Band Hemispherical Fully Electronic Antenna for Aircraft in Flight Entertainment, Alfredo Catalani, Franco Di Paolo, Marzia Migliorelli, Lino Russo, Giovanni Toso, and Piero Angeletti
Volume 2009, Article ID 230650, 7 pages

Flat Array Antennas for Ku-Band Mobile Satellite Terminals, Roberto Vincenti Gatti, Luca Marcaccioli, Elisa Sbarra, and Roberto Sorrentino
Volume 2009, Article ID 836074, 5 pages

Low Profile, Dual-Polarised Antenna for Aeronautical and Land Mobile Satcom, Martin Shelley, Robert Pearson, and Javier Vazquez
Volume 2009, Article ID 984972, 6 pages

Editorial

Active Antennas for Space Applications

Stefano Selleri¹ and Giovanni Toso²

¹ Department of Electronics and Telecommunications, University of Florence, Via C. Lombroso 6/17, 50134 Firenze, Italy

² Antenna and Sub-Millimeter Wave Section, Electromagnetic Division, European Space Agency, ESA-ESTEC, Keplerlaan 1, PB 299, 2200 AG Noordwijk, The Netherlands

Correspondence should be addressed to Stefano Selleri, stefano.selleri@unifi.it

Received 14 April 2009; Accepted 14 April 2009

Copyright © 2009 S. Selleri and G. Toso. This is an open access article distributed under the Creative Commons Attribution License, which permits unrestricted use, distribution, and reproduction in any medium, provided the original work is properly cited.

*Phased arrays produce beams that can be modified, scanned or shaped electronically.
An active array antenna system is defined as an array in which all or part of
the elements are equipped with their own transmitter or receiver, or both [1].*

Active antennas (AAs) are devices combining a radiating sub-system as well as backing active circuits in tight integration, drastically reducing the complexity of the matching networks and filters by carefully designing the radiating element so as to provide the proper load for the active elements.

Although the idea of an AA is not new [2–7], its extended impact on telecommunication industry is recent and there is a large interest, both from researchers and industries, in novel fields of application. These spans from satellite [8] to biomedical applications [9], to radioastronomy [10, 11] and, of course, to personal communication systems, wireless local networks, and RF identification. Recent research threads, selected among the referred journal publications of the last two years, investigate possible band widening [12, 13], polarization diversity [14], applications in MIMO systems [15], and novel radiators [16, 17].

The current lead applications of AA are large electronically scanned arrays [18, 19], and this special issue is indeed focused on this broad topic, with particular attention to satellite applications.

Indeed arrays of active antennas, or active arrays, are well suited for mobile terminals requiring dynamic satellite tracking. The most common approach toward achieving fast-beam scanning is through the integration of monolithic microwave integrated circuit (MMIC) phase shifters, low-noise amplifiers, and solid state power amplifiers with the antenna elements. In some cases, hybrid electro/mechanical arrays combining mechanical steering with electrical steering/shaping are considered. This architecture is often used to

reduce the number of active control elements by limiting the electrical scanning in only one plane. This is often the case for mobile user terminals where azimuth scanning is performed by mechanical rotation and elevation agility is realized by a linear phased array.

Active phased arrays are well known for being complex and expensive antennas and, as a consequence, only few space missions exploited this type of antenna. This is not the case for ground and airborne radars, where major funding, mainly from the US defense programs, has led to large-scale production of T/R modules reaching a goal of a \$100 cost per module already in the 80s. Unfortunately, this background is hardly reusable for space missions, due to the completely different requirements and operational constraints. One interesting exception is the IRIDIUM satellite system, where the main mission antenna has been conceived essentially reusing T/R technology previously developed for radar applications [20].

Another factor limiting a wider application of antenna phased arrays in space missions is linked to their large mass and high power dissipation, especially for the large active phased array configurations. This generates the need for new ultralight technologies and thermal hardware. With the progress in developments of more efficient T/R modules, thermal aspects may become less critical, but the improvement on this parameter is not as quick as expected.

During the past 20 years, the basic radiating elements and feeding lines present in phased array systems have evolved with a variety of microstrip, stripline, and other printed

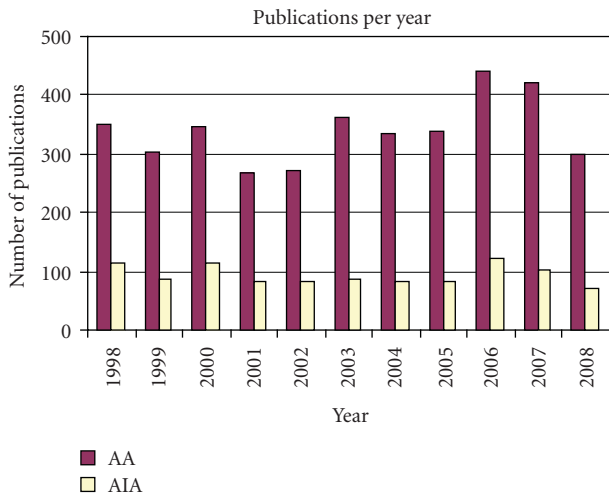


FIGURE 1: Number of publications per year, (journal, conferences and books), on active antennas (purple) and on active integrated antennas (yellow).

radiators replacing the traditional dipoles, slots, or horns, fed by coaxial lines or waveguides. Developments in monolithic and other fabrication processes allowed for the automated production of phased arrays with a high integration level and not by piecewise assembly as in the beginning. Using digital processing or analog devices, the active phased arrays will have time-delay capability to make wideband performance possible. Other important features of array antennas are the distribution of solid-state power amplification with graceful degradation and a lower risk of power handling. Active phased arrays can also be designed to conform to the surface of a spacecraft.

Today phased arrays for space missions are mostly considered when in flight beam reconfigurability or inertialess beam steering is required. However, it is important to note that array antennas may find wider space applications when nongeostationary telecommunication constellations are considered, or as a way to generate very large apertures thanks to digital processing techniques for beamforming.

Active phased array antennas directly radiating or receiving the signal are called "Direct Radiating Arrays" (DRAs). If, on the other hand, they are used to illuminate reflectors the antenna systems are called "Array Fed Reflectors" (AFRs). Feed arrays can compensate for the inherent distortions of large reflectors deployed in space, thanks to techniques monitoring the reflector surface or synthesize a desired radiation pattern by adjusting the feed coefficients and they can assist to move the complete multiple beam pattern over the coverage, therewith handling seasonal deviations in desired scanning/coverages, without moving the satellite thus saving propellant and extending its lifetime.

At last, to give an idea of the relevance of AA in electromagnetic engineering, a survey has been made over the INSPEC bibliographical database concerning scientific publications addressing active antenna issues and covering the last ten years. Figure 1 shows this survey, discriminating between active antennas in general (purple) and the subclass of active integrated antennas. A steady average of nearly 350

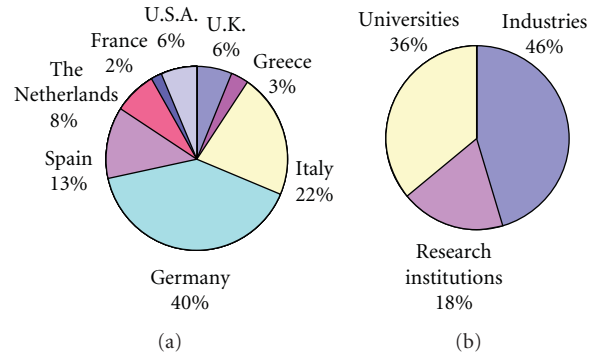


FIGURE 2: Subdivision of authors by country (a) and subdivision of institutions (b).

papers per year has been published on active antennas in the last decade, showing the large interest of researchers and companies on this topic.

This special issue collects fourteen articles, coming from 63 authors of 22 institutions of 8 countries, worldwide. Figure 2 shows some statistics. The fourteen articles have been ideally subdivided into two parts; the first part gathering contributions which are more oriented to research and leading technology issues, the second part containing more technological and applicative papers. The first author and a very brief description of the content are listed here below.

Part I:

- (1) Gaebler et al. present a novel liquid-crystals-based approach to tunable devices for millimeter wave reflectarrays.
- (2) Cabria et al. deal with a novel beamsteering technique for reflectarrays.
- (3) Theodoros N. Kaifas and John N. Sahalos propose the design of oscillators by exploiting interelement coupling in the array.
- (4) Lucci et al. present dielectric resonator antennas harmonic tuning for optimum amplifier loading.
- (5) Mailloux et al. exploit polyomino subarrays to achieve superior sidelobe and band performances.
- (6) Viganò et al. present a sunflower-like array achieving a quasi-rotationally symmetric pattern with adjustable sidelobes and grating lobes level.

Part II:

- (7) Capece describes the COSMO Sky Med SAR array antenna discussing implementation and design issues.
- (8) Younis et al. present a comparison between different implementations of digital beamforming SAR.
- (9) Bachmann et al. investigate pattern modeling techniques in the TerraSAR-X mission.
- (10) Guy investigates the advantages of fully dynamic beam scanning for INMARSAT platform.

- (11) Barba et. al. investigate possible topologies for reducing the beamforming network complexity.
- (12) Catalani et al. present a complete design for an airplane-to-satellite active array.
- (13) Vincenti Gatti et al. describe two novel design for flat fully-steerable antenna arrays for mobile-to-satellite communications.
- (14) Shelley et al. show a low profile antenna for the air or ground terminal mobile-to-satellite link. This latter is a fully mechanically steered antenna but is here included because it provides a reference for the previous two active antenna systems.

Stefano Selleri
Giovanni Toso

References

- [1] IEEE Standard Definitions of Terms for Antennas, IEEE Std 145–1993 (Revision of IEEE Std 145–1983).
- [2] H. H. Meinke, “Active antennas,” *Nachrichtentechnische Zeitschrift*, vol. 19, pp. 697–705, 1966.
- [3] H. A. Wheeler, “Small antennas,” *IEEE Transactions on Antennas and Propagation*, vol. 23, no. 4, pp. 462–469, 1975.
- [4] J. Lin and T. Itoh, “Active integrated antennas,” *IEEE Transactions on Microwave Theory and Techniques*, vol. 42, no. 12, pp. 2186–2194, 1994.
- [5] J. A. Navarro and K. Chang, *Integrated Active Antennas and Spatial Power Combining*, John Wiley & Sons, New York, NY, USA, 1996.
- [6] R. A. York and Z. B. Popovic, *Active and Quasi-Optical Arrays for Solid-State Power Combining*, John Wiley & Sons, New York, NY, USA, 1997.
- [7] A. Mortazwi, T. Itoh, and J. Harvey, *Active Antennas and Quasi-Optical Arrays*, John Wiley & Sons, New York, NY, USA, 1998.
- [8] C. Mangenot, “Space antenna challenges and roadmaps,” in *Proceedings of the 29th ESA Antenna Workshop on Multiple Beams and Reconfigurable Antennas*, Noordwijk, The Netherlands, April 2007.
- [9] S. Jacobsen and Ø. Klemetsen, “Improved detectability in medical microwave radio-thermometers as obtained by active antennas,” *IEEE Transactions on Biomedical Engineering*, vol. 55, no. 12, pp. 2778–2785, 2008.
- [10] S. Jacobsen and Ø. Klemetsen, “Active antennas in medical microwave radiometry,” *Electronics Letters*, vol. 43, no. 11, pp. 606–608, 2007.
- [11] S. W. Ellingson, J. H. Simonetti, and C. D. Patterson, “Design and evaluation of an active antenna for a 29–47 MHz radio telescope array,” *IEEE Transactions on Antennas and Propagation*, vol. 55, no. 3, pp. 826–831, 2007.
- [12] D. Segovia-Vargas, D. Castro-Galan, L. E. Garcia-Munoz, and V. Gonzalez-Posadas, “Broadband active receiving patch with resistive equalization,” *IEEE Transactions on Microwave Theory and Techniques*, vol. 56, no. 1, pp. 56–64, 2008.
- [13] V. Rizzoli, A. Costanzo, and P. Spadoni, “Computer-aided design of ultra-wideband active antennas by means of a new figure of merit,” *IEEE Microwave and Wireless Components Letters*, vol. 18, no. 4, pp. 290–292, 2008.
- [14] G. Yun, “Compact active integrated microstrip antennas with circular polarisation diversity,” *IET Microwaves, Antennas and Propagation*, vol. 2, no. 1, pp. 82–87, 2008.
- [15] M. Sadek, A. Tarighat, and A. H. Sayed, “Active antenna selection in multiuser MIMO communications,” *IEEE Transactions on Signal Processing*, vol. 55, no. 4, pp. 1498–1510, 2007.
- [16] A. Guraliuc, G. Manara, P. Nepa, G. Pelosi, and S. Selleri, “Harmonic tuning for ku-band dielectric resonator antennas,” *IEEE Antennas and Wireless Propagation Letters*, vol. 6, pp. 568–571, 2007.
- [17] L. K. Hady, D. Kajfez, and A. A. Kishk, “Dielectric resonator antenna in a polarization filtering cavity for dual function applications,” in *IEEE Transactions on Microwave Theory and Techniques*, vol. 56, no. 12, pp. 3079–3085, 2008.
- [18] A. K. Agrawal and E. L. Holzman, “Active phased array design for high reliability,” *IEEE Transactions on Aerospace and Electronic Systems*, vol. 35, no. 4, pp. 1204–1211, 1999.
- [19] N. Khandelwal and R. W. Jackson, “Active antenna module for low-cost electronically scanned phased arrays,” *IEEE Transactions on Microwave Theory and Techniques*, vol. 56, no. 10, pp. 2286–2292, 2008.
- [20] J. J. Schuss, J. Upton, B. Myers, et al., “The IRIDIUM main mission antenna concept,” *IEEE Transactions on Antennas and Propagation*, vol. 47, no. 3, pp. 416–424, 1999.

Research Article

Liquid Crystal-Reconfigurable Antenna Concepts for Space Applications at Microwave and Millimeter Waves

A. Gaebler,¹ A. Moessinger,¹ F. Goelden,¹ A. Manabe,² M. Goebel,² R. Follmann,³ D. Koether,³ C. Modes,⁴ A. Kipka,⁴ M. Deckelmann,⁴ T. Rabe,⁵ B. Schulz,⁵ P. Kuchenbecker,⁵ A. Lapanik,⁶ S. Mueller,¹ W. Haase,⁶ and R. Jakoby¹

¹*Institute of Microwave Engineering, TU Darmstadt, 64283 Darmstadt, Germany*

²*Merck KGaA, 64293 Darmstadt, Germany*

³*IMST GmbH, 47475 Kamp-Lintfort, Germany*

⁴*W.C. Heraeus GmbH, 63405 Hanau, Germany*

⁵*Bundesanstalt für Materialforschung und -prüfung, 12205 Berlin, Germany*

⁶*Institute of Condensed Matter, TU Darmstadt, 64283 Darmstadt, Germany*

Correspondence should be addressed to A. Gaebler, gaebler@mwt.tu-darmstadt.de

Received 30 September 2008; Accepted 5 January 2009

Recommended by Giovanni Toso

Novel approaches of tunable devices for millimeter wave applications based on liquid crystal (LC) are presented. In the first part of the paper, a novel concept of a tunable LC phase shifter realized in Low Temperature Cofired Ceramics technology is shown while the second part of the paper deals with a tunable high-gain antenna based on an LC tunable reflectarray. The reflectarray features continuously beam scanning in between $\pm 25^\circ$. Also first investigations on radiation hardness of LCs are carried out, indicating that LCs might be suitable for space applications.

Copyright © 2009 A. Gaebler et al. This is an open access article distributed under the Creative Commons Attribution License, which permits unrestricted use, distribution, and reproduction in any medium, provided the original work is properly cited.

1. Introduction

The shortage in the available frequency spectrum for radio communications and the requirement for more functionality in ever smaller volume requires the development of new concepts in RF technology, especially for space missions. A general approach to solve this problem is the concept of dynamically reconfigurable RF front ends. One possibility for the realization of tunable RF components is the use of special substrate media such as controllable dielectrics. Especially for the higher frequency range (>20 GHz), liquid crystals (LCs) show very good RF performance [1]. Nevertheless, the used fabrication processes prevented a commercialization up to now, because of incompatibilities with standard fabrication processes. One aim of the Liquida project is to overcome that problem in order to develop tunable components for RF applications. The combination of both good RF properties of LC and the advantages of the standard multilayer technology of Low Temperature Cofired Ceramics (LTCC) has a high

potential to enable the realization of cost-effective and high-performance RF components. Therefore, the investigation in terms of fabrication technology aims to accomplish the development of a technique for the fabrication of a Liquid Crystal compatible LTCC material system. measurement results of several LTCC phase shifter devices which can be the key component of tunable-phased array antennas. In the second part of the paper another concept of an LC-tunable high-gain antenna based on a reflectarray topology is presented. Furthermore, some basic investigations for space qualification of Liquid Crystal devices are aimed for.

2. Properties of Liquid Crystal

LCs are an anisotropic material showing both properties of a crystal and a liquid. All further explanations are related to nematic LCs which shows up to now the best dielectric properties at microwave and mm-wave frequencies [2].

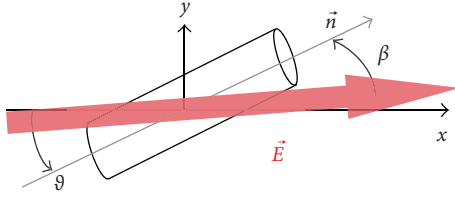


FIGURE 1: Representation of a rod like molecule with the anisotropic dielectric axes.

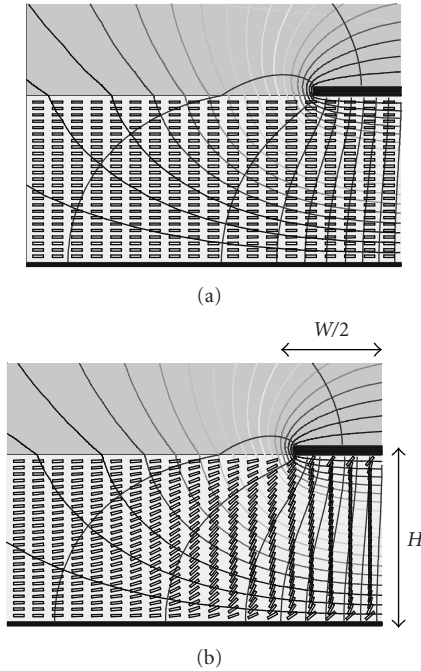


FIGURE 2: Director distribution by surface alignment without (a) and with a bias voltage on the upper electrode.

They can be described as rod-like molecules as shown in Figure 1. The shown rod represents the anisotropic dielectric properties of a molecule and the unit vector \vec{n} pointing in the same direction as the rod is called director.

$\epsilon_{r,\perp}$, the permittivity perpendicular to an incident electrical field, is usually around 2.5 while $\epsilon_{r,\parallel}$ ranges between 2.8 and 3.5, depending on the material.

A bulk of LC molecules represented as such a rod contained between two surfaces which have been specially treated to anchor the molecules parallel to the surface will look like Figure 2(a).

The two electrodes in this figure represent a microstrip line and the respective ground plane. The reorientation of an entire bulk of LC can be achieved by the effect of an external electric bias field. Applying such a field, the molecule's long axis rotates such that the director points mainly towards the same direction as the exciting electric field lines. Figure 2(b) demonstrates this schematically. By using LC in such a way as a dielectric substrate, this mechanism can be used for a continuous tuning of the effective permittivity of transmission lines.

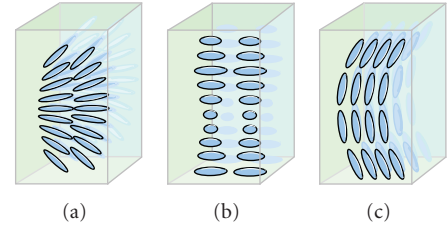


FIGURE 3: (a) The splay, (b) twist, and (c) bend deformation.

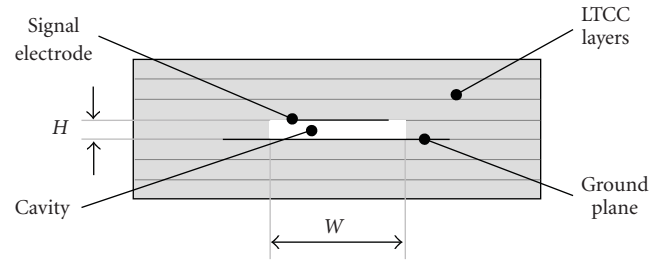


FIGURE 4: Cross-section of an LTCC-based inverted microstrip line.

To describe the director orientation in the biased state, it is necessary to consider the influence of the director dynamics which is described by the so called LC Continuum theory [3]. Looking at the rod-representation as shown in Figure 1, an electric bias-field generates an anisotropic polarization in the LC material. This leads to an electric torque for the considered director given by the cross-product of the bias field with the polarization.

Another torque contribution results from the elastic forces between the molecules themselves. These elastic forces stem from deformations of the director distribution and can conveniently be imagined to be working like deformations in a regular crystal. In liquid crystal bulks generally three basic types of deformations can exist simultaneously: the splay, twist and the bend deformation. The nature of these types is shown in Figure 3.

After the bias voltage is removed these torques lead the molecules back to the original state, caused by the minimum energy principle.

3. Fabrication Process

The realization of phase shifters based on Liquid Crystal combined with LTCC requires the fabrication of cavities which can be filled with LC. Figure 4 shows schematically the cross section of an inverted microstrip line (IMSL) consisting of a ground plane on the bottom of the center cavity and a top electrode. This structure is stacked here by using six layers of LTCC. The challenge is to fabricate a wide cavity or channel (e.g., dimensions of $W = 400 \mu\text{m}$ by $H = 100 \mu\text{m}$ height) and maintaining these dimensions also over a channel length of, for example, 50 mm.

The LTCC manufacturing process uses a screen printing to generate metalized circuit patterns on so called green sheets which make the LTCC layers. Afterwards, the sheets are

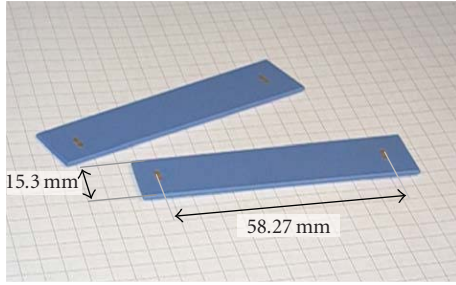


FIGURE 5: Prototype of a LTCC phaseshifter device.

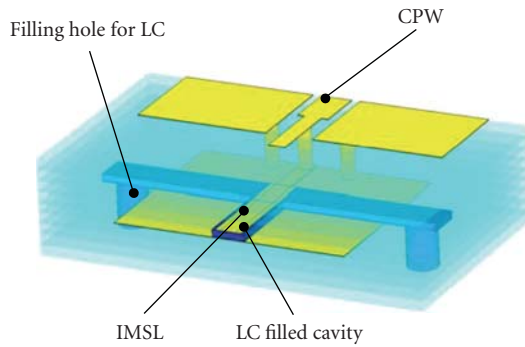


FIGURE 6: LTCC structure of the CPW to IMSL transition.

stacked and laminated by utilizing a combination of multiple lamination steps which also include forming rectangular cavities in the process.

Although the structuring of planar LTCC foils, which are processed and screen printed with thick-films, is straight forward, major problems arise such as delamination or bending of the cavity's top and bottom wall during the sintering process. Therefore, the investigation in terms of the fabrication is focused on the optimization of the process parameters needed to create integrated and well-defined cavities in LTCC.

After the burnout and co-firing process the LTCC device is filled with Liquid Crystal and finally sealed. The whole device is shown in Figure 5.

4. LTCC Phaseshifter

Figure 6 shows the prototype of a LTCC phase shifter schematically. A coplanar waveguide (CPW) is used for the external connection, whereas an inverted microstrip line (IMSL) realizes the liquid crystal filled transmission line phase shifter. This line type provides a high tuning efficiency [4] in the meaning of a big change of the effective permittivities in the steered and unsteered case. After applying an electrical bias field to the CPW center electrode (which has a galvanic connection to the top electrode of the IMSL), the LC can be continuously steered depending on the applied voltage as described in Section 2.

4.1. Measurement Results. The following measurement results were obtained by using the standard nematic LC

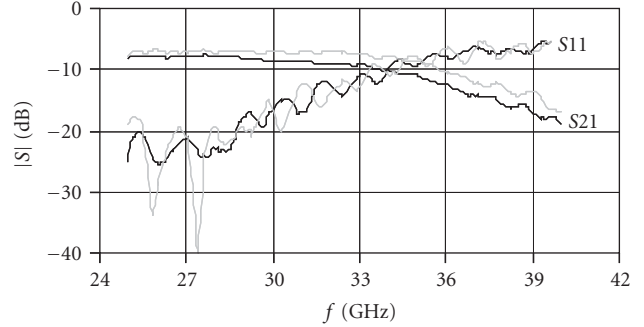


FIGURE 7: Measurement results of the LTCC phaseshifter, without bias voltage (black curves).

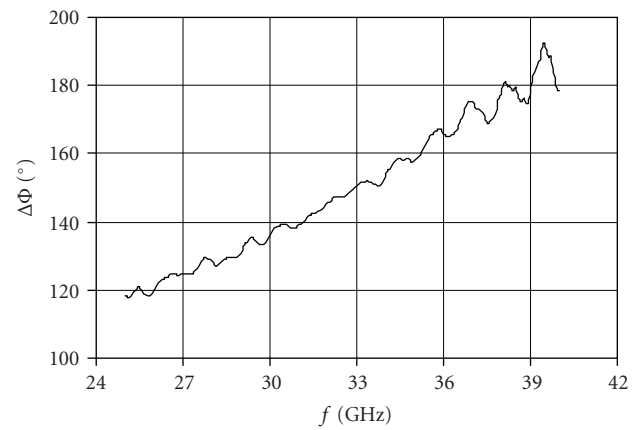


FIGURE 8: Measured phase shift.

TABLE 1: Material parameters of K15 and MDA-03-2838.

Mixture	$\epsilon_{r,\parallel}$	$\epsilon_{r,\perp}$	$\tan(\delta)_{\parallel}$	$\tan(\delta)_{\perp}$
K15	2.85	2.55	0.01	0.03

K15. This commercial available LC is well investigated and its microwave properties are also known at the targeted operation frequencies. These parameters are summarised in Table 1.

The results of the measured insertion loss S_{12} and the attenuation are shown in Figure 7.

As depicted in Figure 7, the insertion loss of the whole device is better than -8.5 dB in the range of 25 to 30 GHz and the reflection is lower than -15 dB for both the biased and unbiased state.

The phase shift $\Delta\Phi$ which can be achieved by using K15 is between 120° and 200° in the measured range from 25 to 40 GHz (Figure 8).

In order to compare this results a quality factor of a phaseshifter as commonly called Figure-of-Merit (FoM), can be defined by the relation of the phase shift to the highest insertion loss at the corresponding frequency. Figure 9 shows the FoM which could be achieved with the presented structure.

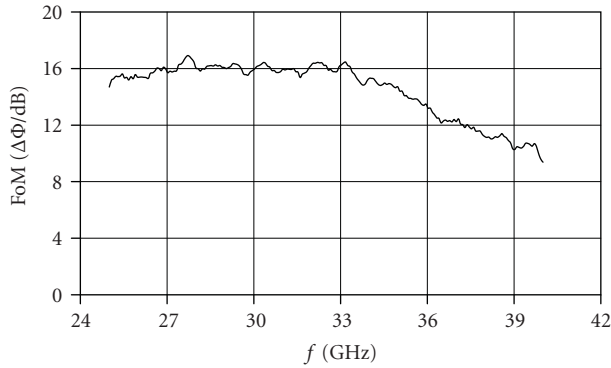


FIGURE 9: FoM of the LTCC phase shifter.

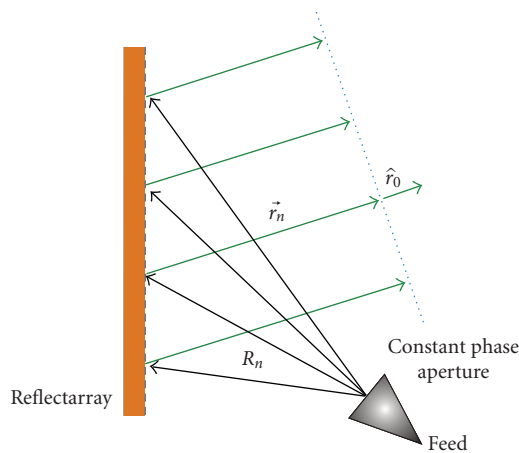


FIGURE 10: Functioning of a microstrip reflectarray.

5. Space Qualification Tests of LC

In order to verify the capability of LCs for space applications, different basic investigations have to be carried out: one test scenario is the reaction of the material under exposing of high energetic protons.

The tests has been carried out at the Forschungszentrum Jülich.

The energy of the protons is fixed to 42 MeV with a maximum current of $10 \mu\text{A}$. This energy was reduced to 15 MeV by using a special graphite iris between the target and the proton gate in order to simulate the typical total radiation dose of a 15 years lifetime space mission in the Low Earth Orbit.

Several test cells have been irradiated with protons, for example, LTCC packaged phase shifters, LC-filled capacitances and pure LC-filled glass tubes each with four different LC mixtures.

The results of the measured values of the capacitances before and after several equivalent years of a space mission are shown in Table 1. The data was obtained by using an LCR meter at 1 KHz.

As can be seen, the reaction depends on the kind of the LC. Big changes of the conductivity could be obtained for K15 and M_A mixtures, whereas no change of those

TABLE 2: Capacitance and conductivity values before and after proton irradiation.

Sample	After irradiation		before	
	C/pF	R/MOhm	C/pF	R/MOhm
K15-1	826,5	6,4	825	26
K15-2	836,0	6,3	834	29,2
M_A-1	927,5	2,9	909,5	22,3
M_A-2	775,9	3,6	759,5	30,2
M_B-1	220,3	138,5	216	infinite
M_B-2	229,4	182,0	225	infinite
M_C-1	153,9	infinite	151,4	infinite
M_C-2	158,0	infinite	157,4	infinite

properties could be measured for the M_C mixture. However, the physical interpretation of all measurements is not finished yet and further tests with electrons and gamma radiation are in planning.

6. Reflectarrays

In place of phase shifters to realize a tunable-phased array another possibility to realize tunable high-gain antennas is a reflectarray antenna.

A reflectarray antenna combines, as its name already suggests, some of the best features of reflector and array antennas. A special type of reflectarray is the microstrip reflectarray. It consists in a basic form of a planar, thin substrate with microstrip antenna elements, for example, patches or dipoles, which are arranged in an equidistant grid on the substrate. The array is illuminated by a feed antenna and the elements of the array, in the following called “unit cells”, are designed to scatter the incident wave with an appropriate phase, required to form a planar phase surface in front of the aperture, as depicted in Figure 10.

This mode of operation is similar in concept to a parabolic reflector that naturally forms a planar phase front, when a feed is placed at its focus.

One of the key features in microstrip reflectarray implementation is how the elements are designed to scatter with the desired phase. One method is to use microstrip patches with different sizes to control the backscattered phase, as proposed in [5]. This method is also the basic functionality of the tunable unit cell presented in this contribution.

Reflectarrays have attracted increasing attention in the past years because of their properties: low loss due to the absence of a corporate feed, ease of fabrication, planarity, and low weight. Reconfigurability is another desirable feature of reflectarrays that would increase their versatility a lot. A novel approach based on nematic LCs will be presented in this contribution in order to realize an electronically reconfigurable reflectarray.

6.1. Tunable Unit Cell. There have been various attempts to achieve electronic reconfigurability of reflectarrays: some of them made use of varactor diodes [6] in order to change the reflection phase, others used tunable materials, such as

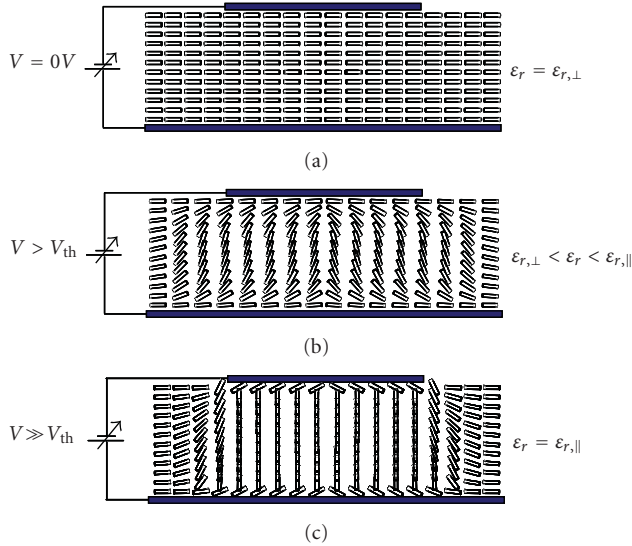


FIGURE 11: Functioning principle of the LC-tunable reflectarray unit cell with single microstrip patch.

Barium Strontium Titanate (BST) [7]. With the advances in the field of MEM-switches, these have become preferred to varactor diodes due to their superior RF properties [8, 9].

The novel approach, presented in this paper, makes use of a substrate whose dielectric properties can be tuned by applying a low bias voltage (<20 V) [10, 11]. Thus all patches will have the same geometrical size, while the effective permittivity of the substrate under each patch will differ causing different backscattered phases which can be electronically tuned independently for each unit cell. One material that provides this functionality is LC. Because of the anisotropy of the molecules in combination with an orientational order, a macroscopically uniaxial anisotropic permittivity is effective [12] as aforementioned.

Using LCs as tunable substrate introduces several constraints in the antenna design. As the name already suggests, LCs are fluid and hence carrier substrates are required to support the metallization and the ground plane. Additionally, the carrier substrates have to form a cavity with a well-controlled thickness in which the LC can be filled in later on. The cavity has to be properly sealed to avoid LC leakage. On the ground plane and on the metallization layer a thin polyimide film has to be spin coated to provide the initial alignment of the LC director. Since the surface alignment mechanism is only functional for thin LC layers, the cavity thickness should not be much larger than 100 μm . This will seriously limit the bandwidth of the microstrip structure, especially for lower frequencies. Hence, the operating frequency of the reflectarray presented in this work is situated in the E-band at 77 GHz.

In Figure 11 a schematic of the cross section of a LC-tunable reflectarray unit cell is presented. The cell consists of a patch printed on a carrier substrate, the ground plane printed on a carrier as well, and the LC cavity between patch and ground. A thin polyimide film (about 300 nm) is spin

coated both on the ground plane and on the patches, cured and finally mechanically rubbed, in order to provide the prealignment of the LC molecules.

The director of the LC-molecules is initially aligned parallel to the patch and ground, owing to the polyimide layer (Figure 11(a)). The applied bias voltage between patch and ground generates the external electric field for reorientating the director \vec{n} .

The RF field, given by the microstrip patch fundamental mode is mainly confined in the LC volume and is essentially perpendicular to the director. Thus, the RF field will perceive an effective permittivity $\epsilon_{r,\text{eff}} = \epsilon_{\perp}$. Applying an increasing bias voltage, the director will begin to rotate as soon as the voltage exceeds a certain threshold voltage V_{th} of a few volts (Figure 11(b)). When the bias voltage is increased even further, the director of the LC molecules will tend to align with the bias field lines, until the molecules are completely aligned parallel to the bias E-field. In this state, the average direction of the main axes of all molecules become parallel to the RF-field and the experienced effective permittivity becomes $\epsilon_{r,\text{eff}} = \epsilon_{\parallel}$ (see Figure 11(c)). The change in relative effective permittivity, $\Delta\epsilon_{r,\text{eff}}$ produces a change in the capacitance per unit length of the microstrip patch. This leads to a shift in the resonance frequency, ω_r , and also to a shift of the phase characteristic as depicted in Figure 12. Since the permittivity variation is continuous, so is the phase tuning at a certain frequency.

6.2. Tunable LC-Reflectarray at 77 GHz. The reflectarray designed for an operating frequency of 77 GHz has been briefly presented in [13]. It consists of 16 times 16 unit cells with an interelement spacing of 0.55λ . The size of a single unit cell is 2.2 mm. From [14], it can be recognized that the single patch unit cell with an LC cavity height of 50 μm has the best overall performance regarding losses and tunable phase range. Hence, this unit cell topology is used to realize the reflectarray.

For the substrate carrying the microstrip patches a glass carrier and for the substrate with the ground plane a metalized silicon wafer is employed. The rigidity of these materials ensures a sufficient precision for the 50 μm cavity.

Spherical spacers having a diameter of 50 μm are mixed together with glue, which is then used to bond the two substrates together. The glue also acts as a seal for the liquid crystal cavity.

Figure 13 shows a photograph of the fully assembled LC reflectarray with feed mounted for measurements. The feed is an open WR-10 waveguide, which is bended to radiate on the reflector.

To simplify the bias control of this first demonstrator, all patches on one row are connected altogether with a thin bias line. Therefore, the same bias voltage will be applied to the entire row and hence this reflectarray is only steerable in one plane. For this reason, there will be no beam focusing on the nonsteerable plane, the H-plane.

The cavity has been filled with the LC mixture BMW10 developed at TU Darmstadt for maximum optical

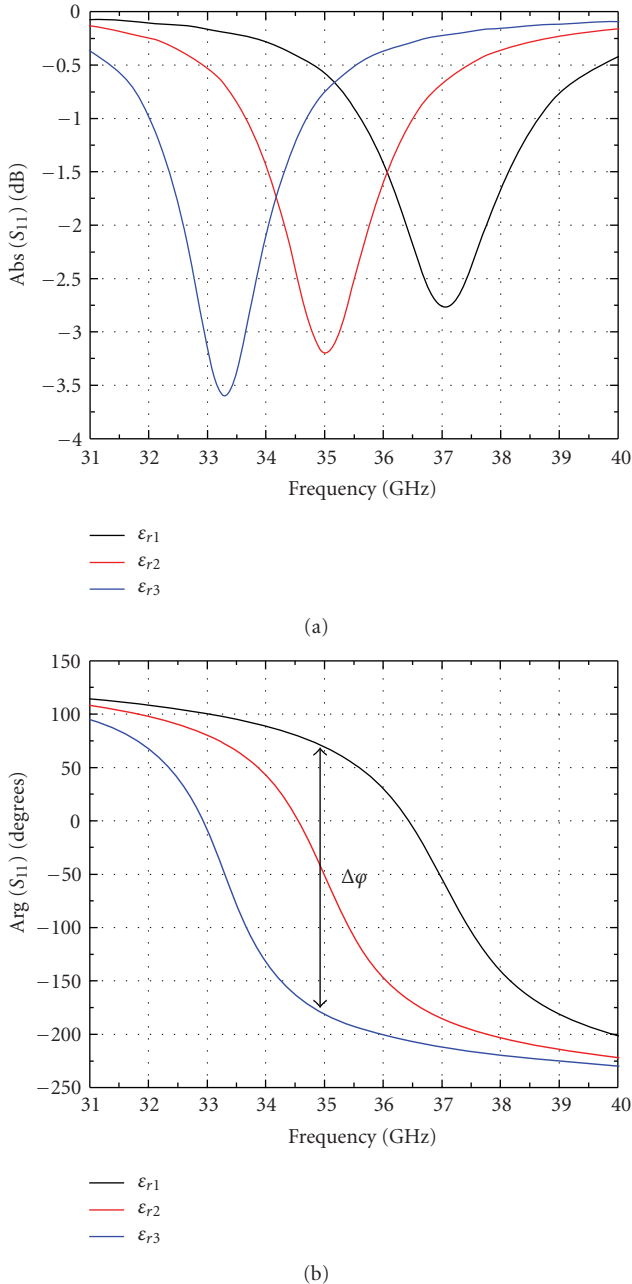


FIGURE 12: Functioning principle of a LC-tunable unit cell.

anisotropy, but featuring also acceptable microwave performance. Its characterization with the cavity perturbation technique at 30 GHz yielded for $\epsilon_{r,\perp} = 2.49$ and $\epsilon_{r,\parallel} = 3.18$. The dielectric losses are $\tan(\delta)_{\perp} = 0.017$ and $\tan(\delta)_{\parallel} = 0.004$.

The power pattern measurements shown in Figure 14 were performed at 77.2 GHz, this is being the frequency where the maximum adjustable phase range of the unit cells was recorded.

In order to illustrate the beam steering capability in the E-plane of the reflectarray, three selected patterns are presented: the main beam directed toward -10° , 0° , and 25° , respectively. The main beam of the reflectarray can

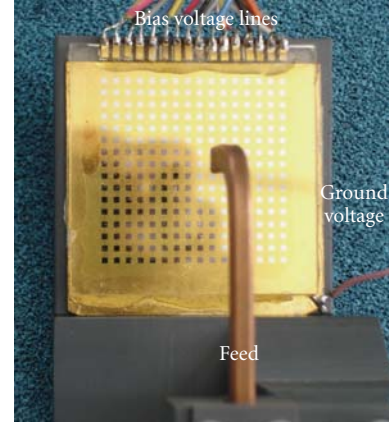


FIGURE 13: Fully assembled 77 GHz LC reflectarray with feed.

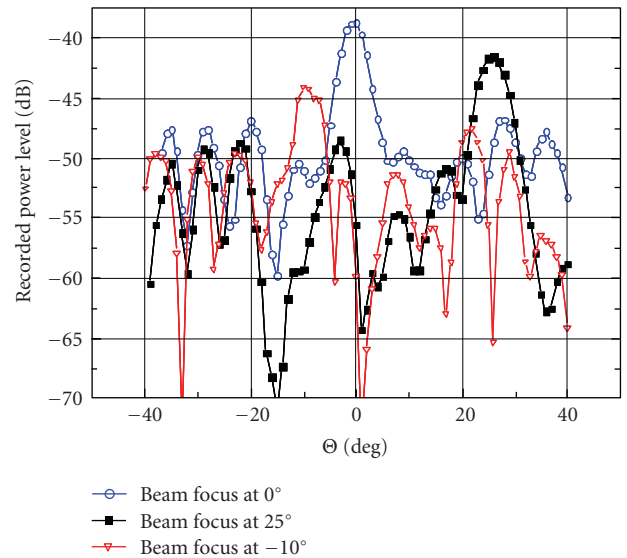


FIGURE 14: Three recorded E-plane patterns for three different voltage configurations, with the main beam pointing at different angles: -10° , 0° , and $+25^\circ$ (at 77.2 GHz).

be continuously scanned between -25° and $+25^\circ$ with a side lobe level of 8 dB for the main beam steered to 0° . Nevertheless, it can be observed that the pattern for the main beam directed to -10° is deteriorated in comparison to the other two. This can be caused by the beam-focusing algorithm, which evaluates only a very limited number of phase/amplitude distributions from the totality of all possible combinations [10]. It is thus not guaranteed that the obtained pattern is the best in terms of gain or side lobe level.

7. Summary

In this contribution, recent results of frequency agile components based on LC are presented. The first section of this contribution deals with tunable phase shifters which are the key component of tunable-phased arrays. Special attention has been paid to develop a technique for the fabrication of

an LC-compatible LTCC material system. The phase shifters presented in this work reached a tunable phase shift of 138° at 30 GHz with a FoM of 16. It should be noted that these first measuring results can be considerably improved by using an LC which is optimized for microwave applications as shown in [1].

In the second part of the paper, a demonstrator of a tunable reflectarray antenna has been presented. With this topology, it is possible to realize tunable high-gain antennas. The realized demonstrator has been designed to operate at 77 GHz and is able to steer the main beam continuously in between $\pm 25^\circ$ by applying bias voltages below 15 V. Its performance could be improved by employing LCs with better microwave features as employed in [14] and by improving the configuration algorithm calculating the bias voltages.

As there are at least some LC mixtures available which prove to be stable in the exposure of protons, tunable devices based on LC seem to be suited to be used in space applications, especially as for this concept no moving mechanical parts are needed.

Acknowledgments

The authors are thankful for CST GmbH for providing the CST Microwave Studio solver. The work presented in this paper has been supported in the frameworks of the Liquida, a project funded and supported by the German Aerospace Center (DLR) and the Federal Ministry of Economics and Technology (BMW), and by the DFG Project Rekonfigurierbare Millimeterwellen-Antennen mit steuerbaren hoch-anisotropen Flüssigkristallen.

References

- [1] S. Mueller, P. Scheele, C. Weil, M. Wittek, C. Hock, and R. Jakoby, "Tunable passive phase shifter for microwave applications using highly anisotropic liquid crystals," in *Proceedings of IEEE MTT-S International Microwave Symposium Digest*, vol. 2, pp. 1153–1156, Fort Worth, Tex, USA, June 2004.
- [2] S. Mueller, *Grundlegende Untersuchungen steuerbarer passiver Flüssigkristall-Komponenten für die Mikrowellentechnik*, Ph.D. dissertation, FG Funk-Kommunikation, TU Darmstadt, Darmstadt, Germany, April 2007.
- [3] J. Anderson, P. E. Watson, and P. J. Bos, *LC3D: Liquid Crystal Display 3-D Director Simulator Software and Technology Guide*, Artech House, Boston, Mass, USA, 2001.
- [4] A. Gaebler, F. Goelden, S. Mueller, and R. Jakoby, "Efficiency considerations of tuneable liquid crystal microwave devices," in *Proceedings of the German Microwave Conference (GeMIC '08)*, pp. 271–274, Hamburg, Germany, March 2008.
- [5] D. M. Pozar, S. D. Targonski, and H. D. Syrigos, "Design of millimeter wave microstrip reflectarrays," *IEEE Transactions on Antennas and Propagation*, vol. 45, no. 2, pp. 287–296, 1997.
- [6] S. V. Hum, M. Okoniewski, and R. J. Davies, "Realizing an electronically tunable reflectarray using varactor diode-tuned elements," *IEEE Microwave and Wireless Components Letters*, vol. 15, no. 6, pp. 422–424, 2005.
- [7] R. R. Romanofsky, J. T. Bernhard, F. W. van Keuls, F. A. Miranda, G. Washington, and C. Canedy, "K-band phased array antennas based on $\text{Ba}_{0.60}\text{Sr}_{0.40}\text{TiO}_3$ thin-film phase shifters," *IEEE Transactions on Microwave Theory and Techniques*, vol. 48, no. 12, pp. 2504–2510, 2000.
- [8] H. Legay, G. Caille, E. Girard, et al., "MEMS controlled phase shifter elements for a linear polarized reflectarray," in *Proceedings of the 28th ESA Antenna Workshop*, Noordwijk, The Netherlands, May-June 2005.
- [9] R. Sorrentino, R. V. Gatti, L. Marcaccioli, and B. Mencagli, "Electronic steerable MEMS antennas," in *Proceedings of the 1st European Conference on Antennas and Propagation (EuCAP '06)*, pp. 1–8, Nice, France, November 2006.
- [10] A. Moessinger, R. Marin, S. Mueller, J. Freese, and R. Jakoby, "Electronically reconfigurable reflectarrays with nematic liquid crystals," *Electronics Letters*, vol. 42, no. 16, pp. 899–900, 2006.
- [11] W. Hu, M. Y. Ismail, R. Cahill, et al., "Liquid-crystal-based reflectarray antenna with electronically switchable monopulse patterns," *Electronics Letters*, vol. 43, no. 14, pp. 744–745, 2007.
- [12] P. Collings and M. Hird, *Introduction to Liquid Crystals: Chemistry and Physics*, Taylor & Francis, London, UK, 1997.
- [13] R. Marin, A. Moessinger, F. Goelden, S. Mueller, and R. Jakoby, "77 GHz reconfigurable reflectarray with nematic liquid crystal," in *Proceedings of the 2nd European Conference on Antennas and Propagation (EuCAP '07)*, pp. 1–5, Edinburgh, UK, November 2007.
- [14] A. Moessinger, R. Marin, J. Freese, S. Mueller, A. Manabe, and R. Jakoby, "Investigations on 77 GHz tunable reflectarray unit cells with liquid crystal," in *Proceedings of the 1st European Conference on Antennas and Propagation (EuCAP '06)*, pp. 1–4, Nice, France, November 2006.

Application Article

Active Reflectors: Possible Solutions Based on Reflectarrays and Fresnel Reflectors

**Lorena Cabria,¹ José Ángel García,¹ Julio Gutiérrez-Ríos,²
Antonio Tazón,¹ and Juan Vassal'lo³**

¹Departamento de Ingeniería de Comunicaciones, Universidad de Cantabria, Avenida los Castros s/n, 39005 Santander, Spain

²Departamento de Tecnología Fotónica, Universidad Politécnica de Madrid, Campus Montegancedo,
28660 Boadilla del Monte Madrid, Spain

³Instituto de Física Aplicada, Consejo Superior de Investigaciones Científicas, Serrano 144, 28006 Madrid, Spain

Correspondence should be addressed to Juan Vassal'lo, ltqvs22@ifa.cetef.csic.es

Received 24 September 2008; Revised 28 November 2008; Accepted 4 February 2009

Recommended by Giovanni Toso

An overview about some of the recent Spanish developments on active reflectors is presented. In the first part, a novel beamsteering active reflectarray is deeply studied. It is based on implementing in each elementary radiator an IQ modulator structure, in which amplitude and phase control of the scattered field is achieved. Finally, a special effort is made in offering solutions to overcome the active antenna integration problems. In the second part, the active concept is firstly extended to Fresnel reflectors. Thanks to the development of a proper simulator, this special structure can be easily analysed. This simulator allows the study of performance of this kind of reflectors and, applying evolutionary algorithms, to find optimal configurations of reflector in accordance with the given specifications for the conformal radiation pattern.

Copyright © 2009 Lorena Cabria et al. This is an open access article distributed under the Creative Commons Attribution License, which permits unrestricted use, distribution, and reproduction in any medium, provided the original work is properly cited.

1. Introduction

Nowadays, the development of antennas with reconfigurable beam pattern capabilities represents one of the keys issues for the future of the telecommunications and remote sensing applications. Considering this aspect, this paper proposes two different reconfigurable reflectors: an active reflectarray and a Fresnel reflector. The reflectarray is formed by resonant microstrip patches coupled to an active circuit which provides the amplitude and phase control of the reflected signal. The Fresnel reflector is based on the use of small reflecting cells, integrating each of them a mechanical control to regulate its position with respect to a reference one.

A reflectarray is a type of antenna that combines the best features of conventional reflector with those of the phased printed arrays. In this structure a horn or small antenna array illuminates a planar array of microstrip radiators, which, by using suitable phasing circuits, converts an incident spherical wave into a plane wave, collimating the reflected field in a desired direction [1]. Their low cost, flatness, and easiness to install and manufacture convert these structures into ideal

solutions to modern communication systems [2]. Moreover, spatial signal distribution avoids the complexity and losses associated to the microstrip feeding distribution network.

The possibility of employing active antennas as reflectarray cells offers additional advantages derived from their power combining features. In this sense, amplifying functions have been already added in individually phased active antenna elements [3]. Nevertheless, only a few works have considered the possibility of varying the scattered field phase from each element, achieving beam steering capabilities [4].

The control over the capacitance, obtained in [4] through the use of a varactor diode, has been also proposed for the design of reconfigurable reflectarrays with scanning capability, either serially connecting two halves of a microstrip patch [5] or phase tuning a high-impedance surface [6]. MEMS are also standing as a promising solution for the design of tuneable reflectarrays, mainly in terms of linearity, power consumption, losses, and size, as suggested from recent results [7].

Despite all their advantages, some problems have to be faced when designing or implementing active reflectarrays.

As a way of illustration, if high gain amplifying stages were employed between the orthogonal feeds of a patch, a poor out of band isolation between feeds might lead to amplifier oscillations. In this type of solutions, attention should be put to the radiator isolation characteristic versus frequency as well as to the detection of instabilities through the use of linear [8] but also nonlinear analysis techniques. In transmitting reflectarrays, especially when power amplifiers are integrated, especial attention should be put to thermal aspects. The available heat sink capability for power dissipation would impose a limit to the device output power level. The introduction of novel highly efficient technologies, as the case of GaN HEMTs, or the application of emerging transmitting concepts, could help overcoming this power handling limit.

With respect to Fresnel reflectors, as it is well-known, their surface efficiency cannot be greater than the provided by a parabolic reflector [9–11]. Nevertheless, they can offer advantages that a parabola cannot provide, as for example, the feeder of a Fresnel reflector can a change of position, out the focal point, without any important variation on performance.

This property is used to develop an active Fresnel reflector, placing a distribution of reflecting cells over a flat surface. Each one of these cells is coupled to an active mechanism which allows a change of position with respect to the feeder. So, any distribution of Fresnel zones can be configured over the whole reflecting surface.

The inclusion of active elements on these kinds of antennas (reflectarrays and Fresnel reflectors) provides a control over the antenna radiation pattern in the reflecting surface. So, the designer can work with a new freedom degree if this possibility is added to the classical control on the feeder.

2. Active Reflectarray Development

In this paper, an active reflectarray with attractive capability of varying the pencil-beam or shaped beam radiation pattern is presented. Based on the vector sum method, the amplitude and phase of the reradiated field from each elementary radiator is controlled by means of applying a DC voltage through the IF port of two double balanced diode mixers in an IQ configuration. This kind of structure can provide a new freedom degree, because the steering can be found from a control of active circuits in the feeder (as in a not very old manner) and also be included in the reflector surface.

By means of an accurate adjustment of each element phase shift, it is possible not only to convert the spherical wave into plane one but also to steer the main beam. In this sense, in order to demonstrate the proposed radiating architecture potentialities, different radiation patterns have been measured.

As the idea is to put in evidence advantages and drawbacks of this kind of antenna, a laboratory demonstrator was designed, manufactured, and measured. To optimize time and efforts, the selected reflectarray was designed to have a planar configuration of 4×2 radiating elements.

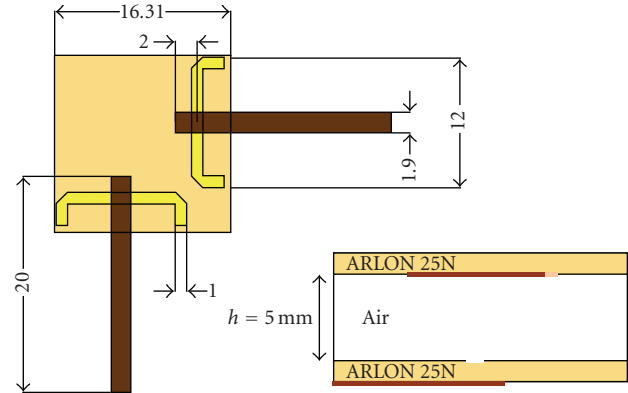


FIGURE 1: Top and side view of the designed square microstrip patch.

2.1. Radiating Element. An aperture coupled microstrip patch [12] with two orthogonal feeds has been selected as a reflectarray elementary radiator. One of its ports is employed to receive the signal from the feeder while the other is used to retransmit it with the amplitude and phase selected in the vector summing unit. Therefore, the square patch has two microstrip feeding inputs placed at perpendicular sides, exciting the TM₀₁ and TM₁₀ orthogonal modes for the same resonating frequency, aimed to the simultaneous reception and retransmission of the microwave signals using orthogonal polarizations. The dual feeding provides a reasonable isolation between its two ports, which is an important characteristic to be achieved when active elements are incorporated. The gain of the active path, from reception to retransmission, is limited by the isolation between both input ports, achieving an unstable state when such condition is not fulfilled.

Figure 1 illustrates the designed square microstrip patch. The active circuit and the feed microstrip lines have been printed in substrate ARLON 25N with $\epsilon_r = 3.38$ and thickness of 30 miles (0.762 mm). In order to improve the gain and the bandwidth, the air is employed as radiator substrate. Consequently, an auxiliary layer is needed to print the patch on it. The working frequency band, around 5.8 GHz in our particular application, determines the dimensions.

A commercial electromagnetic simulator (Ansoft Ensemble) has been employed to design and analyze the structure. In Figure 2, the simulated and measured input matching and isolation between both ports are shown.

2.2. Amplitude and Phase Control Unit. Figure 3 shows a scheme of the amplitude/phase control unit implemented in each elementary radiator. The received signal is equally divided through a 90° hybrid coupler exciting the LO ports of a pair of double balanced diode mixers. By proper adjustment of the DC voltage, applied in the IF port, it is possible to vary the amplitude and to switch the phase, between two values with a 180° shift (depending on the DC sign) of the RF signals. Finally, these output signals are combined employing a Wilkinson circuit achieving a complete (360°) phase control range.

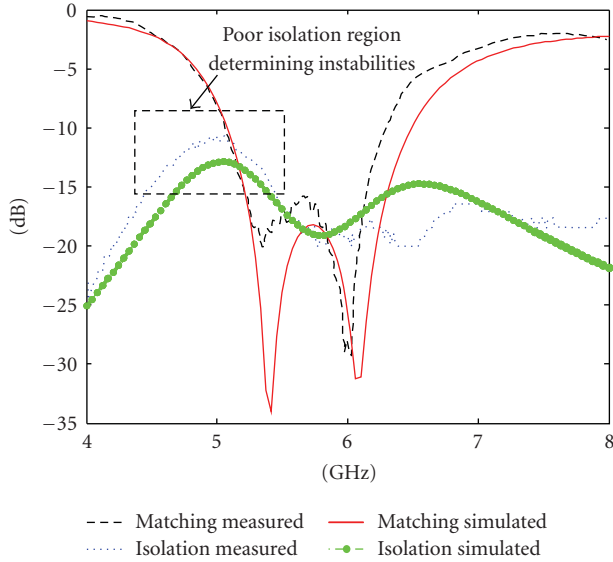


FIGURE 2: Measured and simulated input matching and isolation.

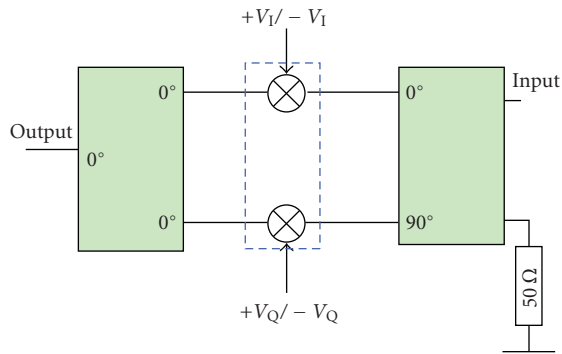


FIGURE 3: Amplitude/phase control unit used in each reflectarray elementary radiator.

In order to clarify this behavior, a summing scheme can be used. The output signal is the resultant vector obtained through a sum of two perpendicular variable vectors. Consequently, using a pair of conveniently selected voltage values, the magnitude and phase of the resultant vector may be controlled in a complete phase range.

2.3. Integration of the Active Circuits on the Radiating Element.

The radiating element and the amplitude/phase control circuitry were integrated in the same PCB employing the (Active Integrated Antenna (AIA)) concept to minimize the cable and feeding line losses in a similar way to [13].

In order to compensate the associated attenuation of the IQ control circuit two commercial amplifiers were added in each unit. In Figure 4, a clarifying schematic as well as a detailed photograph of the active elementary radiating unit can be seen.

In the photograph some parts of the reflectarray unit have been highlighted. The MBA-671 mixers from Minicircuits, and the NBB 400 amplifiers from RF Microdevices

constitute the active parts with a power consumption of 665 mW. In the IQ structure, the input 90° hybrid coupler is a high-quality and small size commercial circuit from Anaren, while the combination of the output signals of each mixer was done through a microstrip Wilkinson circuit specifically designed for it. To accurately adjust the phase/gain of each circuit, different SMA connectors were added to take samples of the signal in different parts.

The active control circuit was measured independently of the patch obtaining a maximum gain of 12 dB. Complete phase range was also measured for different gains.

Once the structure was measured with the SMA connectors and its correct performance verified, the complete radiating structure was probed appearing undesired oscillating frequencies around 5 GHz. The problem came associated to the poor isolation between the antenna ports at this band of frequencies, comparable to the gain of the active path, as it has been highlighted in Figure 2. Consequently, it was necessary to eliminate this unpleasant effect. Taking into account the limited space available in the reflectarray unit, a stub was added to reduce the coupling in the previously mentioned band, as it can be observed in Figure 4.

2.4. Active Reflectarray Implementation. Figure 5 shows the layout of the reflectarray. In such antenna, the selected feeder is an aperture-coupled microstrip patch equal to the reflectarray radiating elements, which transmits a signal in the working band with vertical polarization. The reflectarray active circuits, not included in this illustration in order to clarify the whole radiating structure, were inserted in the feeding layer.

In order to avoid feed blockage an offset feeding configuration was used, placing the feeder at 200 mm down from the center and 55 mm out from the array.

A photograph of the reflectarray feed layer is shown in Figure 6. As it has been previously commented, each unit has two varying bias voltages to control the mixers and one fixed voltage to supply the amplifiers.

Each element demands a phase shift value as a function of its position with respect to the feeder to convert the spherical incident wave to a planar one. There are different ways to achieve the required phase shift per cell: in [14] equal size microstrip patches are employed with passive coupled delay lines of different lengths, while in [15] the phase of the scattered field is controlled by means of the patch size. Although these methods permit to assure the correct antenna performance in a higher bandwidth, the proposed system takes advantage of the total phase control in each element provided by the active circuit. Additionally, the possibility of controlling the phase shift between microstrip patches allows the change of the main beam direction.

In such case, the field phase in each unit is calibrated independently to fulfill, (1) [15, 16]:

$$\phi_i = k_0 \cdot (R_i - \tilde{r}_i \cdot \tilde{r}_0), \quad (1)$$

where R_i is the distance from the feeder phase center to the element, \tilde{r}_i is the vector from the array center to the element, and \tilde{r}_0 is the unit vector in the main beam direction.

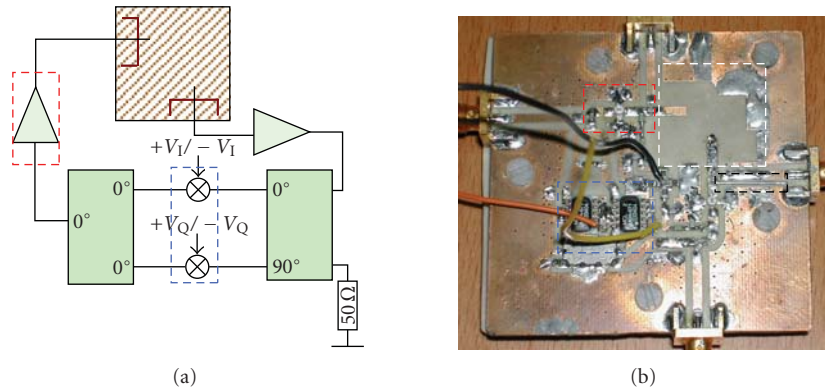


FIGURE 4: (a) Schematic and (b) photograph of the reflectarray unit.

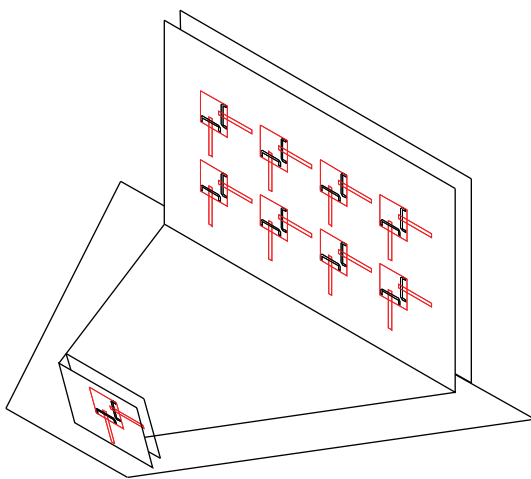


FIGURE 5: Layout of reflectarray, feeder included.

In order to vary the reflectarray beam pointing, the required phase shift values per radiating unit have to be recalculated following (1).

2.5. Measurement Results. A specific test setup was implemented in an anechoic chamber to measure the described antenna. In such scenario, a perfect calibrated horn antenna was employed in reception to measure the reflectarray response, assuring a far field distance between them. As it has been commented before, the radiation pattern phase evolution for each unit was calibrated in the main direction for different gains. In this way, it was possible to select those biasing points per unit to fulfill (1) for different pointing directions.

Due to the huge number of different controlling bias voltages and in order to generate a portable and compactness radiating structure, a special bias control circuitry was also implemented. The required voltages per unit, obtained in a previous step, were then introduced in a hexadecimal table in the PC as a function of the required gain and phase values. By means of an RS232 interface, the PC and the control board

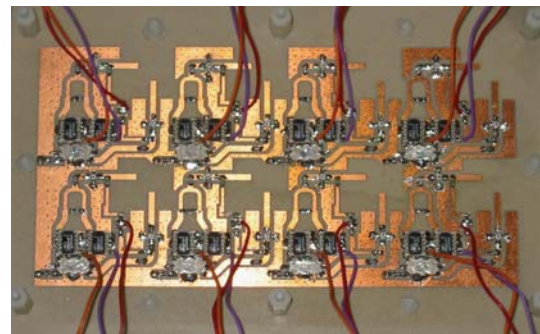


FIGURE 6: Reflectarray feeding layer.



FIGURE 7: Rear view of the final manufactured prototype.

are connected, being able to provide the required bias to each mixer and amplifier. A rear view of the manufactured prototype can be seen in Figure 7.

Finally, the far field radiation pattern of the reflectarray was measured for three main pointing directions (0° , 10° , -10°). The individual amplitude control would also permit to conform different amplitude distributions if desired. In Figures 8, 9, and 10, measurements of normalized radiation patterns for a uniform amplitude distribution have been represented. A comparative study between the resultant measurements and the calculated array factor of the retransmitted patterns has been done and illustrated in these figures.

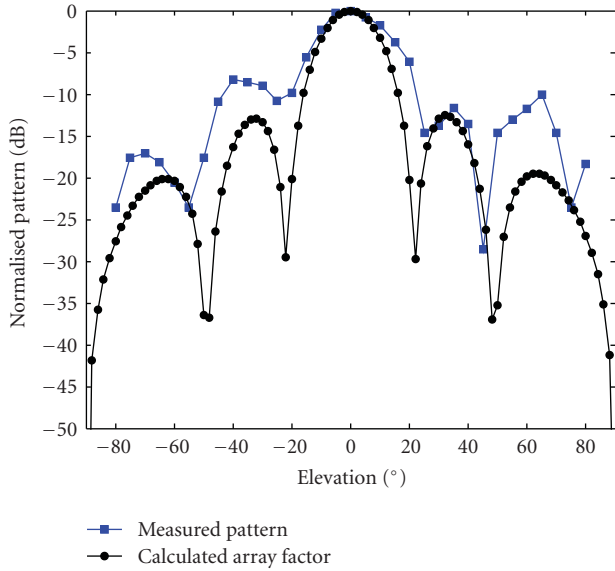


FIGURE 8: Measured and calculated reflectarray radiation pattern, pointing to 0°.

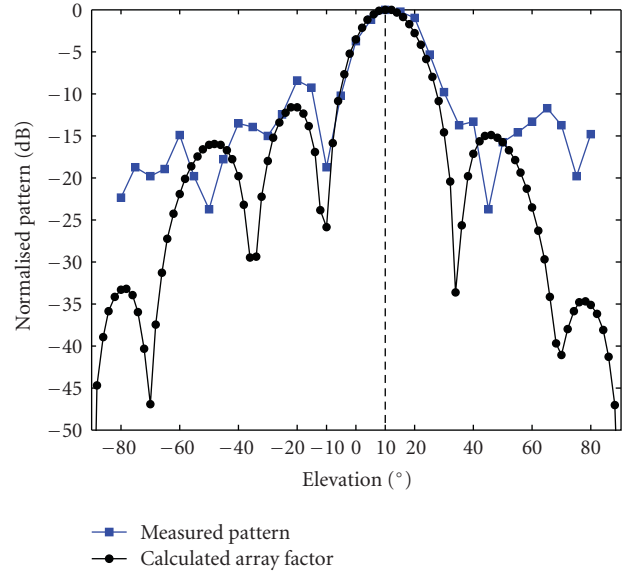


FIGURE 10: Measured and calculated reflectarray radiation pattern, pointing to 10°.

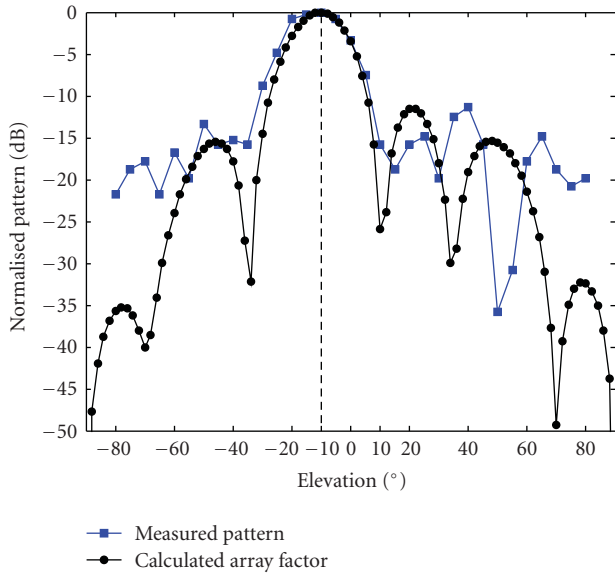


FIGURE 9: Measured and calculated reflectarray radiation pattern, pointing to -10°.

As it can be seen, the similarity among the obtained results and the calculated ones demonstrates the potentiality of the proposed architecture.

2.6. Some Consequences of the Developed Prototype. As it can be seen in the photograph of the demonstrator, one of the drawbacks of the implementation of the active elements on the reflecting surface is the positioning of the control and feeding DC circuitry.

In a reflectarray of small number of elements (only eight radiators), the drawback can be easily solved as it can be seen in the photograph of the developed demonstrator. But

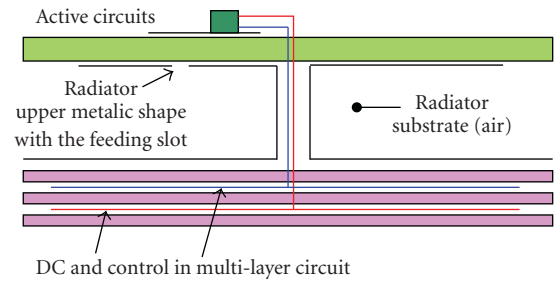


FIGURE 11: Structural concept to integrate DC and control circuit on active reflectarrays.

in the case of reflectarrays with high number of elements, it is necessary to achieve other kinds of solutions.

There are several possibilities now under development, for example, by means of a laser link between each module with a central unit or by using the DC circuitry as link of the control signal at low RF. Obviously, this solution has a better implementation by using a modular design.

Nevertheless, this restriction can be avoided if radiating elements are feeding from its radiating face. In this configuration, active circuits can be placed over the radiating face, and the control and DC circuitry can cross the microstrip patch through a metallic post placed on its center, because this central part of the radiator has a zero per impedance.

Then, the distribution circuitry of control and DC can be easily manufactured on a multilayer substrate and placed behind of the radiator microstrip ground plane. Figure 11 shows this solution.

3. Active Fresnel Reflector Development

Fresnel reflectors having arbitrary main beam transversal section, by means of conformed Fresnel zones, were

presented in [17]. This possibility allows the design of a new concept on active reflectors, based on squared reflecting cells, each one coupled to a mechanical actuator. This configuration provides a degree of freedom about the position of each cell in the z -axis to be able to conform a good approximation to any desired Fresnel reflector geometry.

The idea that is explained in this paragraph is based on a flat structure formed by small reflectors, whose position is electronically controlled by means of mechanical actuators. So, a flat reflector with this configuration can work with any Fresnel distribution. The lattice of small reflecting cells is electronically controlled to provide any Fresnel distribution over the reflector surface and then to have a real control of the radiation pattern.

The number of mechanical actuators can be a problem of manufacturing, weight, and cost of the final prototype, and consequently it can constitute a limit for the approach of different radiation patterns to be generated. Nevertheless, in applications where the number of desired beams is small and previously known, the cell size can be optimized in order to reduce the number of actuators. The consequence is a final prototype of more easy manufacturing process and lower weight and cost.

Reflectors having Fresnel zones with axial symmetry have been analyzed in [18]. Results show that the behavior can be optimized depending of special parameter of this kind of reflectors, as for example, the number of levels of reflecting Fresnel zones. So, a specific simulator for Fresnel reflectors of squared cells has been developed, and its results are to be commented below.

3.1. Active Fresnel Reflector

3.1.1. Electrical Concept. The radiation pattern of a reflected signal can be modified by changes in the geometrical characteristics of the reflecting surface. As it is known, perturbations on parabolic surfaces allow any desired 3 dB transversal section in the main beam, being actually the best solution applied in geosatellite antennas for communication links.

This concept was translated in [17] to the Fresnel reflector technology, and a general behavior of Fresnel reflectors can be seen in [18], being the case of reflectors with 2 or 3 levels as the more interesting ones from performance and manufacturing point of view.

A Fresnel reflector design with 144 actuators of two positions, controlling an array of 12×12 reflecting cells, is to be described in this paper. The antenna has been designed to provide a beam scanning in the principal plane direction, having the main beam at the symmetric direction to the focal position of the feeder from the central point of reflecting surface (see Figure 12).

The selected working frequency was 18.75 GHz, which must be in accordance with the distance separation among levels, which is provided by the selected actuator. The cell size was selected taking into account the supposed application of the example, in order to avoid grating lobes and the area to be covered by the scanning. The desired beam scanning zone is

between 0° and -20° , in the principal plane, which includes the focal point.

Once the geometry of the reference Fresnel configuration is determined, the movement of the synthesized geometry over the reflector surface will provide the beam scanning. So, the Fresnel configuration of reference must be synthesized over a surface bigger than that of the reflector. This allows the changes as it is shown in Figure 13, where there are three reflector configurations for different appointments.

It is obvious that in this structural concept, the feeder is always in the same position. The unique change on the antenna, which provides the desired scanning, is the change of the position of the Fresnel configuration on the reflector surface, as it can be seen in Figure 13. Figure 14 shows the superposition of simulated array factors of the Fresnel configurations to cover the selected scanning area. The evolution of the radiation pattern is shown in Figure 14, and consequently it can be understood that any reflected direction can be obtained by placing the Fresnel configuration at the adequate place over the reflector surface.

3.1.2. Mechanical Concept. To allow the change of Fresnel level of any reflecting cell, each Fresnel level is associated to a different position of the reflecting surface of the cell, thinking that this different position is referred to the perpendicular direction to the reflector surface.

To provide this position change, a commercial actuator (solenoids, series 45B) was selected from the web page of RS AMIDATA. Figure 15 shows the geometry data sheet.

As it can be seen in Figure 16, the actuator is placed under each reflecting cell, and it allows a displacement of the reflecting cell of 4.5 mm, which is electronically controlled. This figure shows two complete active reflecting cells, at both states: 0 and 1, which corresponds to both Fresnel levels. The actuator is placed at the position 1 when there is a voltage of 6 V at the inputs of actuator terminal, and it is placed at the position 0 when the voltage is 0 V. The actuator works over the reflecting cell as it can be seen in Figure 16.

When the aim is to implement reconfigurable Fresnel reflectors with more than two levels, the actuator should be different form that commercially available. However there is not a great technological problem, including a continuous shift solution. We can think about a little screw pin moved by a small electrical motor, step-by-step or continuous type.

Figures 17 and 18 show, a view of the whole Active Fresnel Reflector, respectively with the Fresnel configuration of Figures 13(b) and 12. The case that is shown in Figure 17 corresponds to the synthesized Fresnel configuration which is centered on the surface of the reflector.

3.2. Simulator of Fresnel Reflectors. Performance of Fresnel reflectors depends on the number of levels implemented but the result obtained with a three levels implementation is very reasonable. As a matter of fact, gain of a three levels reflector is usually about 1.5 dB under a same aperture and same focus paraboloid. However Fresnel reflectors have several important advantages: first, the fact being smaller in terms of occupied room. Second, the deployment system is

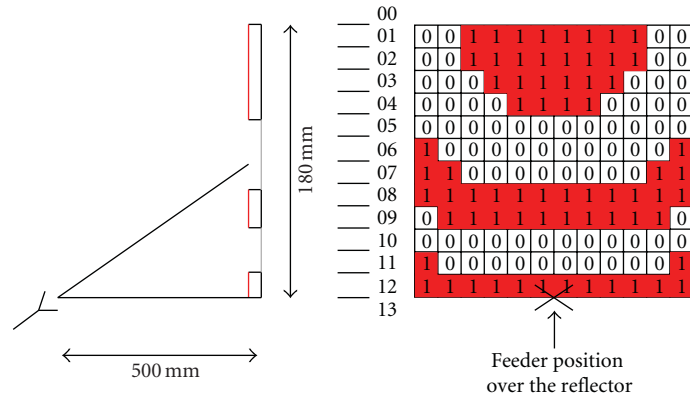


FIGURE 12: Geometry of the synthesized Fresnel reflector configuration.

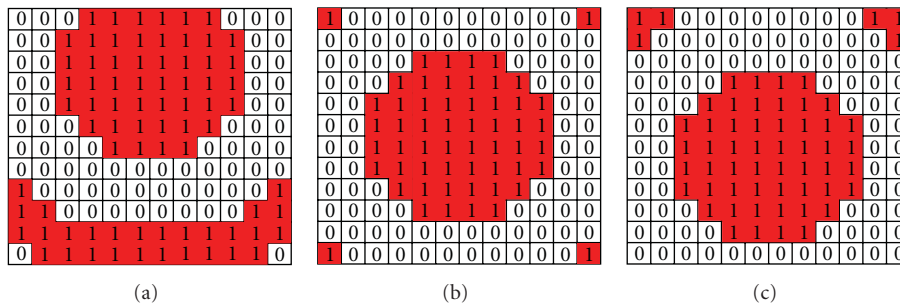


FIGURE 13: Reflector configuration for different positions of the Fresnel configuration.

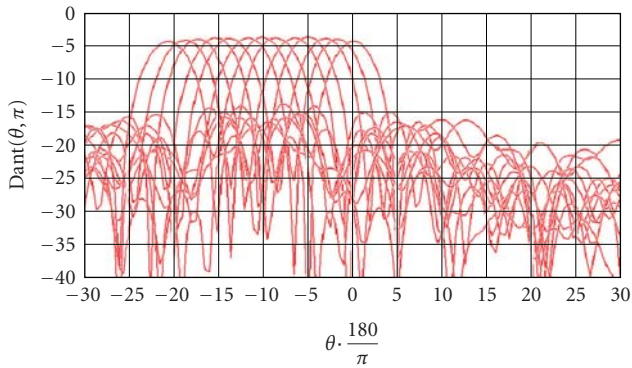


FIGURE 14: Superposition of simulated array factors, which are obtained by movement of the synthesized Fresnel distribution.

easier for them. Third, the possibility of combining several Fresnel distributions in a same reflector surface to get multibeam radiation patterns. Finally, the manufacturing process is very easy and very cheap by means of photoetched procedures.

Fresnel reflectors performance has been widely studied by means of a computer simulator developed by ourselves which is specially adequate and flexible for reflectors with circular symmetry [19–21]. We also have developed a methodology to optimize shaping of Fresnel reflectors [22, 23].

Now, a new simulator has been specifically developed for reconfigurable reflectors composed by squared elements,

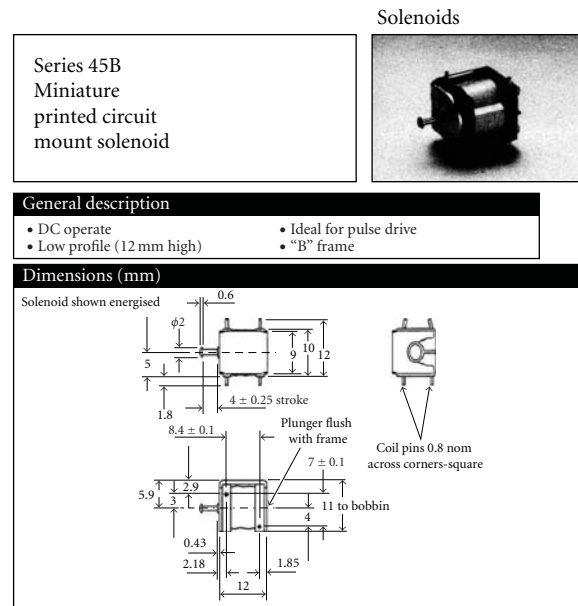


FIGURE 15: Actuator data sheet.

with any number of levels or continuous shifting. In order to get a good efficiency, we have extracted the response of a squared element with uniform illumination. In this way, the response of the reflector is the superposition of the responses of all elements, once situated each one in its location and

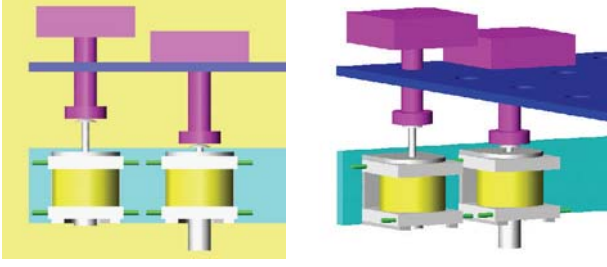


FIGURE 16: Views of two mechanical actuators, working over its respective reflecting cell, at both Fresnel levels: 0 and 1.

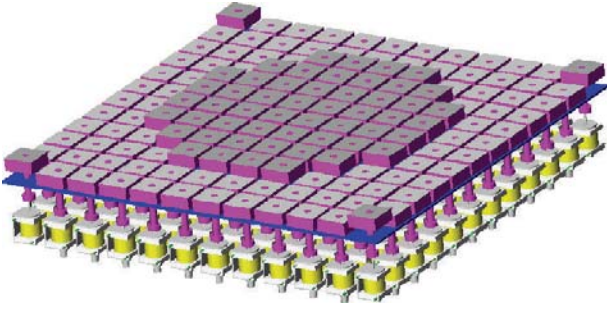


FIGURE 17: View of the active Fresnel reflector with the configuration of Figure 13(b).

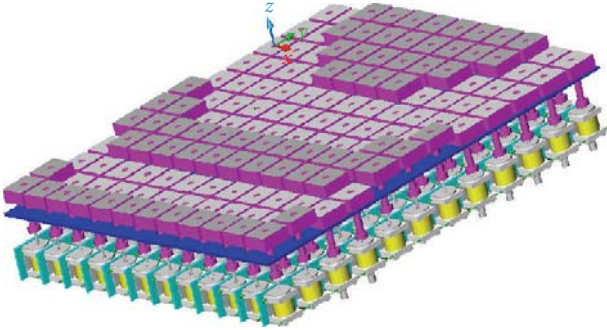


FIGURE 18: View of the active Fresnel reflector with the configuration of Figure 12.

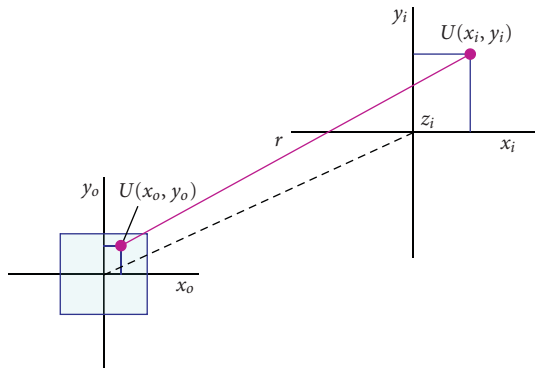


FIGURE 19: Geometry and notation of the radiating cell.

level. The assumption that resonance effects and boundary conditions in edges of squared elements are small enough to be neglected is very reasonable because they affect mainly to radiation far from the main lobes. Besides, there are structural media to minimize those effects, as we will try to prove in the future when physical experimentation becomes possible.

On the other hand, the assumption of uniform illumination in the whole area of each conformable element could not be too much closed to the real case; we use a grid to decompose the surface of the reflecting elements in smaller squares (rectangles in general terms) to the end of getting simulation elements small enough to be considered, each one as uniformly illuminated.

Although the normal case is to have squared elements, we are going to consider rectangular ones for giving more generality and flexibility to the simulator.

3.2.1. Rectangular Reflecting Cell. A rectangular surface is used as a reference. The center of this element will be located at $(x_o, y_o, z_o) = (0, 0, 0)$ as shown in Figure 19. In this case, the function of luminance of a rectangle with dimensions $a \times h$ can be represented by the following expression (2) [24, 25]:

$$U(x, y) = f(x, y) \cdot \Pi\left(\frac{x}{a}\right) \cdot \Pi\left(\frac{y}{h}\right), \quad (2)$$

being $f(x, y)$ the function of luminance inside the rectangle, and $\Pi(u/b)$ a pulse in axis u of amplitude 1 between $-b/2$ and $b/2$. But, if luminance is uniform of amplitude A , function (2) is reduced to

$$U(x_o, y_o) = A \cdot \Pi\left(\frac{x_o}{a}\right) \cdot \Pi\left(\frac{y_o}{h}\right). \quad (3)$$

In order to get the far field radiation pattern of the rectangular element, we will use the Fresnel-Kirchhoff diffraction formula [24] as follows:

$$U(x_i, y_i) = \frac{1}{j\lambda} \iint \frac{\exp(jkr)}{r} \cdot U(x_o, y_o) \cdot dx_o dy_o. \quad (4)$$

According to Figure 19, the distance r of an elementary emitter in x_o, y_o to an arbitrary far field point in a plane x_i, y_i , parallel to the plane of the radiating element will be calculated as follows:

$$\begin{aligned} r^2 &= z_i^2 + (x_i - x_o)^2 + (y_i - y_o)^2, \\ z_i^2 &\gg (x_i - x_o)^2 + (y_i - y_o)^2, \\ r &= z_i \cdot \sqrt{1 + \frac{(x_i - x_o)^2 + (y_i - y_o)^2}{z_i^2}} \\ &\cong z_i \left(1 + \frac{(x_i - x_o)^2 + (y_i - y_o)^2}{2 \cdot z_i^2} \right), \\ r &\cong z_i \frac{x_i^2 + y_i^2}{2 \cdot z_i^2} - \frac{x_i \cdot x_o + y_i \cdot y_o}{z_i}. \end{aligned} \quad (5)$$

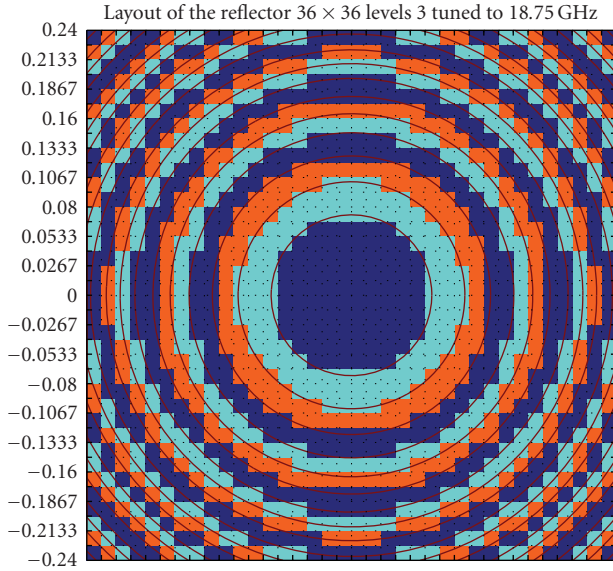


FIGURE 20: Fresnel reflector of square cells and 3 levels.

Then, introducing this expression of r and the luminance in (4) in the Fresnel-Kirchhoff diffraction formula in (5), we get the far field (Fraunhofer space) due to a rectangular element as follows:

$$U(x_i, y_i) = \frac{a \cdot h}{j\lambda \cdot z_i} \exp \left[jk \left(z_i + \frac{(x_i^2 + y_i^2)}{2 \cdot z_i} \right) \right] \cdot \text{sinc} \left(a \frac{x_i}{\lambda \cdot z_i} \right) \cdot \text{sinc} \left(h \frac{y_i}{\lambda \cdot z_i} \right). \quad (6)$$

3.2.2. Fresnel Reflector Conformed by Squared Reflecting Cells. Once developed a method to get the optimal shape for a flat Fresnel reflector [22], the approaching procedure to obtain a reflector conformed by squared reflecting cells will consist of setting every squared cell at the same level that had its central point in the ideal Fresnel reflector.

As an example, Figure 20 shows the layout of a reflector configured by means of a reconfigurable reflector of 480×480 mm and 36×36 elements. The shape of the original reflector has been indicated by circles in the same figure. The reflector has been designed at three levels (each level a different color); the focal distance is 500 mm and has been tuned to 18.75 GHz.

It is easy to see in Figure 20 that there is a misalignment between the optimal shape of the Fresnel reflector and that conformed by squares. Of course, increasing the density of elements, they become smaller, and the approximation to the ideal Fresnel reflector, as well as the efficiency of the reflector, is better. However, the reconfigurable system would be more complex and expensive. We will describe below the procedure to get the fair dimensions.

3.2.3. Grid and Feeding Distribution for Simulation. Simulation process has nothing to do with the configuration of the reflector. Any configuration will be simulated by

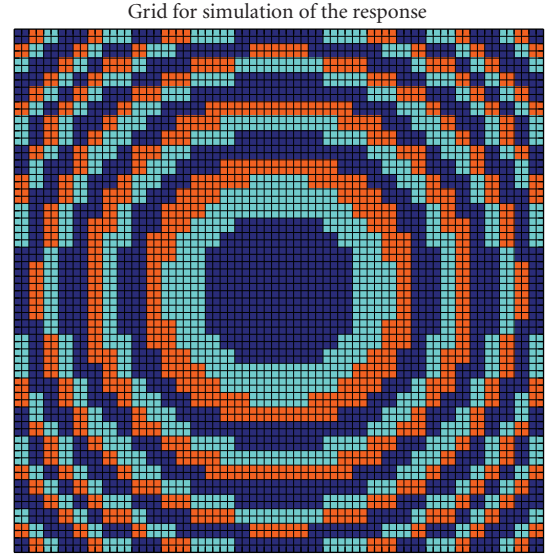


FIGURE 21: Grid for simulation proposal.

iteratively applying formula (6) for each one of the squared (or rectangular if it were the case) elements once moved to the position x, y, z relative to each point of the de radiation pattern one want to find.

This fact implies that we must know the location, the level (z), and the luminance A of every element, and also that we can suppose that squares are uniformly illuminated. The location and shifting of the elements are well-known parameters. However, the fact of being correct or not to, consider uniform illumination on the surface of the elements, depends on the size of the facets and of the feeding conditions as, for example, radiation pattern of the feeder (or feeders), focal distance, or location and orientation of the feeder.

In order to avoid erroneous considerations about this aspect, the simulator has been designed in such a way that the elements for making simulation can be smaller than the real elements. That is, the real elements can be decomposed into any number of squared or rectangular cells, small enough to be able to consider uniform illumination in each cell.

In other words, the grid used to decompose the surface of the reflector will be smaller than the one defined by the moving facets or squared elements of the reflector. Of course, the simulation cells will be an entire fraction of the moving facets. Figure 21 shows a grid for simulation of the Fresnel reflector whose layout is in Figure 20. As it can be seen, the grid has been made dividing each element into 2×2 cells.

Once determined the grid for simulation, the next step consists in calculating the intensity of illumination received by all its cells. Knowing the radiation pattern of the feeding system, this calculus is immediate.

As what we want in principle is to know the behavior of a reconfigurable reflector based on squared elements, we are going to consider an ideal feeder which radiates uniformly in any direction but only in the coverage of the aperture of the

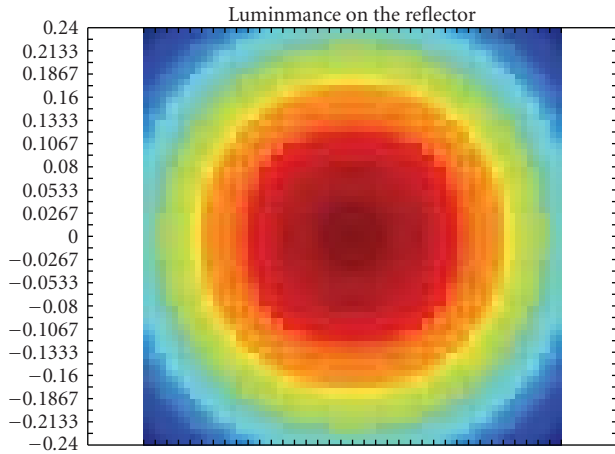


FIGURE 22: Luminance on the grid under ideal feeding conditions.

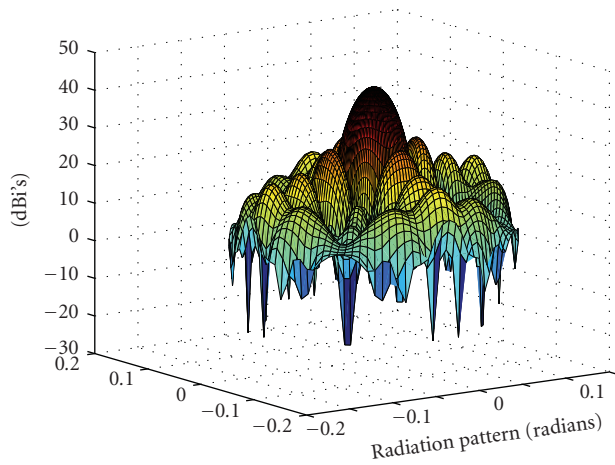


FIGURE 23: Radiation pattern from the 3D simulator.

reflector (squared in this case of study). In Figure 22, it can be seen a color map of the luminance on the grid from the feeder in that conditions.

3.2.4. Response Analysis. As mentioned above, the analysis of the response consists in the superposition of the response of all the cells according to (6). As, in general, the aperture of a reconfigurable reflector can have an arbitrary shape, the radiation pattern will not be symmetrical but will have a different pattern depending on the considered cut. For example, in a squared aperture, as our case of study, the cut of the radiation pattern in a direction parallel to a reflector side will be different from the cut in the direction of a diagonal, or something else. Consequently, it is necessary to specify the angle of the cut to be considered with respect to one of the axis transversal to propagation direction. Another variant we have implemented is the simulator 3D which is able to represent the full diagram, all around the propagation axis (see Figure 23).

Also, to have an idea about performance of the configuration designed and implemented in the reconfigurable

$NX = 36, NY = 36, N = 3nx = 2ny = 2, AX = 0.48, AY = 0.48, f = 0.5,$
 $f_{rn} = 18.75, f_{rr} = 18.75, \phi = 0.7854, \text{gain} = 42.43, \text{gain parab.} = 46.91$

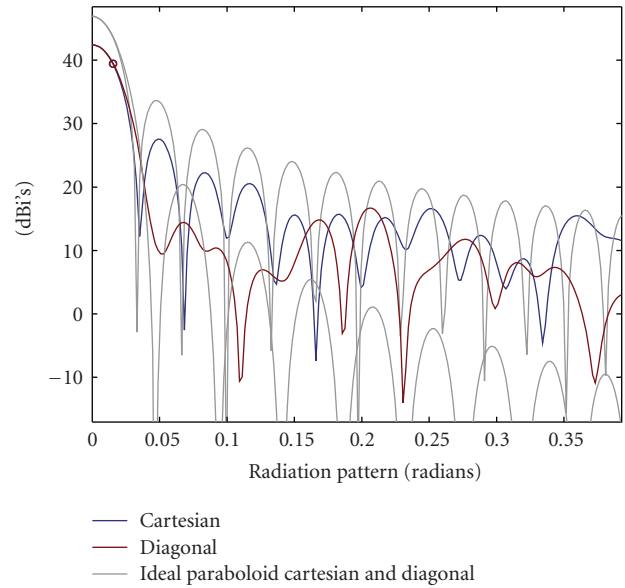


FIGURE 24: Radiation pattern at 0° and 45° obtained from developed simulator.

reflector, we will represent the radiation pattern of an absolutely ideal parabolic reflector of the same aperture. The radiation pattern of our case of study as well as of the absolutely ideal paraboloid of the same aperture, in parallel and diagonal directions can be seen in Figure 24.

What we have adopted as *absolutely ideal paraboloid* is the radiation of its aperture under condition of uniform field in amplitude and phase, that is, the result of applying (6) to the whole aperture. Due to the fact that in our case of study we have not uniform illumination (Figure 22) but uniform radiation of the feeder, a difference of 4.48 dB from ideal paraboloid (Figure 24) is quite acceptable.

However, if we would conform a paraboloid by means of the reconfigurable reflector (supposed that it was permitted by its structure) in the same conditions of feeding as in the case of the squared Fresnel reflector, the difference only is 1.66 dB as can be seen in Figure 25. The results of simulation for the conformed Fresnel reflector used as a case of study in 3D can be seen in Figure 23.

As mentioned above, the selection of the size of the grid is very important for simulation. In fact, if the simulation grid is of the same size as the division in facets of the reconfigurable reflector, simulation can be poor, but if the grid is too much dense, simulation process proves to be very heavy and results can be indistinguishable from those obtained with a less compact grid.

In order to illustrate this simulation effect, we have made simulation of our case of study using grid cells of the same size of the facets (1×1) in comparison with simulation with grid dividing facets in 2×2 and also with a grid 3×3 . As it can be seen in Figure 26, there is a sensible difference between results from 1×1 and 2×2 . However, between 2×2 and 3×3 , difference is negligible.

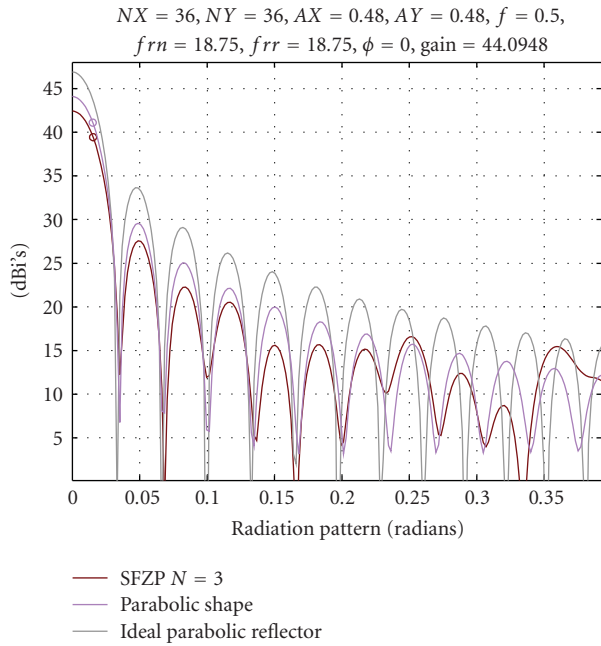


FIGURE 25: Comparison between parabolic shape and Fresnel reflector of squared cells.

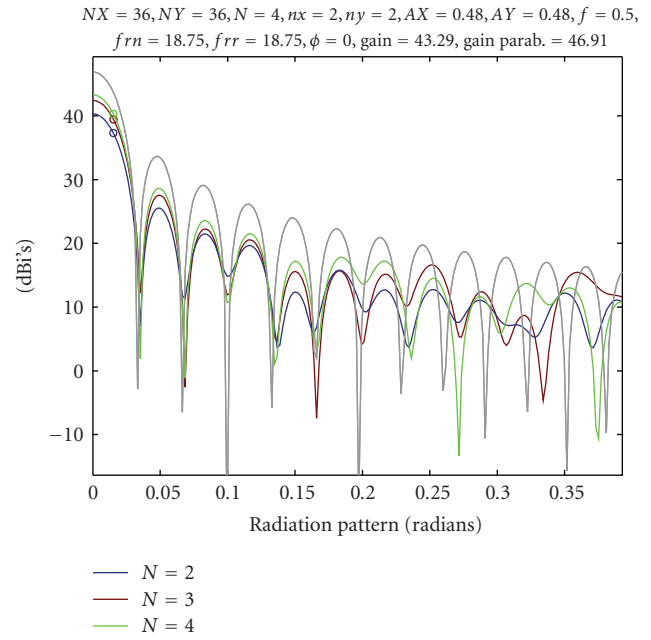


FIGURE 27: Radiation pattern of Fresnel reflectors of squared cells of 2, 3, and 4 levels.

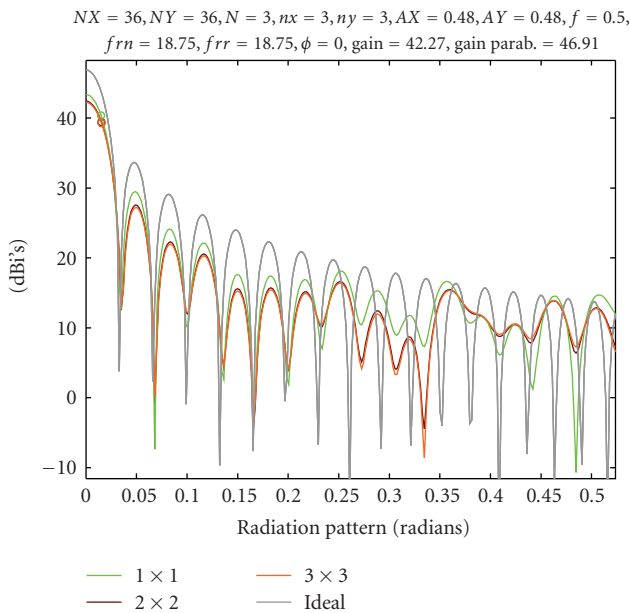


FIGURE 26: Comparison of simulations 1×1 , 2×2 , and 3×3 .

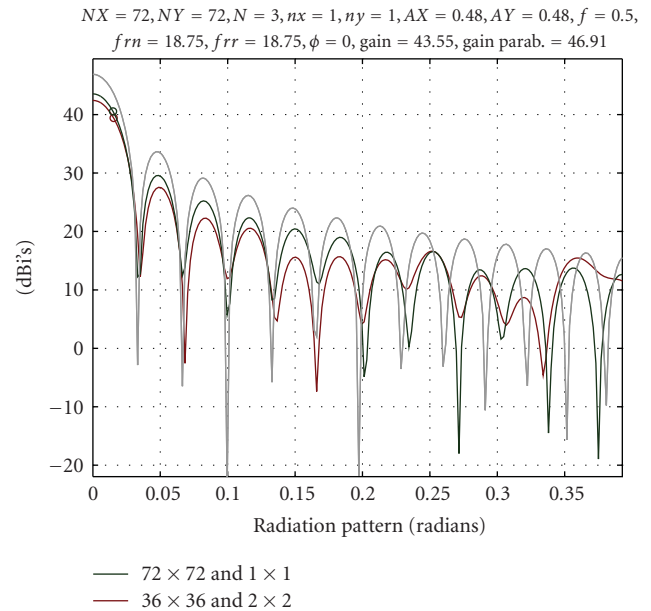


FIGURE 28: Comparison of Fresnel reflectors of 72×72 and 36×36 reflecting squared cells, having the same radiating aperture.

It is also interesting to evaluate the efficiency of the reconfigurable reflector when conforming Fresnel reflectors, depending on the implemented number of levels, that is, the number of steps that can establish the shifting actuator like that shown in Figure 26 whose number of levels is two. However, it is important to take into account that the efficiency versus number of levels is not independent of the size of the facets of the reconfigurable reflector. As a matter of fact, the greater the number of levels is, the narrower the

size of the Fresnel zones will be. On the contrary, the size of the facets can become wider than many Fresnel zones, which means that the approach to the Fresnel reflector of reference could be very poor. Then, it is necessary to use a size of facets according to the wavelength and to the number of levels to be implemented.

For example, in the initial case of having a reflector of 480×480 mm with 36×36 facets, gain varies with the number of implemented levels as follows: 40.3 dB for two levels ($N =$

2), 42.43 dB for three levels ($N = 3$), and 43.29 dB for four levels ($N = 4$). In Figure 27, it can be seen the radiation patterns for these three configurations.

However, if we would use a reconfigurable reflector of the same dimensions but with 72×72 elements instead of 36×36 , performance gets much better since it also betters the approach to the Fresnel reflector of reference. As it can be seen in Figure 28, gain is better with three levels ($N = 3$) in the case of 72×72 than with higher number of levels ($N = 4$) in the case of 36×36 . Concretely, in the first case gain is 43.55 dB, while in the second it is 43.29 dB. In both cases, the grid of simulation is really of 72×72 cells, because in the first case each element of simulation is equal to one facet, while in the second one, each facet is divided in 2×2 simulation cells.

4. Conclusions

An active reflectarray with beam steering capabilities has been designed, manufactured, and measured. Based on an IQ configuration, the amplitude and phase of the scattered field for each of its radiating units have been varied. The obtained phase control permits to achieve the required phase shift, not only to convert the spherical incident wave into a plane one but also to steer the main beam. Furthermore, different amplitude distributions with different gains can be easily implemented by using these elements. The measurements of the radiation pattern pointing to different elevation angles have demonstrated the potentiality of the proposed architecture.

On the other hand, a Fresnel reflector configuration can be electronically modified to provide any desired radiation pattern. Beam steering or radiation pattern reconfigurability is some of the possible applications of this new structural concept on active antennas. The design of a square flat reflector with 144 actuators, working at 18.75 GHz, shows antenna performance.

Simulation of this kind of reconfigurable reflectors having squared (or rectangular) reflecting cells has also been proved to be reliable and efficient. The procedure has been made by means of the superposition of the radiation of all the elements on a simulation grid. The simulation grid consists in a decomposition of the reflector in a grid of cells sub-multiple of the elements or facets of the reflector.

Reconfigurable reflectors are very adequate to conform Fresnel plate zones since they are efficient and require only small shifts of the facets. The efficiency of Fresnel reflectors depends on the number of levels implemented and on the size and number of available facets. A reasonable option is to implement three levels with a size of facets adequate for a good sampling of the corresponding reflector profile.

Acknowledgments

The authors would like to thank the Spanish Ministry of Science and Innovation, by the financial support provided through Projects TIC 2000-0401-P4-09, TIC 2002-04084-C03-03, TEC 2005-07985-C03-01/TCM, and TEC 2008-06684-C03-01/TEC as well as the Collaboration Agreement

between the Polytechnical University of Madrid and the Institute of Applied Physics of CSIC to develop new electrical and structural concepts on reflecting antennas. This work is also a result of the collaboration activities in the framework of COST 284 and IC 0603. The authors also thank Andrés de Frutos by his work on drawings and Roque Vassal'lo by the suggestions about the developed prototype of the active Fresnel reflector.

References

- [1] D. M. Pozar, S. D. Targonski, and H. D. Syrigos, "Design of millimeter wave microstrip reflectarrays," *IEEE Transactions on Antennas and Propagation*, vol. 45, no. 2, pp. 287–296, 1997.
- [2] J. Huang, "Capabilities of printed reflectarray antennas," in *Proceedings of the IEEE International Symposium on Phased Array Systems and Technology (PAST '96)*, pp. 131–134, Boston, Mass, USA, October 1996.
- [3] M. E. Bialkowski, A. W. Robinson, and H. J. Song, "Design, development, and testing of X-band amplifying reflectarrays," *IEEE Transactions on Antennas and Propagation*, vol. 50, no. 8, pp. 1065–1076, 2002.
- [4] L. Boccia, F. Venneri, G. Amendola, and G. Di Massa, "Experimental investigation of a varactor loaded reflectarray antenna," in *Proceedings of the IEEE MTT-S International Microwave Symposium (MWSYM '02)*, vol. 1, pp. 69–71, Seattle, Wash, USA, June 2002.
- [5] S. V. Hum, M. Okoniewski, and R. J. Davies, "Realizing an electronically tunable reflectarray using varactor diode-tuned elements," *IEEE Microwave and Wireless Components Letters*, vol. 15, no. 6, pp. 422–424, 2005.
- [6] P. Ratajczak, P. Brachat, and J.-M. Baracco, "Active reflectarray based on high impedance surface," in *Proceedings of the IEEE Antennas and Propagation Society International Symposium (APS '07)*, pp. 5327–5330, Honolulu, Hawaii, USA, June 2007.
- [7] J. Perruisseau-Carrier and A. K. Skrivervik, "Monolithic MEMS-based reflectarray cell digitally reconfigurable over a 360° phase range," *IEEE Antennas and Wireless Propagation Letters*, vol. 7, pp. 138–141, 2008.
- [8] R. W. Clark, G. H. Huff, and J. T. Bernhard, "An integrated active microstrip reflectarray element with an internal amplifier," *IEEE Transactions on Antennas and Propagation*, vol. 51, no. 5, pp. 993–999, 2003.
- [9] H. D. Hristov, *Fresnel Zones in Wireless Links, Zone Plate Lenses and Antennas*, Artech House, Boston, Mass, USA, 2000.
- [10] A. Pedreira and J. Vassal'lo, *Performance Review of Fresnel Zone Flat Reflectors*, PIERS, Boston, Mass, USA, 2002.
- [11] O. V. Minin and I. V. Minin, *Diffractional Optics of Millimeter Waves*, IOP Publishing, Bristol, UK, 2004.
- [12] D. M. Pozar, "Microstrip antenna aperture-coupled to a microstrip line," *Electronics Letters*, vol. 21, no. 2, pp. 49–50, 1985.
- [13] V. Radisic, Y. Qian, and T. Itoh, "Novel architectures for high-efficiency amplifiers for wireless applications," *IEEE Transactions on Microwave Theory and Techniques*, vol. 46, no. 11, part 2, pp. 1901–1909, 1998.
- [14] D.-C. Chang and M.-C. Huang, "Microstrip reflectarray antenna with offset feed," *Electronics Letters*, vol. 28, no. 16, pp. 1489–1491, 1992.
- [15] D. M. Pozar and T. A. Metzler, "Analysis of a reflectarray antenna using microstrip patches of variable size," *Electronics Letters*, vol. 29, no. 8, pp. 657–658, 1993.

- [16] J. Huang, "Microstrip reflectarray," in *Proceedings of the IEEE Antennas and Propagation Society International Symposium (APS '91)*, vol. 2, pp. 612–615, London, Canada, June 1991.
- [17] J. Vassal'lo, A. Oñoro, F. Ares, et al., "ARCO: a Spanish contribution to the improvement to arrays and reflectarrays with beam control," in *Proceedings of the 28th ESA Antenna Workshop on Space Antenna Systems and Technologies*, vol. WPP-247, pp. 853–860, Noordwijk, The Netherlands, May–April 2005.
- [18] J. Gutiérrez-Ríos and J. Vassal'lo, "Technological aspects of fresnel zone reflectors," in *Advanced on Antennas, Reflectors and Beam Control*, chapter 4, pp. 85–113, Research Signpost, Trivandrum, India, 2005.
- [19] J. Gutiérrez-Ríos and J. Vassal'lo, "Fresnel zone plate reflectors simulation and radiation diagram analysis," in *Proceedings of the 3rd COST 284 Workshop on Innovative Antennas*, pp. 1–4, Budapest, Hungary, April 2003.
- [20] J. Gutiérrez-Ríos and J. Vassal'lo, "Simulación eficiente de la respuesta de reflectores circulares. aplicación a reflectores de fresnel FZP," in *Proceedings of the 18th Simposium Nacional de la Unión Científica Internacional de Radio (URSI '03)*, Coruña, Spain, September 2003.
- [21] J. Gutiérrez-Ríos, J. Vassal'lo, and H. Palacios, "Synthesis and response-analysis of fresnel zone plate reflectors," in *Proceedings of the Joint Spanish URSI/COST 284 Workshop*, Barcelona, Spain, September 2004.
- [22] J. Gutiérrez-Ríos and J. Vassal'lo, "Shape optimization of FZP reflectors," in *Proceedings of the 27th ESA Antenna Technology Workshop on Innovative Periodic Antenas: Electromagnetic Bandgap, Left-Handed Materials, Fractal and Frequency Selective Surfaces*. WPP-222, Santiago de Compostela, Spain, 2004.
- [23] J. Gutiérrez-Ríos and J. Vassal'lo, "Simulated response of Conic Fresnel Zone Plate Reflectors (CFZPS)," in *Proceedings of the 1st European Conference on Antennas and Propagation (EuCAP '06)*, pp. 1–7, Nice, France, November 2006.
- [24] K. Iizuka, "Elements of photonics," in *Free Space and Special Media*, vol. 1, pp. 389–392, John Wiley & Sons, New York, NY, USA, 2002.
- [25] A. Van der Lugt, *Opical Signal Processing*, John Wiley & Sons, New York, NY, USA, 1992.

Research Article

An Iterative Technique for the Synthesis of Active Antenna Oscillator Arrays

Theodoros N. Kaifas and John N. Sahalos

Radiocommunications Laboratory, Aristotle University of Thessaloniki, 54124 Thessaloniki, Greece

Correspondence should be addressed to John N. Sahalos, sahalos@auth.gr

Received 1 September 2008; Revised 16 December 2008; Accepted 5 February 2009

Recommended by Stefano Selleri

A design procedure for the synthesis of a coupled active antenna oscillator array is presented. Such an array is synthesized by deriving two sets of parameters: the radiators' positions and the oscillators' outputs. The outputs are used to excite the radiators. Minimization of the mean square error between the desired pattern and the resulting one is made. Synthesis starts from an initial array, which is perturbed iteratively by varying simultaneously the element excitations and positions. In the iteration, the first variation of the cost function is set equal to zero. The final array results from the last iteration, where the stopping criteria are met. The procedure designs simultaneously both the antenna and the attached coupled oscillator array providing viable solutions. The second by properly configuring the tuning parameters through the use of closed-form formulas. The resulting arrays are shown to comply with the desired pattern and the nonlinear dynamics thus proving the validity of our method.

Copyright © 2009 T. N. Kaifas and J. N. Sahalos. This is an open access article distributed under the Creative Commons Attribution License, which permits unrestricted use, distribution, and reproduction in any medium, provided the original work is properly cited.

1. Introduction

It is well known that the angular distribution of the radiated power from an antenna array depends on the geometry and the excitation of the elements [1]. In a coupled active antenna oscillator linear array consisting of identical and parallel elements, the pattern is expressed in the following form:

$$F(\theta) = \sum_{k=1}^N (\tilde{V}_k) f_k(\theta) e^{j(2\pi/\lambda)z_k \cos(\theta)},$$
$$V_k = |\tilde{V}_k|,$$
$$\phi_k = \angle \tilde{V}_k,$$
(1)

where the excitation \tilde{V}_k is the complex voltage of the oscillator output, ($V_k = |\tilde{V}_k|$ amplitude and $\phi_k = \angle \tilde{V}_k$ the respective phase), $f_k(\theta)$ is the pattern, and z_k is the abscissa of the k th element, respectively. λ is the free-space wavelength at the operating frequency.

The two key sets of parameters that are important in the design are the boxed terms of (1). The antenna array synthesis mainly focuses on the excitation [2–4], while efforts aiming at extracting the positions of the array elements

are scarce [5]. In our present study, we cope either with one of the above or with both sets simultaneously. A perturbation method that provides iteratively the excitation and the placement of the elements in a quest of matching the resulting far—field with the desired one is applied. The whole synthesis is formulated as an optimization problem over a vector containing the excitation and the element positions. The cost function is the mean square error between the desired and the attained pattern.

Apart from attaining the necessary parameters of the antenna array, it is of equal importance the problem of feeding the array by a proper network. In the literature, one can find several approaches to the feeding networks [1], containing corporate feeds and feeding matrices [6]. Apart from passive networks, there are others that utilize active circuitry. Among them, the active feeding networks consisting of coupled oscillator arrays [7] are of specific interest. It has been found that such devices allow for the manipulation of the phase distribution without additional phase-shifting circuitry, suggesting a potential for low-cost beam-scanning systems. In the past, most of the studies on coupled oscillator arrays analyze the problem of beam steering [8–10] and of null control of the pattern, [11–13]. In

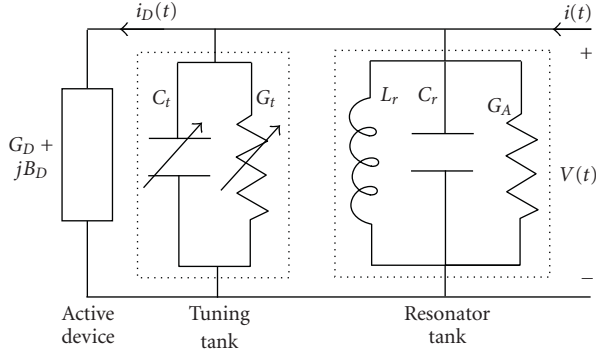


FIGURE 1: The equivalent circuit of the oscillator in the current-sum form.

the current work, we extend the functionality of the coupled oscillator arrays to more general pattern synthesis problems.

It is noticed that there are cases where a uniform excitation of a linear phased array and a nonuniform placement is enough to solve the synthesis problem. In this case, constraining the oscillators' output voltage to a common value reduces the nonlinear dynamics of the system. Alternatively, one can keep the phases equal and seek a design for different amplitudes. The required excitation distribution for all the simplifying cases, and for the general one (see the design examples), can be readily implemented with proper tune of control parameters, such as the varactor capacitance and the PIN conductance of the oscillators. The relative closed-form formulas are presented for the case of the mutually synchronized coupled oscillator array.

The paper is organized as follows. In Section 2, the coupled oscillator array (COA) theory is reviewed, and the key aspects related to the present study are underlined. The system that contains both, the antenna and the oscillators, is presented in Section 3, where closed-form formulas are derived to design the mutually synchronized oscillator array. The formulation and the solution of the radiation pattern shaping optimization problem for the above active antenna array are given in Section 4. In Section 5, design examples that verify the effectiveness of the method follow. Finally, some concluding remarks are given in Section 6.

2. The Coupled Oscillator Array

2.1. Single Oscillator Description. A model that has been widely used for microwave oscillator circuits is the canonical oscillator model in a parallel current-sum form which leads to the Van der Pol equation for certain nonlinearities [14, 15]. The equivalent circuit of the oscillator can be extracted from measurements [16] or from simulation [17], and is given in Figure 1.

The oscillator is assembled by three distinct parts: the active device, the tuning tank, and the resonator tank. The active device provides the nonlinear voltage dependent negative conductance. The tuning tank is responsible for the adjustment of the tuning parameters in order to feed the attached antenna element with the proper excitation. Last,

the resonator tank includes the parallel resonance circuit of the oscillator and the antenna elements.

In detail, the active device is represented as a negative conductance as follows:

$$G_D(|V|) = -a + b|V|^2, \quad (2)$$

where $|V|$ is the amplitude of the output voltage, and a , b are constants characterizing the nonlinear device.

The voltage-dependent susceptance of the nonlinear device is denoted by $B_D(|V|)$. Usually, the susceptance is independent on the device characteristics and can be neglected. In this case, which is the one that we follow, the current of the nonlinear device obeys

$$i_D(t) = Y \cdot V(t) = G_D \cdot V(t) = (-a + b \cdot V^2(t)) \cdot V(t). \quad (3)$$

The reactive energy of the circuit is stored into the LC parallel circuit giving a free-running circular frequency of

$$\omega_{o,k} = \frac{1}{\sqrt{L_r C_{o,k}}} = \frac{1}{\sqrt{L_r (C_r + C_{o,t})}} \quad (4)$$

for the k th oscillator.

In our case, the capacitance C_t would be a varactor that is controlled by a voltage. This voltage will be the tuning parameter which for the k th oscillator is V_k^t . The varactor capacitance follows the well-known equation [18]:

$$C_{t,k} = \frac{2C_{o,t}}{(1 + V_k^t/V_o)^\Gamma}, \quad (5)$$

where $V_o = 1.2V$ (for a GaAs device), $C_{o,t} = 1pF$ is the capacitance for V_o tuning voltage, and Γ is the varactor exponent (usually taken equal to unity, a choice also followed here). Alternatively, other types of voltage controlled capacitors [19, 20] or even voltage controlled inductors [21] can be used instead.

The conductance G_t represents additional losses in the oscillator circuit. This would be the second (together with the $C_{t,k}(V_k^t)$) tuning parameter. In our case, the conductance G_t would be a PIN diode variable resistor controlled by its forward current I_k^t . The PIN conductance follows the well-known equation [22, 23]:

$$G_{t,k} = \frac{v_o}{I_k^t}. \quad (6)$$

Here, we use $v_o = 20mV$. Alternatively, other types of variable resistors can be used instead [24].

To find the total conductance, one should add to G_t the input conductance G_A of the radiating element of the array.

Let us now compute the total admittance Y of the circuit:

$$i(t) = \left(\underbrace{Y_D}_{=-G_D} + \underbrace{Y_C}_{=j(C_t+C_r)\omega} + \underbrace{Y_L}_{=1/jL_r\omega} + Y_{G_t} + Y_{G_A} \right) V(t) \\ \Rightarrow Y = -(G_D(|V|) - G_t - G_A) + j(C_t + C_r) \frac{\omega^2 - \omega_o^2}{\omega}. \quad (7)$$

We assume that the resonant circuit of the oscillator is of high Q . Thus, the output voltage follows, nearly, a sinusoidal waveform with the following phasor representation:

$$\begin{aligned} V(t) &= V_0(t) \cos(\omega t + \phi(t)) \\ &= \text{Re}\{V_0(t)e^{j\phi(t)}e^{j\omega t}\} \\ &= \text{Re}\{\tilde{V}(t) \cdot e^{j\omega t}\}. \end{aligned} \quad (8)$$

2.2. Coupled Oscillator Array Description. To complete the analysis, we suppose (see Figure 2) that we have N oscillators which are joined together using a linear coupling network [25].

The governing equation reads

$$Y_i \cdot \tilde{V}_i + \sum_{j=1}^N Y_{ij} \cdot \tilde{V}_j = 0, \quad (9)$$

where Y_i is given by (7), and \tilde{V}_i is defined in (8) as the complex output voltage of the i th oscillator. Also,

$$Y_{ij} = G_{ij} + jB_{ij} \quad (10)$$

is the mutual admittance between the output nodes of the i th and j th oscillators. Using the above, it can be shown [16–27] for the voltage amplitude V_k of the k th oscillator that

$$\begin{aligned} \frac{dV_k}{dt} + \frac{\omega_{o,k}}{2Q_k} V_k \left[1 - \frac{(-a_k + b_k V_k^2)}{G_{t,k} + G_A} \right] \\ = \frac{1}{2C_k} \left(\sum_{l=1}^N V_l [G_{lk} \cos(\phi_l - \phi_k) - B_{lk} \sin(\phi_l - \phi_k)] \right), \end{aligned} \quad (11)$$

where

$$Q_k = \frac{\omega_{o,k} C_k}{(G_{t,k} + G_A)}, \quad (12)$$

with $C_k = C_{t,k} + C_r$.

Often the following substitution is made:

$$\begin{aligned} 1 - \frac{(-a_k + b_k V_k^2)}{G_{t,k} + G_A} &\approx \mu_k (a_{o,k}^2 - |V_k|^2), \\ a_{o,k} &= \sqrt{\frac{a_k + G_{t,k} + G_A}{b_k}}, \\ \mu_k &= \frac{b_k}{G_{t,k} + G_A}, \end{aligned} \quad (13)$$

where μ_k is a parameter that characterizes the oscillator, while a_o is the free-running amplitude of the output voltage. This weak quadratic nonlinearity is the simplest nonlinearity that approximates the behavior of a wide range of active devices.

Apart from the time evolution of the voltage amplitudes given in (11) for the phase, we have

$$\begin{aligned} \frac{d\phi_k}{dt} &= -\omega + \omega_{o,k} + \frac{1}{2V_k C_k} \\ &\times \left(\sum_{l=1}^N V_l [G_{lk} \sin(\phi_l - \phi_k) + B_{lk} \cos(\phi_l - \phi_k)] \right). \end{aligned} \quad (14)$$

Equation (11) in conjunction with (14) fully describes the coupled oscillator array. The above should provide a framework for the design of an antenna oscillator array.

3. Design of the Mutually Synchronized Array

In Figure 3 [28], an antenna array with the corresponding oscillators is presented. In this mutually synchronized array, each oscillator is bilaterally coupled to the neighboring array elements. The configuration of Figure 3 was first proposed by Stephan [8, 15] and named as “interinjection-locked” oscillators. Mutual coherence is achieved via the injection-locking process. The steady-state phase relationships of each oscillator depend on its neighbors’ amplitude and phase. A nonlinear system of simultaneous equations must be solved to determine the self-consistent amplitude and phase relationships [26]. In such systems, (11) and (14) take the form

$$\begin{aligned} \frac{dV_k}{dt} &= \frac{V_k}{2C_k} [G_{t,k} + G_A + a_k - b_k V_k^2] \\ &+ \frac{1}{2C_k} \sum_{l=1}^N [V_l \kappa_{lk} \cdot \cos(\phi_l - \phi_k + \Phi_{lk})] \\ \frac{d\phi_k}{dt} &= -\omega + \omega_{o,k} + \frac{1}{2C_k} \sum_{l=1}^N \left[\frac{V_l}{V_k} \kappa_{lk} \cdot \sin(\phi_l - \phi_k + \Phi_{lk}) \right], \end{aligned} \quad (15)$$

where κ_{lk} are different from zero only when $|l - k| \leq 1$ since only the nearest neighbor coupling is assumed. There are various sets of parameters in (15). Those are the oscillator detuning, $(\omega - \omega_{o,k})$, the un-normalized coupling strengths, $(\kappa_{lk} = |G_{lk} + jB_{lk}|)$, and the coupling phases, $(\Phi_{lk} = \angle(G_{lk} + jB_{lk}))$. There are also the capacitance and the conductance of each one of the oscillators. Since our aim is to manipulate the amplitude and the phase distribution of the active antenna array, any set of parameters could be used for control. Here, we eliminate the coupling phases and we use the conductance of the PIN diodes and the capacitance of the varactors to control the steady state of the amplitudes and phases.

Before we present the followed procedure, some issues relative to the coupling network should be addressed. To couple the oscillators, we use resistively loaded lines [29], whose characteristic impedance Z_0 and phase Φ of the electrical length are

$$Z_0 = R, \quad \Phi = 2\pi. \quad (16)$$

For such lines, it is

$$Y_{ij} = \begin{cases} \frac{n_i}{2R}, & i = j, \\ -\frac{1}{2R}, & |i - j| = 1, \\ 0, & \text{otherwise,} \end{cases} \quad (17)$$

where $n_i = 2$ except for the edge elements where it is equal to one.

Using this coupling network, closed-form expressions for the tuning parameters can be derived. So, for Y_{ij} given in

(17), (15), for the steady state, where the time derivatives vanish, reads

$$\begin{aligned}
 & V_k [G_{t,k} + G_A + a_k - b_k V_k^2] \\
 &= \frac{-1}{2R} \begin{cases} V_1 - V_2 \cos(\phi_2 - \phi_1), & k = 1, \\ -V_{k-1} \cos(\phi_{k-1} - \phi_k) + 2V_k \\ -V_{k+1} \cos(\phi_{k+1} - \phi_k), & k \neq k, N, \\ V_N - V_{N-1} \cos(\phi_{N-1} - \phi_N), & k = N, \end{cases} \\
 & \left(\omega - \frac{1}{\sqrt{L_r C_k}} \right) 4RC_k \\
 &= \begin{cases} \frac{\sin(\phi_2 - \phi_1) V_2}{V_1}, & i = 1, \\ + \frac{\sin(\phi_{k-1} - \phi_k) V_{k-1}}{V_k} \\ - \frac{\sin(\phi_{k+1} - \phi_k) V_{k+1}}{V_k}, & k \neq k, N, \\ - \frac{\sin(\phi_{N-1} - \phi_N) V_{N-1}}{V_N}, & i = N. \end{cases}
 \end{aligned} \tag{18}$$

Using

$$\begin{aligned}
 S_k &= \begin{cases} 1 - \cos(\phi_2 - \phi_1) \left(\frac{V_2}{V_1} \right), & k = 1, \\ -\cos(\phi_{k-1} - \phi_k) \left(\frac{V_{k-1}}{V_k} \right) + 2 \\ -\cos(\phi_{k+1} - \phi_k) \left(\frac{V_{k+1}}{V_k} \right), & k \neq 1, N, \\ 1 - \cos(\phi_{N-1} - \phi_N) \left(\frac{V_{N-1}}{V_N} \right), & k = N, \end{cases} \\
 U_k &= \begin{cases} \sin(\phi_2 - \phi_1) \left(\frac{V_2}{V_1} \right), & i = 1, \\ + \sin(\phi_{k-1} - \phi_k) \left(\frac{V_{k-1}}{V_k} \right) \\ - \sin(\phi_{k+1} - \phi_k) \left(\frac{V_{k+1}}{V_k} \right), & k \neq k, N, \\ - \sin(\phi_{N-1} - \phi_N) \left(\frac{V_{N-1}}{V_N} \right), & i = N, \end{cases}
 \end{aligned} \tag{19}$$

the solution for the tuning parameters, $C_{t,k}(V_k^t)$ and $G_{t,k}(I_k^t)$, in terms of V_k , ϕ_k is

$$\begin{aligned}
 C_k &= C_{o,k} \left(\frac{1}{2} \left[1 \pm \sqrt{1 + \frac{U_k}{R} \sqrt{\frac{L_r}{C_{o,k}}}} \right] \right)^2, \\
 C_{t,k} &= C_k - C_r,
 \end{aligned}$$

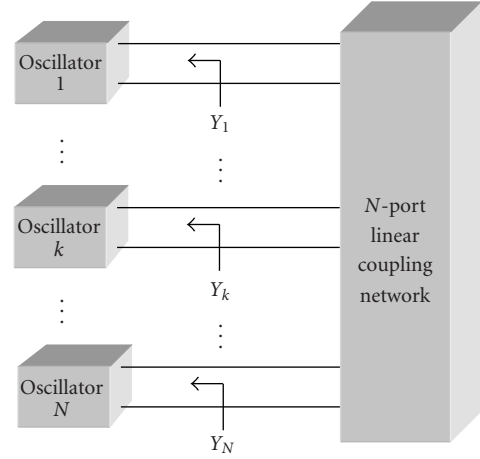


FIGURE 2: The coupled oscillator array.

$$\begin{aligned}
 V_k^t &= V_o \left[\left(\frac{C_{o,k}}{(C_k - C_r)} \right)^{1/\Gamma} - 1 \right], \\
 G_{t,k} &= \frac{-S_k}{2R} - a_k + b_k V_k^2 - G_A, \\
 I_k^t &= \frac{v_o}{G_{t,k}}.
 \end{aligned} \tag{20}$$

Before closing the section, the design procedure and check of the stability of the solution for the coupled oscillator array are listed. So, to design the mutually synchronized oscillator array in order to produce a given output voltage distribution (amplitudes and phases), the following steps are implemented.

- (i) The given output amplitudes and phases, V_k , ϕ_k , are inserted into (19) to produce the intermediate parameters S_k and U_k .
- (ii) In turn, S_k and U_k are inserted into (3). This results in computing the tuning parameters $C_{t,k}(V_k^t)$ and $G_{t,k}(I_k^t)$.
- (iii) Inserting $G_{t,k}$ and $C_{t,k}$ into the differential equations (15) provides the evolution of the amplitudes and phases with time.

The key step of computing the proper V_k , ϕ_k is addressed next.

4. The Synthesis Method

The system of Figure 3 with the restriction of nonvarying interelement distance, ($\Delta z = z_k - z_{k-1} = \text{const}$), has been used to control linear phased arrays in the limited cases of beam steering and pattern null in certain directions [8–13]. In the current study, we attempt a more general (not limited in certain cases) pattern synthesis. The system is designed by

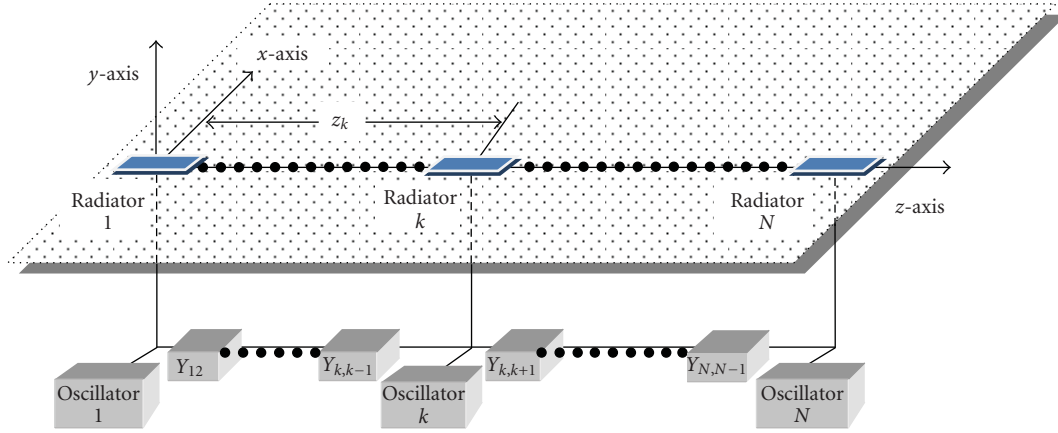


FIGURE 3: Bilateral injection-locking or mutual synchronization coupled oscillator's array.

providing the proper values for the positions of the radiators and for the voltage outputs of the oscillators. It is obvious that the proposed design offers specific advantages due to the degrees of freedom that make use.

To start the design of the array, we derive the cost function C of the following form:

$$C = \|F^d - F\|^2, \quad (21)$$

where

$$\|F^d - F\|^2 = \int_0^\pi |F^d(\theta) - F(\theta)|^2 \sin(\theta) d\theta. \quad (22)$$

We define

$$A \circ B = \int_{\theta=0}^{\pi} A(\theta) \cdot B^*(\theta) \cdot \sin(\theta) d\theta. \quad (23)$$

From (23), (22) becomes

$$\|F^d - F\|^2 = (F^d - F) \circ (F^d - F), \quad (24)$$

where $F^d(\theta)$ is the desired pattern, $F(\theta)$ is the resulting pattern, and $\|F^d - F\|^2$ is the mean square error. By taking into account the output voltage of the coupled oscillators, the resulting pattern can be expressed as

$$F(\theta) = \sum_{k=1}^N \underbrace{[V_k e^{j\phi_k}]}_{F_k} F_k, \quad (25)$$

where $F_k = f_k(\theta) e^{j(2\pi/\lambda)z_k \cos(\theta)}$.

We suppose a perturbation of the excitation of the oscillator outputs and of the position of the elements of the array. Due to the perturbation of the excitation, the new output of the k th oscillator becomes $V_k + \Delta V_k$; $\phi_k + \Delta\phi_k$. Also

the new position of the k th element is $z_k + \Delta z_k$. The pattern of the array results in

$$\begin{aligned} F(\theta) &= F_0(\theta) + \delta F(\theta) \\ &\approx \sum_{k=1}^N F_k V_k e^{j\phi_k} + \sum_{k=1}^N F_k e^{j\phi_k} \cdot \Delta V_k \\ &\quad + j \sum_{k=1}^N F_k V_k e^{j\phi_k} \cdot \Delta\phi_k + \sum_{k=1}^N \frac{\partial F_k}{\partial z_k} \cdot V_k e^{j\phi_k} \cdot \Delta z_k, \end{aligned} \quad (26)$$

where $F_0(\theta)$ is the initial pattern of the array.

It is shown in the Appendix that after assembling the perturbed values of the output voltage, ($\Delta V_k, \Delta\phi_k$), of the oscillators and the position, (Δz_k), of the elements in an unknown vector $[\Delta]$, the solution of the optimization problem leads to

$$[\Delta] = [B]^{-1}[A], \quad (27)$$

where $[A]$ and $[B]$ are proper matrices that include information relative to the specific problem. Expression (27) gives the appropriate perturbed values of the output voltage of the oscillators and the position of the elements. It is supposed that the desired pattern is not much different than the resulting one. In this case, the perturbation will produce the necessary changes in the excitation and the position of the elements. If $\|F^d - F\|^2$ is large, then the perturbation technique is applied iteratively until the mean square error becomes less than a given threshold. For further details on the functionality and the problems relative to the convergence of the proposed iterative method, the reader is referred to [5].

5. Design Examples

In the design examples that follow, the array can be derived by varying the excitation (amplitude and phase) simultaneously with the element positions. The desired far-field

TABLE 1: Van der Pol parameters of the employed oscillators.

Osc. #	I (~1 GHz)	II (~4.4 GHz)	III (~10 GHz)
Reference	[18]	[26]	[15]
a	20.9657	0.0232	0.0036
b	34.8669	0.0382	0.01
L_r	0.214 pH	0.24 nH	10 pH
C_r	105 nF	5.45 pF	23 pF
$R_A = 1/G_A$	50 Ω	58 Ω	32 Ω

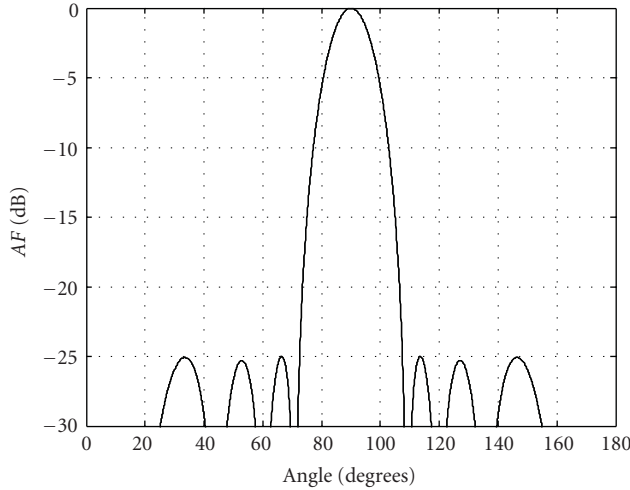


FIGURE 4: The attained pattern for the general design case.

pattern is a Chebyshev one with HPBW = 15 degrees and SLL = -25 dB. We start from an array of 9 elements with uniform initial excitation and 0.45λ interelement distance. We apply the synthesis method for three different cases. In *case A*, the excitations and the positions are to be derived. In *case B*, the phase of the excitations is set equal to zero, and in *case C*, the amplitude of the excitation is equal to unit.

For each one of the cases A, B, C, three different oscillators are employed to produce the respective far-field. The Van der Pol parameters of those oscillators are taken from published data (see Table 1).

The parameters of the coupling network are the same for all the examples as follows:

$$Z_o = R = 270 \Omega. \quad (28)$$

5.1. General Design Example. In this first example, both the element placement and the excitation are allowed to vary. After 20 iterations, the designed antenna array produces a pattern that is given in Figure 4.

The respective element placement and the excitations are given in Table 2.

The tuning parameters, V_k^t and I_k^t , of the oscillators are computed after inserting the last two columns of Table 2 into (19)-(3). For the present case, the relative results are presented in Table 3.

TABLE 2: Details on the general design case.

Element number	Element position (λ): z_k	Relative excitation amplitude: V_k	Excitation phase (degrees): ϕ_k
1	-1.78	0.534	0.034
2	-1.17	0.842	-0.806
3	-0.73	0.628	-0.515
4	-0.36	1	0.516
5	0	0.624	0.724
6	0.36	1	0.516
7	0.73	0.628	-0.515
8	1.17	0.842	-0.806
9	1.78	0.534	0.034

The evolutions of $V_k(t)$ and $\phi_k(t)$ versus t are produced after inserting into (15):

- (1) the parameters of Table 1 and (28),
- (2) the tuning parameter values, $C_{t,k}(V_k^t)$ and $G_{t,k}(I_k^t)$, and
- (3) the initial, at $t = 0$, amplitudes and phases:

$$V_k(t = 0) = \text{random number uniformly distributed into } 10^{-2} + (0, 1) \cdot 10^{-3} \text{ V,}$$

$$\phi_k(t = 0) = \text{random number uniformly distributed into } (0, 2\pi) \cdot 10^{-3}.$$

In Figure 5, it is demonstrated that the designed coupled oscillator array can produce the necessary solution (see Table 2 and Figure 4) and furthermore, this solution is stable. In Figure 5(a), the voltage amplitudes of the nine oscillators versus time are given. Also, in Figure 5(b), the time evolution of the successive phase differences (output voltage phase of the k th oscillator minus the output oscillator phase of the $(k - 1)$ th oscillator) are given. It is clear that the amplitudes and phases converge to the correct values (continuous horizontal lines).

5.2. Placement and Amplitude Design Example-Constant Phases. From Table 2, it is shown that the phase of the elements is close to zero. Also, the final array is nonuniform in the excitation and the geometry. Namely, our solution is more complicated than the classical one for Chebyshev patterns [1, 2]. Since we try to have a technically simple feeding network, we will solve the same problem with no phase difference between the elements and with only three different excitations. In Table 4, the final placement and the excitation of the elements, after 20 iterations, are given.

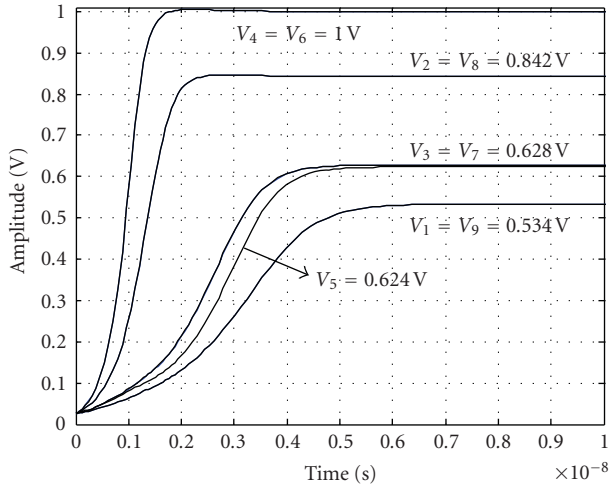
Also in Figure 6, the pattern of the array is presented. In the pattern, a difference of less than 0.5 dB between the desired and the resulting one is observed.

Comparing Table 2 with Table 4, one can see that the second solution gives simpler results.

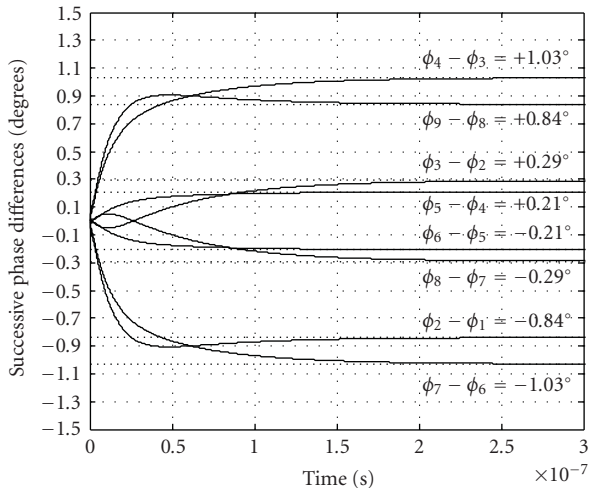
For the present case, the tuning parameters are given in Table 5.

TABLE 3: The tuning parameters for the general design case.

Element number	OSC. I (1.06 GHz)		OSC. II (4.21 GHz)		OSC. III (10.38 GHz)	
	V_k^t (mV)	I_k^t (mA)	V_k^t (mV)	I_k^t (mA)	V_k^t (mV)	I_k^t (mA)
1, 9	1231.20	314	1207.79	0.440	1203.15	0.200
2, 8	1182.68	1402	1195.61	2.216	1198.22	1.455
3, 7	1171.23	593	1192.68	0.920	1197.03	0.547
4, 6	1212.10	2148	1203.04	3.460	1201.23	2.342
5	1215.63	581	1203.92	0.910	1201.59	0.542



(a)



(b)

FIGURE 5: The coupled oscillator array response evolution with time for the general design case. (a) The evolution of the amplitudes. (b) The evolution of the phases.

In Figure 7, the time evolution curves for the amplitudes show the stability of the solution.

Note that comparing Figure 7 with Figure 5(a), different converging times are observed. In general, this fact is to be expected since the converging times, apart from the initial conditions $V_k(t = 0)$, $\phi_k(t = 0)$, depend on the

TABLE 4: Details on the constant phase design case.

Element number	Element position (λ): z_k	Relative excitation amplitude: V_k	Excitation phase (degrees): ϕ_k
1	-1.779	0.4	0
2	-1.386	0.4	0
3	-0.961	0.8	0
4	-0.464	1	0
5	0	1	0
6	0.464	1	0
7	0.961	0.8	0
8	1.386	0.4	0
9	1.779	0.4	0

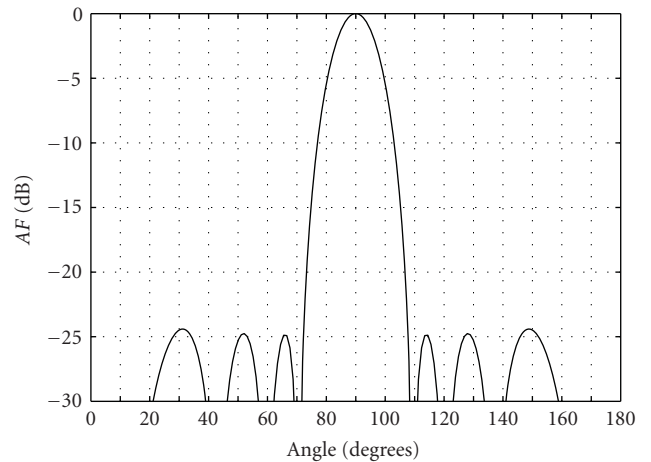


FIGURE 6: The attained pattern for the constant phase design case.

tuning parameter values that are different for the two design examples.

5.3. Placement and Phase Design Example-Constant Amplitudes. In this last case, we provide a design where the amplitudes are equal. The attained solution is given in Table 6.

The produced far-field pattern is given in Figure 8.

It is noted that in this case, the SLL criterion of -25 dB is not fulfilled, (SLL = -21.5 dB). The above shows that the phases of the elements are not enough to solve the problem.

TABLE 5: The tuning parameters for the constant phase design case.

Element number	OSC. I (1.06 GHz)		OSC. II (4.21 GHz)		OSC. III (10.38 GHz)	
	V_k^t (mV)	I_k^t (mA)	V_k^t (mV)	I_k^t (mA)	V_k^t (mV)	I_k^t (mA)
1, 9	1200	314.1	1200	0.445	1200	0.203
2, 8	1200	313.4	1200	0.483	1200	0.240
3, 7	1200	2515	1200	4.196	1200	2.892
4, 6	1200	4166	1200	7.019	1200	4.918
5	1200	4166	1200	7.028	1200	4.924

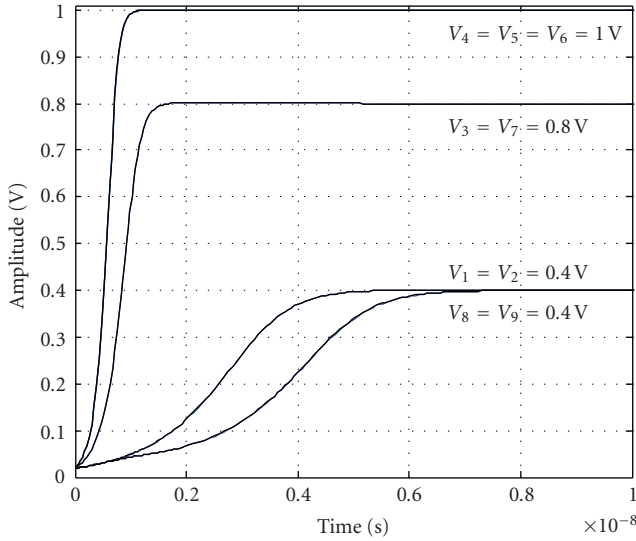


FIGURE 7: The coupled oscillator array response evolution with time for the constant phase design case. The evolution of the amplitudes.

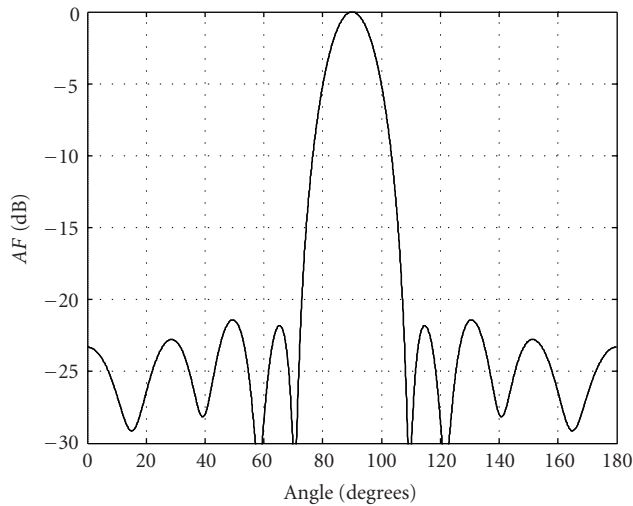


FIGURE 8: The attained pattern for the constant amplitude design case.

For the present case, the tuning parameters are given in Table 7.

For the resulting pattern, the respective evolution curves are given in Figure 9.

TABLE 6: Details on the constant amplitude design case.

Element number	Element position (λ): z_k	Relative excitation amplitude: V_k	Excitation phase (degrees): ϕ_k
1	-1.59	1	-0.043
2	-0.98	1	-4.121
3	-0.70	1	+4.909
4	-0.26	1	-6.975
5	0	1	-5.936
6	0.26	1	-6.975
7	0.70	1	+4.909
8	0.98	1	-4.121
9	1.59	1	-0.043

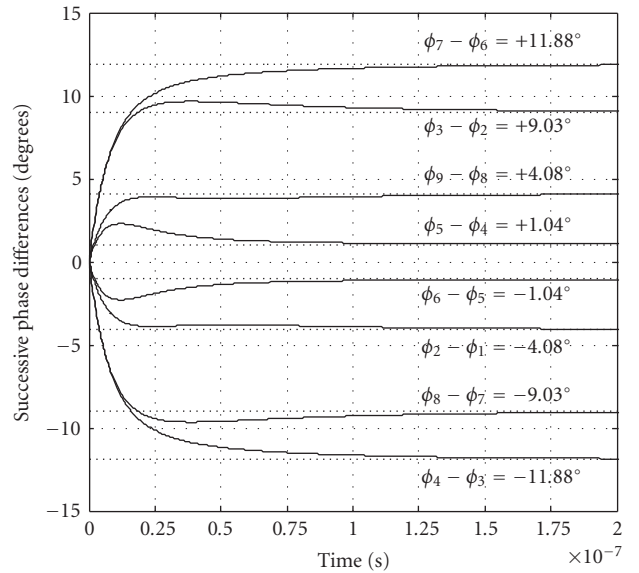


FIGURE 9: The coupled oscillator array response evolution with time for the constant amplitude design case. The evolution of the phases.

It is obvious that in the array synthesis, one must tradeoff the simplicity of networks, the size of the array, and the number and type of the different excitations. From the presented cases, it is assessed that the general one is rather complex, while the constant amplitude case fails to comply

TABLE 7: The tuning parameters for the constant amplitude design case.

Element number	OSC. I (1.06 GHz)		OSC. II (4.21 GHz)		OSC. III (10.38 GHz)	
	V_k^t (mV)	I_k^t (mA)	V_k^t (mV)	I_k^t (mA)	V_k^t (mV)	I_k^t (mA)
1, 9	1298.56	314.0	1224.13	0.401	1209.73	0.203
2, 8	930.27	314.0	1125.81	0.401	1169.32	0.203
3, 7	1805.51	314.0	1328.56	0.400	1250.49	0.202
4, 6	934.48	314.0	1127.07	0.400	1169.85	0.203
5	1249.32	314.0	1212.25	0.401	1204.95	0.203

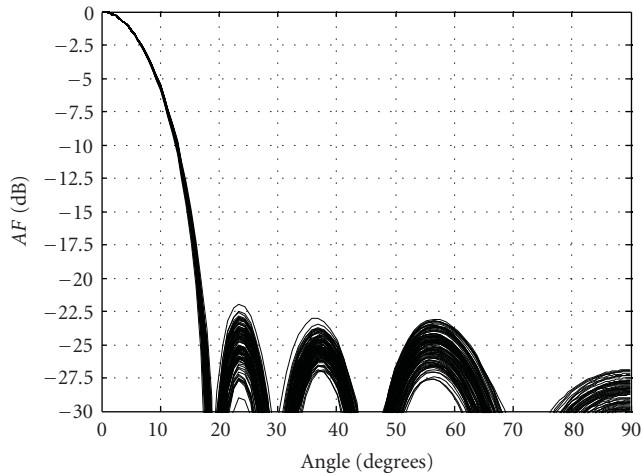


FIGURE 10: The attained amplitude sensitivity pattern for the general design case.

with the desired pattern. It seems that the constant phase case presents a better compromise between complexity and performance of the device under study.

Before closing the section, to evaluate the validity of the presented method and the viability of the listed results, some comments are in order. Both phase and amplitude control should be implemented with a relatively easy way. Varactor and PIN diodes are simple electronic elements that should be used. That is because varactor diodes are extensively used as tuning elements in conventional VCOs, and also PIN diodes are employed as variable resistors for vector modulator circuits. The issue that raises concern is the imprecise setting of the values of the tuning parameters and the effect that manufacturing tolerances will have on the overall performance of the system. Fabrication and tuning inconsistencies among individual oscillators in an array lead to differences in the free-running frequencies and amplitudes. This randomness causes phase and amplitude errors that are expected to result in pattern deformation manifested in beam-pointing and SLL errors [1, 30].

To provide understanding of the relationships among random tuning error distribution and pattern deformation, a statistical study, focused on the sensitivity analysis, is provided through Monte Carlo simulation. The element placement, the tuning voltage, and the tuning current are treated as random vectors following normal probability distribution with means given by the previous analysis

and varying values of variance. In each statistical experiment, after choosing the placement and tuning parameters, $C_{t,k}(V_k^t)$ and $G_{t,k}(I_k^t)$ are used to extract the time evolution of $V_k(t)$ and $\phi_k(t)$. At the steady state, the far field of the array is computed. The results show that when only I_k^t is varied and if two or three dBs degradation on SLL performance are acceptable, then the variance should be no more than 10% of the parameters nominal value. This is shown in Figure 10 when all the patterns resulted from a 100-run relative Monte Carlo experiment are depicted. Nearly, for one and two orders of magnitude, less variation is needed for attaining the same results when position and phase are varied, respectively. This means that position and amplitudes setting problems are expected to be less harsh compared to the problems that have already encountered in setting the phase [31], in conventional VCOs. If the previously-stated performance degradation is unacceptable, properly chosen calibration procedure should be considered [32, 33].

6. Conclusion

A design procedure for the synthesis of active antenna arrays is presented. Those arrays are sets of radiator oscillator couples with each element connecting through a coupling network to the others. Such a system presents the designer with two sets of parameters: the radiators' positions and the oscillators' outputs, the second used to excite the first.

The procedure designs simultaneously both the antenna and the attached coupled oscillator array providing viable solutions. In this way, the current work demonstrates how to control the dynamics of coupled oscillator arrays in order to achieve pattern shaping. Whereas previous work has been almost exclusively devoted to beam steering and null formation, this technique extends the versatility of coupled oscillator arrays through manipulation of the aperture amplitude and phase distribution. Furthermore, simultaneously an amplitude space taper distribution, ($\Delta z \neq 0$), is attained to produce the desired far-field pattern.

The implementability of our method is based first on the actually monitoring of the time evolution of the oscillators' outputs (27). Afterward, the existence of the proper varactors and PINs by using (3) is addressed. It is obvious that the limited range of their values should set some constraints on the resultant pattern. So, in some cases, a proper iterative combination between the capacitance and conductance and the desired pattern is important.

For all design cases, and independently on the complexity of the specific problem, the required excitation distribution can be readily implemented with proper tune of control parameters, such as the varactor capacitance and the PIN conductance of the oscillators. The relative closed-form formulas are presented for the case of the mutually synchronized coupled oscillator array.

Appendix

Following (25) and (26), the matrix form the initial pattern and its first variation can be written as

$$\begin{aligned}
F_0(\theta) &= [F]^T [\tilde{V}] = [\tilde{V}]^T [F], \\
\delta F(\theta) &= \text{diag}\left(\frac{[\tilde{V}]}{[V]}\right) [F]^T [\Delta V] \\
&\quad + j \text{diag}([\tilde{V}]) [F]^T [\Delta \phi] + \text{diag}([\tilde{V}]) [\dot{F}]^T [\Delta z] \\
&= \left[\text{diag}\left(\frac{[\tilde{V}]}{[V]}\right) [F]^T \quad j \text{diag}([\tilde{V}]) [F]^T \quad \text{diag}([\tilde{V}]) [\dot{F}]^T \right] \\
&\quad \times \begin{bmatrix} [\Delta V] \\ [\Delta \phi] \\ [\Delta z] \end{bmatrix}, \tag{A.1}
\end{aligned}$$

where

$$\begin{aligned}
[F] &= [F_1 \ \cdots \ F_k \ \cdots \ F_N]^T, \\
[\tilde{V}] &= [V_1 e^{j\phi_1} \ \cdots \ V_k e^{j\phi_k} \ \cdots \ V_N e^{j\phi_N}]^T, \\
[1] &= [1 \ \cdots \ 1 \ \cdots \ 1]^T, \\
[\Delta V] &= [\Delta V_1 \ \cdots \ \Delta V_k \ \cdots \ \Delta V_N]^T, \\
[\Delta \phi] &= [\Delta \phi_1 \ \cdots \ \Delta \phi_k \ \cdots \ \Delta \phi_N]^T, \\
[\Delta z] &= [\Delta z_1 \ \cdots \ \Delta z_k \ \cdots \ \Delta z_N]^T, \tag{A.2}
\end{aligned}$$

where $[\cdot]^T$ stands for the transpose operation. Following (A.1) and (A.2), the new pattern is written as

$$\begin{aligned}
F(\theta) &= F_0(\theta) + \delta F(\theta) \\
&= \text{diag}([\tilde{V}]) [F]^T [1] + \text{diag}\left(\frac{[\tilde{V}]}{[V]}\right) [F]^T [\Delta V] \\
&\quad + j \text{diag}([\tilde{V}]) [F]^T [\Delta \phi] + \text{diag}([\tilde{V}]) [\dot{F}]^T [\Delta z]. \tag{A.3}
\end{aligned}$$

Inserting (A.3) into (24), after defining a vector Δ as

$$[\Delta]^T = [[\Delta V]^T \quad [\Delta \phi]^T \quad [\Delta z]^T], \tag{A.4}$$

we have

$$\begin{aligned}
\|F^d - F\|^2 &= \|F^d - F_0\|^2 - [\Delta]^T [A] - [A]^T [\Delta] \\
&\quad + [\Delta]^T [B] [\Delta]. \tag{A.5}
\end{aligned}$$

In (A.5), it is

$$\begin{aligned}
A &= \left(\begin{bmatrix} \text{diag}\left(\frac{[\tilde{V}]}{[V]}\right) [F] \\ j \text{diag}([\tilde{V}]) [F] \\ \text{diag}([\tilde{V}]) [\dot{F}] \end{bmatrix} \circ (F^d - F_0) \right), \\
B &= \left(\begin{bmatrix} \text{diag}\left(\frac{[\tilde{V}]}{[V]}\right) [F] \\ j \text{diag}([\tilde{V}]) [F] \\ \text{diag}([\tilde{V}]) [\dot{F}] \end{bmatrix} \circ \begin{bmatrix} \text{diag}\left(\frac{[\tilde{V}]}{[V]}\right) [F] \\ j \text{diag}([\tilde{V}]) [F] \\ \text{diag}([\tilde{V}]) [\dot{F}] \end{bmatrix}^T \right). \tag{A.6}
\end{aligned}$$

By zeroing the first variation of $\|F^d - F\|^2$ with respect the $[\Delta]^T$, we have

$$\frac{\delta \|F^d - F\|^2}{\delta [\Delta]^T} = -[A] + [B][\Delta] = 0. \tag{A.7}$$

The above gives the vector $[\Delta]$:

$$[\Delta] = [B]^{-1} [A]. \tag{A.8}$$

References

- [1] R. C. Hansen, *Phased Array Antennas*, John Wiley & Sons, New York, NY, USA, 1998.
- [2] C. L. Dolph, "A current distribution for broadside arrays which optimizes the relationship between beamwidth and sidelobe level," *Proceedings of the IRE*, vol. 34, no. 6, pp. 335–348, 1946.
- [3] H. J. Orchard, R. S. Elliott, and G. J. Stern, "Optimising the synthesis of shaped beam antenna patterns," *IEEE Proceedings H: Microwaves, Antennas and Propagation*, vol. 132, no. 1, pp. 63–68, 1985.
- [4] J. N. Sahalos, *Orthogonal Methods for Array Synthesis: Theory and the ORAMA Computer Tool*, John Wiley & Sons, West Sussex, UK, 2006.
- [5] T. N. Kaifas and J. N. Sahalos, "On the geometry synthesis of arrays with a given excitation by the orthogonal method," *IEEE Transactions on Antennas and Propagation*, vol. 56, no. 12, pp. 3680–3688, 2008.
- [6] R. Mailloux, *Phased Array Antenna Handbook*, Artech House, Boston, Mass, USA, 2nd edition, 2005.
- [7] K. Chang, R. A. York, P. S. Hall, and T. Itoh, "Active integrated antennas," *IEEE Transactions on Microwave Theory and Techniques*, vol. 50, no. 3, pp. 937–944, 2002.
- [8] K. D. Stephan and W. A. Morgan, "Analysis of inter-injection-locked oscillators for integrated phased arrays," *IEEE Transactions on Antennas and Propagation*, vol. 35, no. 7, pp. 771–781, 1987.
- [9] P. Liao and R. A. York, "A new phase-shifterless beam-scanning technique using arrays of coupled oscillators," *IEEE Transactions on Microwave Theory and Techniques*, vol. 41, no. 10, pp. 1810–1815, 1991.
- [10] R. J. Pogorzelski, R. P. Scaramastra, J. Huang, R. J. Beckon, S. M. Petree, and C. M. Chavez, "A seven-element S-band coupled-oscillator controlled agile-beam phased array," *IEEE Transactions on Microwave Theory and Techniques*, vol. 48, no. 8, pp. 1375–1384, 2000.

- [11] T. Heath, "Simultaneous beam steering and null formation with coupled, nonlinear oscillator arrays," *IEEE Transactions on Antennas and Propagation*, vol. 53, no. 6, pp. 2031–2035, 2005.
- [12] A. Georgiadis, A. Collado, and A. Suarez, "Pattern nulling in coupled oscillator antenna arrays," *IEEE Transactions on Antennas and Propagation*, vol. 55, no. 5, pp. 1267–1274, 2007.
- [13] T. Heath, "Beam steering of nonlinear oscillator arrays through manipulation of coupling phases," *IEEE Transactions on Antennas and Propagation*, vol. 52, no. 7, pp. 1833–1842, 2004.
- [14] K. Kurokawa, "Injection locking of solid-state microwave oscillators," *Proceedings of the IEEE*, vol. 61, no. 10, pp. 1386–1410, 1973.
- [15] K. D. Stephan, "Inter-injection-locked oscillators for power combining and phased arrays," *IEEE Transactions on Microwave Theory and Techniques*, vol. 34, no. 10, pp. 1017–1025, 1986.
- [16] K. Y. Chen, P. D. Biernacki, A. Lahrichi, and A. Mickelson, "Analysis of an experimental technique for determine Van der Pol parameters of a transistor oscillator," *IEEE Transactions on Microwave Theory and Techniques*, vol. 46, no. 7, pp. 914–922, 1998.
- [17] S. Yang, V. F. Fusco, and D. E. J. Humphrey, "Ring-coupled-oscillator sequentially rotated active antenna," *IEEE Transactions on Microwave Theory and Techniques*, vol. 49, no. 8, pp. 1492–1497, 2001.
- [18] S. Drew and V. F. Fusco, "A software tool for active antenna array dynamical evaluation," *International Journal of Numerical Modelling: Electronic Networks, Devices and Fields*, vol. 10, no. 3, pp. 169–176, 1997.
- [19] N. H. W. Fong, J.-O. Plouchart, N. Zamdmer, et al., "A 1-V 3.8-5.7-GHz wide-band VCO with differentially tuned accumulation MOS varactors for common-mode noise rejection in CMOS SOI technology," *IEEE Transactions on Microwave Theory and Techniques*, vol. 51, no. 8, pp. 1952–1959, 2003.
- [20] P. Andreani and S. Mattisson, "On the use of MOS varactors in RF VCO's," *IEEE Journal of Solid-State Circuits*, vol. 35, no. 6, pp. 905–910, 2000.
- [21] R. Mukhopadhyay, Y. Park, P. Sen, et al., "Reconfigurable RFICs in Si-based technologies for a compact intelligent RF front-end," *IEEE Transactions on Microwave Theory and Techniques*, vol. 53, no. 1, pp. 81–93, 2005.
- [22] Microsemi Corporation, *The PIN Diode Circuit Designer's Handbook*, Microsemi, Lowell, Mass, USA, 1998.
- [23] U. L. Rohde and D. P. Newkirk, *RF/Microwave Circuit Design for Wireless Applications*, John Wiley & Sons, New York, NY, USA, 2000.
- [24] A. H. E. Ashtiani, S.-I. Nam, A. d'Espona, S. Lucyszyn, and L. D. Robertson, "Direct multilevel carrier modulation using millimeter-wave balanced vector modulators," *IEEE Transactions on Microwave Theory and Techniques*, vol. 46, no. 12, part 2, pp. 2611–2619, 1998.
- [25] R. A. York, P. Liao, and J. J. Lynch, "Oscillator array dynamics with broadband N-port coupling networks," *IEEE Transactions on Microwave Theory and Techniques*, vol. 42, no. 11, pp. 2040–2045, 1994.
- [26] R. A. York, "Nonlinear analysis of phase relationships in quasi-optical oscillator arrays," *IEEE Transactions on Microwave Theory and Techniques*, vol. 41, no. 10, pp. 1799–1809, 1993.
- [27] D. E. J. Humphrey and V. F. Fusco, "Active antenna array lumped ring configuration," *IEEE Transactions on Antennas and Propagation*, vol. 46, no. 9, pp. 1279–1284, 1998.
- [28] R. A. York and T. Itoh, "Injection- and phase-locking techniques for beam control," *IEEE Transactions on Microwave Theory and Techniques*, vol. 46, no. 11, part 2, pp. 1920–1929, 1998.
- [29] R. J. Pogorzelski, "On the design of coupling networks for coupled oscillator arrays," *IEEE Transactions on Antennas and Propagation*, vol. 51, no. 4, pp. 794–801, 2003.
- [30] J. Litva and T. Lo, *Beamforming in Wireless Communication*, Artech House, Boston, Mass, USA, 1996.
- [31] J. Shen and L. W. Pearson, "The phase error and beam-pointing error in coupled oscillator beam-steering arrays," *IEEE Transactions on Antennas and Propagation*, vol. 53, no. 1, part 2, pp. 386–393, 2005.
- [32] C. T. Charles, *A calibrated phase and amplitude control system for phased-array transmitters*, Ph.D. thesis, University of Washington, Seattle, Wash, USA, 2006.
- [33] R. J. Pogorzelski, "A 5-by-5 element coupled oscillator-based phased array," *IEEE Transactions on Antennas and Propagation*, vol. 53, no. 4, pp. 1337–1345, 2005.

Research Article

Cylindrical Dielectric Resonator Antennas with Harmonic Control as an Active Antenna Radiator

L. Lucci,¹ G. Manara,² P. Nepa,² G. Pelosi,¹ and S. Selleri¹

¹Department of Electronics and Telecommunications, University of Florence, Via C. Lombroso 6/17 - 50137 Firenze, Italy

²Department of Information Engineering, University of Pisa, Via G. Caruso 16, 56126 Pisa, Italy

Correspondence should be addressed to L. Lucci, leonardo.lucci@unifi.it

Received 30 September 2008; Accepted 19 January 2009

Recommended by Giovanni Toso

A cylindrical dielectric resonator antenna is proposed as a radiator for an active integrated antenna. Harmonic tuning, which is the key step in designing active antenna radiators, is achieved via a combination of shape factor control over the resonator and insertion of reactive elements in the feed system. Numerical simulations are carried out in a finite elements framework and a layout for the complete antenna is proposed, aimed at compactness for subsequent utilization of the radiator as an element in an active array for satellite communications.

Copyright © 2009 L. Lucci et al. This is an open access article distributed under the Creative Commons Attribution License, which permits unrestricted use, distribution, and reproduction in any medium, provided the original work is properly cited.

1. Introduction

Active integrated antennas (AIAs) are microwave systems which integrate on a single substrate several functions, at least one of which is that of a radiating element and another is that of an active device, be it a power amplifier for a transmitting AIA, or a low noise amplifier for a receiving AIA.

Albeit more complex functions can be embedded in the AIA, as frequency conversions with its own local oscillator, phase locking and many more, the key feature of an AIA is the tight integration between the active device and the radiating element.

Conventional antenna system design leads to radiators whose input impedance is matched to 50Ω via some appropriate matching network, and to amplifier which are themselves matched to the same 50Ω via some appropriate matching network. The two devices are then connected via a 50Ω transmission line. The two matching network can be fairly complex, especially the one which must be designed for a power amplifier (PA). In this case the matching network needs not only to match the output of the PA to 50Ω at the working frequency, but must also provide an appropriate load for the higher harmonics. The essence of AIAs is to eliminate both matching networks and the interconnecting line, by designing the radiating element so

that it provides the correct load to the PA at the fundamental frequency and higher harmonics. In transmission mode, in particular, the antenna should provide a given, generally complex, load for the power amplifier at the system working frequency in order to optimize the system performance, while for the first two higher harmonics, the impedance must be typically purely imaginary, be it capacitive or inductive.

By attaining this the overall system is simplified and reduced in size, by removing two matching networks, the losses in the lines are of course reduced, hence higher efficiencies, and lower power consumptions, attained. These characteristics make AIAs very attractive in wireless communications. The possibility of integrating also some sort of phase control in the AIA, for example, with a voltage controlled oscillator (VCO) leads to very attractive possibilities in the field of smart antennas and electronically steering phased arrays for vehicle-to-satellite broadband communications [1, 2].

As stated before AIAs are devices in which the radiating element and the active circuit, the amplifier, are treated as a single entity. The radiating element, which will be the focus of this paper, is to be seen as a filter, output matching circuit, and harmonic tuner in addition to its characteristics of load and radiating element. The core issue is that radiating elements are either broad band or resonating structures.

Broadband antennas are usually large and unsuitable for commercial telecommunications usage, since standards give fairly narrow bands. Resonating antennas are much more compact but, being resonant, have the strong tendency to behave in a very similar way at the working frequency and at its harmonics, at least for what concerns the input impedance. This implies that higher harmonics have an input impedance which is essentially real. To allow for a resonant radiator to be embedded in an AIA some modifications are necessary to attain its harmonic tuning, that is, the separate design of the input impedance at the fundamental frequency and at at least the first two higher harmonics.

In literature there are several works presenting different patch and slot antenna configurations for harmonic tuning, most of them relies on the suppression of higher resonances. Rectangular patches can be loaded with shortening posts [3] or with notches [4] or by feeding them with photonic band-gap structures [5], while circular ones can have a slice chopped of as in [6]. Slot antennas can be loaded with reactive components shortening higher frequencies, as in [7, 8], leading to excellent harmonic suppression, but slot antennas tend to have poor radiating characteristics.

In this paper a harmonic tuning technique for a dielectric resonator antenna (DRA) working in Ku band at 14.25 GHz is described. DRAs are a class of antennas which has interesting characteristics for usage as an AIA radiator. They exhibit low losses and, if fed via ground plane slot coupling, allow for a decoupling between the DRA, which lies on one side of the ground plane, and the substrate with its circuits and active elements, which lies on the other side of the ground plane. The absence of a substrate on the radiating side has additional benefits in array configurations, eliminating the possible interantenna coupling due to surface wave excitation.

In literature several kinds and shapes of DRAs have been considered, rectangular (RDRA), cylindrical (CDRA), hemispherical (HDRA) and all of these received much attention for what concerns antenna efficiency, compactness [9–11], and bandwidth. Nevertheless, there have been very few studies regarding the behavior of DRAs at higher harmonics for their usage as AIAs. More recent papers are focused on RDRA harmonic tuning [12, 13] while few preliminary results on CDRA harmonic tuning were presented in [14, 15].

Here a study of a slot-coupled cylindrical DRA configuration is presented, analyzing its harmonic response first at a shape factor level, then by introducing reactive elements in the coupling slot, and lastly by introducing additional slots. A complete design ready to be integrated with a PA is then presented.

The paper is organized as follows. In Section 2 the slot-coupled CDRA is described, with particular attention to higher-order resonant modes, to devise a possible optimal shape factor. Section 3 will present two modified configurations for the optimization of the resonator antenna electromagnetic performance at fundamental frequency and higher harmonics. Section 4 will present the final design

suitable for the integration with a power amplifier and Section 5 will draw some conclusions.

2. Shape Factor Tuning

A first investigation is done by analyzing the modes which are theoretically present on a cylindrical resonator of radius a and height $2d$ made by a dielectric characterized by a permittivity ϵ and a permeability μ . The resonant frequencies are [16]

$$f_{nmp} = \frac{1}{2\pi a \sqrt{\mu\epsilon}} \sqrt{[X_{np} | X'_{np}]^2 + \left(\frac{\pi a}{2d}(2m+1)\right)^2}, \quad (1)$$

where $n = 1, 2, 3, \dots$, $m = 1, 2, 3, \dots$, and $p = 0, 1, 2, \dots$ are three integer numbers, and $[X_{np} | X'_{np}]$ are either the p th zeros of the Bessel function of the first kind and order n or the zeros of the derivative of the Bessel function of the first kind and order n , respectively.

If the zeros of the Bessel function are used the frequencies of the TE_{nmp} modes are obtained. If the zeros of the derivative are used then the TM_{nmp} modes are obtained. It is easy to obtain that the fundamental mode in a cylindrical resonator is the TM_{110} , which is relevant to $X'_{11} = 1.841$.

It is then quite easy to invert (1) so as to obtain the value of a as a function of d which leads to a desired fundamental mode frequency f_0 :

$$a = \frac{X'_{11} 2d}{\pi \sqrt{4(f_0/c)^2 (2d)^2 - 1}} \quad (2)$$

being $c = 1/\sqrt{\epsilon\mu}$ the speed of light in the dielectric.

By choosing an appropriate range for $2d$ and by computing the relevant values of a via (2) a set of resonators whose fundamental mode frequency is 14.25 GHz is obtained. By applying on this set (1) the frequencies of all the other modes can be computed as a function of $2d$. Figure 1 shows such a diagram, presenting the values of $2d$ on the y axis and the frequencies on the x axis. TE modes are represented with solid lines, while TM modes represented with dashed lines. It is apparent how the fundamental frequency, being a vertical line, does not vary with $2d$. In this preliminary analysis a relatively low permittivity resonator ($\epsilon = 9.8$) is used.

While the fundamental mode is of course fixed at the desired value independently of $2d$, nearly all other modes are $2d$ dependent. The first step will then be that of choosing $2d$ so that no modes are present at the harmonics of the fundamental frequencies $2f_0$ and $3f_0$, represented with pale blue stripes in the figure.

While this is possible for $2f_0$ by choosing a relatively low thickness resonator, for what concerns $3f_0$, there is a TE mode which is independent of $2d$ and exactly at $3f_0$. This implies that the second harmonic will be more critical and that it will be impossible to handle it by resorting only to the resonator shape factor.

Figure 2 shows a practical CDRA setup. The resonator, whose height is halved to d , is placed on a ground plane and slot-coupled to a feeding microstrip. The dimensions of the setup are given in Table 1, the substrate has $\epsilon = 10.2$, and

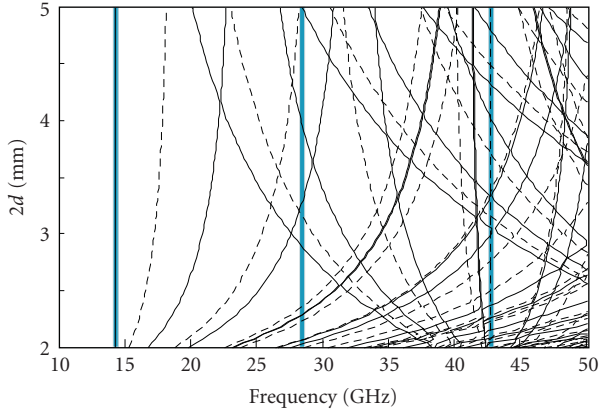


FIGURE 1: Curves of the resonant frequencies of the modes of the CDRA under analysis, as a function of resonator height having let radius to vary so that the first resonance remains fixed at 14.25 GHz. TE modes: solid lines; TM modes: dashed line.

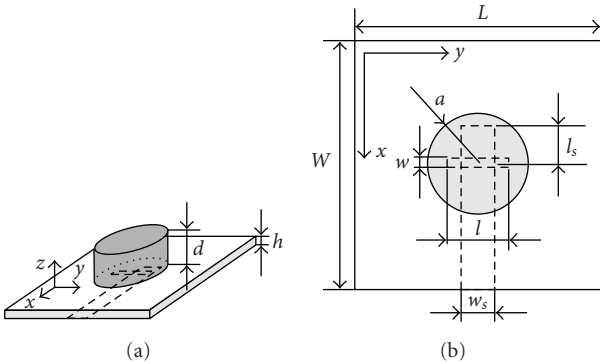


FIGURE 2: Geometry of the CDRA under exam, top view (right) and 3D view (left).

TABLE 1: CDRA setup dimensions [millimeters].

W	L	t	w_s	l_s	w	l
16	16	0.635	4	2.88	0.7	4.7

the whole set up has been analyzed with the finite elements method (FEM) in an enclosing box featuring perfectly matched layer (PML) radiation boundary conditions.

If a parametric analysis is performed over an appropriate range for d and over the whole $f = 10\text{--}45$ GHz frequency range, with the values of a computed by (2), the return loss at the microstrip port can be represented as a surface graph function of d and f . Figure 3 shows such a surface as a contour plot. Only the lines where $|S_{11}|$ is equal to -10 and -20 dB are reported for the sake of clearness.

It is evident from Figure 3 how the fundamental mode is well matched for any d value, even if the full wave analysis of the DRA over a finite ground leads to a slight dependence of the matching frequency with d (i.e., the zone of matching is not a vertical line). Then there are zones, at higher frequencies, where the antenna is more or less matched, and these zones assume a form which is quite similar to the lines

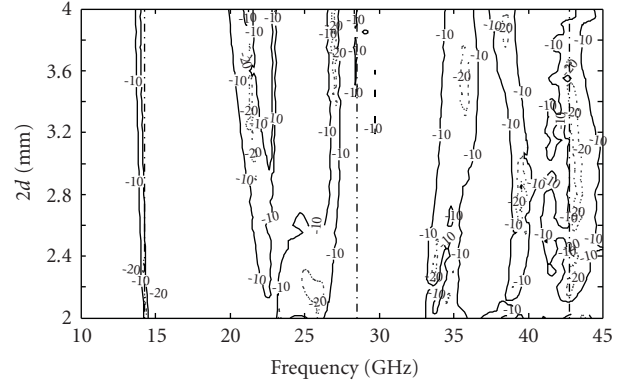


FIGURE 3: Contour plot of the magnitude of the S_{11} parameter at the microstrip port of the antenna.

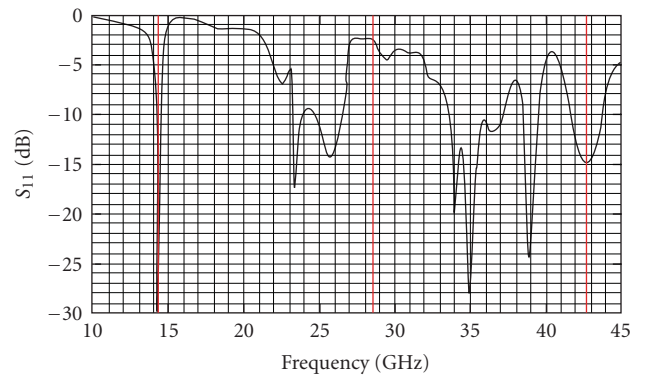


FIGURE 4: Return loss numerically computed for the CDRA setup of Figure 2. Good matching at the fundamental frequency is evident, while mismatch at first and second higher-order harmonics is insufficient.

in the dispersion graph in Figure 1. Lines are less numerous than in Figure 1 due to the fact that the coupling slot, due to its symmetries, does not excite all the possible modes and that matching has its own band, so neighboring lines easily merge in a single matched area. Around $2f_0$ the reflection coefficient amplitude is high for low d and gets lower as d increases, confirming that, a low d value is desirable. In the end, as expected, the reflection coefficient at $3f_0$ is generally quite low. As a first conclusion a $d = 1$ mm will be the first choice, and, for this value of the resonator height, in Figure 4 the return loss as a function of the frequency is reported from 10 GHz to 45 GHz, to show the antenna behavior at fundamental frequency and at first and second harmonics.

3. Slot Harmonic Suppression

Working only on the shape factor does not lead to a complete control over the reflection coefficient at higher harmonics. The $3f_0$ one in particular being extremely critical as the previous section showed.

As an upgrade to the previously shown configuration a parasitic element has been inserted in the coupling slot, in a fashion similar to [7, 8]. It is worth noticing how the “T”

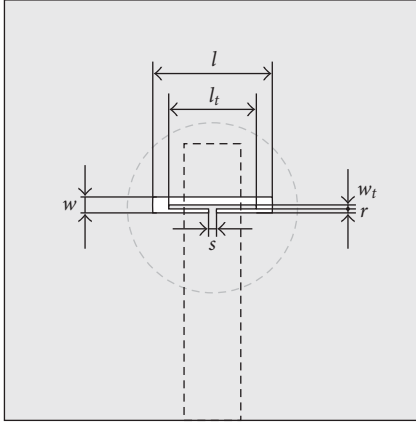


FIGURE 5: Geometry of the modified slot coupling. Inside the slot a parasitic reactive dipole provides higher harmonic rejection.

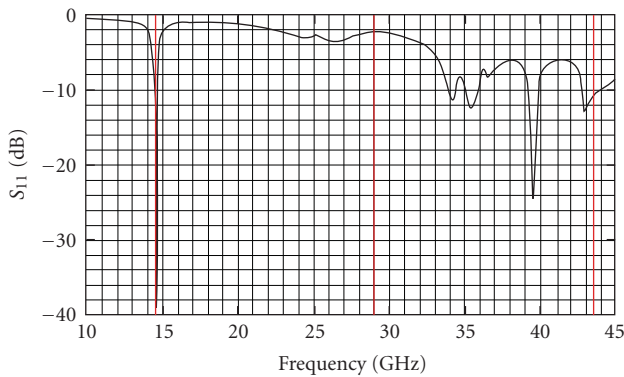


FIGURE 6: Return loss of the modified structure exhibiting the in-slot parasitic element as sketched in Figure 5.

shape metalization inserted has to be designed differently since the slot itself is not resonant in our case. In Figure 5 the geometry of the proposed structure is reported. Dimensions are $w = 0.6$ mm, $w_t = 0.26$ mm, $l = 6.3$ mm, $l_t = 5.48$ mm, $r = 0.34$ mm, and $s = 1.1$ mm.

In Figure 6 the return loss as a function of the frequency is reported from 10 GHz to 45 GHz, to show the antenna behavior at fundamental frequency and at first and second harmonics. For this structure the antenna input impedance is about $Z_{11} = 45 + j5 \Omega$ at f_0 and $Z_{11} = 85 + j28 \Omega$ at $2f_0$.

A real full control of the second harmonic using the parasitic element is not possible, due to both the reduced size of the slot and a further phenomenon which will be described in detail in the following section. Hence, to further improve the antenna performances at the second harmonic, two parallel additional slots have been added to the previous configuration as shown in Figure 7, where $w = 0.6$ mm, $w_t = 0.26$ mm, $w_a = 0.4$ mm, $l = 6.3$ mm, $l_t = 5.48$ mm, $l_a = 2.0$ mm, $r = 0.34$ mm, $d_1 = 2.8$ mm, $s = 1.1$ mm, and $d_2 = 1.4$ mm.

In Figure 8 the return loss as a function of the frequency is reported from 10 GHz to 45 GHz, to show that the antenna behavior at the second harmonics has been improved. In

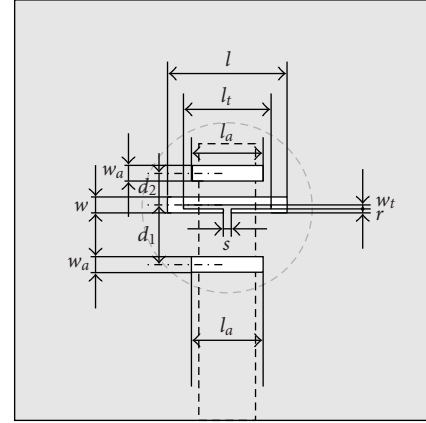


FIGURE 7: Geometry of the modified slot coupling with two additional parallel slots.

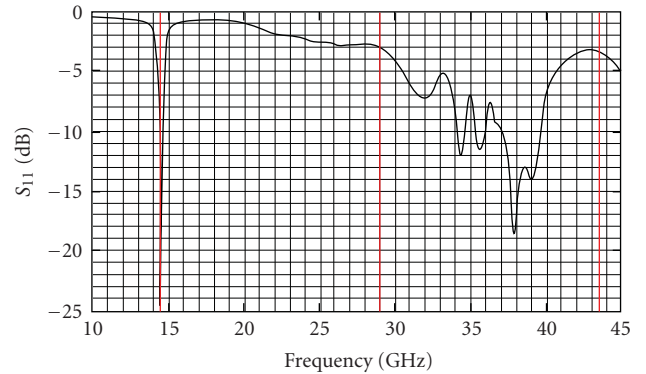


FIGURE 8: Return loss of the modified structure with two additional parallel slots as sketched in Figure 7.

particular for this modified structure the antenna input impedance is about $Z_{11} = 50 + j5 \Omega$ at f_0 , $Z_{11} = 10 + j17 \Omega$ at $2f_0$ and $Z_{11} = 35 + j25 \Omega$ at $3f_0$. The reason why the insertion of additional slots might help in rejecting higher-order harmonics lies in the fact that they perturb these more, due to their reduced wavelength. A deeper insight can be found in [12].

4. Final Layout

In this section a complete design ready to be integrated with a PA is presented. The design comprises not only the pad where the PA output is to be placed but also the line for the DC feed of the PA front-end. This latter has been designed so as to help in rejecting the second harmonic, while an additional stub shortening the third harmonic is also present. As shown in Figure 9, where the geometry of the final layout is reported, the parasitic element in the slot presented in the previous section has been retained, while the two additional slots have not, since their influence is relatively small and they can be replaced by the aforementioned stub. The geometric parameters defining the dimensions of the structure are as follows: $l = 6.224$ mm, $w = 611 \mu\text{m}$, $l_t = 5$ mm, $w_t =$

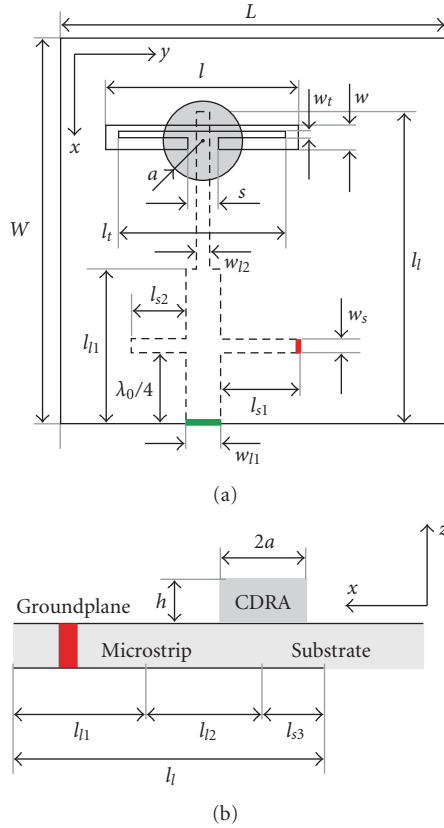


FIGURE 9: Geometry of the final layout: top view (a) and side view (b). The green rectangular area represents the DC feed, whereas the red rectangular pad represents the area where the PA output is to be soldered.

TABLE 2: Final layout input impedance.

Frequency [GHz]	Z_{11} [Ω]	Requested Z_{11} [Ω]
f_0	$17.7 + j17.7$	$15 + j18$
$2f_0$	$21.5 + j94.71$	$j100$
$3f_0$	$53.81 + j28.61$	$j17$

$220 \mu\text{m}$, $s = 1.107 \text{ mm}$, $a = 1.39 \text{ mm}$, $h = 1.21 \text{ mm}$, $l_{11} = 6.124 \text{ mm}$, $l_{12} = 8.876 \text{ mm}$, $l_{s1} = 2.243 \text{ mm}$, $l_{s2} = 1.754 \text{ mm}$, $l_{s3} = 283 \mu\text{m}$, $w_{11} = 521 \mu\text{m}$, $w_{12} = 400 \mu\text{m}$, $w_s = 380 \mu\text{m}$, and $\lambda_0 = 21.053 \text{ mm}$ being λ_0 the wavelength along the microstrip at fundamental frequency f_0 .

To show the active antenna electromagnetic performances in Figure 10 the input impedance is reported as a function of frequency, zooming around the fundamental frequency and the first two harmonics. Table 2 summarizes the input impedance simulation results at the above mentioned frequency together with the desired values as given by the PA designers [17].

In Figure 11 the electric field maps on the $y = 0$ plane at fundamental frequency and at the first and second harmonics are represented. It is evident that the fundamental frequency radiates, while the second harmonic does not. This is due to the DC feed line for the power amplifier, which is loaded by the DC source which in turn is essentially a

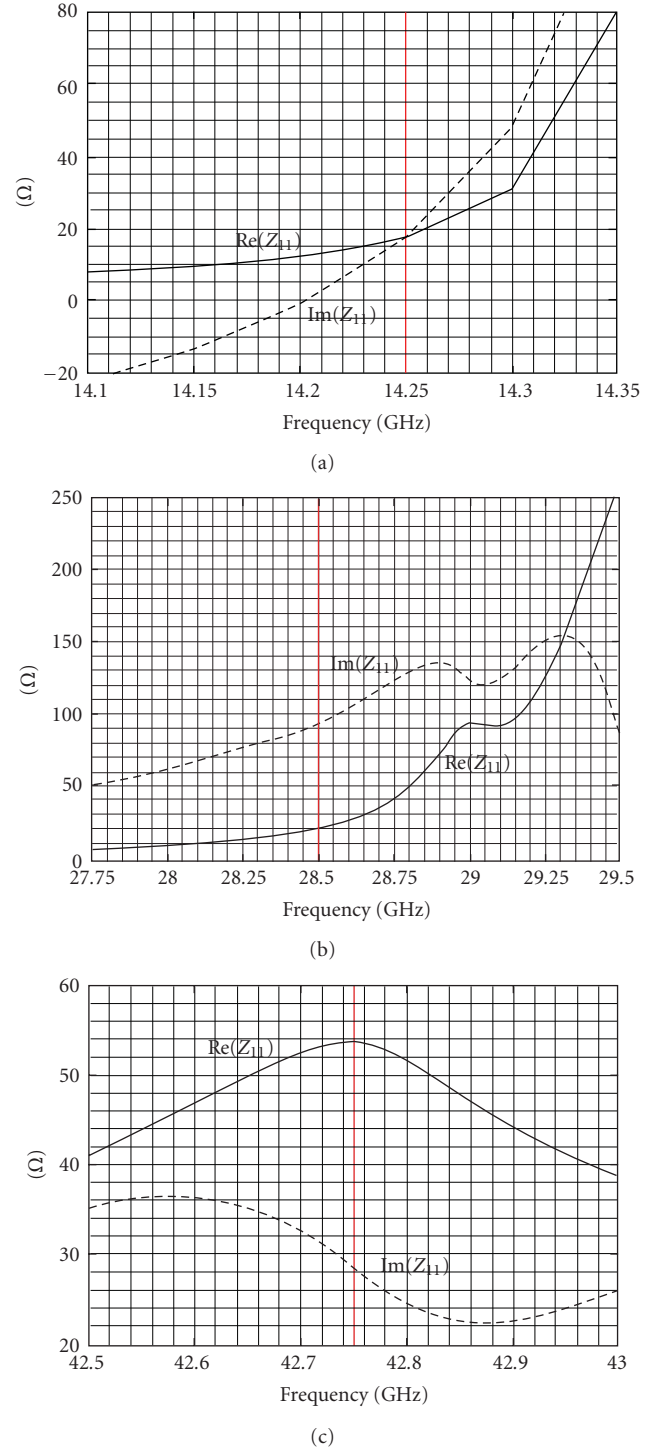


FIGURE 10: Final layout: input impedance at central frequency (a), at first harmonic (b), and at second harmonic (c).

short circuit at radio frequency. The feed is $\lambda_0/4$ wavelength away from the PA output at f_0 , hence the short circuit reverts to an open one and no energy is present on the stub at f_0 (see Figure 11(b)). On the other hand, at the first harmonic, $2f_0$, the same stub is $\lambda/2$ long and hence the PA output is almost shortened. This explains the strong standing wave

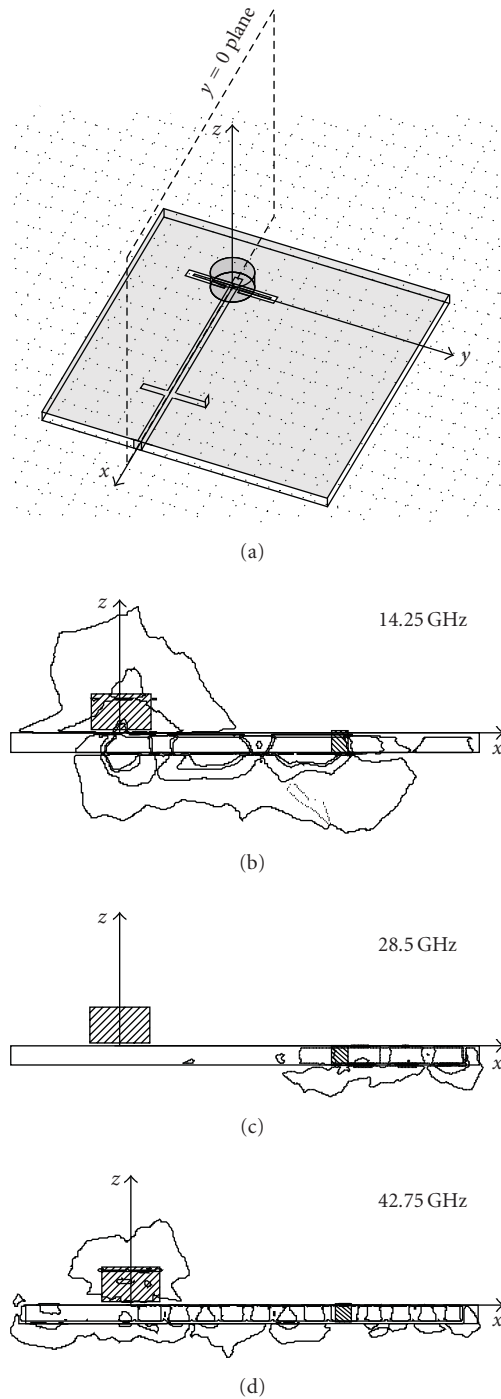


FIGURE 11: Final layout: (from top to bottom) observation plane geometry, electric field maps on $y = 0$ plane at 14.25 GHz, 28.5 GHz, and 42.75 GHz.

which can be seen in Figure 11(c). The issue still lies in the third harmonic because, even if the additional stub l_{s2} should shorten it, the slab is not thin with respect to λ at $3f_0$ hence surface waves can arise quite easily. Indeed the presence of a surface wave originating at the matching stub immediately below the coupling slot is very evident in

Figure 11(d). Radiation from both the CDRA and the open-ended feeding line stub accounts for the much higher real part of the third-order input impedance.

5. Conclusions

In this paper, a harmonic tuning technique for a dielectric resonator antenna working in Ku band at 14.25 GHz has been described. As a first study a slot-coupled cylindrical DRA configuration has been considered, studying its harmonic response at a shape factor level, with particular attention to higher-order resonant modes, to devise a possible optimal shape factor.

As a second step of the study the basic resonator antenna layout has been modified by introducing a parasitic reactive element in the coupling slot to improve antenna performances at first and second harmonics. This configuration allows us to obtain a significant improvement of the antenna performances at first harmonic but a real full control of the second harmonic is not yet possible, both mainly due to the reduced size of the slot. Yet this issue is of minor importance due to the fact that the power generated by the PA at the second harmonic is a few percent of the total one.

At last, a complete design suitable for the integration with a PA has been presented, where the feeding line has been optimized as well to achieve full impedance matching at fundamental frequency and higher harmonics.

Acknowledgments

This work was partially supported by the Italian Ministry of Education, University and Research, under the PRIN research Project 005098437 "Active Integrated Antennas for High-Efficiency Mobile Terminals".

References

- [1] K. Chang, R. A. York, P. S. Hall, and T. Itoh, "Active integrated antennas," *IEEE Transactions on Microwave Theory and Techniques*, vol. 50, no. 3, pp. 937–944, 2002.
- [2] Y. Qian and T. Itoh, "Progress in active integrated antennas and their applications," *IEEE Transactions on Microwave Theory and Techniques*, vol. 46, no. 11, part 2, pp. 1891–1900, 1998.
- [3] V. Radisic, Y. Qian, and T. Itoh, "Novel architectures for high-efficiency amplifiers for wireless applications," *IEEE Transactions on Microwave Theory and Techniques*, vol. 46, no. 11, part 2, pp. 1901–1909, 1998.
- [4] S. Kwon, B. M. Lee, Y. J. Yoon, W. Y. Song, and J.-G. Yook, "A harmonic suppression antenna for an active integrated antenna," *IEEE Microwave and Wireless Components Letters*, vol. 13, no. 2, pp. 54–56, 2003.
- [5] Y. J. Sung and Y.-S. Kim, "An improved design of microstrip patch antennas using photonic bandgap structure," *IEEE Transactions on Antennas and Propagation*, vol. 53, no. 5, pp. 1799–1804, 2005.
- [6] M. J. Cryan, G. R. Buesnel, and P. S. Hall, "Analysis and control of harmonic radiation from active integrated oscillator antennas," *IEEE Transactions on Microwave Theory and Techniques*, vol. 50, no. 11, pp. 2639–2646, 2002.

- [7] H. Kim, K. S. Hwang, K. Chang, and Y. J. Yoon, "Novel slot antennas for harmonic suppression," *IEEE Microwave and Wireless Components Letters*, vol. 14, no. 6, pp. 286–288, 2004.
- [8] H. Kim and Y. J. Yoon, "Microstrip-fed slot antennas with suppressed harmonics," *IEEE Transactions on Antennas and Propagation*, vol. 53, no. 9, pp. 2809–2817, 2005.
- [9] A. Petosa, A. Ittipiboon, Y. M. M. Antar, D. Roscoe, and M. Cuhaci, "Recent advances in dielectric-resonator antenna technology," *IEEE Antennas and Propagation Magazine*, vol. 40, no. 3, pp. 35–47, 1998.
- [10] R. K. Mongia and A. Ittipiboon, "Theoretical and experimental investigations on rectangular dielectric resonator antennas," *IEEE Transactions on Antennas and Propagation*, vol. 45, no. 9, pp. 1348–1356, 1997.
- [11] A. A. Kishk, "Dielectric resonator antenna elements for array applications," in *Proceedings of IEEE International Symposium on Phased Array Systems and Technology (PAST '03)*, pp. 300–305, Boston, Mass, USA, October 2003.
- [12] A. Guraliuc, G. Manara, P. Nepa, G. Pelosi, and S. Selleri, "Harmonic tuning for Ku-band dielectric resonator antennas," *IEEE Antennas and Wireless Propagation Letters*, vol. 6, pp. 568–571, 2007.
- [13] A. Guraliuc, G. Manara, P. Nepa, G. Pelosi, and S. Selleri, "Investigation on harmonic tuning for active Ku-band rectangular dielectric resonator antennas," *International Journal of Antennas and Propagation*, vol. 2008, Article ID 437538, 6 pages, 2008.
- [14] L. Lucci, G. Manara, P. Nepa, G. Pelosi, L. Rossi, and S. Selleri, "Harmonic control in cylindrical DRA for active antennas," in *Proceedings of IEEE Antennas and Propagation Society International Symposium (APS '07)*, pp. 3372–3375, Honolulu, Hawaii, USA, June 2007.
- [15] A. R. Guraliuc, L. Lucci, G. Manara, P. Nepa, G. Pelosi, and S. Selleri, "Investigation on mutual coupling level in DRA sub-arrays for Ku-band active integrated antennas," in *Proceedings of IEEE Antennas and Propagation Society International Symposium (AP-S '08)*, pp. 1–4, San Diego, Calif, USA, July 2008.
- [16] S. A. Long, M. W. McAllister, and L. C. Shen, "The resonant cylindrical dielectric cavity antenna," *IEEE Transactions on Antennas and Propagation*, vol. 31, no. 3, pp. 406–412, 1983.
- [17] P. Colantonio, F. Giannini, R. Giofrè, et al., "Active integrated antennas for efficient mobile terminals," in *Proceedings of the 11th International Symposium on Microwave and Optical Technology (ISMOT '07)*, pp. 625–628, Rome, Italy, December 2007.

Research Article

Irregular Polyomino-Shaped Subarrays for Space-Based Active Arrays

R. J. Mailloux,^{1,2} S. G. Santarelli,² T. M. Roberts,² and D. Luu²

¹ *Electrical and Computer Engineering Department, University of Massachusetts, Amherst MA, 01003, USA*

² *Sensors Directorate, Electromagnetic Technology Division, Antenna Technology Branch, Air Force Research Laboratory, MA, 01731, USA*

Correspondence should be addressed to R. J. Mailloux, robert.mailloux@hanscom.af.mil

Received 27 October 2008; Accepted 22 January 2009

Recommended by Stefano Selleri

This paper presents new results showing the application of polyomino-based subarrays to limited field of view and wideband, wide-angle scanning. This technology can reduce the number of phase controls in arrays used for limited sector coverage or the number of time delay devices for wideband radar or communications, and so can reduce the cost of space-based active arrays. We concentrate on the wideband application. Results are presented by comparing the gain and peak sidelobe results of irregular polyomino subarray-based arrays with those of rectangular subarrays. It is shown that using irregular polyomino subarrays can result in a major decrease in sidelobes while presenting, in most cases, only a few tenths of a dB gain reduction compared to rectangular subarrays.

Copyright © 2009 R. J. Mailloux et al. This is an open access article distributed under the Creative Commons Attribution License, which permits unrestricted use, distribution, and reproduction in any medium, provided the original work is properly cited.

1. Introduction

The increasing use of large scanning arrays for space applications emphasizes a growing need for subarray technology to reduce the number of controls in systems that scan over limited fields of view (LFOV) or to minimize the number of time delays for arrays with active phase control at the element level. These two applications are addressed by the same subarray technology, and so these will be discussed together initially before presenting detailed results for the wideband case. Subarray configurations for the two applications are illustrated in Figure 1.

LFOV applications include synchronous satellites, where the earth subtends a conical angle of 8.7° half angle. Other satellite systems sometimes scan a high-directivity beam over even smaller angles to do detailed mapping. In the LFOV configuration shown at left in Figure 1, there is no phase shift at the element level, but phases are introduced at the input port to each subarray. The subarray is used as an oversized element and the gain and pointing accuracy is maintained by phase control at the subarray input ports. In the time-delayed configuration of Figure 1, the subarray has phase shifters at the element level and time delays at each subarray input [1].

The phase shifters scan the subarray beam direction, but the time delays are required to keep the array pattern stationary for all frequencies within the frequency band.

The subarrays most commonly used for either application are rectangular groups of elements. When placed in a periodic array these radiate discrete sidelobes called quantization lobes at the location of the grating lobes of the array factor.

Solid-state modules with phase shift pattern control are now being used in many space applications, and they can be designed to have good performance over wide bandwidths but the phenomenon of beam “squint” limits their use operationally. Beam squint is the property of a phase steered array that results in frequency-dependent pointing angles. This can result in severely limited instantaneous bandwidth for large phase-steered arrays. Time-delay-steered arrays do not exhibit this phenomenon.

Time delay control of scanning arrays remains an expensive and often impractical option, because of the difficulty of implementing long time delays at the element level or switched time delay tree networks. Digital or optical beam forming networks can introduce time delay at element or subarray level but for reasons of economy it

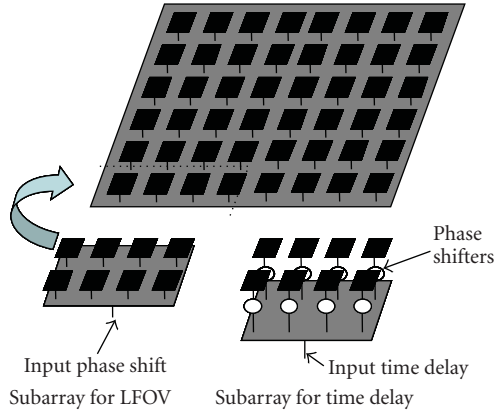


FIGURE 1: Subarray applications to LFOV and time-delayed wide-band arrays.

is often convenient to introduce time delay at the subarray level. New and projected applications with requirements for bandwidths up to limits of 10:1 place increasingly severe restrictions on the size of phase steered arrays or on the subarray technology that enables the use of relatively few time delay networks.

The two cited applications for subarray technology exhibit similar behavior and suffer the same deficiencies. Quantization lobes occur in the limited field of view array because the subarrays are arranged periodically in the array. At broadside (and for a uniform array), the array appears continuous and no extraneous lobes are radiated. When the array is scanned by the phase shifters behind the subarrays, the aperture phase is quantized because the subarrays themselves have a pattern that radiates broadside. The array factor of this array of subarrays is, however, scanned to the new chosen scan angle, giving rise to quantization lobes that are only suppressed at broadside.

An upper bound for LFOV scanning in one dimension is that for idealized subarrays with spacings of dimension D , and maximum scan angle θ_0 , the subarray size D is given by the following relationship:

$$\left(\frac{D}{\lambda_0}\right) \sin |\theta_0| \leq 0.5. \quad (1)$$

This limit is reached using an idealized subarray pattern that is pulse-shaped, with a flat top over that range [2].

For LFOV, therefore, the quantization lobes occur because the subarray pattern is stationary, while the array factor is scanned. However, in the case of using time delays for broadband radiation, the phase shifters in each subarray do scan the subarray patterns correctly at center frequency, and the time-delayed array of subarrays remains at the chosen scan angle for all frequencies. However, away from center frequency, the phase-steered subarray patterns do not scan to the chosen location u_0 ; but “squint” to the new location $u_0(f_0/f)$ for $u_0 = \sin \theta_0$. Since the subarray patterns and the array factor peaks are no longer aligned, this case also radiates quantization lobes.

This usage is indicated on the right side of Figure 1, where it shows a subarray with element level phase shifters and time delay at the subarray input. For modest bandwidth, an upper bound on the system bandwidth in this case is again obtained by the idealized case in which the subarray spacing D is limited by the following equation:

$$\frac{\Delta f}{f_0} \left(\frac{D}{\lambda_0}\right) \sin |\theta_0| \leq 1.0. \quad (2)$$

Reaching this limit is again only achieved if the subarray is designed to produce the “ideal” pulse-shaped pattern.

Throughout this paper, the data that are presented pertain to the wideband scanning case. It should be understood that the results apply equally well to the LFOV case. The LFOV case results are readily inferred from (1) and (2) resulting in the relationship of (3) for scan to some maximum angle θ_{\max} [3]:

$$\frac{\Delta f}{f_0} \sin (|\theta_0|) = 2 \sin (|\theta_{\max}|). \quad (3)$$

We have not discussed the issue of impedance matching elements over such wide bandwidths. The element lattice periodicity requires element spacing on the order of 0.5λ at the highest frequency, and this makes them very closely spaced at the lowest frequency. This close spacing actually improves the array wideband impedance match, as discussed in the text by Munk [4]. Vivaldi elements, connected dipole arrays and matched microstrip patch elements, have all been used in wideband arrays.

2. Subarray Technology for Space Applications

The several upper bound equations noted above make it clear that there can be completely different applications for various subarray sizes. In the LFOV case, the subarray sizes can vary from about 3 wavelengths for ± 10 degrees of scan to about 14 wavelengths for ± 2 degrees of scan, and even larger for less scan. The wide instantaneous bandwidth is required for lower orbiting radars and communication arrays, where scanning requirements can exceed $\pm 20^\circ$ and array sizes up to hundreds of thousands of elements. Subarrays used to insert such time delay can be very large.

The technology for producing large subarrays with the qualities to suppress these quantization lobes depends upon the size of the subarray. Large subarrays have been constructed by dividing the array into an irregular group of elements and building special power divider networks for each subarray [5], or by using so-called dual-transform or overlapped subarray networks [6, 7]. These networks use a multiple beam feed and a focusing lens to form overlapping distributions to radiate pulse-shaped subarrays that approximate the ideal flat-topped subarray radiation pattern. Such large subarrays formed in this manner can vary from 10 to perhaps 50 elements on a side and so are useful for very limited scan coverage or very narrow bandwidth scanned performance, as dictated by (1) and (2). Their advantage, however, is the huge savings in phase or time delay control devices and resulting cost savings.

Small subarrays have been fabricated to produce overlap and an approximation to the pulse-shaped radiation patterns that have wider but still limited field of view [8, 9], or to applications involving very wide band radiation. Other technologies applicable to smaller subarrays include using simple rectangular subarrays but rotating them [10] or randomly spacing them to suppress the quantization lobes but radiate with reduced gain in proportion to the reduced filling of the aperture. The use of unequal size rectangular subarrays that do fill the aperture [11–13], or to use some sort of irregular subarrays that fill the aperture [14–16]. Of these, the randomly spaced subarrays produce excellent suppression of extraneous lobes, but radiate with reduced gain in proportion to the reduced filling of the aperture. The use of dissimilar irregular subarrays introduces problems in excitation of the subarrays because of the need to use different power divider combinations within the array. The proposed method that we introduce employs only one type of irregular subarray within the array, and these are rotated (or rotated and flipped) to completely fill the array. The result is to form an array with non-periodically spaced subarray phase centers but with a tiled (filled) aperture that has full array gain.

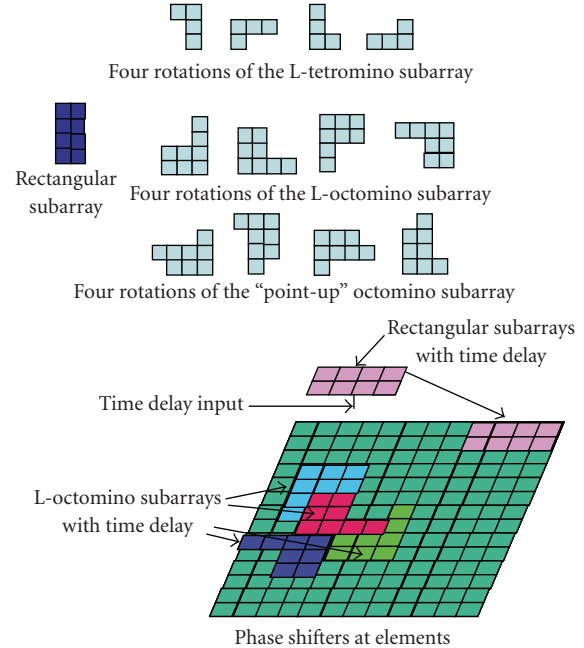


FIGURE 2: Irregular and rectangular subarrays.

3. Irregular Polyomino Subarrays

Figure 2 shows an array with subarrays and indicates the array filling with L-octomino subarrays. It also shows four rotations of an L-tetromino and two kinds of octominoes, an L-octomino and a “point-up” octomino, that we use to fill the array. In this paper, we are concerned only with shapes that completely fill, or “tile” the array area, because the fully filled area has maximum aperture gain. There are many other polyomino shapes and sizes that can be used for tiling an array, and the branch of mathematics that is closest to polyomino tilings is called combinatorics, of which polyominoes are a subset.

A more basic combinatoric problem may query whether a collection of identical polyominoes could be tiled as to exactly fill a rectangle. Such collections are called rectifiable. One researcher, Michael Reid [17], has a compact, permanent link for the subject [18]. A study limited to octominoes will yield, in a recognized Wolfram reference [19], a list of 369 distinct octominoes. These few topics are evidence of a concentrated and vibrant area of mathematical research.

Throughout this work, we have dealt exclusively with polyominoes that fully tile the apertures but have allowed some or many polyominoes to extend beyond the boundaries of the aperture, assuming that those squares outside of the aperture need not be excited.

Figure 3 shows a group of three-dimensional patterns radiated by an array of 64×64 elements at $f/f_0 = 1.3$ and $u_0 = v_0 = 0.5$, where $u_0 = \sin \theta_0 \cos \phi_0$, $v_0 = \sin \theta_0 \sin \phi_0$, and θ_0 , and ϕ_0 define the direction of scan. The array has a 40 dB Taylor taper, and therefore has low side lobes at broadside and/or center frequency. All element patterns are assumed to have a $\cos \theta$ angular dependence. The left pattern in Figure 3 is that of an array with time delay at every element. This pattern exhibits the design sidelobes

of -40 dB with a pattern gain of 37.3 dB as determined by integration. The center pattern corresponds to an array in which the individual elements are grouped into 512 rectangular subarrays (two elements in the elevation plane and four in the azimuth plane). This pattern has a gain of 37.03 dB (approximately a 0.3 dB loss due to phase error compared to the left pattern) and has five quantization lobes. The largest of these lobes is 11.45 dB below the gain at broadside. The pattern at right is produced by an array of 512 L-octominoes and radiates a main beam with a 36.83 dB gain (only 0.2 dB less than the array of rectangular subarrays). This pattern has no quantization lobes and has side lobes that are all at least 26.6 dB below the broadside gain.

These data are typical of results that have been presented previously to describe this work. In general, the various polyomino-based arrays have been found to have nearly the same gain but much smaller sidelobes than arrays of periodic, rectangular subarrays. Note that these residual side lobes are *not* suppressed quantization lobes, since the quantization lobe size remains constant relative to the main beam as array size is changed. Rather, we see that the residual side lobes of the polyomino-based arrays are reduced as the inverse of the array area. Our experience with arrays of up to 128 elements on a side indicate that the peak sidelobes continue to decrease by 5 to 6 dB with each quadrupling of array area.

Figure 4 addresses the question as to why the polyomino-based arrays are successful at eliminating the quantization lobes. Clearly the procedure breaks up the periodicity of the array, and so one would expect a better result than with contiguous rectangular subarrays, but with this figure we investigate much suppression due entirely to the

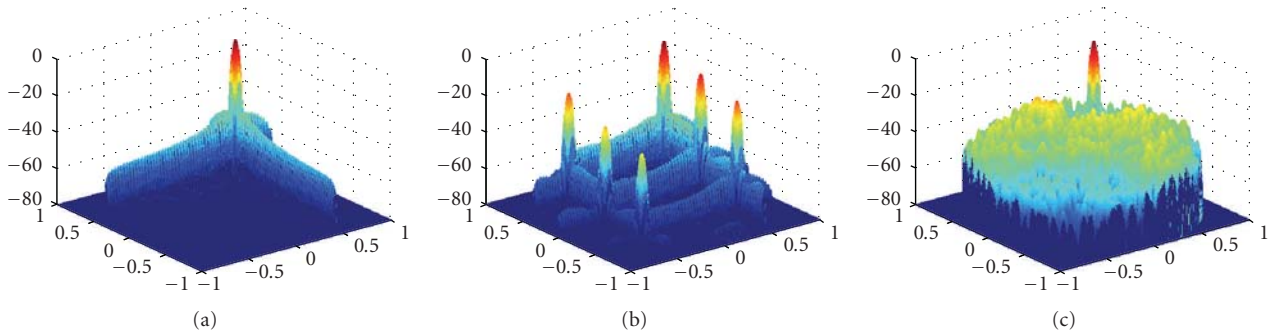


FIGURE 3: Radiation patterns at $f/f_0 = 1.3$ for an array with time delay at element level (a), at rectangular subarray inputs (b) and at L-octomino subarray inputs (c).

quasi-randomness and how much due to the changes in the subarray pattern amplitude as each is rotated.

Figure 4(a) shows an array of rectangular subarrays and the final pattern for an array of rectangular subarrays with $f/f_0 = 1.3$ and scanned to $u_0 = v_0 = 0.5$. The elements are 0.5λ apart in both planes, and the inter-subarray spacing of the eight element subarrays is λ in azimuth and 2λ in elevation. The array has 18 elements in azimuth and 24 in elevation. The contour levels are set at dB values of -3 , -10 , -15 , and -20 . The scanned pattern, shown at right in Figure 4(a), has a set of 5 quantization lobes, with varying degrees of suppression due to the subarray pattern. Figure 4(b) shows the array factor for the array with the subarray patterns assumed omnidirectional, as illustrated on the left of Figure 4(b). All the quantization lobes of Figure 4(a) are present at the same locations, but are now grating lobes unattenuated by the subarray pattern. A comparison of the numerical data shows that the resulting array factor of Figure 4(a) has its grating lobes suppressed at least 12 dB by the subarray pattern. These peak quantization lobes are at the same levels for much larger arrays.

Figures 4(c) and 4(d) present the same situations as Figures 4(a) and 4(b), but for the case of irregular (point-up) subarrays. Figure 4(c) shows an actual subarray configuration of “point-up” polyominoes and the pattern for that array. Although the array is small, the figure again demonstrates significantly lower sidelobes than the array of rectangular subarrays Figure 4(a). All of the larger sidelobes are in the neighborhood of -20 dB, or 8 dB below those of the rectangular subarrays, and they are no longer located at the quantization lobe angles. The pattern shows that no quantization lobes remain. Figure 4(d) shows the array factor of the polyomino based array with the subarray patterns replaced by omnidirectional one. This pattern thus includes only the effect of the aperiodic grid of phase centers. This pattern shows that only one peak sidelobe remains at the quantization lobe locations shown in 4(b), while other peaks do not correspond to the quantization lobe locations. Note that some of these peaks are greater than -10 dB since there are no element patterns to suppress them. The peak sidelobes now are distributed throughout a much wider area of space and our experience has shown that unlike the data of Figure 4(a), they continue to decrease with

array size. Comparing Figures 4(a) and 4(c) shows that the combination of the rotating subarray patterns and the phase center displacement produce a much larger role in sidelobe suppression than phase center displacement alone, but the phase center displacement is the major contributor to the successful result.

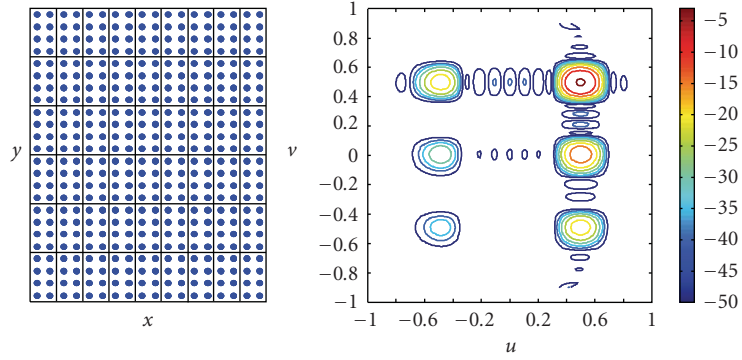
4. Power Dividers for Tetrominos and Octominoes

In general, one would expect that assembling an array from irregular subarrays would entail some extra burden in fabrication or assembly. However, there is little added assembly cost for an array of polyominoes that are all identical but rotated in the plane. Therefore we have chosen to use polyominoes that have 2^n elements for $n = 2$, and 3 for this paper, so that the subarrays can be excited by lossless power dividers. Other polyominoes of larger size “ n ” can also be used, but larger polyominoes have less bandwidth (or for LFOV they have a more limited scan region), and we have not investigated these limits. Very few larger polyominoes can actually tile rectangular areas without leaving voids in the surface, and it seems that with the exception of rectangular shapes one would need to use a multiplicity of higher-order polyominoes to properly tile a rectangular surface. The array elements themselves are on a fully periodic grid and so the aperture is unchanged from conventional apertures. Only the feed matrix is constrained to introduce the aperiodicity needed to eliminate quantization lobes.

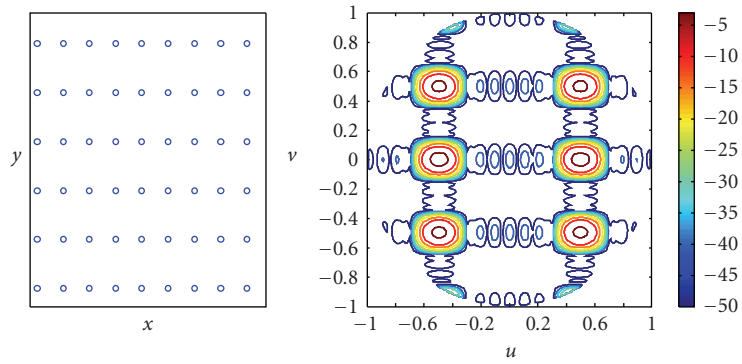
Figures 5, 6, and 7 show the power dividers and feed points (black rectangles) and a section of the filled arrays corresponding to the shapes noted in Figure 2 and investigated in this paper. Notice that all power dividers in any figure are identical, but because of the rotation the excitation points form an irregular pattern.

5. Peak Sidelobe Behavior of Tetrominos and Octominoes

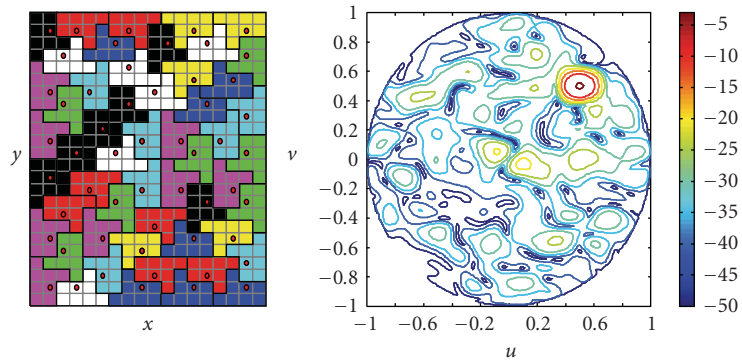
Peak sidelobes are not readily predicted analytically for arrays of irregular subarrays and so numerical results have been used to relate them to the rectangular subarray case. The peak



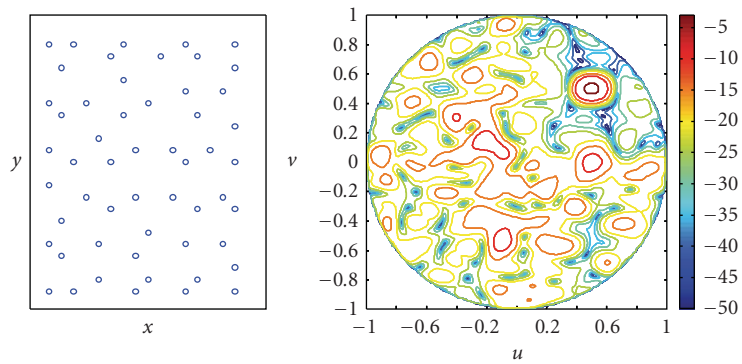
(a) Array of rectangular subarrays



(b) Array of omnidirectional elements at rectangular subarray phase centers



(c) Array of octomino subarrays. Subarray phase centers are indicated by red dots



(d) Array of omnidirectional elements at octomino subarray phase centers

FIGURE 4: Sidelobe structure for 18×24 element array of 54 subarrays of rectangular or L-octomino subarrays.

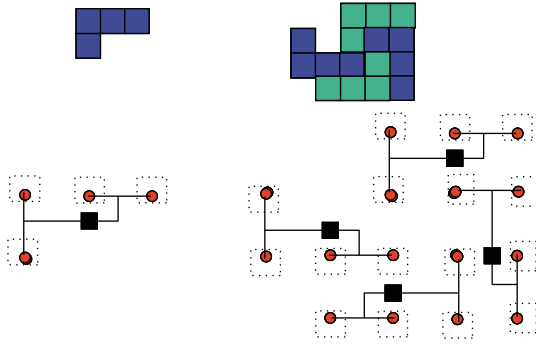


FIGURE 5: L-tetromino power divider and array section.

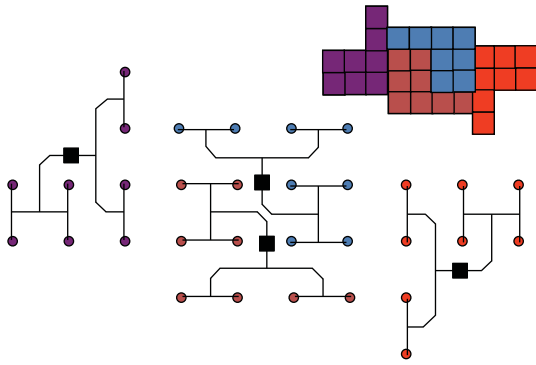


FIGURE 6: L-octomino power divider and array section.

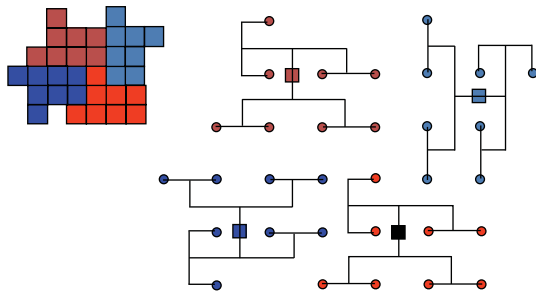
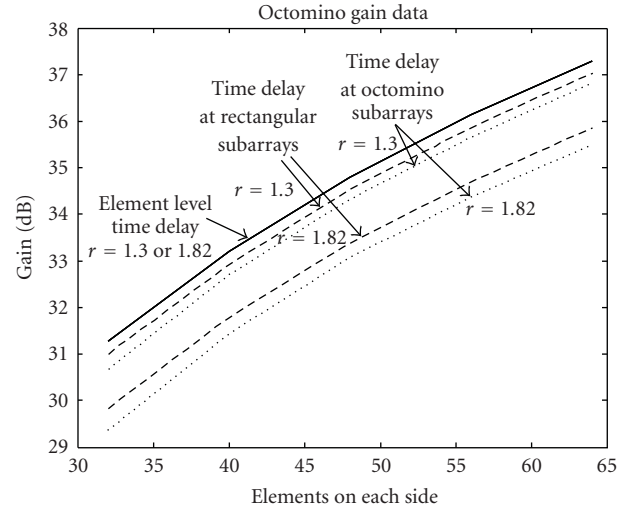
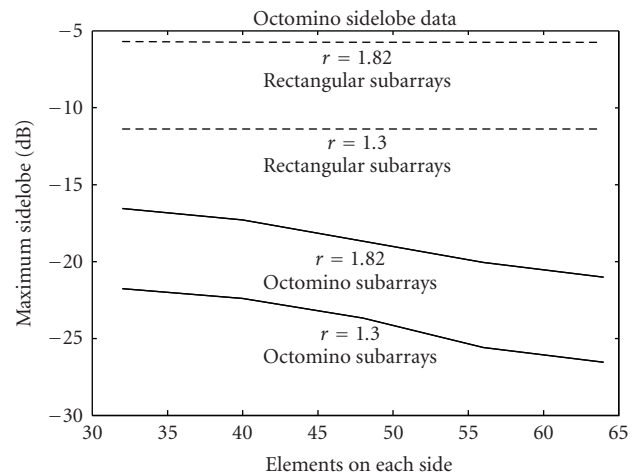


FIGURE 7: Point-up power divider and array section.

sidelobes depend upon scan angle and, for the wideband case, frequency offset ratio “ r ”, but once these parameters are chosen, the peak sidelobes decrease monotonically with array size and very nearly like a constant times $1/N$ for a large N -element planar array. The array gain increases with array area modified by the phase error introduced within each subarray.

The bandwidth of polyomino subarrays is primarily determined by gain falloff with scan, since there are no quantization lobes, and the peak sidelobes continue to decrease monotonically with array size. At the highest-frequency the element spacing is chosen to be spaced a half wavelength apart to avoid the element level grating lobes.

Figure 8 shows five sets of gain curves for square arrays as the array size is varied. These, and all other gain curves shown in this paper, were computed by integrating the array pattern using an assumed $\cos \theta$ element pattern. The figure

FIGURE 8: Gain comparison of arrays with time delay at element levels versus time delay at rectangular and L-octomino subarrays $r = f/f_0 = 1.3$ and 1.82 .FIGURE 9: Peak sidelobe level of rectangular and L-octomino subarrays $r = f/f_0 = 1.3$ (moderate bandwidth) and $r = 1.82$ (wide band).

compares the gain of arrays with time delay at the subarray level for rectangular or octomino subarrays. The gain of arrays with time delay at the element level is given as the solid curve. This represents the ideal array gain and is higher than any subarrayed case because there is no phase error.

The several time-delayed subarray cases plotted include one with about 2:1 bandwidth ($r = f/f_0 = 1.3$) for the upper-band limit, and one with about 10:1 bandwidth ($r = 1.82$ upper-frequency) and the design low-frequency of $r = 0.182$ (lower-frequency band not shown). We have not shown the lower-frequency results for this ultra wideband case because at this lower limit the subarray spacing is so small that there are no quantization lobes in real space. Unlike the narrower band situations where there are quantization lobes at both high and low-frequency extremes, here the subarray imposes no low-frequency limit; only the element spacing

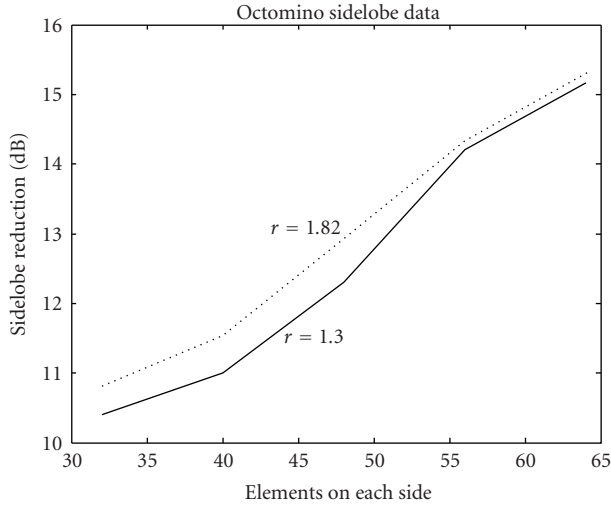


FIGURE 10: Sidelobe reduction factor (max rectangular subarray quantization lobe level—largest octomino sidelobe level) dB for moderate and wide band signals.

and impedance considerations provide any low-frequency limitation. In the cases discussed, the low-frequency could be chosen as low as the element design would allow, with no limitation imposed by the subarraying technique.

The curves shown in Figure 8 include the solid curve with full element level time delay and four curves with time delay at the input port to each subarray. The dashed curves are for rectangular subarrays (2×4 elements), one with high-frequency $r = 1.3$ (bandwidths $r = f/f_0 = 0.7$ to 1.3) and one with much higher bandwidth ($r = f/f_0 = 0.182$ to 1.82 , a 10:1 bandwidth).

The solid curve at the top of the figure is the gain using time delay at each element. These integrated data are almost exactly equal to the usual large array approximation for an aperture with aperture efficiency ϵ_a :

$$G = 4\pi \frac{A}{\lambda^2} \epsilon_a \cos \theta. \quad (4)$$

Notice that this single curve is the array gain for both frequency offsets; $r = 1.3$ and 1.82 , because the element spacing is set to 0.5λ at each frequency, so the array size is the same in normalized terms and the gain is also the same. The curves for time delay at the subarray input ports are shown dashed for rectangular subarrays and are approximately 0.27 dB below the time delayed array data at $r = 1.3$ and 1.45 dB below the curve at $r = 1.82$. The added loss is caused by the incremental phase error across the 8-element subarrays. The two dotted curves of Figure 8 give the corresponding gain for the L-octomino subarray based arrays, and lie approximately 0.2 dB below the curves for the rectangular subarrays, owing to the slightly greater phase error in the polyomino subarrays.

Figure 9 shows the corresponding peak sidelobe levels for the subarrayed cases of Figure 8. The peak sidelobe level for the element level time delayed array is not shown because it is just the idealized Taylor pattern with -40 dB peak sidelobes.

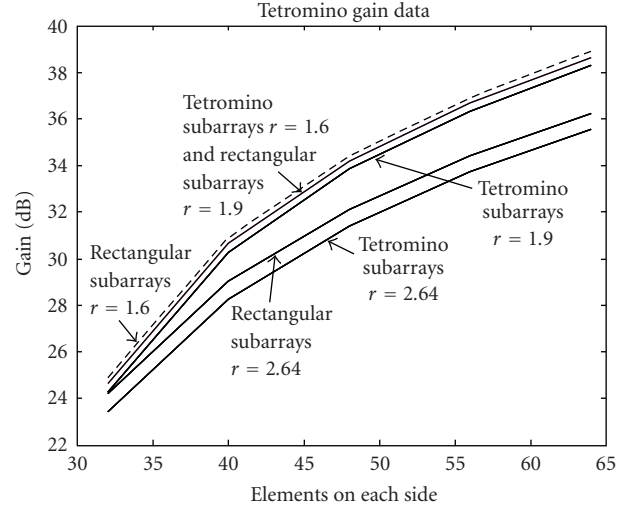


FIGURE 11: Gain comparison of arrays with time delay at element levels versus time delay at rectangular and L-tetromino subarrays $r = f/f_0 = 1.6$, $r = 1.9$ and $r = 2.64$ (wide band).

In this Figure the dashed patterns give the peak sidelobe level of arrays of rectangular (2×4) subarrays and show constant levels of 11.4 dB for $r = 1.3$, and -5.75 dB below the broadside gain (or only 4.23 dB below the projected area gain at $u_0 = v_0 = 0.50$) for $r = 1.82$. The quantization lobe level is independent of array size because the lobe samples the subarray pattern at the same point for any size array. The two solid curves in Figure 9 are the peak sidelobes for arrays of L-octomino subarrays for the two frequencies noted. Note that the improvement in comparison with the rectangular subarray results is nearly the same at both frequencies. Figure 10 shows this added sidelobe reduction to vary from about 10.5 dB for arrays 32 elements on a side to about 15.5 dB for 64 element arrays, but more interestingly this sidelobe reduction is almost the same whether the rectangular subarray peak sidelobes are -11.4 dB (for $r = 1.3$) or -5.75 (for the $r = 1.82$). This indicates that these limited results can be expected to be useful for estimating behavior of the arrays at other frequencies. The rectangular subarray data of Figure 9 are very simple to compute, but using the result of Figure 10, one can obtain a good estimate of peak sidelobe level for nearly any frequency range that one would want to estimate. In addition, we have found it a general rule for all the cases we have tested, that quadrupling the array size results in at least a 5 dB increase in this sidelobe reduction factor, so one can extrapolate these data to get results for various sizes as well as various frequencies.

Figures 11–13 show similar results for L-tetrominos when these are operated over about twice the bandwidth. The normalized upper frequency ranged from $r = 1.6$ to 2.64 . Figure 11 shows the gain of an array of the 4 element subarrays, comparing rectangular (square) 2×2 subarrays with the L-tetromino subarrays. The difference in gain between the four element rectangular subarrays and the L-tetromino subarrays is about 0.2 dB maximum at the $r = 1.6$ frequency limit, and about 0.8 dB at the higher $r = 2.64$ frequency limit. Figure 12 shows the sidelobe behavior of

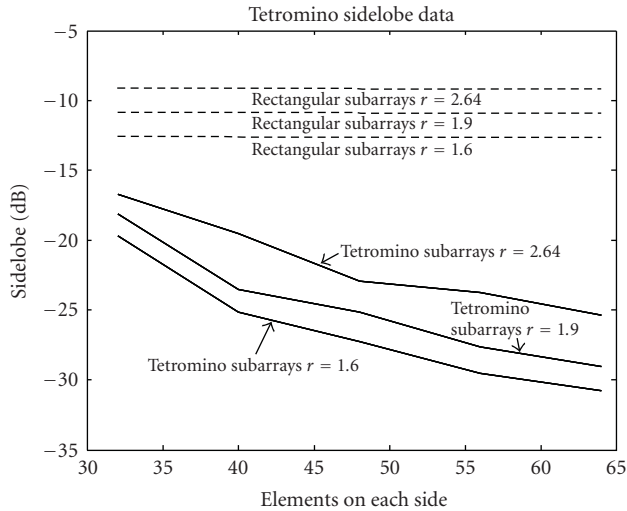


FIGURE 12: Peak sidelobe level of rectangular and L-tetromino subarrays $r = f/f_0 = 1.6$ (moderate bandwidth), $r = 1.9$ and $r = 2.64$ (wide band).

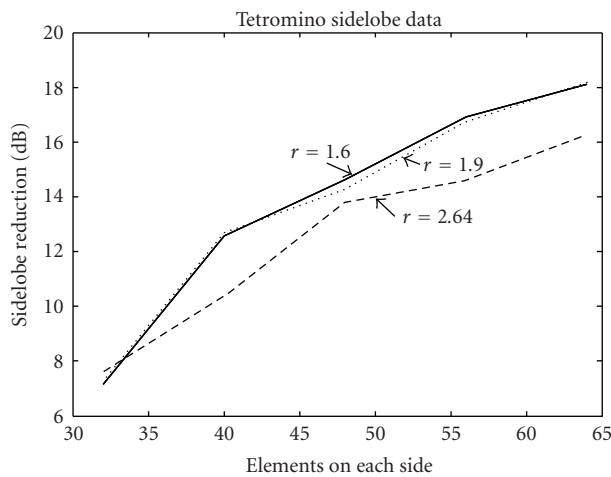


FIGURE 13: Sidelobe reduction factor (max rectangular subarray quantization lobe level—largest octomino sidelobe level) dB for moderate and wide band signals.

the arrays at both frequencies, and Figure 13 compares the sidelobe reduction for these cases. Here the reduction varies over a wider range than the octomino case but the slope of the curve is approximately the same for larger arrays. Even for the wideband $r = 2.64$ case the sidelobe reduction is within 2 dB of the lower bandwidth cases, again indicating the utility of these curves in generalizing to other frequencies and array sizes.

6. Conclusion

This paper has presented new results showing the application of polyomino-shaped subarrays to large space-based arrays that scan over a limited field of view with modest bandwidth, or over wider bandwidth and wide scan angles. In both cases,

subarray technology may be necessary to reduce cost by decreasing the number of phase shifters or time delay devices.

The paper compares the use of irregular polyomino versus the corresponding rectangular subarrays and shows that with only few tenths of a dB gain reduction the 8-element polyomino subarrays can reduce the peak sidelobes by more than 15 dB for 64×64 element arrays. Potentially much lower sidelobes can be obtained for larger arrays since sidelobe reduction improves by 5–6 dB for each quadrupling of array size. Results for smaller (tetromino) subarrays are in accord and provide even wider bandwidth.

Finally, it is shown that this sidelobe reduction is primarily a function of array size, not the frequency of operation. This leads to the useful conclusion that by focusing attention on the sidelobe reduction itself, it is possible to estimate peak sidelobe levels for tetromino and octomino arrays directly from the available rectangular subarray data.

Acknowledgments

This work was supported in part by the Air Force Office of Scientific Research, under Dr. A. Nachman, and in part by the Center for Advanced Sensor and Communications Antennas, Department of Electrical and Computer Engineering, University of Massachusetts, Amherst, Mass, USA. The work was conducted at the Sensors Directorate, Air Force Research Laboratory, Hanscom AFB, Mass, USA.

References

- [1] R. Tang, "Survey of time delayed beam steering techniques," in *Phased Array Antennas: Proceedings of the 1970 Phased Array Antenna Symposium*, pp. 254–260, Artech House, Dedham, Mass, USA, 1972.
- [2] R. J. Mailloux, *Electronically Scanned Arrays*, Morgan & Claypool, San Rafael, Calif, USA, 2007.
- [3] R. J. Mailloux, "Subarray technology for large scanning arrays," in *Proceedings of the 2nd European Conference on Antennas and Propagation (EuCAP '07)*, pp. 1–6, Edinburgh, UK, November 2007.
- [4] B. A. Munk, *Finite Antenna Arrays and FSS*, Wiley-IEEE Press, New York, NY, USA, 2003.
- [5] U. R. O. Nickel, "Monopulse estimation with subarray output adaptive beamforming and low sidelobe sum and difference beams," in *Proceedings of IEEE International Symposium on Phased Array Systems and Technology*, pp. 283–288, Boston, Mass, USA, October 1996.
- [6] S. P. Skobelev, "Methods of constructing optimum phased-array antennas for limited field of view," *IEEE Antennas and Propagation Magazine*, vol. 40, no. 2, pp. 39–49, 1998.
- [7] J. S. Ajioka and J. L. McFarland, "Beamforming feeds," in *Antenna Handbook: Theory, Applications and Design*, Y. T. Lo and S. W. Lee, Eds., chapter 19, Van Nostrand Reinhold, New York, NY, USA, 1988.
- [8] J. S. Herd, S. M. Duffy, and H. Steyskal, "Design considerations and results for an overlapped subarray radar antenna," in *Proceedings of IEEE Aerospace Conference (AERO '05)*, pp. 1087–1092, Big Sky, Mont, USA, March 2005.
- [9] S. M. Duffy, D. D. Santiago, and J. S. Herd, "Design of overlapped subarrays using an RFIC beamformer," in *Proceedings*

- of *IEEE Antennas and Propagation International Symposium (AP-S '07)*, pp. 1949–1952, Honolulu, Hawaii, USA, June 2007.
- [10] P. Russo, “Antenna which assures high speed data rate transmission links between satellites and between satellites and ground stations,” US patent no. 5262790, November 1993.
 - [11] R. L. Haupt, “Optimized weighting of uniform subarrays of unequal sizes,” *IEEE Transactions on Antennas and Propagation*, vol. 55, no. 4, pp. 1207–1210, 2007.
 - [12] H. Wang, D.-G. Fang, and Y. L. Chow, “Grating lobe reduction in a phased array of limited scanning,” *IEEE Transactions on Antennas and Propagation*, vol. 56, no. 6, pp. 1581–1586, 2008.
 - [13] P. Rocca, L. Manica, M. Benedetti, R. Azaro, and A. Massa, “Simultaneous optimization of subarray weights and sizes for low sidelobe synthesis of large array antennas,” in *Proceedings of IEEE International Symposium on Antennas and Propagation (APS '08)*, pp. 1–4, San Diego, Calif, USA, July 2008.
 - [14] V. Pierro, V. Galdi, G. Castaldi, I. M. Pinto, and L. B. Felsen, “Radiation properties of planar antenna arrays based on certain categories of aperiodic tilings,” *IEEE Transactions on Antennas and Propagation*, vol. 53, no. 2, pp. 635–644, 2005.
 - [15] R. J. Mailloux, S. G. Santarelli, and T. M. Roberts, “Wideband arrays using irregular (polyomino) shaped subarrays,” *Electronics Letters*, vol. 42, no. 18, pp. 1019–1020, 2006.
 - [16] K. C. Kerby and J. T. Bernhard, “Sidelobe level and wideband behavior of arrays of random subarrays,” *IEEE Transactions on Antennas and Propagation*, vol. 54, no. 8, pp. 2253–2262, 2006.
 - [17] <http://www.math.ucf.edu/~reid/Polyomino/index.html>.
 - [18] <http://tinyurl.com/qsrz8>.
 - [19] <http://mathworld.wolfram.com/Octomino.html>.

Research Article

Sunflower Array Antenna with Adjustable Density Taper

Maria Carolina Viganó,¹ Giovanni Toso,² Gerard Caille,³ Cyril Mangenot,² and Ioan E. Lager¹

¹International Research Centre for Telecommunications and Radar (IRCTR), Delft University of Technology, Mekelweg 4, P.O. Box 5031, 2628 GA Delft, The Netherlands

²European Space Agency, ESA-ESTEC, 2200 AG Noordwijk, The Netherlands

³Thales Alenia Space, 26 Avenue J. F. Champollion, 31037 Toulouse, Cedex 1, France

Correspondence should be addressed to Maria Carolina Viganó, m.c.vigano@tudelft.nl

Received 24 September 2008; Accepted 5 January 2009

Recommended by Stefano Selleri

A deterministic procedure to design a nonperiodic planar array radiating a rotationally symmetric pencil beam pattern with an adjustable sidelobe level is proposed. The elements positions are derived by modifying the peculiar locations of the sunflower seeds in such a way that the corresponding spatial density fits a Taylor amplitude tapering law which guarantees the pattern requirements in terms of beamwidth and sidelobe level. Different configurations, based on a Voronoi cell spatial tessellation of the radiative aperture, are presented, having as a benchmark the requirements for a typical multibeam satellite antenna.

Copyright © 2009 Maria Carolina Viganó et al. This is an open access article distributed under the Creative Commons Attribution License, which permits unrestricted use, distribution, and reproduction in any medium, provided the original work is properly cited.

1. Introduction

Communication satellites use multiple beam antennas providing downlink and uplink coverages over a field of view for high data rate, multimedia, or mobile personal communication applications. High gain, multiple overlapping spot beams, using both frequency and polarization reuse, provide the needed coverage. In order to generate high gain spot beams, electrically large antenna apertures are required. These apertures may be generated by either reflectors or phased arrays. Phased arrays would be a natural choice to generate multiple beams but up to now the poor efficiency, the high cost, and the deployment complexity of active arrays have been their main drawbacks, limiting their use onboard satellites. These drawbacks are mainly due to the required distributed and tapered power amplification which is inducing poor power efficiency.

Aperiodic arrays with equiamplitude elements permit to mitigate these limitations and represent a valid alternative to traditional periodic phased arrays with amplitude tapering. Resorting to aperiodic arrays with equiamplitude fed elements is particularly effective for the design of large arrays working in transmission. This type of antenna architecture is considered extremely promising for achieving a multibeam coverage on the Earth from a geostationary satellite [1–4].

Unequally spaced arrays have several interesting characteristics and may offer some potential advantages with respect to periodic arrays [2]. Firstly, aperiodic arrays allow the reduction of the sidelobe level (SLL) without resorting to an amplitude tapering. A second useful property of aperiodic arrays is the possibility to reduce the number of elements in one assigned aperture without major impact on the beamwidth. The reduction in the number of elements, with respect to the corresponding periodic array, depends on the required aperture efficiency and on the field of view where the assigned sidelobe level is imposed (based on the desired scanning range and regulatory aspects). Thirdly, sparse arrays can effectively be employed for spreading out the energy that would otherwise accumulate in grating lobes (GL) due to the wide interelement spacing.

In terms of limitations, nonperiodic arrays exhibit a reduced aperture efficiency when identical, non-equispaced elements are used. As a consequence, a reduced maximum equivalent isotropically radiated power (EIRP) is obtained if not compensated by an increase of the power radiated by each active chain. Furthermore, implementation constraints, as a nonregular lattice, may jeopardize the use of generic building blocks, with consequences on the costs. This particular drawback may be mitigated by implementing a set of different types of subarrays to fill the whole aperture.

Up to now, sparse and thinned arrays have been rarely used, essentially because of the complexity of their analysis and synthesis with a reduced knowledge, as a consequence of their radiative properties. The main concern in the design of sparse arrays is to find an optimal set of element spacing to meet the array specifications, while assuming a uniform excitation for practical convenience.

The synthesis of aperiodic arrays is a known problem in the antenna community [5–22]. It is interesting to observe that while in the 1960s and 1970s mainly deterministic solutions have been proposed, in the last years procedures based on statistic global optimization techniques have been mainly presented. Recently, in [22], the simple and elegant spatial tapering deterministic solution introduced in the papers of Doyle [11] and Skolnik [17], and qualitatively in the work of Willey [7], has been revisited and improved. Deterministic solutions present two important advantages with respect to statistical algorithms: they allow obtaining results in real time and offer a solution with a controllable accuracy. Moreover, the results obtained applying deterministic solutions may be directly used or adopted as starting point for a further optimization based on a numerical technique which can take into account other constraints (like maximum and minimum spacing between the radiators, etc.).

The problem of aperiodic arrays has recently gained a renewed interest especially for the design of multibeam satellite antennas [1–4]. Most of the techniques presented for the design of aperiodic arrays deal with the case of linear arrays. When approaching the planar case, the designer has a higher number of degrees of freedom but the problem increases also in complexity. In some papers, an aperiodic planar lattice organized in rings has been proposed [12–14]. Arrays organized in rings permit having a pattern with good symmetry properties, allow the reduction and control of GL, and their design is simplified because the elements positions can be expressed as the product of two functions one controlling the angular position of the elements and one controlling the distance of the rings from the center.

In this paper, the equiamplitude elements constituting the aperiodic array are placed on a lattice reproducing the positions of the sunflower seeds, opportunely adjusted according to a desired amplitude tapering. This type of lattice is selected essentially because it guarantees a really good radial and azimuthal spreading in the element positions. As a consequence, the pattern in the sidelobes and grating lobes region tends having a plateau-like shape [9, 16], avoiding the presence of high narrow peaks. Moreover, by adjusting the element positions using a simple parametric equation, a beamwidth can be selected and the SLL kept under an assigned value.

An aperiodic planar array with the elements organized according to a sunflower lattice has been already proposed in [23]. However, the spatial density of the elements in [23] is uniform. As a consequence, since the elements are equiamplitude, the equivalent amplitude tapering is uniform as well so that this type of array guarantees only a good suppression of the GL, without the ability of controlling the SLL.

The hereby proposed sunflower lattice is completely adjustable in order to follow stringent requirements on the beamwidth and the SLL without using any amplitude taper. This planar array can be considered in the design of a transmitting direct radiating array for a satellite communication antenna on a geostationary satellite.

The paper now proceeds as follows. In Section 2 the radiation pattern is introduced for a generic array, in Section 3 the definition of the element density function is given and discussed for the uniform case. In Section 4 a procedure to adjust the spatial density according to a Taylor amplitude tapering is presented. In Section 5 the requirements of a typical telecommunication multibeam antenna are introduced. Finally, in Section 6 some numerical results, in order to test the functionality of the proposed configuration, are presented. Additionally, the appendixes provide more general information on spirals and discuss the normalized element density that is used in the course of the element placement.

2. Array Radiation Pattern

The antenna radiation pattern of a planar array is given by

$$E(\theta, \phi) = \sum_{n=1}^N a_n F_n \exp(jk[x_n \sin(\theta) \cos(\phi) + y_n \sin(\theta) \sin(\phi)]), \quad (1)$$

where N is the total number of elements, a_n represents the excitation coefficient for the n th element and F_n its radiation pattern, x_n and y_n are the n th element positions in the xOy plane, θ is the elevation angle measured from the Oz axis, and ϕ is the azimuth angle measured in the xOy plane with respect to the Ox axis. Because the variables to be derived (x_n and y_n) appear inside an exponential function, the optimization problem is not linear. Moreover, F_n , unlike in periodic arrays, can change from element to element if a requirement on the minimum aperture efficiency (hence on the minimum gain) is enforced.

In the following section, a particular spiral configuration will be introduced as a starting point before the space taper is applied.

3. Spiral Array with Uniform Spatial Density

A well-known spiral is the Fermat one (see Figure 12) which has the property of enclosing equal areas within each turn. This spiral is often found in nature, as indicated in the appendix. The elements are placed along this spiral according to the following equations:

$$\rho_n = s\sqrt{\frac{n}{\pi}}, \quad \text{for } n = 1, \dots, N + 1, \quad (2)$$

$$\phi_n = 2\pi n\beta_1, \quad \text{for } n = 1, \dots, N + 1, \quad (3)$$

where ρ_n is the distance from the spiral center to the n th element, the parameter β_1 controls the angular displacement ϕ between two consecutive elements, and the parameter s

denotes the distance between the elements in the xOy plane. Assume a sparse array deployed on a circular aperture of radius R_{ap} along the Fermat spiral, with element locations given by (2) and (3). Note that ρ_N is taken to correspond to R_{ap} , whereas ρ_{N+1} is a virtual element places outside the aperture, its use is becoming obvious in what follows.

Let us now introduce a normalized element density function:

$$\tilde{d}(\rho_n) = \frac{(R_n^2 - R_{n-1}^2)_{\min}}{(R_n^2 - R_{n-1}^2)}, \quad \text{for } n = 1, \dots, N, \quad (4)$$

where R_{n-1} and R_n are the inner and outer radii of the annular rings enclosing the n th element, respectively, with R_0 being always taken as zero (see the appendix) for a justification for this choice of defining the normalized density function). Here, a choice is made to take the radii R_n as

$$R_n^2 = \frac{\rho_{n+1}^2 + \rho_n^2}{2} \quad \text{for } n = 1, \dots, N. \quad (5)$$

As recognizable from (4), the normalized density function corresponds to the current of a single element divided by the area of the relevant annular ring.

The lattice in [23] (see Figure 1) is characterized by a uniform density. On account of (5) and (2), it can be easily shown that

$$\tilde{d}(\rho_n) = \frac{2(R_n^2 - R_{n-1}^2)_{\min}}{(\rho_{n+1}^2 - \rho_{n-1}^2)} = \frac{\pi R_{ap}^2}{Ns^2} = 1. \quad (6)$$

This property is attractive when the interest focuses on avoiding GL only, without a control of the SLL. As for the SLL, it remains around 17 dB, irrespective of the number of elements in the array and the spacing factor s . This is consistent with the element distribution replicating a uniform current distribution on a circular aperture.

It is now clear that the only possibility to control the SLL as well is by introducing a density taper. In the following section, it will be demonstrated how, by translating a Taylor amplitude tapering law [24] into a corresponding spatial density law, the SLL can be drastically reduced.

4. Spiral Array with Density Tapering

The spiral aperiodic lattice with a uniform element density introduced in the previous section is an excellent starting point to apply a space tapering process. The spreading of the elements in the spiral arms guarantees an optimal behavior in terms of GL even when the interelement spacing is larger than λ . In order to be able to control the SLL, it is possible to vary the elements positions with respect to the array center, thus obtaining an effect similar to an amplitude taper.

The space taper technique presented here consists of choosing a reference amplitude distribution whose pattern satisfies the assigned requirements and emulates it by varying the radiator distance from the center. Concretely, a Taylor amplitude taper law with a certain SLL and \bar{n} [24] is selected as a reference. The locations of the elements in the sparse

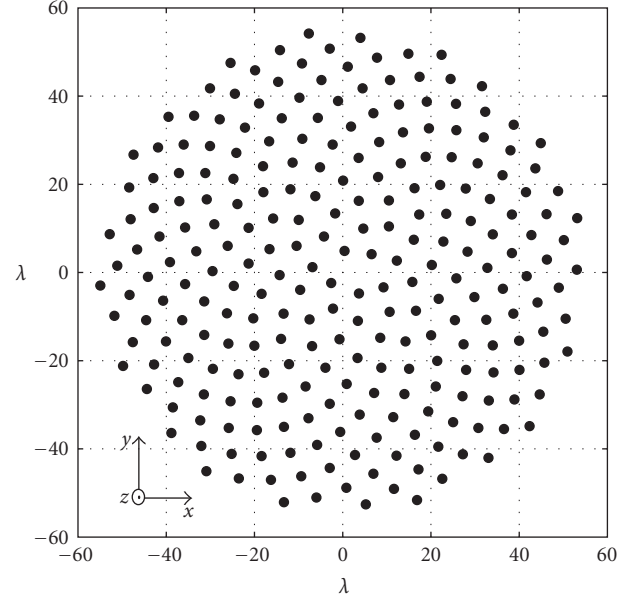


FIGURE 1: Distribution of the 250 elements in the uniform sunflower array antenna, as reported in [23].

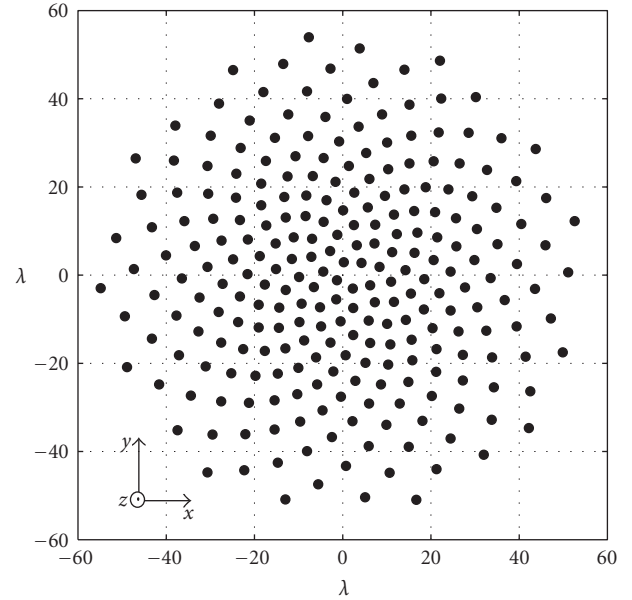


FIGURE 2: Distribution of the 250 elements in the tapered sunflower array antenna.

array are determined by means of a simple, 2 step algorithm: firstly N circles of increasing radii ρ_n , $n = 1, 2, \dots, N$ are selected by sequentially applying the relations

$$2\pi \int_{R_{n-1}}^{\rho_n} A(r)r dr = \frac{2\pi}{2N} \int_0^{R_{ap}} A(r)r dr, \quad (7)$$

$$2\pi \int_{R_{n-1}}^{R_n} A(r)r dr = \frac{2\pi}{N} \int_0^{R_{ap}} A(r)r dr, \quad (8)$$

starting from R_0 that is taken to be 0. Here, $A(r)$ denotes the Taylor amplitude taper and R_{ap} is the radius of the complete

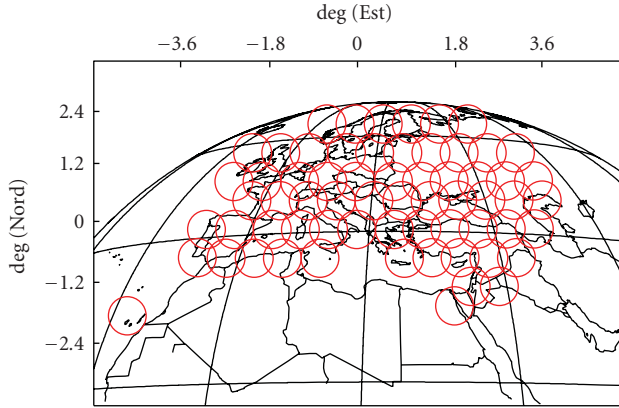


FIGURE 3: European multibeam coverage in a 1 : 4 frequency re-use scheme from a geostationary satellite.

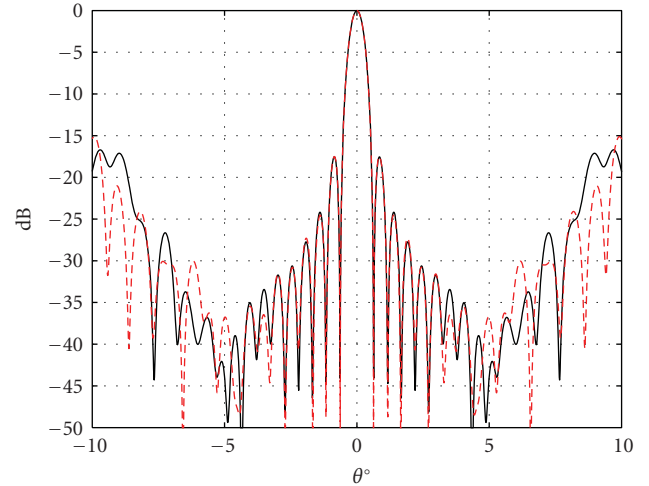
circular aperture. Note that (7) emulates the desired taper by equating the surface integral over the annular ring delimited by R_{n-1} and ρ_n to half of the N th part of the total aperture excitation. Subsequently, the element positions are determined by choosing their pertaining azimuth angle ϕ_n according to (3). The result of this placement strategy is illustrated in Figure 2 where a 56λ aperture is filled with 250 elements distributed in a manner such to obtain a pattern similar to the one achievable with a Taylor amplitude law characterized by $SLL = 32$ dB and $\bar{n} = 4$. A total number $N = 250$ is selected as a good compromise between the performance in scanning and the cost. The choice for these values will be clearer in the following sections.

5. Typical Requirements for a Multibeam Satellite Application

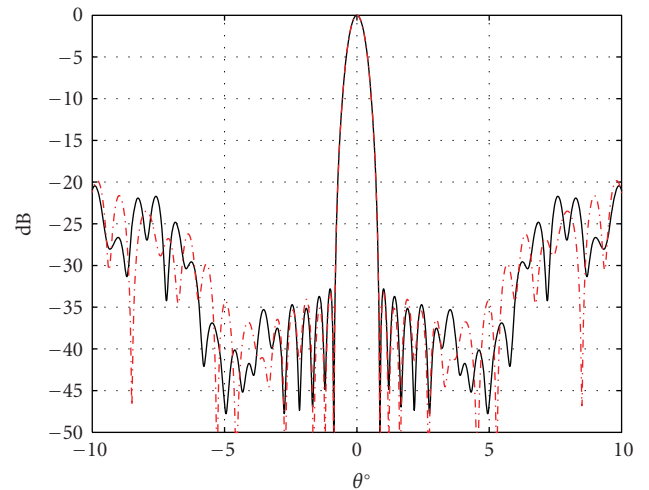
The transmitting antenna considered in this study is operating in Ka-band (19.7–20.2 GHz) and may have a maximum diameter of 1.3 m. The starting point considers the circular direct radiating array with dimensions deemed as sufficient to provide the required maximum gain and beamwidth. The array must generate 64 spot beams. The total frequency band is divided into 4 subbands, and each of them being assigned to a set of beams so that there are no adjacent pencil beams using the same resource. Figure 3 shows the footprint on the Earth of the 64 pencil beams.

In the last 3 rows of Table 1, the maximum sidelobe level in three different regions has been specified. The value in dBi has been preferred to the dB one as the configurations analyzed in Section 5 have different maximum directivity values.

In Figure 4, the array factor of the configurations presented in Figures 1 and 2, respectively, is plotted for two different ϕ cuts. In both uniform and tapered sunflower configurations, the array factor is remarkably stable in ϕ , resulting in the area of interest, in practically rotationally symmetric radiation patterns. The array factor in Figure 4(b) is following the expected behavior until a certain θ angle at which the effects of the first pseudograting lobe (the



(a)



(b)

FIGURE 4: Array Factor, two different ϕ cuts ($\phi = 0^\circ$ in red dotted line and $\phi = 90^\circ$ in black), for the array configuration in Figures 1 and 2, respectively.

TABLE 1: Mission requirements.

Number of spots	64
Spot diameter	0.65°
Inter-spot distance	0.56°
Rx band	29.5–30.0 GHz
Tx band	19.7–20.2 GHz
Frequency reuse	1 : 4
EOC gain	43.8 dBi
SLL in the first $\mp 4^\circ$	20 dB
SLL in the first $\mp 8^\circ$	25 dB
SLL in the first $\mp 90^\circ$	30 dB

energy of which being spread over a wider θ interval due to the nonperiodic placement) become visible. Considering the previous example in which the maximum interelement

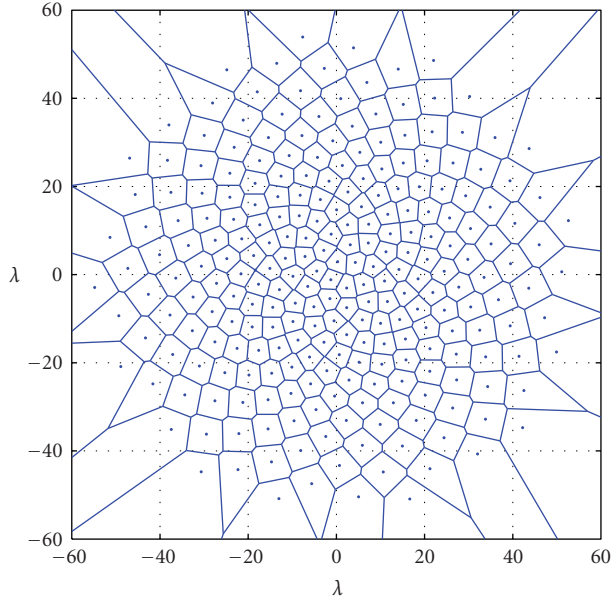


FIGURE 5: The Voronoi tessellation consisting of the cells enclosing the chosen phase centers.

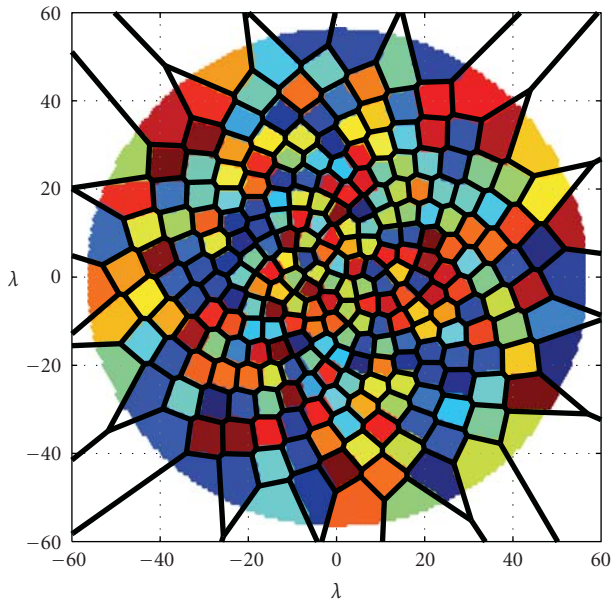


FIGURE 6: Subarray allocation and aperture subdivision corresponding to the Voronoi tessellation in Figure 5.

distance $D_{\max} = 8.43 \lambda$, the first contribution of the grating lobe is expected at

$$\theta_{\text{GL}} = \sin^{-1}\left(\frac{1}{D_{\max}}\right) = 6.81^\circ. \quad (9)$$

In fact, in Figure 4(b), the pattern starts exceeding the imposed SLL around this θ_{GL} .

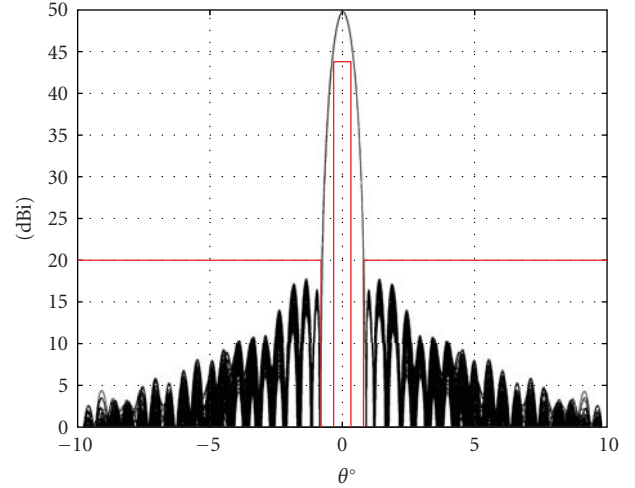


FIGURE 7: Array pattern for the configuration depicted in Figure 6. The beam is scanned to boresight. The red line corresponds to the requirement mask.

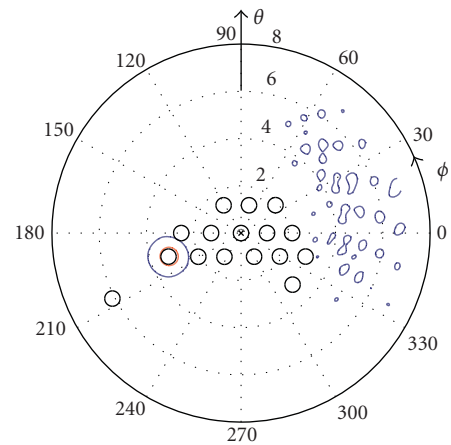


FIGURE 8: Array pattern for the configuration depicted in Figure 6. The beam is pointing at Europe edges. The red line represents the iso-level curves at 43.8 dBi, and the blue ones the iso-level curves at 20 dBi. The black circles represent the interfering area.

6. Validation of the Technique

The locations provided by the space taper process (see Figure 2) have been used as phase centers of the radiators in a planar array. Two different techniques are used to select the radiators.

6.1. First Approach: Using the Entire Aperture. The circular aperture with a maximum radius of 56λ is completely filled with patches disposed on a regular lattice. The triangular grid is chosen because of its better performances compared to the regular rectangular one. The analytical equations in [25] are used to express the field of the elementary patch antenna, radiating on a ground plane, with side lengths equaling 0.42λ and a rectangular cell surrounding it with side lengths $0.8 \lambda \times 0.85 \lambda$. In order to cover the complete

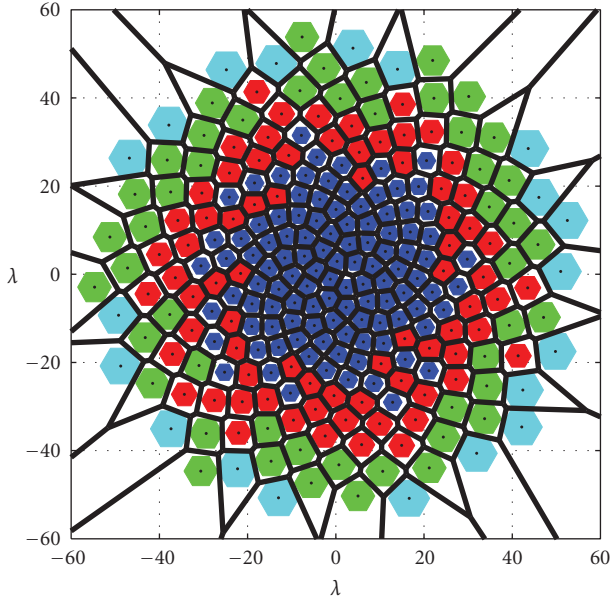


FIGURE 9: Hexagonal subarray positions and dimension after postprocessing.

aperture, with this patch choice, more than 15 thousands patches are required. These patches are then collected into subarrays.

The positions of the phase centers of the subarrays for $N = 250$ are derived with the formulation presented in the previous section following a Taylor taper presented in the previous section following a Taylor taper with $SLL = 32$ dB and $\bar{n} = 4$. The subarray positions are then superimposed on the uniform array, as indicated in Figure 6. Each patch center is assigned to the closest subarray center that can be interpreted as assigning the relevant patch to the Voronoi cell [26] corresponding to the computed phase center. Note that the Voronoi surface division (see Figure 5) provides an optimum tessellation of the available real estate.

To obtain the total radiation pattern, each radiation pattern of the subarray F_n has been calculated and multiplied by the exponential that takes into account the positions of the phase center of that subarray given in (1).

Since the Voronoi cell shapes are close to circular ones, the subarray patterns result to be almost rotationally symmetric. This is an important property when the beam is scanned.

In Figure 7, the pattern for the beam pointing at boresight is plotted for 360ϕ cuts (one at every degree). The red line in this figure indicates the mask requirements given in Table 1. Figure 8 represents the radiation pattern when the beam is pointed at the Europe's edges: the blue and red lines are iso-level curves at 20 dBi and 43.8 dBi, respectively, while the black circles enclose the regions of the coverage in which the same resource is used. As it can be seen from Figure 8, even when the beam is pointed at the Europe's edges, the pattern remains compliant with the requirements given in [1].

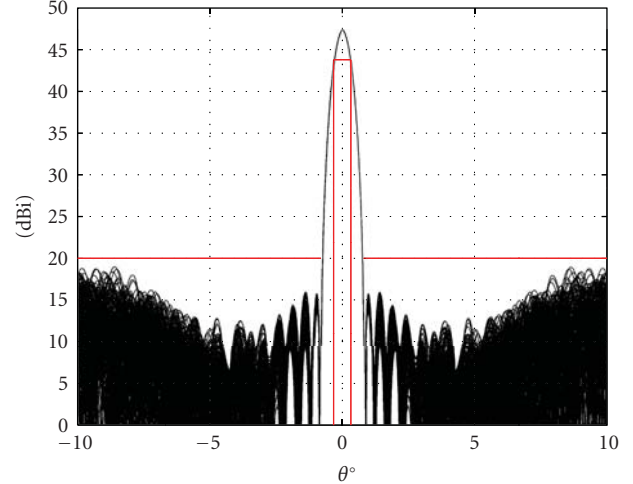


FIGURE 10: Array pattern for the configuration depicted in Figure 9. The beam is scanned to boresight. The red line corresponds to the requirement mask.

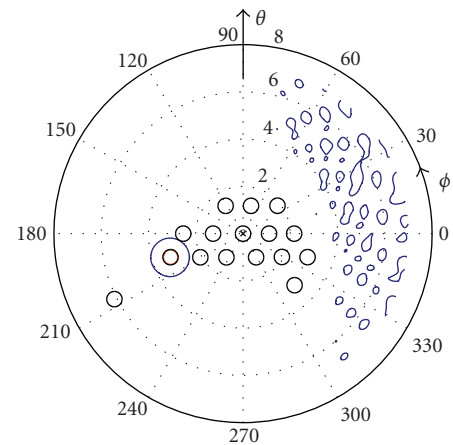


FIGURE 11: Array pattern for the configuration depicted in Figure 9. The beam is pointing at Europe edges. The red line represents the iso-level curves at 43.8 dBi, and the blue ones the iso-level curves at 20 dBi. The black circles represent the interfering area.

With this method, the entire surface available is used maintaining at the same time a very small number of controls (one for each subarray).

6.2. Second Approach: 4 Different Types of Subarrays. In this case, a more technology-oriented approach is considered: the aperture is filled as much as possible with predefined hexagonal subarrays. A limited number of these subarrays is selected as a compromise in order to keep the complexity and the cost limited while offering good performances. Four subarrays with different sizes have been selected and used to fill the array aperture. All the subarrays have a hexagonal shape and consist of 2, 3, 4, or 5 rings of elements surrounding the central one on a regular triangular lattice. The patches used in the subarrays are the same as the ones described in the previous subsection.

modified in order to fit a reference amplitude tapering. The design technique has been applied for the preliminary design of a Direct Radiating Array for a multibeam satellite communication mission.

Appendices

A. Fibonacci Spirals

Spirals are one of the most common regular shapes in nature: from the snail shell to the sunflower seed placement, to the Milky way arms. Different kinds of spirals are known in literature. Using a spiral placement for the elements of a planar array guarantees a good spreading of the energy associated to the side and grating lobes. Furthermore, a spiral lattice permits obtaining a quite uniform filling of a given aperture compared to other planar lattices like the ones organized in rings. A well-known spiral is the Fermat spiral (Figure 12) which has the property of enclosing equal areas within every turn. Its equation can be expressed in polar coordinates as

$$\rho = a\sqrt{\phi}, \quad (\text{A.1})$$

where ρ is the distance from the spiral center, and ϕ is the angle that identifies the point position respect to the x axis; the parameter a controls the distance between the spiral turns.

This spiral is quite often found in nature. In particular, there are leafs and seeds whose positions can be obtained by sampling a Fermat spiral equation, that is,

$$\begin{aligned} \rho &= \sqrt{nb}, \\ \phi &= \frac{2\pi n}{c}, \end{aligned} \quad (\text{A.2})$$

and when it is important having a uniform subdivision of the space the parameters b and c are closely related to the Golden Ratio, also known as Fibonacci number since it represents the solution of the Fibonacci quadratic equation. For instance, the leaves around a stem use this positioning to share in an optimal way the space and the light [27].

The Fibonacci sequence is known since 1202 d.C., thanks to Leonardo son of Bonaccio from Pisa and his book Liber Abaci. This sequence has been widely analyzed and applied in different fields: from the description of particular plants to computer science, from crystallography to electrical engineering. By solving the Fibonacci quadratic equation [28]:

$$\beta^2 A_n = \beta A_n + A_n, \quad (\text{A.3})$$

the following two roots are obtained:

$$\begin{aligned} \beta_1 &= \frac{\sqrt{5} + 1}{2} = \tau, \\ \beta_2 &= \frac{1 - \sqrt{5}}{2} = -\frac{1}{\tau}. \end{aligned} \quad (\text{A.4})$$

In most of the applications, the first value has been used, but to characterize the spiral, both of them are usable. The divergence angle, also referred to as the golden angle, is defined as

$$\text{golden angle} = \frac{360^\circ}{\beta_1^2} = 360^\circ - \frac{360^\circ}{\beta_2^2}. \quad (\text{A.5})$$

Because this value is irrational, it is impossible to have two or more elements in the spiral array characterized by the same ϕ angle. The element packing results to be efficient. Interesting Fermat spirals could be also the ones with other irrational coefficients like $\sqrt{2}$. In the patent [23], β_1 is used for the element disposition along the spiral according to the formulation presented in (2) and (3). As it can be easily noticed, the positions of the elements in the sunflower array depend only on n via a trivial equation.

The second type of spirals employed in this study is the Fibonacci one, namely, a particular kind of logarithmic spiral, where the ratio between radii evaluated at each 90° is related to the golden ratio number. It is interesting to note that in a sunflower array configuration, when the elements are placed on a Fermat spiral at every β_1 degrees, the elements form sets of clockwise and anticlockwise Fibonacci spirals. The number of spirals in each set are two consecutive terms of the Fibonacci series as it can be seen in Figures 13(a) and 13(b). Another particular characteristic of this configuration is that in order to obtain for example the 5 clockwise spirals, it is sufficient to connect the elements on the Fermat spiral whose numbers difference is exactly 5.

B. Normalized Element Density Function

Assume the case when a continuous, strictly positive, rotationally symmetric, *normalized* current amplitude distribution $A(r)$ on a circular aperture of radius R_{ap} needs to be mimicked by means of N equiamplitude elements located at *monotonically increasing* distances ρ_n , $n = 1, \dots, N$. (All distances r or radii R employed in this appendix are considered with respect to the aperture center.) Let R_n ($n = 0, \dots, N$) be $N + 1$ radii chosen such that $R_{n-1} < \rho_n < R_n$ for $n = 1, \dots, N$, with R_0 being taken to be zero. Note that for reasons that will be elaborated upon later, R_N may be, and in most cases is, taken to be (slightly) larger than R_{ap} . The monotonic increasing of the values ρ_n combined with the choice for the radii R_n ensures that inside in each annular ring of inner radius R_{n-1} and outer radius R_n there is only one radiator. With these prerequisites, an equivalent discrete amplitude density function can be defined by means of the expression

$$d(\rho_n) = \frac{K}{\pi(R_n^2 - R_{n-1}^2)}, \quad \text{for } n = 1, \dots, N, \quad (\text{B.1})$$

where the K denotes the *constant* excitation of each of the N elements. In view of ensuring the consistency of this definition, the radii R_{n-1} and R_n are chosen such that

$$\int_{R_{n-1}}^{R_n} A(r)r \, dr = K, \quad \text{for } n = 1, \dots, N. \quad (\text{B.2})$$

Furthermore, in view of ensuring identical aggregate excitation over the aperture, the constant K is adopted as

$$K = \frac{1}{N} \int_0^{R_{\text{ap}}} A(r) r \, dr. \quad (\text{B.3})$$

By now invoking the mean function theorem, the area of the annular ring in the denominator of (B.1) can be rewritten as

$$\begin{aligned} \pi(R_n^2 - R_{n-1}^2) &= \frac{1}{A}(\xi_n) \int_{R_{n-1}}^{R_n} A(r) r \, dr \\ &= \frac{K}{A}(\xi_n), \quad \text{for } n = 1, \dots, N, \end{aligned} \quad (\text{B.4})$$

with ξ_n ($n = 1, \dots, N$) being an unspecified point in the intervals $[R_{n-1}, R_n]$. Substituting (B.4) in (B.1) then yields

$$d(\rho_n) = A(\xi_n), \quad \text{for } n = 1, \dots, N. \quad (\text{B.5})$$

Due to the choice for ρ_n and ξ_n , the distance $|\rho_n - \xi_n|$ is bounded above by $R_n - R_{n-1}$, which, in view of complying to (B.3) and of the continuity of $A(\rho)$, becomes arbitrarily small for arbitrarily large N -s. Consequently, the (discrete) amplitude density function can be made to approximate with arbitrary accuracy of the original current density.

In order to prevent possible above unit values of the discrete amplitude density $d(\rho_n)$ that may occur in the case when N is small, this quantity is now normalized to its largest value. By accounting for the fact that $\max[d(\rho_n)]|_{n=1, \dots, N}$ corresponds to the minimum $R_n^2 - R_{n-1}^2$ difference, it is found that

$$\tilde{d}(\rho_n) = \frac{\min(R_n^2 - R_{n-1}^2)|_{n=1, \dots, N}}{R_n^2 - R_{n-1}^2}, \quad \text{for } n = 1, \dots, N, \quad (\text{B.6})$$

which is the expression that was used in Section 3.

Some remarks are due with respect to the hereby discussed choice for a (normalized) discrete amplitude density function. Firstly, in view of the correspondence between ρ_n and R_n , it is obvious that R_N exceeds ρ_N . In many cases, the aperture will be construed as the area effectively covered by individual radiators, a choice that allows mapping the beamwidth requirement on a maximum element to center spacing. In that case, $\rho_N = R_{\text{ap}}$ and, thus, $R_N > R_{\text{ap}}$, as anticipated above. This fact does not conflict with the definition of the density function, the continuous $A(\rho)$ being amenable to extrapolation beyond R_{ap} , while the normalization in (B.6) recalibrates the maximum $\tilde{d}(\rho_n)$ to 1.

Secondly, the determination of the radii R_n according to the condition to yield equal surface integrals of $A(\rho)$ over the relevant annular rings can be easily carried out when the amplitude density is known, as demonstrated in Section 4. However, the handling of the converse situation, when the location of the elements is known and the (equivalent) amplitude density needs being calculated is less evident. To circumvent this difficulty, the radii R_n were chosen in Section 3 based on the intrinsic properties of the Fermat spiral, a choice that eventually allowed *verifying* that the amplitude density function $\tilde{d}(\rho_n)$ is, indeed, constant.

References

- [1] Y. Cailloce, G. Caille, I. Albert, and J. M. Lopez, "A Ka-band direct radiating array providing multiple beams for a satellite multimedia mission," in *Proceedings of the IEEE International Symposium on Phased Array Systems and Technology*, pp. 403–406, Dana Point, Calif, USA, May 2000.
- [2] G. Toso, C. Mangenot, and A. G. Roederer, "Sparse and thinned arrays for multiple beam satellite applications," in *Proceedings of the 2nd European Conference on Antennas and Propagation (EuCAP '07)*, pp. 1–4, Edinburgh, UK, November 2007.
- [3] M. C. Viganó, G. Toso, S. Selleri, C. Mangenot, P. Angeletti, and G. Pelosi, "GA optimized thinned hexagonal arrays for satellite applications," in *Proceedings of the IEEE Antennas and Propagation International Symposium*, pp. 3165–3168, Honolulu, Hawaii, USA, June 2007.
- [4] G. Caille, Y. Cailloce, C. Guiraud, D. Auroux, T. Touya, and M. Masmousdi, "Large multibeam array antennas with reduced number of active chains," in *Proceedings of the 2nd European Conference on Antennas and Propagation (EUCAP '07)*, pp. 1–9, Edinburgh, UK, November 2007.
- [5] H. Unz, "Linear Arrays with arbitrarily distributed elements," *IRE Transactions on Antennas and Propagation*, vol. 8, no. 2, pp. 222–223, 1960.
- [6] Y. T. Lo and S. W. Lee, "A study of space-tapered arrays," *IEEE Transactions on Antennas and Propagation*, vol. 14, no. 1, pp. 22–30, 1966.
- [7] R. E. Willey, "Space tapering of linear and planar arrays," *IEEE Transactions on Antennas and Propagation*, vol. 10, no. 4, pp. 369–377, 1962.
- [8] R. Harrington, "Sidelobe reduction by nonuniform element spacing," *IRE Transactions on Antennas and Propagation*, vol. 9, no. 2, pp. 187–192, 1961.
- [9] A. Ishimaru, "Theory of unequally-spaced arrays," *IRE Transactions on Antennas and Propagation*, vol. 10, no. 6, pp. 691–702, 1962.
- [10] H. Schjaer-Jacobsen and K. Madsen, "Synthesis of nonuniformly spaced arrays using a general nonlinear minimax optimisation method," *IEEE Transactions on Antennas and Propagation*, vol. 24, no. 4, pp. 501–506, 1976.
- [11] W. Doyle, "On approximating linear array factors," Tech. Rep. RM-3530-PR, RAND Corporation, Santa Monica, Calif, USA, February 1963.
- [12] T. A. Milligan, "Space-tapered circular (ring) array," *IEEE Antennas and Propagation Magazine*, vol. 46, no. 3, pp. 70–73, 2004.
- [13] M. Vicente-Lozano, F. Ares-Pena, and E. Moreno, "Pencil-beam pattern synthesis with a uniformly excited multi-ring planar antenna," *IEEE Antennas and Propagation Magazine*, vol. 42, no. 6, pp. 70–74, 2000.
- [14] R. L. Haupt, "Optimized element spacing for low sidelobe concentric ring arrays," *IEEE Transactions on Antennas and Propagation*, vol. 56, no. 1, pp. 266–268, 2008.
- [15] G. Toso, M. C. Viganó, and P. Angeletti, "Null-matching for the design of linear aperiodic arrays," in *Proceedings of the IEEE Antennas and Propagation International Symposium*, pp. 3149–3152, Honolulu, Hawaii, USA, June 2007.
- [16] Y. Chow, "On grating plateaux of nonuniformly spaced arrays," *IEEE Transactions on Antennas and Propagation*, vol. 13, no. 2, pp. 208–215, 1965.

- [17] M. I. Skolnik, "Nonuniform arrays," in *Antenna Theory, Part I*, F. J. Collin and R. E. Zucker, Eds., chapter 6, pp. 207–234, McGraw-Hill, New York, NY, USA, 1969.
- [18] J. Sahalos, "The orthogonal method of nonuniformly spaced arrays," *Proceedings of the IEEE*, vol. 62, no. 2, pp. 281–282, 1974.
- [19] R. L. Haupt, "Thinned arrays using genetic algorithms," *IEEE Transactions on Antennas and Propagation*, vol. 42, no. 7, pp. 993–999, 1994.
- [20] A. Trucco, "Synthesis of aperiodic planar arrays by a stochastic approach," in *Proceedings of the MTS/IEEE Conference (OCEANS '97)*, vol. 2, pp. 820–825, Halifax, Canada, October 1997.
- [21] S. Holm, A. Austeng, K. Iranpour, and J. F. Hopperstad, "Sparse sampling in array processing," in *Sampling Theory and Practice*, F. Marvasti, Ed., chapter 19, Springer, New York, NY, USA, 2001.
- [22] O. M. Bucci, M. D'Urso, T. Isernia, P. Angeletti, and G. Toso, "A new deterministic technique for the design of uniform amplitude sparse arrays," in *Proceedings of the 30th ESA Workshop on Antennas for Earth Observation, Science, Telecommunication and Navigation Space Missions*, Noordwijk, The Netherlands, May 2008.
- [23] D. W. Boeringer, "Phased array including a logarithmic spiral lattice of uniformly spaced radiating and receiving elements," US patent no. 6433754 B1, Silver Spring, Md, USA, April 2002.
- [24] T. Taylor, "Design of circular apertures for narrow beamwidth and low sidelobes," *IRE Transactions on Antennas and Propagation*, vol. 8, no. 1, pp. 17–22, 1960.
- [25] J. L. Volakis, *Antenna Engineering Handbook*, McGraw-Hill, New York, NY, USA, 4th edition, 2007.
- [26] A. Okabe, B. Boots, K. Sugihara, and S. N. Chiu, *Spatial Tessellations: Concepts and Applications of Voronoi Diagrams*, John Wiley & Sons, Chichester, UK, 2nd edition, 1999.
- [27] P. Atela, C. Golé, and S. Hotton, "A dynamical system for plant pattern formation: a rigorous analysis," *Journal of Nonlinear Science*, vol. 12, no. 6, pp. 641–676, 2002.
- [28] R. A. Dunlap, *The Golden Ratio and Fibonacci Numbers*, World Scientific, Singapore, 1997.

Review Article

Active SAR Antennas: Design, Development, and Current Programs

P. Capecce

Thales Alenia Space Italia, Via Saccomuro 24, 00131 Roma, Italy

Correspondence should be addressed to P. Capecce, pasquale.capecce@thalesalieniaspace.com

Received 17 October 2008; Revised 2 January 2009; Accepted 11 February 2009

Recommended by Giovanni Toso

The paper presents the design guidelines for Active SAR Antennas followed for the development of COSMO Sky Med SAR Antenna Subsystem. They have brought to define the antenna architecture, the RF, and electrical requirements for all the antenna RF, digital and power units, taking into account the available technologies and achievable performance. The antenna design is described for what the main subsystems is concerned, such as RF, power, digital, including mechanical and thermal aspects. Finally the paper reports also a brief description of the most recent development carried out in Canada and in Europe in the last ten years, including the on-going programs.

Copyright © 2009 P. Capecce. This is an open access article distributed under the Creative Commons Attribution License, which permits unrestricted use, distribution, and reproduction in any medium, provided the original work is properly cited.

1. SAR Antenna Requirements and Design

The SAR Antenna requirements include several RF, electrical, mechanical, and thermal parameters. The most important are the required beam shaping and steering capabilities, which implies the necessity to consider an active-phased array instead of alternative solutions such as multifeed reflector antennas, or passive-phased array, which do not have the required flexibility. Available technology for radiating linear array, Transmit/Receive (T/R) modules, and electronics strongly impacts other fundamental parameters such as the mass, the RF efficiency, the DC power efficiency, and the thermal dissipation. The consequence is that the antenna dimensioning will be the best compromise among all the mentioned aspects.

Main RF requirements to be considered are the following:

- (i) the beam size in azimuth and the minimum elevation beamwidth,
- (ii) the beam shaping capability,
- (iii) the azimuth and elevation steering angles,
- (iv) the central frequency and the bandwidth,
- (v) the EIRP,
- (vi) the noise figure,
- (vii) dual polarization.

As consequence the following aspects have to be fixed:

- (i) the technology of the radiating elements, that has some impacts also the mechanical and thermal designs of the whole system,
- (ii) RF subsystem, including passive and active units,
- (iii) digital subsystem,
- (iv) power subsystem,
- (v) mechanical design,
- (vi) thermal design.

Moreover it is necessary to divide the antenna in electronics subassemblies to allow the production chain to guarantee the needed rate and to perform all the required acceptance test in short time.

1.1. RF Technologies. Central frequency, bandwidth, ohmic losses, cross-polarization purity, but also mass and manufacturing cost, impacts on the selection of the technology used to realize the linear array. Typically two technologies have been used up to now for the RF radiator of SAR Antennas: slotted waveguides and linear array of patch elements. The first presents very good performance in terms of ohmic losses and cross-purity, but it is applicable only for bandwidth up to 2%, and have as major drawback a strong mutual coupling phenomena, which implies accurate modelling of

the antenna surface to control the antenna sidelobes and to avoid high active mismatch. The electromagnetic design becomes complex in case dual polarization is needed. In this case different waveguides design has to be considered for the vertical and horizontal polarizations and the two waveguides, needed to realize the dual polarization, have to fit in the elevation steering spacing which is typically in the order of $0.7/0.75$ wavelength. Finally the mass can be considered acceptable in case of carbon fiber waveguides are considered and for frequencies of 5/10 GHz or higher. Linear array of patches is simpler to be designed and manufactured, cheap and lightweight, presents larger bandwidths (up to 4/5% or more for accurate design). Cross-level can be improved by sequential rotation techniques, while the major drawback consists in higher ohmic losses due to the microstrips used for the RF Beamformers. Patch array can be used from lower frequency (P band) up to X band. At higher frequency only an accurate design and manufacturing can improve the cross-polarization purity and maximize the efficiency, while eliminating the glues from microstrips surface it is possible to reduce the ohmic losses of the whole assembly.

Concerning the EIRP and the noise figure, they strongly depend on the amplifiers performance. For such antennas distributed T/R modules are used to maximize the antenna aperture control to shape and steer the antenna beam. The TR module typically consists of a hybrid which includes a Tx channel and an Rx channel, each having few chips per channel. Multipack hybrids with 2/4 or 8 Tx and Rx channels have been also studied and produced in the past, but the experience demonstrated that these configurations, have a worst yield and cannot reduce the antenna cost.

Packaging and substrates are an important issue for mass production; thick film and thin film technologies over alumina/multilayer ceramics have been largely used in the past. A single LTCC substrate is today the baseline for TR module packaging, reducing the number of steps and the cost in production. Another important aspect is the electrical connections to the external circuits and the RF I/Fs. RF Blind mate connectors and solder-less contacts are adopted to allow a simple mounting/dismounting of the module also during the assembly and testing phases.

The Tx section of the module is typically based on a cascade of two chips in GaAs technology: the RF driver and the HPA. Chips based on HBT and P-HEMPT technologies are the most used for the final power chip. The available output power depends on the frequency and the chip dimension. It can be used as single chip or in tandem configuration to reach the wanted power. Typical Pout of an HPA depends on the central frequency: 10/12 W are today available for C band, which reduces to 8/10 W for the X band. Concerning the receive path, the noise figure is affected by the limiter needed to protect the LNA from unwanted reflected high power caused by open/short circuits. Achievable Figures are in the range of 3/3.5 dB for the mentioned frequencies.

The amplitude and phase control can be obtained by used separated attenuator/phase shifter chips or a multifunctional chip (core chip), which includes both the controls plus amplification and switching capabilities. These controls are used both to select the amplitude and phase of the module,

in Tx and in Rx mode, but also to compensate the amplitude and phase changes caused by the temperature variation on the whole RF chain in the applicable thermal range. In fact in space, for large active antennas, it is very difficult to stabilize the operative temperature, especially when high dissipation is generated internally by the antenna electronics. As consequence it is necessary to compensate the gain and phase variation with temperature of the TR modules by an external digital controller which receive the wanted setting from a central beam controller and, on the basis of the temperature of the module, sets the amplitude and phase steps to stabilize the overall amplitude gain and phase.

1.2. Electronic Front End. In order to allow the TR modules to work correctly, two additional conditioning circuits are needed:

- (1) a digital I/F able to receive/transmit the data from the Tile controller and to implement electronic protection of the hybrids; this is achieved by a dedicated ASIC, which reduces the circuit complexity;
- (2) a power section, which includes the capacitor bank to work in pulsed way, and the high-current switches, to switch on/off the RF Tx and Rx chains.

These circuits can be placed inside each the TR module, or can be mounted on dedicated PCB externally to drive a group (4 or 8) TR modules. The whole assembly is named (Electronic Front End) EFE and includes also the RF combiners/dividers for the TR modules. The EFE hybrids directly interface the antenna radiators and the RF dividers through the blind mate connectors placed on the bottom of the module, while digital controller and power supply are interfaced on the other two narrow sides of the hybrid module.

1.3. True Time Delay Lines and Array Bandwidth. Also if all the SAR antennas are typically based on RF distribution networks equally phased in the whole frequency band by equal RF paths from the antenna input port to the TR modules, the frequency bandwidth of a large-phased array is limited by the beam pointing variation when $0-360^\circ$ degrees phase shifters are used to generate the aperture phase slope to steer the beam. As reported in [1], the beam pointing changes with the frequency for a given phase setting to the TR modules phase shifters: the pointing angle at frequency f is given by the simple formula

$$\sin(\theta) = \left(\frac{f_0}{f}\right) * \sin(\theta_0), \quad (1)$$

being: θ the pointing at the frequency f ; f_0 the central frequency; θ_0 the pointing at f_0 .

In Figure 1 the beam pointing versus frequency variation at different steering angles is reported for a generic-phased array. For SAR Antennas with a typical bandwidth of 2% and 15° of steering angle along the elevation plane, the pointing variation expected will be in the order of 0.3° . This value has to be compared with the antenna beamwidth along

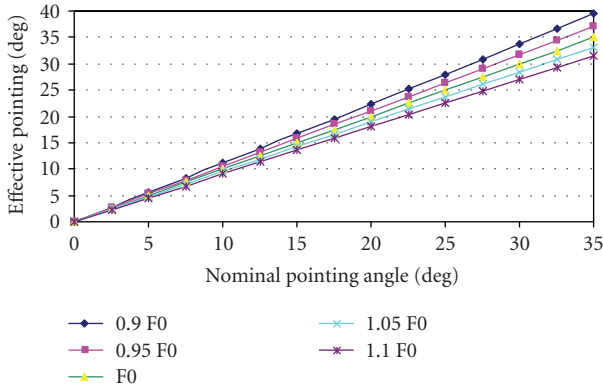


FIGURE 1: Beam pointing versus frequency in degrees.

that plane. The pointing variation is due to the fact that a constant phase distribution is applied by the phase shifters in the whole bandwidth, while the nominal phase distribution should change with the frequency to maintain the same beam pointing.

If the pointing variation is small with respect to the beamwidth, in the order of 5–10%, it can be tolerated, while if the beam pointing variation corresponds to an important fraction of the beamwidth, it is necessary to introduce True Time Delay Lines (TTDL) in the beam forming network, each acting over a part of the antenna surface. The TTDL realizes a variable delay, typically in terms of multiple of wavelength, according to the steering angle and the position of the subarrays, implementing a phase slope versus frequency which allow to correct the phase distribution over the antenna surface in the frequency band. Also in case true time delay lines are used, the residual beam pointing variation with the frequency is an inverse function of the size of the subarray fed by a single true time delay line and of the minimum step of the TTDL. Fast switching is necessary in case fast beam change or steering is required. As switches, ferrite circulators can be used with waveguide technology, or more integrated solution based on MMICs switches and microstrip lines can be also adopted, but they require additional amplification.

1.4. Digital Subsystem. The objective of the digital subsystem is to control the setting of the TR modules in order to allow the antenna to generate the wanted beam. It consists of a central beam controller which knows all the wanted settings for each TR module inside the antenna for each desired beam, and a number of distributed controllers which directly act on a group of TR modules (typically from 16 to 32) to set the modules, implementing also the thermal compensation.

The central antenna controller communicates to the distributed secondary controllers all the wanted setting; the secondary controllers send to the TR modules the setting data suitable corrected to take into account the TR module temperature. It is important to note that the compensation loop acts almost in real time in order to minimize the RF drift of the device in the thermal range. Typically the control loop for temperature compensation is performed in

fractions of a second, and it is based on a look-up table which contains the compensation data for each TR module. In case of TTDLs are present in the antenna BFN, they also need to be compensated versus temperature, and this is achieved still acting on the TR module level setting (the TR modules amplitude and phase are used to compensate also the TTDL variation versus temperature).

The digital controller is internally or externally redounded, considering that all the TR modules driven by the controller will be lost in case of the controller failure.

1.5. Power Subsystem. The power subsystem is based on a suitable dimensioning of the satellite power system, such as the battery and the solar arrays, a dedicated unit which main function is to switch on/off and filtering the several distributed power supplies of the antenna panels and, finally, by the capacitor banks placed on the EFE cards. The continuous switch on/off of the TR modules with the pulse repetition frequency generates a ripple on the power bus that can disturb other units. As consequence the control loop of the power supply has to be adjusted in order to avoid to much strong current ripple on the primary bus, but also to limit as possible the voltage variations on the TR modules that can affect the HPA performance. Filtering circuit is close to the switching section in order to reduce the emission towards the battery. The number of power supplies on the antenna depends on the number of TR modules to be fed, their power consumption, the duty cycle, the reliability performance, and the total number of TR modules in the antenna. In case of a large antenna is considered, the number of power supplies can reach several tens. If the reliability Figure of the single power supply is able to guarantee that only one or two units over the whole number could be lost in the operative life, it is possible to avoid the redundancy of the power supplies, saving at the same time cost and mass.

1.6. Mechanical Design. The SAR antenna has a large aperture of several square meters and typically is divided into mechanical panels that are in stowed condition at the launch and then deployed when the satellite has reached the final orbit. This implies the presence of hold down and release mechanisms, able to take in stowed configuration the antenna during the launch and to support the mechanical loads in this phase, and deployment mechanisms to open the antenna when it is in flight. Concerning the panels, two configurations are possible: (1) the electronics are integrated in subassemblies (the Tiles), which are mounted on a panel supporting frame; (2) all the electronic is integrated in large and closed panel structures.

An alternative configuration is based on Tiles directly mounted on a sidewall of the satellite: this implies a spacecraft having a length close to the antenna dimension, that can occur only for antenna not longer than 4/5 m.

Antennas having a length of 5/7 m, can be organized in two or three mechanical panels, with the two external ones are deployable.

In case of longer antennas of a dimension of 10/12 m, the number of mechanical panels increases up to 4 or 5. In



FIGURE 2: COSMO sky med active SAR antenna (stowed & deployed).

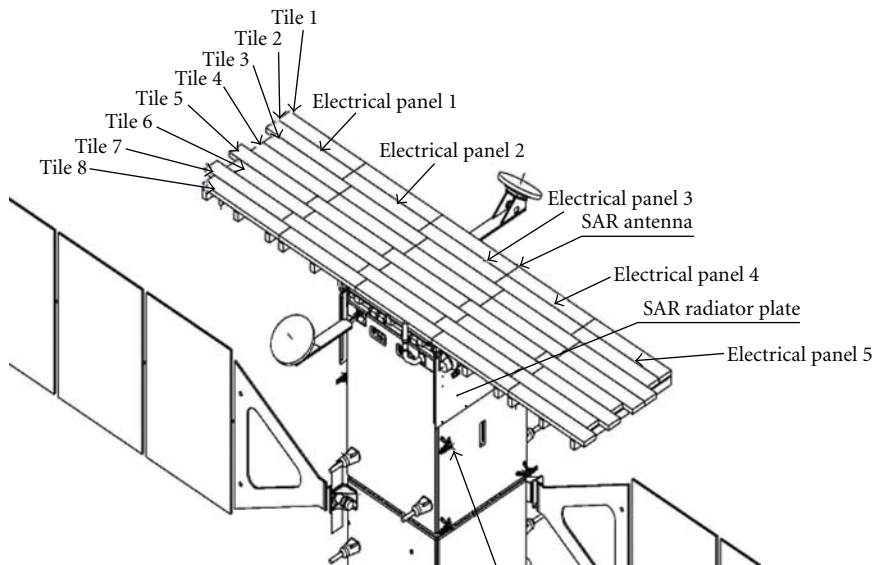


FIGURE 3: Antenna organization in tiles.

this case couples of panels can be grouped to realize lateral wings, each having a double deployment. The hold down and release mechanisms are typically based on pyrocutter devices, while the deployment mechanisms can be driven by motors or springs. In case of motors are used, driver electronic unit is also necessary to control the deployment, while spring-based mechanisms are mechanically controlled by dumpers and do not need control electronics.

One of the most critical aspects for mechanical design is to guarantee the antenna planarity and therefore reduced thermal distortion during the antenna functioning, to guarantee patterns stable performance. The amount of acceptable distortion of the antenna plane is inverse to the RF frequency of the antenna; typically 1.5/2 mm is still acceptable for X band, while 3/4 mm can be tolerated in C band.

The use of very low (Coefficient of Thermal Expansion) CTE material for Tiles and supporting frames, such as carbon fiber reinforced plastic (CFRP), having a CTE in the order of 1-2 parts per million (ppm) per °K, improves the dimensional stability at the expense of poorer thermal conductivity due to low thermal conductivity of the resins.

Aluminium, with good thermal conductivity, is also largely used for these antennas, improving, with respect to the CFRP, the heat transfer from the TR modules to the main frames and towards to the thermal radiators areas. Nevertheless higher CTE (24-25 ppm per °K) implies that, in case of different temperature between the upper surface and bottom side of the antennas, the aperture surface can be warped along the azimuth plane (thermal distortion). This problem can be solved by accurate thermal design of the heat vias from the hot to the cold areas of the antenna. Heat pipes can be also used to minimize all the thermal gradients and the thermal distortion.

1.7. Thermal Design. The thermal design is of particular importance because it has to guarantee the limited thermal excursion as applicable to electronic devices inside the antenna, considering the required continuous functionality.

The thermal configuration study will optimize the working thermal range of the antenna and the heater power system demand, considering the functional requirements such as and the number of images per orbit, duration of

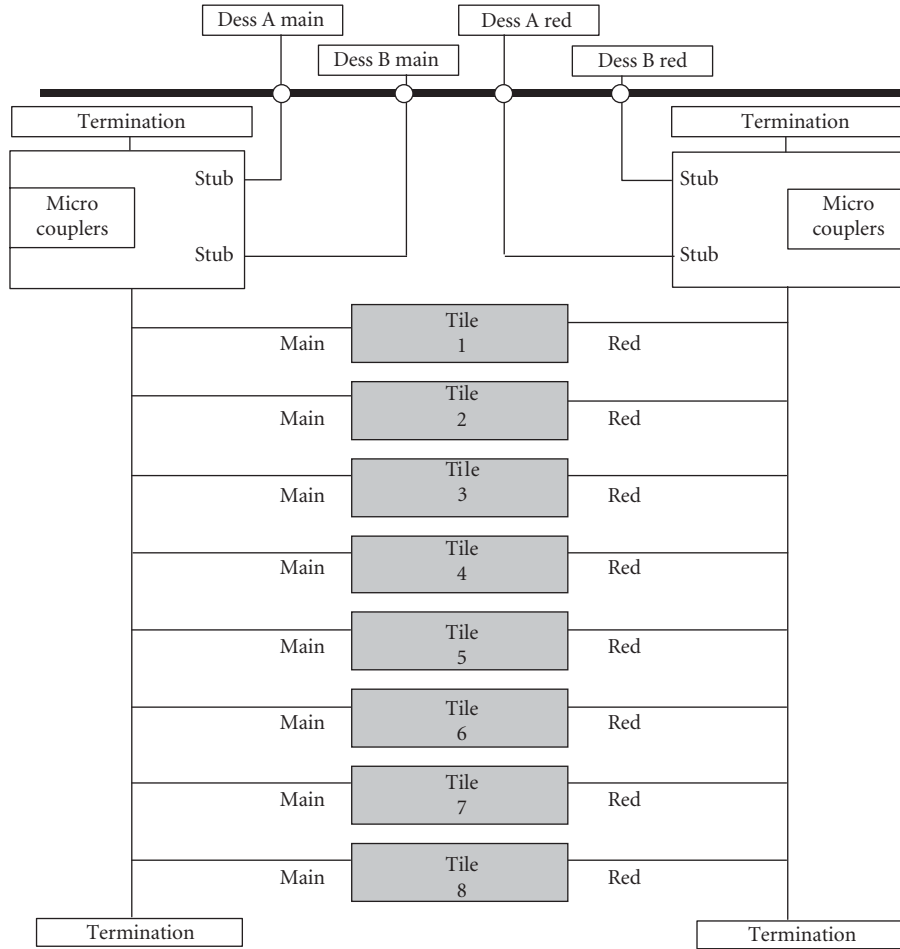


FIGURE 4: 1553 digital busses for each column of 8 tiles.

the continuous acquisition in image modes, and single or dual looking operations which can determine a rapid grow up of the temperature. The fast temperature increment is controlled mainly from the thermal capacity of the antenna, in particular by the parts which are in good thermal contact with the hot spots of the electronics (the TR modules and power supplies). Then the accumulated heat can be dissipated by the front and/or back side during the rest of the orbit.

An important aspect of the thermal design is the capability of the antenna to work in front to sun or back to sun condition. In the first case the heat dissipation can occur mainly through the back side of the antenna, while the heat from the sun can be limited by using RF transparent sunshield. The major drawback for this configuration is that the satellite body blocks the dissipation of the central panels or parts of the lateral panels, as consequence heat pipes and dedicated thermal radiators have to be used to remove the heat.

When exposed to the sun with the back side, the antenna can radiate through the radiating linear arrays, if their thermal conductivity and surface is adequate. The best case occurs when the antenna is able to work in both the two cases, improving the revisit time of the mission.

2. In Flight Active Phased Array SAR Antennas

The above design considerations are fully applicable to the SAR antennas developed in the last years for Earth Observation missions.

Hereafter the description of the antenna designed, manufactured, and tested by Thales Alenia Space Italy for the COSMO Sky Med mission is reported. Moreover, other similar antennas developed in Europe and Canada, in the last ten years, are also briefly described and discussed.

2.1. COSMO Sky Med Antenna. COSMO-SkyMed (Constellation of Small Satellites for Mediterranean basin Observation) is a 4-satellite constellation funded by (Agenzia Spaziale Italiana) ASI and Italian Ministry of Defence [2]. It is a “dual-use” mission being the overall objective of this program the global Earth observation and the relevant data exploitation for the needs of both the military and the civil (institutional and commercial) communities [3]. The first three satellites have been launched on June, December 2007 and October 2008, respectively. Each of the four satellites is equipped with an SAR operating in X-band with multimode (spotlight, stripmap, and scansar) and multipolarisation capability.

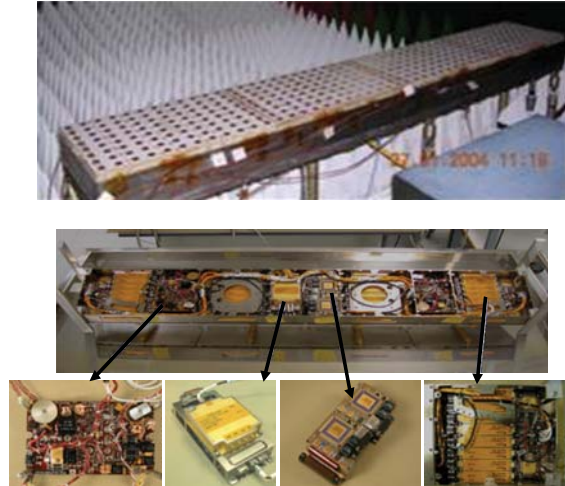
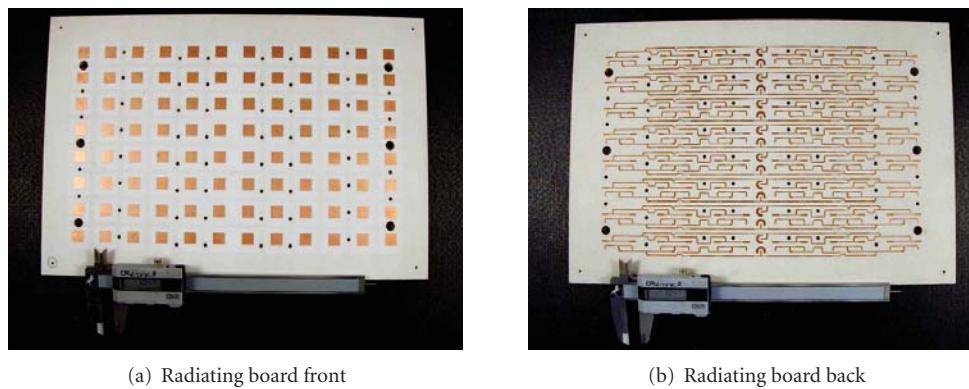


FIGURE 5: Tile external & internal view: TPSU, TTDL, digital controller and EFE with 8 TR modules are shown (from left to right).



(a) Radiating board front

(b) Radiating board back

FIGURE 6: Radiating board: patches side and BFNs side.

The dual-use objective requires for an high operational flexibility (multimode, access area, left and right looking) which is one of the major mission requirements driving the selection of a system based on a phased array, in particular having good steering capabilities on both the elevation and the azimuth planes. In addition to the operational flexibility, the demand on image quality in terms of spatial resolution, swath extension, and ambiguity suppression led to some of the system solutions (instantaneous bandwidth, beam shaping capability in the elevation plane, and beam setting separately in Tx and Rx on a pulse repetition frequency basis) which constrained the selected architecture and drove the selection of an active phased array for the antenna subsystem. The protoflight antenna mounted on the satellite in stowed and deployed condition is shown in Figure 2.

The antenna consists of an active phased array organized into five electrical panels, each consisting of a column of 8 Tiles, grouped in three mechanical panels. The electrical panels are grouped into three mechanical panels, two deployable lateral panels with two columns of 8 tiles each, and a fixed central panel, with a single column of tiles,

mounted on the S/C top floor. In Figure 3 the antenna organization in panels and tiles is shown.

The tile is the fundamental brick of the antenna [4] and includes linear arrays, TR modules and it is characterized by the presence of the TTDL.

The TTDL is required to stabilize the beam pointing when the beam is steered in azimuth and in elevation. The Tiles are mounted on an aluminum panel frame, which supports also the hold down and release mechanisms (4 for each panel), the deployment mechanisms, the antenna harness, and two beam forming networks (one for the RF Tx/Rx distribution and one for calibration purposes).

The digital control of the antenna is achieved by five rerouted 1553 digital busses, one for each column of 8 Tiles. The digital distribution of one column of 8 tiles is shown in Figure 4, where the links to the Digital Electronic Sub-System (DESS) main and redundant are indicated. Two 1553 microcouplers are used to allow both the DESS to communicate with the main and redundant Slave Beam Controller sections placed inside each Tile.

Concerning the Tile, two main objectives have been reached during its design and development:

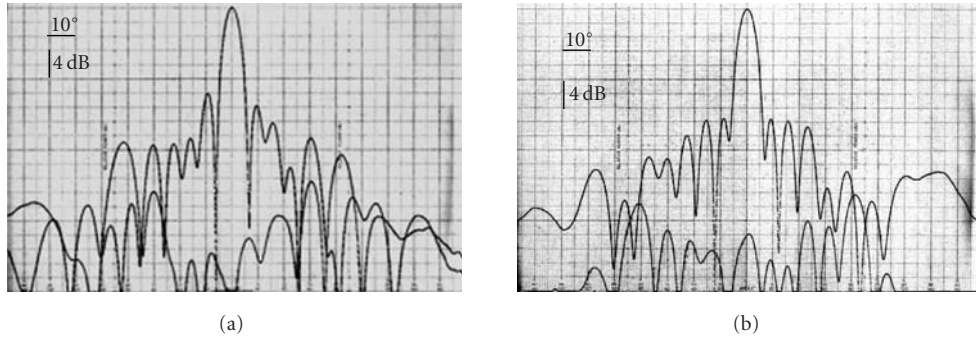


FIGURE 7: Radiating board measured pattern azimuth plane at 9.6 GHz, H & V pol. ($\pm 90^\circ$ x axis; 40 dB y axis).

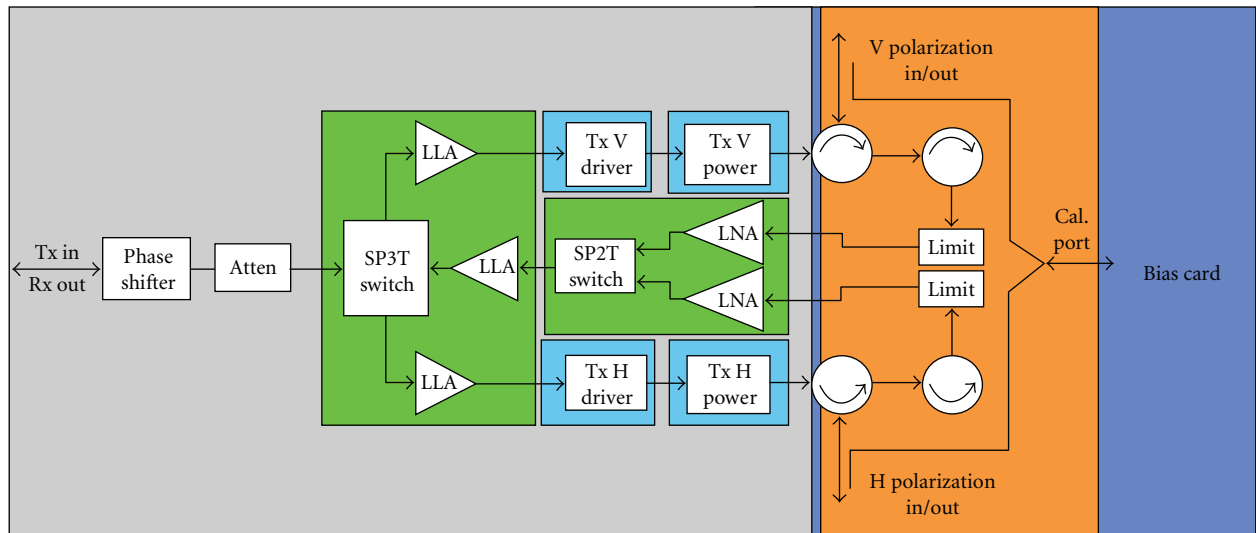


FIGURE 8: T/R module and RF layout.

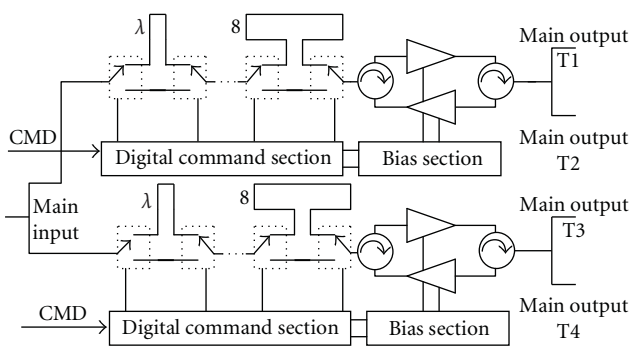


FIGURE 9: True delay line block diagram.

- (i) to design and develop a compact, modular self standing unit;
- (ii) to simplify the production line for the antenna.

The first objective has been achieved by including all the electrical and electronic functions inside the unit. This means that the antenna is made of tiles and other passive parts such as harness, BFN, and structure, but no electronics are outside

the tile. This allows also to have a modular approach for the antenna: different antennas in size and performance can be achieved just changing the number of tiles, the harness, the beam forming networks and structural parts, but without any modification to the electronics of the tile. The digital controller of each tile compensates in temperature all the RF chains, including TR modules, and RF cables. The TTDL is set according to the beam steering and the tile position in the antenna to stabilize the beam in the frequency band.

Concerning the mechanical design of the tile, a particular effort was spent in the mass reduction of each electrical part, achieving the goal to have a mass less than 10 kg.

The Tile is internally divided into seven separated rooms, four for the T/R modules, two for the power supply units, and one for the digital controller and the TTDL, each closed with a proper cover. The external and internal view of a tile are shown in Figure 5.

The main RF functions of the tile are implemented by the radiating linear arrays, grouped into four radiating boards, able to work in double linear polarisation, by the T/R modules, organized in blocks of eight on four EFEs cards, which amplify both the transmitted and received signals and are also able to control amplitude and phase for

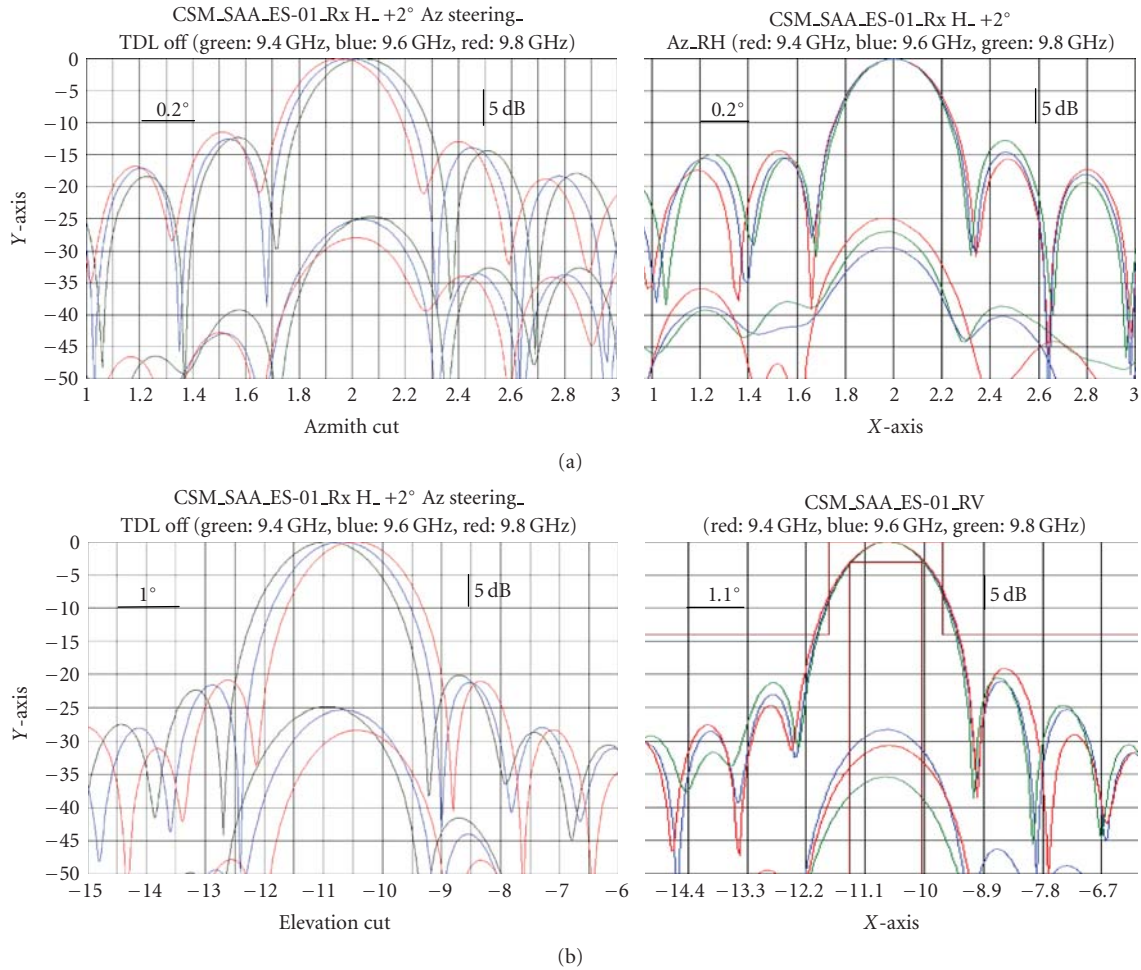


FIGURE 10: Example of the beam stabilization in the frequency band by using the TTDL (central and extremes frequencies are shown). (a) Azimuth plane (+2° of steering); (b) Elevation plane (-10.7° of steering).



(a)



(b)

FIGURE 11: TR module production lines: two in parallel lines were developed to meet the required production rate up to 300 TR modules/month.

beam steering and shaping, and finally by the TTDL which amplifies the RF signals (transmitted and received) and it is able to apply up to 15 wavelength of delay (4 bits device) for beam stabilisation in frequency under steering condition.

Concerning the digital functions used to drive the Tile, it is realized by the Slave Beam Controller (SBC). This

unit receives commands and beams data from the central digital unit of the Radar by 1553 serial digital bus, and sends to the T/R modules and the TTDL the wanted settings through two parallel serial busses. A look-up table (LUT) is used to compensate their variation in the temperature range.



FIGURE 12: Tile production line is shown with 2 ATE (automatic test equipment) working in parallel on two tiles to perform test in temperature of all the 128 RF chains.

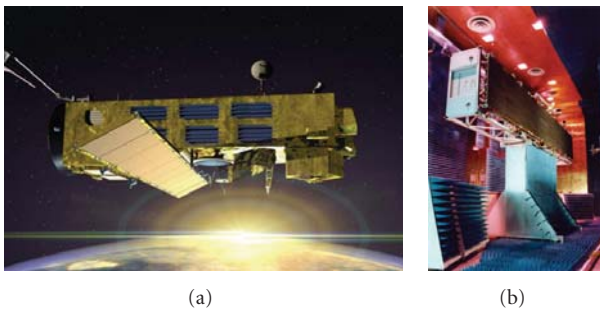


FIGURE 13: Pictorial view of the ASAR antenna on ENVISAT and in near field.

The power sub-system of the Tile is based on two Tile Power Supply Units, named TPSU, able to feed both the T/R modules, the EFEs cards and the TTDL. The two TPSU's of the Tile are able to supply up to 260 W to the EFEs, T/R modules and, TTDL, with an efficiency better than 80% for all the possible thermal conditions and bus voltage.

The mechanical design of the Tile is based on an aluminium box which includes all the electronics and supports the radiating boards. Concerning the thermal design, it has to be pointed out that the antenna functioning will be not continuous but with a limited duration (typically from few to ten minutes per orbit). The thermal design is therefore based on the necessity to control the temperature during this periods considering the dynamic evolution of the temperature. In this case the thermal capacity of the Tile has an important effect on the slope of the temperature increasing. Sunshield is used to improve the thermal isolation towards the sun in right looking orientation (front to sun). The thermal dissipation is achieved through 7 separated covers mounted on the back side of the Tile. (second surface mirrors) SSMs and/or silver Teflon tape are used to improve the thermal dissipation to the deep space. The SSMs improve also the thermal control in the back to sun antenna orientation. The T/R modules are mounted by screws to the box, while the thermal exchange with the Tile is improved by thermal filler placed on the hot area of the modules. Hereafter some design and technological aspects of the RF units inside the tile are discussed.

Linear Arrays. The RF radiator consists of a dual-polarized linear array of 12 stacked patches, electromagnetically coupled through slots to the distribution networks. Two distribution networks are used, one for each linear polarization, to feed the 12 stacked patches. Blind mate connectors allow a simple assembly with the active modules. Eight radiating arrays are manufactured together and assembled into a single radiating board. The radiating board is shown in Figure 6, while measured patterns in H & V polarizations are reported in Figure 7.

The ohmic losses have been minimized by supporting the microstrip dividers with dielectric spacers, avoiding glues over the microstrips. The complete assembly results into a lightweight compact radiating board that can be assembled at tile level by six screws. Bandwidth and mass performance fully meet the given specification of 260 grams per board.

EFE & T/R Module. The EFE is a printed circuit board (PCB) which is housed in a dedicated room inside the mechanical structure of the Tile. The EFE PCB has two main functions:

- (i) digital and power supply distribution,
- (ii) RF distribution.

The first is developed on an eight-layer polyimide PCB, supporting the digital and power supply sections and the T/R Modules, while the second is achieved by two layers PCB in PTFE, mechanically fixed (screwed) to the first one.

The T/R module design is based on use of MMICs and includes two Tx channels and two Rx channels to reduce the ohmic losses and to improve the output power and the noise figure. The RF circuit and block diagram of the T/R module is shown in Figure 8.

The T/R module is designed in compliance with requirements needed for space applications.

TTDL. The TTDL is a four-bit device able to reach up to 15 wavelengths of slope compensation. It is based on MMICs switches and microstrip lines. The unit has also the function to amplify both the Tx and the Rx signals. The TTDL includes RF dividers to feed the 4 EFEs, each interfacing with 8 T/R modules. The True Delay Line block diagram is shown in Figure 9. The Unit provides amplification and phase control on the RF signals between the common I/O port and four I/O ports. In addition, a separate 1:4 divider/combiner is included for the calibration path. The main functions of the unit are

- (i) amplify RF signal for recovering the lines losses;
- (ii) select the insertion delay between 0 and 15λ (4 bits);
- (iii) receive and decode the digital command data
- (iv) bias the amplifiers during the operative part of the period.

The TTDL has to be intended as two separated units which have a common mechanical housing but operating independently, with above mentioned functions and the supply voltages separated.

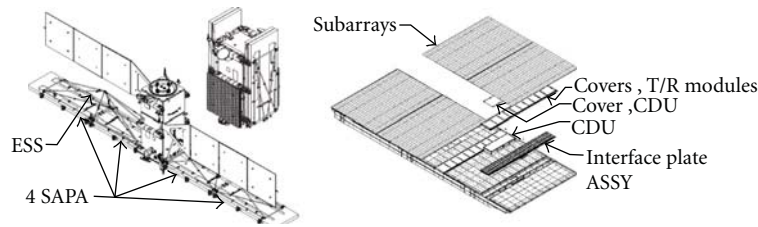


FIGURE 14: Radarsat 2 antenna, panel and ESS, from [6].

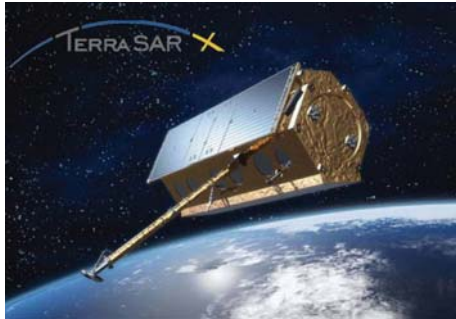


FIGURE 15: TerrasarX (Astrium Ge) [7].

In Figure 10 the stabilization effects of the TTDL over the antenna beam pointing for both the azimuth and elevation main planes, for 2° of azimuth steering and 10.7° of elevation steering are shown (4% of bandwidth).

Production Lines. In order to manufacture and test the 4 antennas for COSMO Sky Med, a dedicated production line for Tiles have been developed. It consists in two main sections:

- (i) the TR module production line,
- (ii) the Tile production line.

The TR module production is based on two parallel lines each equipped with an automatic pick and place machine and a wire bonding system, as shown in Figure 11.

After to be assembled, the TR module is submitted to an acceptance test campaign which also include an automatic test system.

Concerning the Tiles, also in this case two parallel lines have been developed. The most demanding test is the in temperature characterization/compensation test. Each line is therefore equipped with a thermal chamber and two measurement systems to test in parallel two tiles, as shown in Figure 12.

2.2. Other in Flight SAR Antennas. In the last 10 years other three missions with SAR payload having an active Antenna have been developed and launched for institutional and commercial applications.

- (1) ASAR on Envisat Satellite, developed in Europe, under (European Space Agency) ESA contract; the Envisat satellite was launched on 2002;

- (2) Radarsat 2, developed by MDA, under (Canadian Space Agency) CSA contract; launched at the end of 2007.
- (3) Terrasar X, developed in Germany, funded by the German Aerospace Center (DLR), launched on june 2007;

Apart Envisat, all the other satellites were launched in 2007, demonstrating the increasing of interest and funding by the national space agencies.

All the above SAR Antennas have the typical architecture of the active phased array based on the use of large aperture filled by a number of linear arrays, arranged in columns and rows, each supplied by a Transmit/Receive module. These antennas adopt separate amplitude and phase distribution laws for azimuth plane (typically uniform) and for the elevation plane, where about hundred beams can be generated with different size and steering angles by suitable weighting the amplitude (in Rx mode only) and the phase (in Tx and Rx). The three missions use the C band (ASAR, Radarsat 2) or the X band (TerrasarX) with bandwidths that ranges from 1% to 3%. Hereafter a summary of their characteristics is reported as available from the literature [5–7].

The ASAR Antenna, shown in Figure 13, has an aperture of $10\text{ m} \times 1.3\text{ m}$ divided in 10 columns of 32 linear array, [5]. The antenna is organized in five panels with 4 Tiles each, and the 320 TR modules are grouped into 20 Tiles. The panels are in stacked configuration at the launch and deployed by the DEM which includes 4 hinge lines and the relevant step motors. The panels supporting frame is realized in CFRP. It supports the 4 tiles, the RF radiators, the RF distribution network, based on CFRP waveguides, the harness the hold down & release mechanisms, and the deployment mechanism.

The Tile includes 16 linear arrays mounted on an supporting plate, with the TR modules and the relevant service electronics such as 4 power supplies and the tile controller.

The Radarsat 2 Antenna is 15 m length and 1.4 m large [6]. It is organized in two wings of two mechanical panels each, as shown in Figure 14. The panel includes 4 columns of 32 linear arrays. The mechanical panels consists on a aluminum box in which all the RF, power and digital distribution, four columns of TR modules, the relevant service electronics to supply and control the modules, are included. The deployment of the wings is performed by dedicated HRMs and (Extendible Supporting Structure) ESS.

The Terrasar X satellite, shown in Figure 15, has an Antenna with 384 linear arrays organized in 12 columns of 32 radiators, as described in [7]. Each column of TR modules corresponds to a tile, inside which two power supplies, two digital controllers, harness, and RF distribution are mounted. The dual-polarized linear arrays in waveguide technology realize also the mechanical supporting frame for the tile electronics. The Tiles are directly mounted to a side wall of the satellite.

3. New Programs

At the moment new programs are under ways in Europe and in Canada. Concerning the ESA, it is involved in a new program named Sentinel 1. Thales Alenia Space Italy is the Prime contractor and will furnish the satellite and the EFEs with the TR modules in C band for the active antenna which is under responsibility of Astrium Ge, while the Radar electronics is under development in Astrium UK.

In Germany a new mission, named TandemX is under way, which consists in one satellite which will work together with TerrasarX to realize an interferometric mission.

In Italy the manufacturing of the last satellite of Cosmo constellation is on-going, together with the radar payload for (Korean Aerospace Research Institute) KARI, which include an active antenna in X band.

In Canada the Radarsat Constellation Mission is a follow-on project to Radarsat 2, currently developed by MDA. The constellation will consist of a fleet of three spacecrafts. The primary purpose of the RCM is to provide C-Band data continuity for RADARSAT-2 users, as well as adding a new series of applications enabled through the constellation approach, such as interferometric mission, improving also the revisit time.

4. Conclusions

The paper has summarized the design guidelines followed in Europe and Canada for the development of large active phased array for SAR application. Cosmo Sky Med design and implementation has been also presented. All these antennas have similar radiators arrangement on rectangular grid, except for Cosmo Sky Med which is a dual-use mission and therefore implement a different radiator arrangement to improve also the azimuth steering performance. From mechanical point of view different approaches are mainly due to the extensive use of carbon fiber composite material for linear arrays and supporting structure from one side, in opposition to aluminium-based configurations developed on the same frequencies and for similar antenna dimensions. While the advantages for thermal aspects are clear for the aluminium case, the CFRP-based solution can guarantee a major aperture stability, at the expense of lower thermal conductivity. Comparison among these antennas have shown also a similar approach based on tile arrangement, the larger difference is for Cosmo Sky Med which utilizes also TTDL for beam stabilization in steering and tiles staggering to improve the grating lobes control.

The main development ongoing are directed to improve the revisit time of the satellite on observed area of interest, moving towards to the constellation systems as minimum to perform radar interferometry and to improve the revisit time for commercial images application.

Acknowledgments

The Author wishes to thank the Italian Space Agency (ASI) and the Minister Of Defence for the support given by during the whole development of COSMO Sky Med program, and the whole Thales Alenia Space Team placed in Rome, L'Aquila, Milan, and Turin for the large efforts demonstrated during the design, development and production of COSMO SAR Antennas.

References

- [1] R. C. Hansen, *Phased Array Antennas*, John Wiley & Sons, New York, NY, USA, 1998.
- [2] F. Caltagirone, G. Angino, A. Coletta, F. Impagnatiello, and A. Gallon, "COSMO-SkyMed program: status and perspectives," in *Proceedings of the 3rd International Workshop on Satellite Constellations and Formation Flying*, Pisa, Italy, February 2003.
- [3] F. Caltagirone, P. Spera, G. Manoni, and L. Bianchi, "COSMO-SkyMed: a dual use earth observation constellation," in *Proceedings of the 2nd International Workshop on Satellite Constellations and Formation Flying*, Haifa, Israel, February 2001.
- [4] P. Capece, L. Borgarelli, M. Di Lazzaro, U. Di Marcantonio, and A. Torre, "COSMO SkyMed active phased array SAR instrument," in *Proceedings of IEEE International Radar Conference (RADAR '08)*, pp. 1–4, Rome, Italy, May 2008.
- [5] R. Torres, "ASAR instrument stability," in *Proceedings of the CEOS Working Group on Calibration/Validation-SAR Workshop*, pp. 42–48, London, UK, September 2002.
- [6] S. Riendeau and C. Grenier, "RADARSAT-2 antenna," in *Proceedings of the IEEE Aerospace Conference*, pp. 1–9, Big Sky, Mont, USA, March 2007.
- [7] S. Buckreuss, R. Werninghaus, and W. Pitz, "The German satellite mission TerraSAR-X," in *Proceedings of IEEE International Radar Conference (RADAR '08)*, pp. 1–5, Rome, Italy, May 2008.

Application Article

Performance Comparison of Reflector- and Planar-Antenna Based Digital Beam-Forming SAR

Marwan Younis, Sigurd Huber, Anton Patyuchenko, Federica Bordoni, and Gerhard Krieger

Microwaves and Radar Institute, German Aerospace Center (DLR), 82230 Wessling, Germany

Correspondence should be addressed to Marwan Younis, marwan.younis@dlr.de

Received 15 October 2008; Revised 23 January 2009; Accepted 17 March 2009

Recommended by Giovanni Toso

The trend in the conception of future spaceborne radar remote sensing is clearly toward the use of digital beamforming techniques. These systems will comprise multiple digital channels, where the analog-to-digital converter is moved closer to the antenna. This dispenses the need for analog beam steering and by this the used of transmit/receive modules for phase and amplitude control. Digital beam-forming will enable Synthetic Aperture Radar (SAR) which overcomes the coverage and resolution limitations applicable to state-of-the-art systems. On the other hand, new antenna architectures, such as reflectors, already implemented in communication satellites, are being considered for SAR applications. An open question is the benefit of combining digital beam-forming techniques with reflector antennas. The paper answers this question by comparing the system architecture and digital beam-forming requirements of a planar and a reflector antenna SAR. Further elaboration yields the resulting SAR performance of both systems. This paper considers multiple novel aspects of digital beam-forming SAR system design, which jointly flow into the presented system performance.

Copyright © 2009 Marwan Younis et al. This is an open access article distributed under the Creative Commons Attribution License, which permits unrestricted use, distribution, and reproduction in any medium, provided the original work is properly cited.

1. Introduction

Synthetic aperture radar (SAR), utilizing digital beam-forming, is increasingly being considered for future missions. This is evident both from research activities [1, 2] and space qualified technology demonstrations [3]. One of the reasons for this trend is that state-of-the-art SAR systems cannot fulfill the heterogeneous demand on products at the required performance level. The motivation for using Digital Beam-Forming (DBF) techniques is their ability to provide a simultaneous wide swath (coverage) and high resolution. In this paper, systems utilizing the various forms of DBF, such as SCan-On-REceive (SCORE), multiple azimuth receive channels, and transmit phase center variations are jointly referred to as SMART, which stands for Smart Multi-aperture Radar Techniques. In the most general sense SMART sensors allow a relaxation of the system design parameters, by increasing the degrees of freedom. Specifically, for a given geometric resolution this results in systems with higher Signal-to-Noise Ratio (SNR) and lower ambiguity-to-signal ratio, both being key

requirements on SAR systems. Equipped with digital receive channels, SMART sensors do not require phase and amplitude control of the received signals (analog beam-forming); this yields an RF hardware free of transmit/receive modules and complex control and calibration units. Instead, SMART will push the development of onboard digital signal processing capable of handling multiple channels of high data rate.

This paper discusses the use of SMART in conjunction with two different antenna concepts. On one side a planar array, consisting of a single small transmit antenna and a receive antenna array with multiple subapertures in elevation is considered. The array is equipped with digital receive channels and onboard DBF is performed on the data. On the other side we consider a reflector antenna with a feed consisting of multiple transmit/receive elements in elevation. Here beam-forming is performed both on transmit and on receive by selecting the active elements of the array.

The paper analyzes and compares the system concepts in terms of realization complexity, space suitability, hardware issues, digital processing requirements and, last but not least,

the resulting SAR performance. The focus of the paper is on different antenna issues, rather than the SMART SAR operational modes which are detailed for example in [1].

The paper starts by introducing digital beam-forming in elevation and azimuth in Section 2. Next the system architecture and signal processing approach for each of the planar and reflector system are described in Section 3. The parameters used to characterize the SAR performance are defined in Section 4, which includes several new performance criteria necessary for DBF systems. Then, in Section 5, the performance requirements are stated and the design parameters common to both systems are given. This is followed by the specific design and SAR performance analysis of each system in Sections 6 and 7. Finally Section 8 summarizes the paper and gives an outlook to future prospects.

2. System Operation

2.1. Digital Beam-Forming in Elevation. In 1981 Blythe [4] suggested a basic approach for analog beam-steering such that the receive beam moves over the swath in accordance with the direction of reflection. About twenty years later, his idea finds a more detailed description and justification in the independent and almost contemporary works by Kare [5], and Suess and Wiesbeck [6].

The patent by Kare in [5] presents the Moving Receive Beam as a technique to improve the quality of “high-resolution SAR imagery over a wide target area,” by reducing the edge losses and the range ambiguities. Different approaches for the steering of the receiving beam are suggested: based on an a priori assumption on the acquisition geometry, open-loop system on the actual receive data, close-loop system or on test pulses. Moreover, Kare describes different analog feed implementation options, involving both planar array and reflector architectures, showing a thorough understanding of the implications in the reflector case. The necessity to take into account the temporal extension of the pulse in the steering mechanism is mentioned, and in particular for chirp pulses, the possibility to adapt the position of the beam to the frequency of the received signal.

In [6, 7] for the first time digital beam-forming techniques are presented in conjunction with a time varying receive beam-steering in elevation. A quantitative description of the steering law, comprehensive of a compensation for the time spread of chirp pulses by using a frequency dependent steering is given.

The SCan-On-Receive (SCORE) mode of operation is primarily based on generating a wide transmit beam that illuminates the complete swath and a narrow, high-gain beam on receive that follows the pulse echo on the ground. The high-gain SCORE beam results in an increased signal-to-noise ratio compensating the low-gain (wide beam) transmit antenna loss. Specifically at the swath edges (half-power beamwidth angles) the typical two-way loss of a monostatic system is reduced. Further, the narrow receive beam has the advantage of attenuating the range ambiguities. For a strictly spherical Earth model, that is, no topographic height, the direction of arrival of the received echo is a function of the

slant range. This results in a one-to-one relation between the required beam steering angle and the time variable. DBF is used to combine the signals received by the subapertures, in order to obtain at each instant a sharp and high-gain pattern, steered toward the expected direction of arrival of the echo. The specific beam-forming implementation depends on the system involved, but can in general be described by a complex and time varying weighting of the subaperture followed by a summation. This effectively reduces the data rate by eliminating the redundancies; thus, in the ideal case the data reduction is lossless. (This reduction of data rate is the case for DBF in elevation, where the channels are combined. In general, however, DBF results in a higher data rate since it facilitates a higher resolution and wider coverage, that is, higher information rate.)

2.2. Digital Beam-Forming in Azimuth. Multiple phase centers in along-track (azimuth) enable an improved azimuth resolution, while requiring the data streams from each azimuth channel to be recorded separately for on-ground processing [8]. Here, in contrast to the elevation operation, the multiple channels yield in a higher data volume resulting from the increased resolution. The principle behind multiazimuth channel operation is different for the planar and reflector systems, which requires a separate treatment.

For the planar system, shown in Figure 1(a), all subapertures cover the same angular segment, thus “seeing” identical Doppler spectra. Considering a single subaperture, the spacial separation between the samples, as determined by the pulse repetition frequency (*PRF*), is such that the Doppler spectrum is undersampled, that is, aliased or ambiguous. It is only through the combination of the spacial samples of all subapertures, that the Doppler spectrum can be recovered unambiguously. Each subaperture can thus be considered as an additional spacial sample in the along-track direction carrying nonredundant information. In general the system operation will be such that the *PRF* will result in a nonuniform spacial sampling; this makes the combination of the channels a nontrivial task, requiring a reconstruction of the Doppler spectrum which is detailed in [9] based on a generalization of the sampling theorem [10, 11].

A reflector system of multiple azimuth phase channels will require multiple feeds displaced in along track direction as shown in Figure 1(b). In contrast to the planar case, here each azimuth element “looks” at a different angle and by this the angular segment (Doppler span) covered by each element does not overlap with those of the others. Thus each element samples a narrow Doppler spectrum corresponding to the half-power-beamwidth of the corresponding pattern. The *PRF* must be high enough such that the spacial sampling for each channel is adequate. If the Doppler spectra of the elements are contiguous, they jointly yield a higher azimuth resolution [2]. Here also, each channel carries nonredundant information.

The above description pointed out the multiazimuth channel operation for improved resolution. However, the systems detailed in this paper do not utilize multiple azimuth channels, since this is not the issue of this paper.

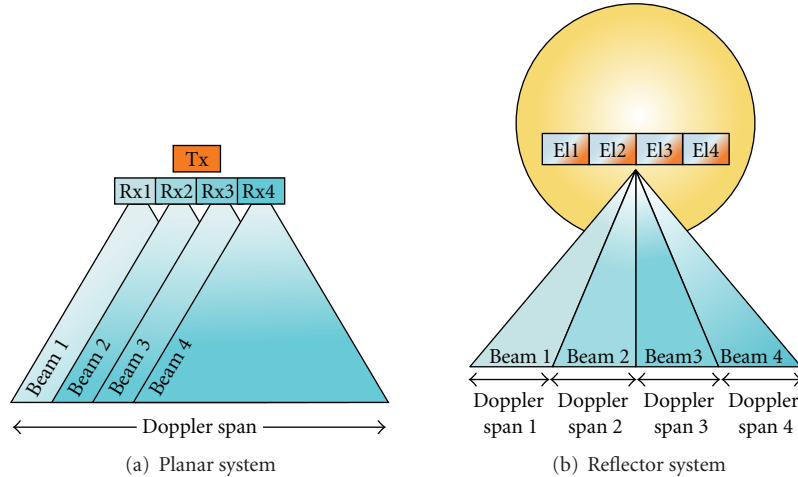


FIGURE 1: MultiAzimuth channels yield identical wide Doppler span for each channels in case of the planar system (a), and narrow Doppler spans of different Doppler centroid in the case of the reflector system (b).

3. Basic Architecture

Although the beams generated by the two systems are similar to each other, the underlying system architecture, used to generate these beams, is quite different. Therefore in the following the system architecture of each system is described.

3.1. Planar System. The planar receive array consists of N_{pl} subapertures, uniformly placed in the plane perpendicular to the flight direction, with DBF capabilities in elevation, as shown in Figure 2. In spaceborne SAR, patch elements or slotted waveguide antennas are commonly used. For the basic operation mode considered in this paper, no beam-forming capabilities are required on transmit and thus a single separate transmit antenna is used. The pattern of the transmit antenna coincides with that of each receive subaperture, by this each subaperture “sees” the same area on the ground. The echoes from the ground are received by each subaperture, amplified, downconverted and digitized. (Depending on the carrier frequency future systems may use direct digitization without a dedicated down conversion.) From this, it is evident that this system will require the capability to handle N_{pl} digital data streams, furthermore onboard DBF capability is required.

The data stream $s_i(t)$ of each channel i is multiplied by a time varying complex coefficient $w_i(t)$. Then the data values are summed up resulting in the output signal, given in (1), which is saved onboard the instrument for later downlink.

$$s_{pl}(t) = \sum_{i=1}^{N_{pl}} w_i(t) \cdot s_i(t). \quad (1)$$

The complex multiplication and summation is equivalent to forming a narrow, time varying beam, which follows the echo on the ground. The beam will scan the complete swath within the time period of one pulse repetition interval ($PRI = 1/PRF$). Any imprecision in determining the complex weights will lead to a beam which is not steered in the signal's

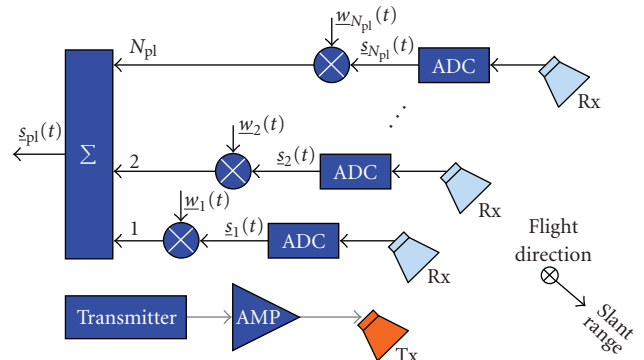


FIGURE 2: General system architecture for planar system; some components such as LNAs, mixers, filters etc. are not shown to maintain a clear representation.

direction-of-arrival and consequently to a loss in power. The generation of frequency dispersive beams (cf. later discussion on pulse extension loss in Section 4) as suggested in [6, 7] is also possible by introducing an additional time shift and adapting the weights; this can still be implemented in the time domain, that is, without a significant increase in processing complexity.

3.2. Reflector System. The reflector system consists of a parabolic reflector and a feed array of transmit/receive elements, as shown in Figure 3. The feed elements are arranged in the plane perpendicular to the flight direction and facing the reflector. Each element results in a beam, illuminating a region on the ground, which partially overlaps with the region illuminated by the beams of the adjacent elements. To illuminate a given angular segment in elevation, the corresponding feed elements are activated. Depending on the scan angle, one or more elements need to be activated, to avoid SNR loss (cf. Section 7). Similar to the planar system, the receive beam will scan the complete swath within the time period of one PRI , however here each element is only

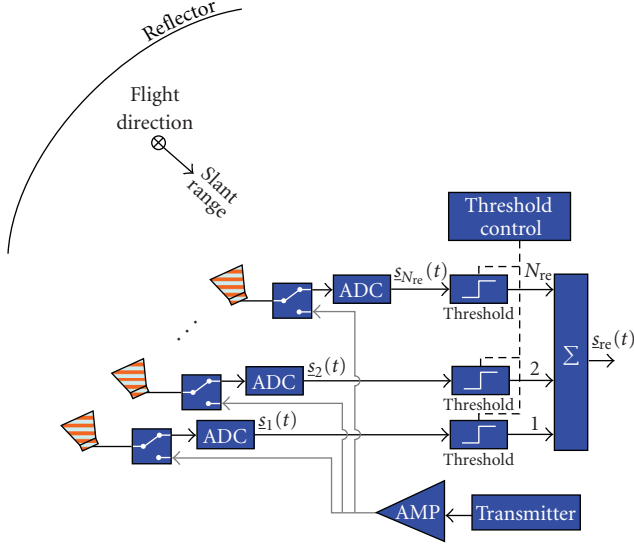


FIGURE 3: System architecture for reflector system; some components such as LNAs, mixers, filters etc. are not shown to maintain a clear representation.

active during a subinterval of this time period. On transmit all N_{re} elements are activated generating a wide beam. (Note the difference to the planar case where a single subaperture generates a wide beam).

In the case of the reflector system, DBF consists of selecting a subset of the feed elements and summing up the corresponding data streams. For the given number of adjacent active elements, N_{act} , the output signal is given by:

$$\underline{s}_{re}(t) = \sum_{i=n}^{n+N_{act}} \underline{s}_i(t), \quad 1 \leq n, N_{act} \leq N_{re}. \quad (2)$$

Clearly the data handling complexity is below that of the planar system. An attractive realization of the subset selection is to use digital threshold detectors, to determine whether a data stream is passed to the summation or nulled. The argumentation here is that an echo from a certain direction-of-arrival will only contribute to the signal level of a few feed elements, corresponding to this direction-of-arrival. The threshold levels need to be adapted to the (slow) variation of the reflectivity for different scenes, which causes a variation of the average power level at the receiver. For the same reason, the threshold levels of the different channels cannot be determined independently from each other. Thus the threshold ensures that at each time instance only the information relevant channels are summed up. For the SAR processing it is important to record which signals are summed at each instance in order to be able to reconstruct the actual antenna pattern.

4. SAR Performance Parameter Definition

This section provides a definition of the quantities involved in the evaluation of the SAR system performance.

Range-Ambiguity-to-Signal Ratio (RASR) quantifies the disturbance due to echoes from preceding and succeeding pulses, which arrive simultaneously with the echo of interest. The *RASR* is defined as the ratio between the total power received from these ambiguous signals and the power of the useful signal. The definition of the *RASR* as a function of slant range R is given by [12]

$$RASR(R) = \frac{R^3 \cdot \sin \eta}{|C_{2way,el}(\vartheta)|^2} \sum_{l \neq 0}^{N_F} \frac{|C_{2way,el}(\vartheta_l)|^2}{R_l^3 \cdot \sin \eta_l}, \quad (3)$$

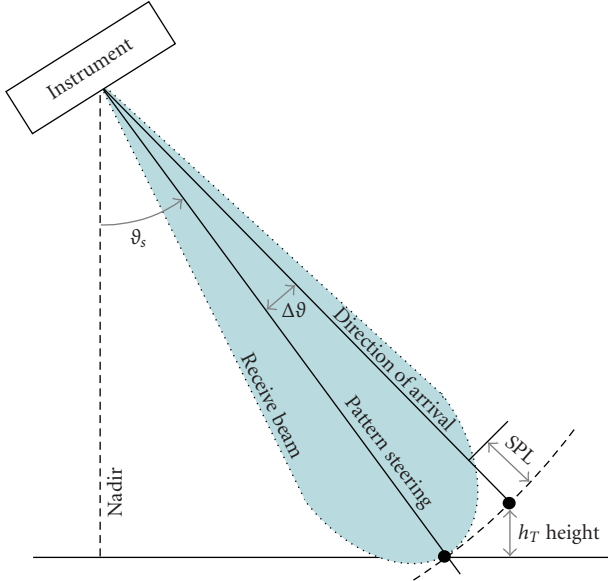
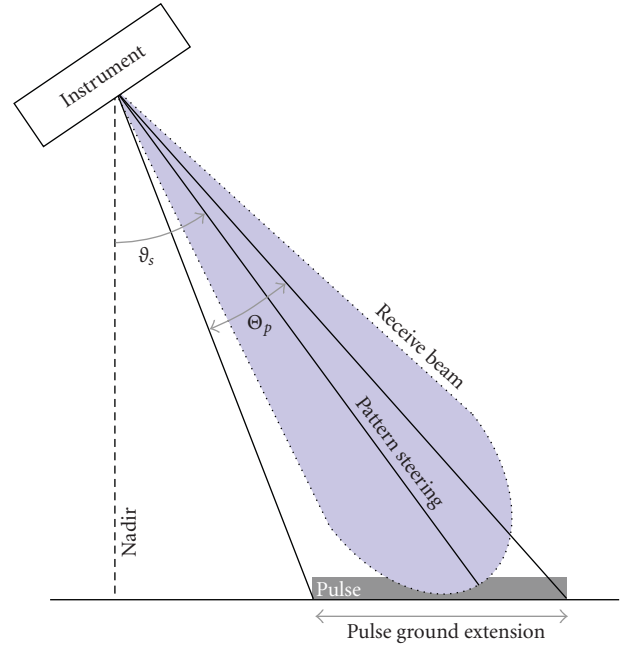
where $C_{2way,el}(\vartheta) = C_{T,el}(\vartheta) \cdot C_{R,el}(\vartheta)$ represents the two-way antenna pattern in elevation; ϑ is the beam steering angle; η the local incidence angle corresponding to the signal; and N_N , N_F the number of ambiguities considered in the calculation in near and far range, respectively. (Note that in the case of SCORE the transmit $C_{T,el}(\vartheta_l)$ and receive $C_{R,el}(\vartheta_l)$ elevation patterns are substantially different from each other (cf. Section 2.1)). The subscript l denotes the corresponding quantities associated to the ambiguous signals. In the above expression the variation of the surface reflectivity with incidence angle is only considered through the $\sin \eta$ term, representing the geometrical projection of the surface area on the normal to the line-of-sight vector; otherwise the expression would include the radar backscatter coefficient (RCS).

Azimuth-Ambiguity-to-Signal Ratio (AASR) quantifies the aliasing generated by the finite sampling of the Doppler spectrum at intervals of the pulse repetition frequency (PRF). In fact, the Doppler spectrum is not strictly band limited due to the sidelobes of the azimuth antenna pattern. As a consequence, Doppler frequency components outside the sampling interval $-PRF/2 \leq f_D < +PRF/2$ are folded back into the processed Doppler frequency range, producing ambiguities. The *AASR* is defined as [12]

$$AASR = \frac{\sum_{m \neq 0, m=-N_A}^{N_A} \int_{-B_p/2}^{B_p/2} |C_{2way,az}(f_D + m \cdot PRF)|^2 df}{\int_{-B_p/2}^{B_p/2} |C_{2way,az}(f_D)|^2 df} \quad (4)$$

where f_D is the Doppler frequency; B_p is the processed azimuth bandwidth; $C_{2way,az}(f_D)$ the two-way (transmit/receive) azimuth antenna pattern as a function of the Doppler frequency; N_A the number of ambiguities considered in the calculation. Note that there is a one-to-one correspondence between the the Doppler frequency and the azimuth angle, ϕ , given by $f_D = 2V \sin \phi / \lambda$, where V is the platform velocity. This allows to express the azimuth pattern either through the Doppler frequency or through the azimuth angle. Further, the processed Doppler bandwidth, B_p , is fixed by the required azimuth resolution, δ_{az} , through $B_p \approx V/\delta_{az}$.

Noise-Equivalent Sigma Zero (NESZ) is a measure of the sensitivity of the system to areas of low radar backscatter. It is given by the value of the backscatter coefficient

FIGURE 4: SCORE pattern loss SPL .FIGURE 5: Pulse extension loss PEL .

corresponding to a signal-to-noise ratio of unity, $SNR = 1$. The $NESZ$ as a function of slant range R is given by [13]

$$NESZ(R) = \frac{2(4\pi)^3 P_n \cdot PRF}{c_0 \lambda^2 \cdot P_{av} \cdot G_T G_R} \frac{N_{az} \sin(\eta)}{\delta_{az}} \cdot \frac{1}{\left| C_{2way,el}(\vartheta) \cdot \sum_{i=1}^{N_{az}} \left(C_{2way,az}(\phi_i) / R^2(\phi_i, \vartheta) \right) \right|^2}, \quad (5)$$

where P_n represents the equivalent receiver noise power; P_{av} is the average transmit power; G_T , G_R are the antenna gain in transmission and reception, respectively; λ is the radar wavelength; c_0 the speed of light; δ_{az} is the azimuth resolution; $N_{az} = \lambda R \cdot PRF / 2\delta_{az} \cdot V$ is the number of integrated pulses during the azimuth compression.

SCORE Pattern Loss (SPL) is a measure of the antenna gain loss due to topographic height such as mountains and relief. In fact, the SCORE steering direction is computed based on an Earth model, that is, not including topographic height. As a consequence, in a realistic scenario characterized by mountains and relief, there is a mismatch between the actual direction of arrival of the signal echo and the steering direction. This results in a gain loss with respect to the ideal operational condition.

As shown in Figure 4 the SPL results because of the angle difference, $\Delta\vartheta$, between the steering direction, ϑ_s (the maximum of the pattern), and the echo actual direction of arrival. Since the antenna steering angle is computed using the correspondence between the signal delay and angle of arrival, which is in general based on a simplified geometrical model of the Earth, any steering error will also result in a SCORE pattern loss. For each instant of time the SPL is defined by the value of the elevation receive pattern at

the angle $\vartheta_s + \Delta\vartheta$ normalized to the maximum value of the pattern at that time:

$$SPL = \frac{C_{R,el}(\vartheta_s + \Delta\vartheta)}{C_{R,el}(\vartheta_s)}. \quad (6)$$

Note that in the context of the above definition negative SPL values indicate a loss in gain. (The transmit pattern does not appear in the expression since it does not affect the SPL .)

Pulse Extension Loss (PEL) is the loss associated to the non-vanishing pulse duration, as shown in Figure 5. In fact the backscattered echo is characterized by an instantaneous extension $c_0 \tau_p / 2 \sin \eta$, on the ground simultaneously contributing to the received power at each instance of time. When the angular segment, Θ_p , corresponding to this extension becomes comparable to, or larger than the receive beamwidth, a loss occurs. The PEL is defined as the ratio of Θ_p weighted by the receive pattern steered to the pulse center to Θ_p weighted by the maximum of the pattern (Due to the finite number of elevation patterns the maximum of the pattern may not be at the pulse center, however, the loss caused by this pulse switching is already accounted for in the computation of the $NESZ$, for which it is not included in the PEL .) Then, the PEL is computed according to

$$PEL = \frac{1}{C_{R,el}(\vartheta_s) \cdot \Theta_p} \cdot \int_{\vartheta_s - \Theta_p/2}^{\vartheta_s + \Theta_p/2} C_{R,el}(\vartheta) d\vartheta, \quad (7)$$

where the angular pulse ground extension $\Theta_p(\tau_p, \eta)$ is a function of the pulse duration τ_p and incidence angle η , and the integral limits are taken to be symmetrical with respect to the maximum of the pattern at ϑ_s .

It is worth noting that the PEL is an integral loss including all point scatterers within the pulse extension at

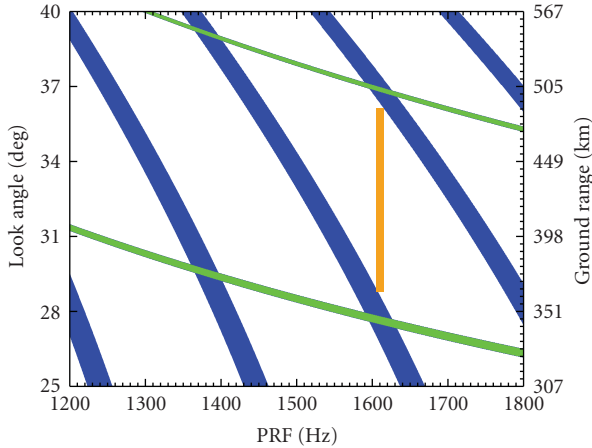


FIGURE 6: Timing (diamond) diagram for an orbit height of 650 km and a transmit duty cycle of 8%. For a given PRF the diagram shows the restrictions on the receive window due to transmit instances (wide dark strips) and nadir echos (thin light strips).

any instance of time. Thus, the PEL does not characterize the response of an individual point scatterer over time. In fact the received chirp signal from any single point scatterer will show an amplitude and phase modulation. This modulation can deteriorate the impulse response in range for narrow receiver patterns or a large number of beam switchings.

5. SAR Requirement and Common Design Parameters Definition

5.1. Performance Requirements. Table 1 collects the main performance requirements on SAR image quality, which has been assumed to design the reference system. The reported values have been selected according to the most advanced or forthcoming SAR mission performance. It is worth noting that a standard on SAR image quality does not exist. For comparison, current satellite missions, such as COSMO-SkyMed [14] and TerraSAR-X [15], deliver products with a coverage ranging from 10 km to 200 km and a corresponding resolution ranging from 1 m to 100 m, respectively. The ambiguity and $NESZ$ level are in the order of -21 dB and -24 dB, respectively.

5.2. Common Design. In the following the system design parameters common to both systems are stated. This is the basis for the individual planar array and reflector antenna system designs in Sections 6 and 7, respectively, which are optimized to yield the best individual SAR performance.

The systems considered in this paper operate at C-band frequencies, however the presented findings are mostly also applicable to other frequency bands. Further, for simplicity, the investigation is for a single polarization system.

The orbit height selection has a major influence on the radar parameters, such as the incidence angle range to cover a given swath, the path attenuation and by this the SNR , as well as the resulting mission scenario such as repeat cycles. Here

TABLE 1: Requirement on performance parameters.

Parameter		Value
Frequency	C-Band	5.4 GHz
Swath width		≥ 120 km
Global coverage		Within one repeat cycle
Resolution (range, azimuth)	δ_{rg}, δ_{az}	8×8 m
Ambiguity-to-signal ratio	$RASR, AASR$	-20 dB
Noise-equivalent sigma zero	$NESZ$	-25 dB
SCORE loss @1.5 km	SPL	≤ 1 dB

a 650 km orbit is selected. This together with a requirement of a 120 km swath will allow a global coverage of the Earth within a single repeat cycle of 23 days.

Next an investigation of the timing is due in order to determine the specific range of incidence angles and PRF values. The timing diagram indicates whether the backscattered echo from a point on the ground can be received, that is, whether the echo delay is such that the signal does not superimpose neither on the transmit instances nor on the nadir echoes. The timing diagram is a function of the pulse repetition frequency and the angular position of the backscattering point within the swath. Figure 6 shows the timing diagram for a transmit pulse duty cycle of 8%. Choosing $PRF = 1610$ Hz results in a receive window, which covers the look angle range $[28.8^\circ, 36.1^\circ]$, which corresponds to a maximum swath width of 125 km.

For the simple stripmap mode of operation considered here, the look angle range directly gives the half power beamwidth in elevation for the transmit antenna, which is set to $\Theta_{T,el} = 7.3^\circ$. The corresponding receive half power beamwidth is not a common design parameter, since its value will be different for the planar and reflector system (cf. Sections 6 and 7).

The half power beamwidth in azimuth is determined by the requirement on the azimuth resolution δ_{az} and, to some extent, the required $AASR$. For the systems considered here, the transmit and receive antennas have the same coverage in azimuth. For a given resolution, the half power beamwidth can be approximated by $\Theta_{az} \approx \lambda/2\delta_{az}$. This results in a half power beamwidth in the order of 0.2° .

A design parameter, which is crucial both for the SAR performance and the instrument design, is the transmit power. Here the average transmit power together with the hardware efficiency influences (1) the amount of heat dissipation and by this the thermal design of the instrument; (2) the size of the solar panel and the orbit usage of the instrument; (3) the $NESZ$ of the SAR. On the other side, the maximum peak power determines the minimum duty cycle (for a given $NESZ$) which in turn influences the timing. Both systems analyzed in this paper have the same average transmit power of $P_{av} = 300$ W and a duty cycle of 8%.

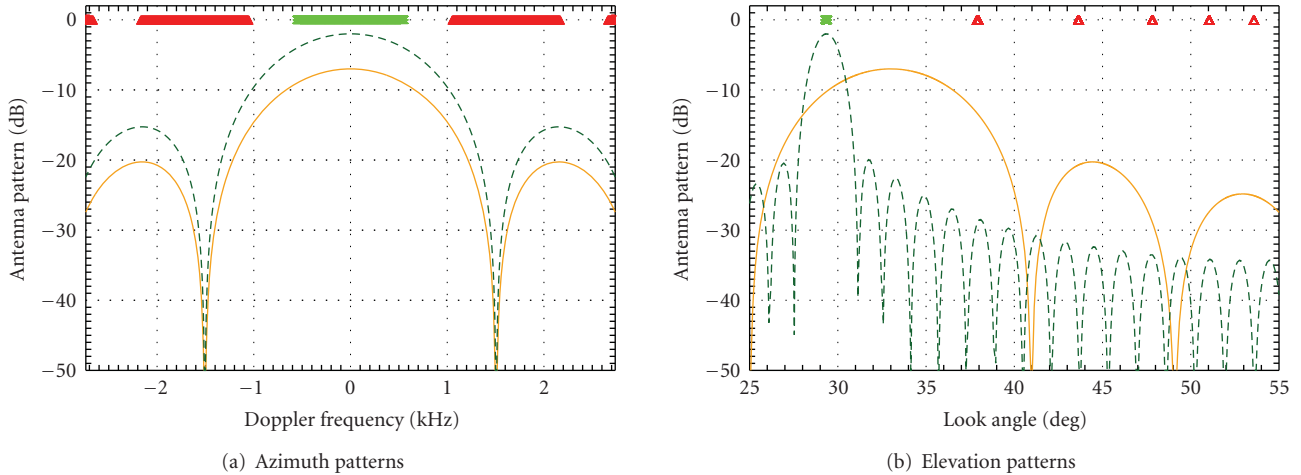


FIGURE 7: Transmit (solid line) and receive patterns (dashed line) of the planar antenna system in azimuth and elevation. All patterns are normalized to the maximum gain of the uniformly tapered receive array.

6. Design and Performance of Planar System

In the following, first the design of the planar system is derived, which is mainly the dimensioning of the antenna, then the SAR performance of the system is given.

6.1. Planar System Design. In the case of the planar array antenna structure, the receive antenna is composed of 20 subapertures, placed in the elevation direction and only a single azimuth subaperture (channel) is employed. The dimensions of the antenna strongly affect the system performance; here the azimuth ambiguity requirement is the driving factor for the antenna length. In particular, the length of both transmit and receive antennas is set to 10 m, which is affordable from a practical point of view in terms of cost and launcher requirement. To limit the azimuth ambiguities, the processed Doppler bandwidth is reduced at the cost of a worsened azimuth resolution. The azimuth patterns are shown in Figure 7(a), no amplitude taper is applied in azimuth, and transmit and receive patterns are identical, however, the patterns are normalized to the maximum gain of a uniformly tapered receive array, which results in the difference in the level between the two azimuth patterns.

The elevation dimension of the transmit antenna is set in order to illuminate the swath of interest with the mainlobe pattern. For a uniform rectangular aperture illumination the half beamwidth is roughly given by the radar wavelength normalized by the antenna length $0.89 \cdot \lambda/d$. For the half power beamwidth of Section 5.2 this corresponds to an antenna height of ≈ 0.4 m. The elevation patterns are shown in Figure 7(b) where an amplitude taper is applied to the receive array in order to reduce the side lobe level to 20 dB. It is worth remarking that for a given average transmitted power, the *NESZ* performance mainly depends on the antenna area. Thus increasing the antenna height allows improving the radiometric resolution, however at the cost of an increased sensitivity of the system to surface topographic height and an increased pulse extension loss.

For the system under study, the receive antenna height is 2 m such that the half power beamwidth of the receive pattern is about 1.6° .

6.2. Planar System Performance. The ambiguity performance of the planar system is shown in Figure 8 versus the ground range position on the swath. The *AASR* is constant all over the swath, due to stripmap operational mode. Its value, which depends on the *PRF*, the antenna length, and the processed azimuth bandwidth is around -22 dB for an azimuth resolution of $\delta_{az} = 6$ m.

The *RASR* varies over the swath and is below -30 dB. The range ambiguity suppression is mainly achieved by the narrow *SCORE* receive beam, rather than by the transmit beam (see also Figure 7(b) where the first range ambiguity is within the main lobe of the transmit beam). In fact, the useful echo is always, that is, for each point on the swath, weighted by the maximum of the receive pattern, whereas the ambiguous echoes are strongly attenuated by the receive pattern sidelobes. The total ambiguity-to-signal ratio, that is, the sum of *AASR* and *RASR*, is mainly determined by the *AASR* since it is about 10 dB larger than the *RASR*.

Figure 9 shows the *NESZ* versus ground range position along the swath. The *NESZ* is below -26 dB all over the swath. This assessment is mainly related to the transmitted power and to the area of the antenna in transmission and reception. The trend of the curve along the swath is due to the transmit pattern shape. Here, the antenna tilt angle is such that the maximum of the transmit antenna pattern is closer to the far range. This improves the *NESZ* in far range with respect to the near range, so that the resulting *NESZ* is symmetric in near and far range.

Figure 10 describes the effect of topographic height on *SCORE* performance. The dotted curve corresponds to a source with elevation 1500 m. The solid one, reported as a benchmark, corresponds to a source with no elevation. Figure 10(a) shows the displacement between the receive pattern steering angle and the actual direction of arrival,

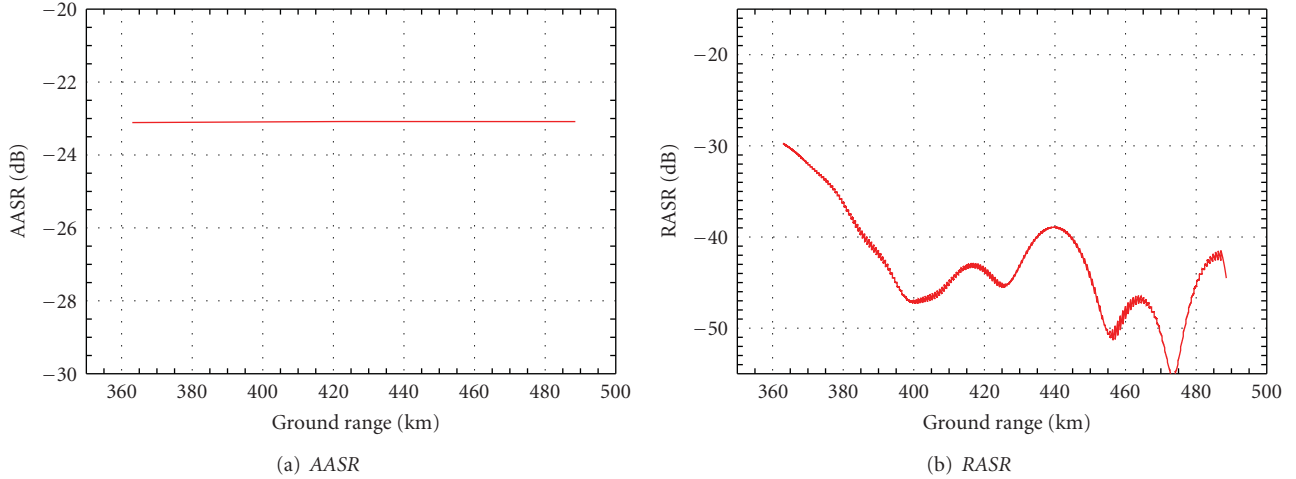


FIGURE 8: Ambiguities versus ground range.

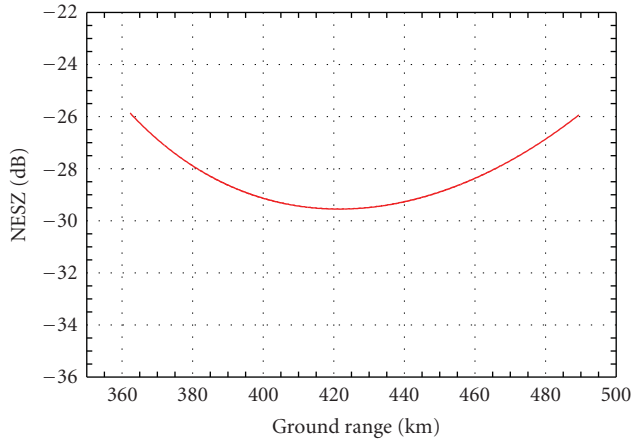


FIGURE 9: The noise-equivalent sigma zero of the planar system versus ground range.

versus the location of the source along the swath. The steering error is more severe in near range than in far range, due to the spherical geometry of the earth surface. Its value is in the order of 0.2° . The corresponding SCORE pattern loss depends on the beamwidth of the receive pattern: the broader the beamwidth, the more the system is robust to surface elevation. For the current system the loss varies over the range between -0.15 dB and -0.25 dB.

The dashed line in Figure 10 shows that the *SPL* for a topographic height of 5 km may get in the order of -2.5 dB. Although it is not common to have elevation variations of this order within one imaged scene, however different Earth regions may well have height variations of several kilometers. As a result it is concluded that the instrument commanding, that is, beam steering, should take the scene height into account, however an adaptation of the beam steering within one data take is not required.

The pulse extension loss of the planar system, shown in Figure 11, is below 0.4 dB throughout the swath. This is due to the low duty cycle of 8% which results in a pulse

extension much smaller than the beamwidth of the elevation pattern. To be able to operate SCORE with a low *PEL* even with long chirp pulses [6, 7] suggests an additional frequency dependent beam steering. This can be understood as an intentional frequency dispersion which exploits the linear frequency variation within a pulse (chirp). Effectively, different beams are generated for different frequencies which correspond to different steering directions. This technique, which is implemented through modification of the SCORE steering coefficients, effectively removes the *PEL*.

7. Design and Performance of Reflector System

In analogy to the previous section, a design example, based on the reflector antenna principle, with a feed array shall be demonstrated.

7.1. Reflector System Design. As stated in Section 5, the design goal is to achieve similar half power beam widths in elevation and azimuth as in the planar array case, in order to meet the performance requirements presented in Table 1. The degrees of freedom for the conceptual design are the focal length, the diameter, and the feed array geometry [16].

The schematic design of the reflector antenna with feed array is presented in Figure 12. The feed array is positioned symmetrically in front of the reflector in the focal plane $z = F$, neglecting the effect of blockage. Here the elevation plane is defined in the Cartesian reflector coordinate system with $y = 0$, with the azimuth direction orthogonal to this plane. The diameter d of the reflector is 10 m. With a focal length F of 5.7 m, the shape parameter a , which defines the z -coordinate of each surface point of the paraboloid, can be determined as $a = 1/4F$.

The feed array is a linear array consisting of 26 elements, facing the plane $z = F$. This allows beam steering in elevation direction. The spacing Δx_f of adjacent elements is 0.58λ . For quadratic 0.4λ patches, the dimensions of the (passive) patch array, allowing for sufficient margin, is approximately $85 \text{ cm} \times 5 \text{ cm}$. The array design is not

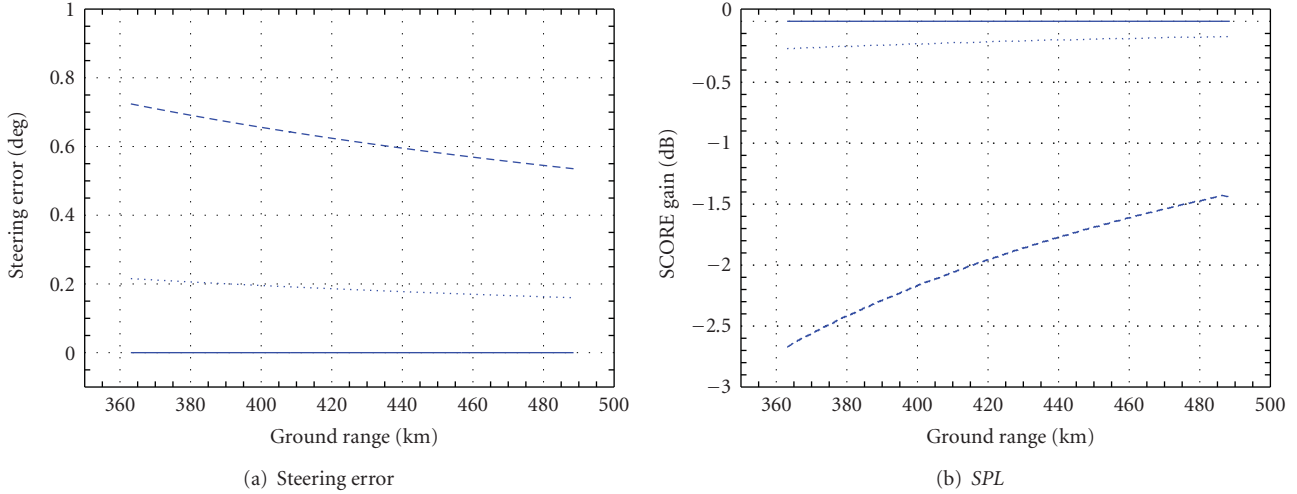


FIGURE 10: SCORE performance versus ground range for 0 m (solid line), 1500 m (dotted line), and 5 km (dashed line) topographic height, respectively.

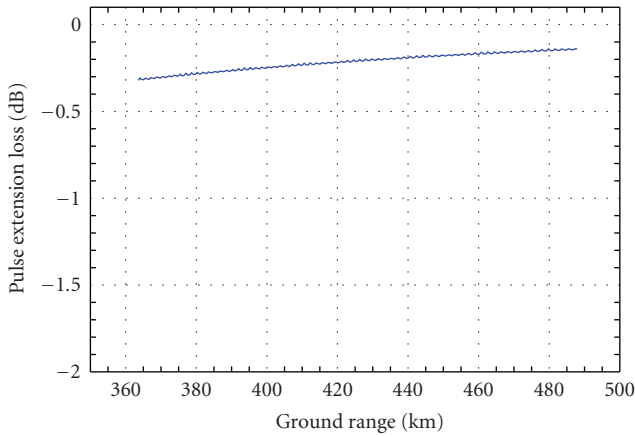


FIGURE 11: The pulse extension loss of the planar system versus ground range.

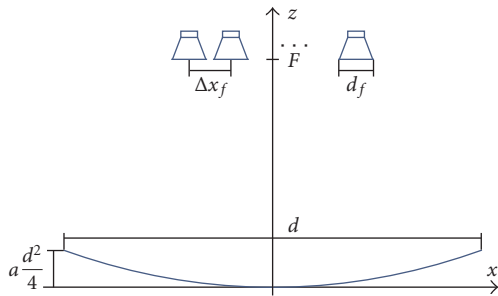


FIGURE 12: C-Band reflector and feed array geometry.

required to allow for the generation of multiple azimuth beams (cf. discussion in Section 2.2), since a single azimuth beam provides sufficient Doppler bandwidth to achieve the required azimuth resolution of 8 m (see Table 1).

A simplified Geometrical Optics approach was used for the pattern and field computations of the system under consideration. The results were verified with reference data obtained from commercial software (GRASP9), showing a maximum relative error $\leq 1.5\%$ within the angular range of the 5th order sidelobe.

SCORE Feed Selection. The beam-forming capabilities of a reflector antenna are more restricted compared to a planar antenna, since the subpatterns do not overlap substantially. Therefore the pattern is generated by turning feed elements on or off. As the pulse travels over ground, the field distribution in the focal plane changes and other elements have to be switched on. The feed selection has a significant impact on the system performance in terms of *NEZ* and *RASR*. The goal of the feed selection strategy is to optimize these parameters.

In general, the optimum selection is the one which results in the maximum antenna gain or equivalently the highest illumination efficiency. As indicated by the dotted curves in Figure 13, the highest gain is achieved with two activated feed elements. A single active element will increase the spill over and by this decrease the illumination efficiency (gain), whereas three or more activated elements will reduce both spill over and aperture efficiency, which also results in a lower gain. Nevertheless, two active receive elements would result in a high pulse extension loss. Consequently, the minimum number of active elements has to be increased for a wider beamwidth. In case of the system given here, four active elements are required, at the cost of a reduced gain. Note that this is a particularity of the system architecture considered here for the reflector system. Other solutions, overcoming these limitations, are discussed in Section 8.

The field strength distribution on the feed plane due to an extended pulse is also indicated in Figure 14, where the field is concentrated over a subset of feed elements. The activated elements are represented by black patches, and

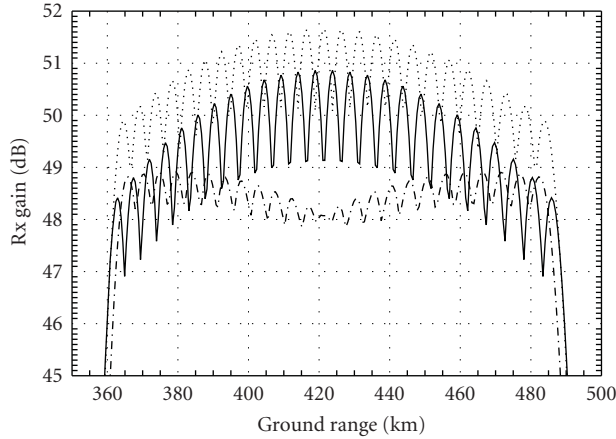


FIGURE 13: Reflector gain pattern versus ground range with one (solid), two (dotted) and four (dashed) feed elements activated.

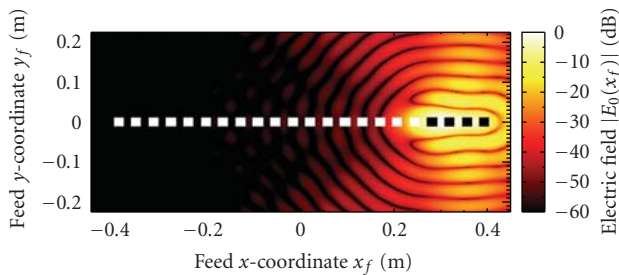


FIGURE 14: Normalized electric field on the feed array due to an extended pulse on the swath edge.

clearly activating only two elements would result in a power loss.

To get an impression of the pattern shapes, the transmit pattern and one receive pattern have been computed. Figure 15 shows a polar plot of the transmit pattern, C_T , weighted with the maximum gain. Here all 26 feed elements are activated, generating a narrow beam in azimuth and a broad homogeneous beam in elevation, with a half power beamwidth $\Theta_{T,el} = 7.3^\circ$.

In the receive case an example of the antenna pattern is presented in Figure 16, where the same four off-center feed elements are activated as in Figure 14. Due to the reciprocity principle, the pattern has basically the same shape as the field distribution. The half power beamwidth in elevation, $\Theta_{R,el}$, is in the order of 1.2° , covering the complete pulse on ground.

Figure 17(a) shows a cut in the azimuth plane. The solid lines represent the transmit patterns (all elements turned on), while the dashed curves indicate the receive patterns when only four center elements are turned on. All patterns are normalized to the maximum gain which would be achieved for an optimum aperture efficiency (note that this maximum gain is not reached for the system considered here). Both plots show the high directivity of the receive pattern with respect to the transmit pattern; the difference is approximately 8.6 dB. In azimuth, Figure 17(a), only a single beam is generated; however this beam slightly depends on

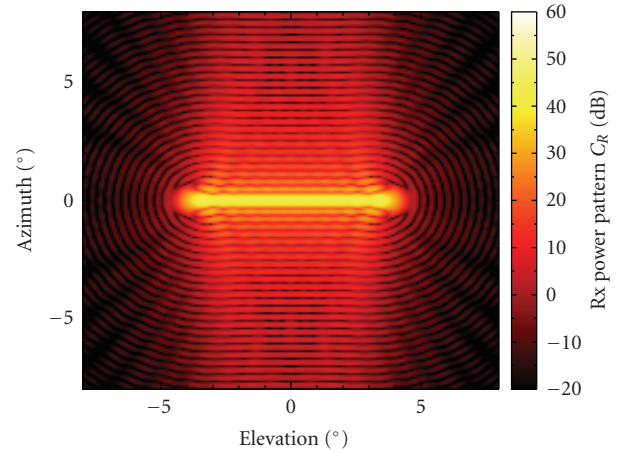


FIGURE 15: Transmit power pattern with 26 elements activated.

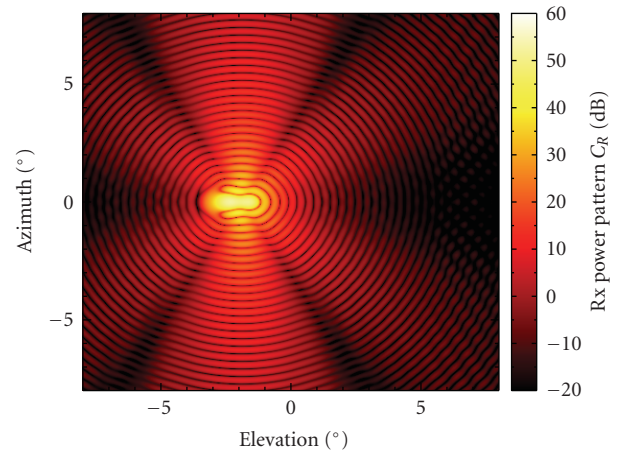


FIGURE 16: Receive power pattern with 5 elements activated.

the number of active elevation elements as can be seen by the slight shift in position of the first nulls. The plot for the elevation plane, depicted in Figure 17(b), shows a nearly rectangular shaped transmit pattern, a property inherent to reflector antennas. This results in an efficient concentration of the transmitted energy to the ground region of interest and manifests itself through an improved *NESZ* performance.

7.2. Reflector System Performance. The ambiguity performance in terms of *AASR* and *RASR* is shown in Figure 18. The processed Doppler bandwidth, B_p , has been adapted to achieve the same *AASR* of ≈ -22 dB as in the planar array system. The processed Doppler bandwidth is indicated by the center bar at the top of Figure 17(a); further the ambiguous spectral domains, marked with the off-center bars, coincide well with the first pattern nulls. The processed Doppler bandwidth is 1150 Hz, yielding an azimuth resolution, δ_{az} , of approximately 6 m.

For the range-ambiguity-to-signal ratio the low *PRF* has the opposite effect as for the azimuth ambiguities. Principally a lower *PRF* will improve the *RASR*. The angular

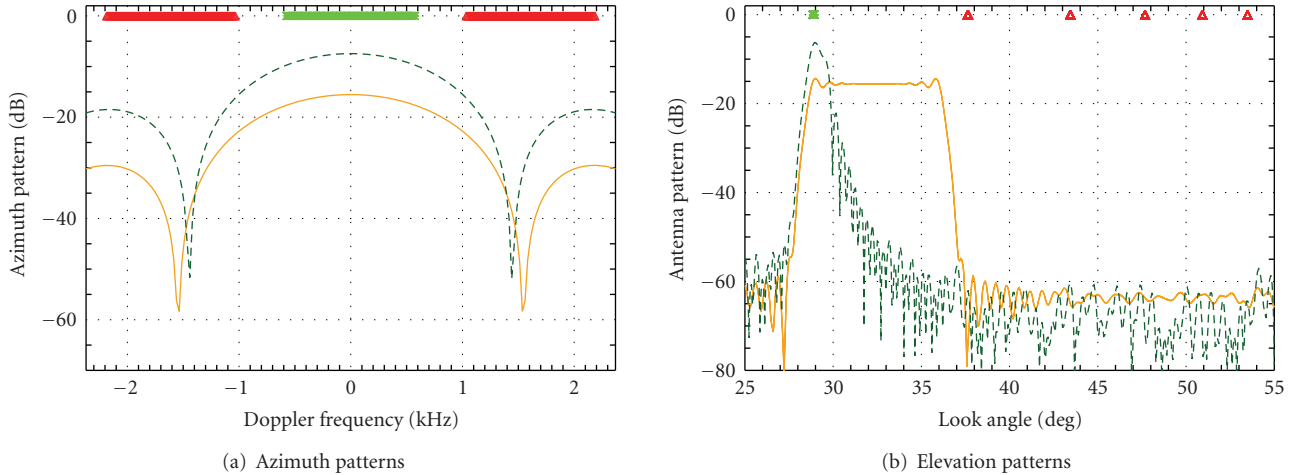


FIGURE 17: Transmit (solid line) and receive patterns (dashed line) of the reflector antenna system. All patterns are normalized to the gain achieved for a optimum aperture efficiency.

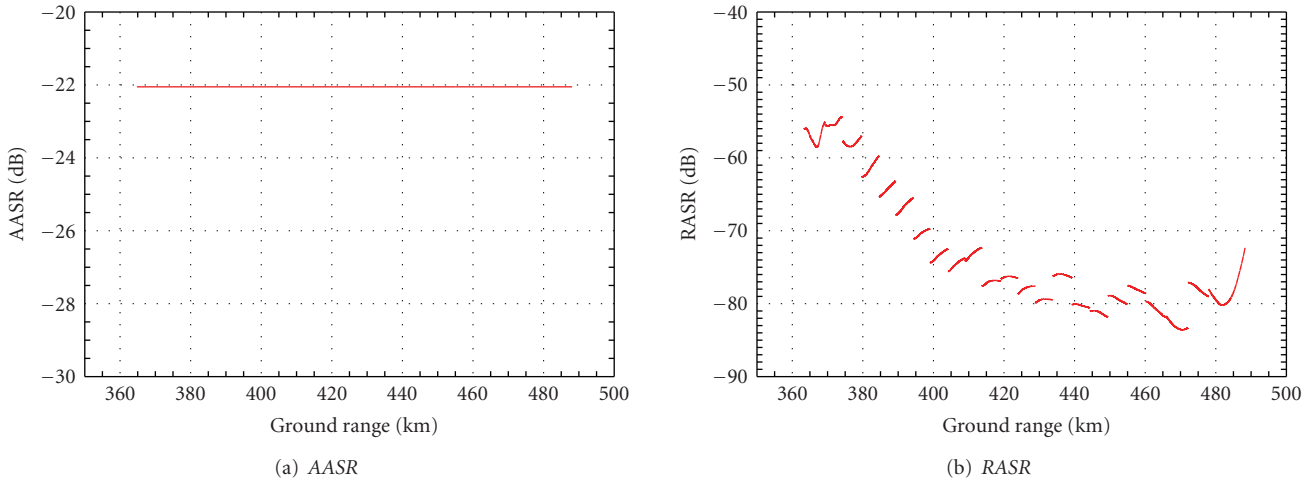


FIGURE 18: Ambiguities versus ground range for the reflector system.

position of the first range ambiguity is outside the main-lobe of the transmit and receive patterns, as can be seen in Figure 17(b). This results in the good range-ambiguity-suppression in Figure 18(b) of better than -50 dB. For a real reflector the realistic suppression will be less and dictated by imperfections which deteriorate the ideal pattern.

The NESZ over ground range is presented in Figure 19. The two curves are computed for the cases that either two or four successive elements are activated. The loss in NESZ in the four element case (upper curve) results from the reduced receive gain. The notches in the curve shape mark the switching of the active elements and the corresponding pattern switching.

The NESZ at the swath borders can be compensated for with a slightly increased feed array, however, due to the rectangular transmit pattern shape, the NESZ will be worse in the far range of the swath (an adaption of the tilt angle to compensate, as done for the planar system, is not possible here). The reason for showing the NESZ of two

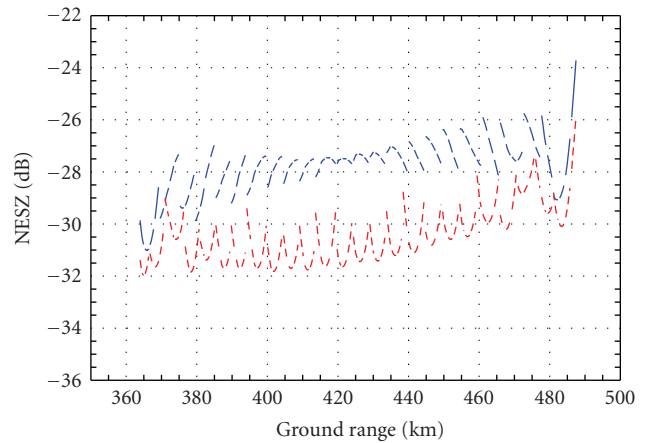


FIGURE 19: The noise-equivalent sigma zero of the reflector system versus ground range for two (solid curve) and four (dashed curve) active feed elements.

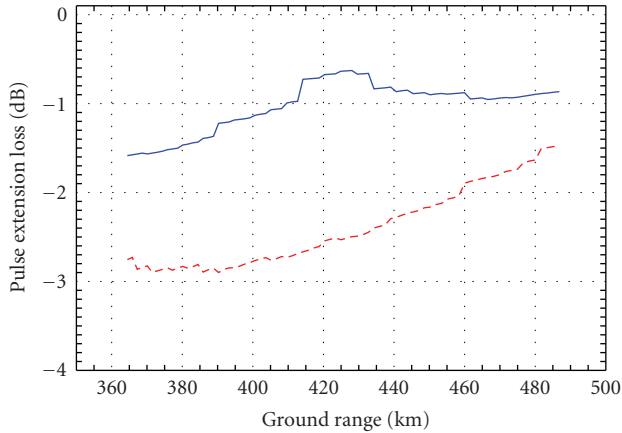


FIGURE 20: The pulse extension loss of the reflector system versus ground range with four (solid line) and two (dotted line) active elements.

active elements (lower curve), is that a more sophisticated digital signal processing could enable this improve in *NESZ* by compensating the reduced beamwidth (see Section 8).

The pulse extension loss of the reflector system (cf. Figure 20 solid line) is higher than for the planar system and reaches values up to 1.7 dB at near range. Here, the *PEL* is an additional loss also effecting the value of the *NESZ*, that is, the curves in Figure 19 are shifted by an amount corresponding to the *PEL*. Increasingly unsymmetrical patterns for off-center beams cause an increased loss (see definition of *PEL* in Section 4). For comparison the *PEL* for two activated elements is also included in the plot (dashed line) indicating the higher loss of up to 3 dB in this case.

8. Conclusion

This paper compares two innovative antenna architectures that employ the technique of digital beam-forming on receive to improve the imaging performance and radiometric resolution of future SAR systems without losing wide swath coverage. Both architectures rely on the side-looking geometry of a spaceborne imaging radar where the scattered echoes arrive at each instance of time only from a very narrow range of angles. A real time angular steering of a high-gain receiver beam is hence well suited to collect all scattered radar echoes from a wide swath without any information loss. The originally suggested architecture for such a digital beam-forming radar employed a planar antenna array [7]. The beam steering in this architecture requires the combination of all recorded antenna signals in a complex real time processor. This puts a high demand on the digital hardware, especially if one seeks for a high receiver gain by using an extended Rx array with a large number of antenna elements.

As an alternative to a planar antenna, we have introduced the novel idea to combine a reflector antenna with a digital feed array to enhance the performance of future SAR systems. Large unfoldable reflectors are now a mature technology with extensive flight heritage in space telecommunications

and lightweight mesh reflectors with diameters of 20 m and more will be deployed in space in the near future. Unfoldable reflector antennas have therefore a high potential to significantly increase the receiving aperture and by this both the range ambiguity suppression and the *NESZ* if compared to planar arrays where the size of the antenna is usually restricted by the limited space in the launcher fairing. This is indicated in the computed *NESZ* values for the two systems (compare Figures 9 and 19) which show an *NESZ* improvement for the reflector system when operated with two active receive elements.

The reflector concentrates at each instant of time the signal power of the received wave fronts from the swath echoes onto a small number of feed elements. In consequence, only a small subset of all feed element signals has to be combined in real time, thereby reducing the complexity of the beam-forming processor also for large apertures. A very simple implementation of a “digital beamformer” is provided by a mere switching between individual feed elements. The element selection can be made signal adaptive, for example, by choosing only those feed elements that exceed a given threshold or by selecting the feed element(s) that receive(s) maximum signal power. This fully automatized feed selection eases the instrument commanding and avoids moreover the beam steering loss from topographic height induced mispointings.

Long chirp signals and large reflectors may, however, require more sophisticated signal processing techniques to optimize the performance. In fact, in this case, the achievable beamwidth is smaller than the instantaneous ground scattering field induced by a long chirp signal. The straight-forward solution for long chirp signals could be a simple increase in the number of selected feed elements and a subsequent summation of their output signals, but this will inevitably reduce the antenna gain, thereby making only suboptimum use of the high Rx-gain capabilities of a large reflector. Such a gain loss from long chirps can be avoided by taking into account that each feed element receives at each instant of time only a fraction of the scattered radar pulse and hence only a corresponding portion of the transmitted frequency spectrum. It is therefore possible to split the incoming signals from the feed elements into multiple frequency subbands and to select for each sub-band again only the element(s) with maximum signal power. This trick can be regarded as providing a dispersive Rx-beam that ensures a high antenna gain for every frequency component of a long chirp. In consequence, one can take full advantage of the large apertures provided by present and future deployable reflector antennas. Reflectors with digital feed arrays are therefore a promising concept for future SAR systems with high potential to outperform planar arrays with regard to the SAR imaging performance for a given weight, size and cost budget.

Acknowledgment

The authors greatly appreciate the detailed comments and suggestions of the anonymous reviewers, which pushed them to an in-depth treatment of the subject leading to a significantly improved paper.

References

- [1] G. Krieger, N. Gebert, and A. Moreira, "Multidimensional waveform encoding: a new digital beamforming technique for synthetic aperture radar remote sensing," *IEEE Transactions on Geoscience and Remote Sensing*, vol. 46, no. 1, pp. 31–46, 2008.
- [2] G. Krieger, N. Gebert, M. Younis, F. Bordoni, A. Patyuchenko, and A. Moreira, "Advanced concepts for ultra-wide swath SAR imaging," in *Proceedings of the 7th European Conference on Synthetic Aperture Radar (EUSAR '08)*, Friedrichshafen, Germany, June 2008.
- [3] C. Fischer, C. Schaefer, and C. Heer, "Technology development for the HRWS (High Resolution Wide Swath) SAR," in *Proceedings of International Radar Symposium (IRS '07)*, Cologne, Germany, September 2007.
- [4] J. H. Blythe, "Radar systems," U.S. Patent 4 253 098, February, 1981.
- [5] J. T. Kare, "Moving receive beam method and apparatus for synthetic aperture radar," U.S. Patent 6 175 326, January 2001.
- [6] M. Suess and W. Wiesbeck, "Side-looking synthetic aperture radar system," European Patent EP 1 241 487, September 2002.
- [7] M. Suess, B. Grafmueller, and R. Zahn, "A novel high resolution, wide swath SAR system," in *Proceedings of International Geoscience and Remote Sensing Symposium (IGARSS '01)*, vol. 3, pp. 1013–1015, Sydney, Australia, July 2001.
- [8] M. Younis, C. Fischer, and W. Wiesbeck, "Digital beamforming in SAR systems," *IEEE Transactions on Geoscience and Remote Sensing*, vol. 41, no. 7, part 2, pp. 1735–1739, 2003.
- [9] G. Krieger, N. Gebert, and A. Moreira, "Unambiguous SAR signal reconstruction from non-uniform displaced phase centre sampling," *IEEE Geoscience and Remote Sensing Letters*, vol. 1, no. 4, pp. 260–264, 2004.
- [10] A. Papoulis, "Generalized sampling expansion," *IEEE Transactions on Circuits and Systems*, vol. 24, no. 11, pp. 652–654, 1977.
- [11] J. L. Brown Jr., "Multi-channel sampling of low-pass signals," *IEEE Transactions on Circuits and Systems*, vol. 28, no. 2, pp. 101–106, 1981.
- [12] J. C. Curlander and R. N. McDonough, *Synthetic Aperture Radar Systems and Signal Processing*, John Wiley & Sons, New York, NY, USA, 1991.
- [13] M. Younis, "General formulation of NESZ," Technical Note TN-SAR-Tech-001, German Aerospace Center, Microwaves and Radar Institute, Wessling, Germany, March 2008.
- [14] S. Mezzasoma, A. Gallon, F. Impagnatiello, et al., "COSMO-SkyMed system commissioning: end-to-end system performance verification," in *Proceedings of IEEE Conference on Radar (RADAR '08)*, pp. 1092–1096, Rome, Italy, May 2008.
- [15] TerraSAR-X, German Aerospace Center (DLR), September 2008, <http://www.dlr.de/TerraSAR-X/>.
- [16] C. Balanis, *Antenna Theory: Analysis and Design*, John Wiley & Sons, New York, NY, USA, 1997.

Application Article

Accurate Antenna Pattern Modeling for Phased Array Antennas in SAR Applications—Demonstration on TerraSAR-X

Markus Bachmann, Marco Schwerdt, and Benjamin Bräutigam

German Aerospace Center (DLR), Oberpfaffenhofen, 82234 Weßling, Germany

Correspondence should be addressed to Markus Bachmann, markus.bachmann@dlr.de

Received 22 October 2008; Revised 10 February 2009; Accepted 13 March 2009

Recommended by Stefano Selleri

The high flexibility and tight accuracy requirements of today's spaceborne synthetic aperture radar (SAR) systems require innovative technologies to calibrate and process the SAR images. To perform accurate pattern correction during SAR processing, an Antenna Model is used to derive the multitude of different antenna beams generated by active antenna steering. The application of such an Antenna Model could be successfully demonstrated for the TerraSAR-X mission, launched in 2007. The methodology and the results of the inorbit verification with an achieved accuracy of better than ± 0.2 dB is reviewed in this paper in detail showing its outstanding accuracy.

Copyright © 2009 Markus Bachmann et al. This is an open access article distributed under the Creative Commons Attribution License, which permits unrestricted use, distribution, and reproduction in any medium, provided the original work is properly cited.

1. Motivation

The accurate knowledge of the antenna patterns of a synthetic aperture radar (SAR) is of main importance for precise SAR image processing. The antenna patterns are required to correct the antenna characteristics visible in the image, as shown in Figure 1. On the left, the uncorrected image is shown with a high brightness in the centre and a decreasing illumination to the borders of the image in range direction. This is caused by the antenna pattern spanning over range. The right image presents the same acquisition after antenna pattern correction, the characteristics of the antenna are eliminated.

Early SAR systems like ERS1/2 or XSAR/SRTM with a low number of possible antenna beams used inorbit antenna pattern measurements for correction. The Envisat/ASAR instrument, for example, acquires SAR images with only eight different antenna beams [1]. Although already at ASAR an Antenna Model was implemented, the more accurate antenna patterns were obtained from inorbit measurements. Images over homogeneously distributed targets were used to determine the reference patterns for each individual beam.

In contrast to these systems, actual SAR satellites enable a very high number of different acquisition modes like stripmap, ScanSAR or other wide swath and high resolution

modes. Thus, a multitude of different antenna beams and hence antenna patterns are needed for consistent calibration of the modes to each other and within the SAR image itself.

Enabling object detection and classification novel SAR systems have also very tight accuracy requirements. They produce images with high resolution in the meter-range and accurate measures of the backscatter down to a few tenth of dB.

A further important point for satellite calibration is the duration of the calibration process, the commissioning phase of the satellite in space. Current SAR systems are no longer experimental systems designed for scientific experiments having uncritical schedule constraints. In fact they shall, to a great extend, be used for commercial applications. Driven by paying customers, the system has to be available as early as possible or at least at an exactly determined date. Hence, a short duration of the commissioning of the satellite is evident.

Reviewing these points, innovative methods are necessary to calibrate complex SAR systems. In this context, the most important key element is the Antenna Model approach described below. It derives the antenna patterns from mathematical models in combination with onground measurements characterising parts of the array antenna. With this approach it becomes possible to calibrate a high

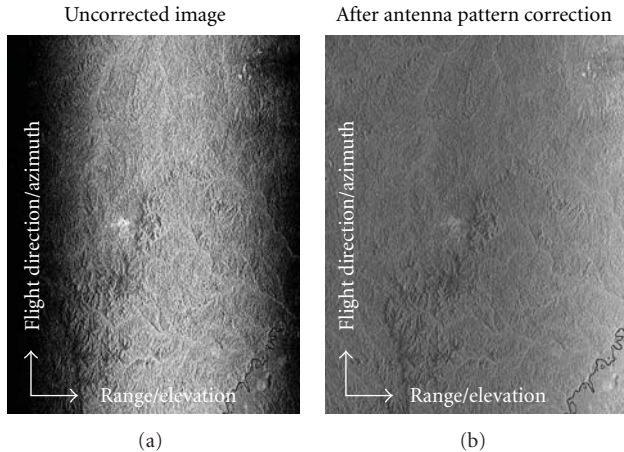


FIGURE 1: SAR image before and after pattern correction.

number of used antenna beams not only with high accuracy but also very time and cost effective. This is demonstrated in example of the TerraSAR-X system.

2. Introduction on the TerraSAR-X System

The TerraSAR-X satellite [2], launched in June 2007, is a versatile X-Band SAR satellite built in a Public Private Partnership (PPP) between the German Aerospace Center (DLR) and Astrium GmbH. The main payload of TerraSAR-X is an SAR instrument to acquire high quality radar images of the Earth's surface.

The SAR instrument comprises an active phased array antenna which allows flexible beam forming. The antenna with its 4.8m length and 0.7m width consists of 384 subarrays composed by two slotted wave-guides, one for each polarisation (horizontal and vertical). These are arranged in 12 panels in azimuth direction (columns) each composed of 32 subarrays (rows) [3]. The nominal antenna pointing in elevation is 33.8° away from nadir. Right and left looking acquisition is realised by satellite roll manoeuvres. Each individual subarray is driven by a Transmit/Receive Module (TRM) adjustable in amplitude and phase by applying complex excitation coefficients. This enables beam steering and adaptive beam forming in both azimuth and elevation direction. More than 12 000 different beams can be commanded for the multitude of standard acquisition modes possible on TerraSAR-X. These are the nominal Stripmap, ScanSAR or Spotlight modes as well as several experimental modes like quad-polarisation mode, wide band operation, or along-track interferometry.

3. Antenna Model Approach

The Antenna Model is used to compute this huge amount of antenna patterns needed by the processing system to correct the impact of the antenna characteristics on the radar images. In elevation, the antenna patterns are then used for

direct image correction over range. The azimuth pattern is represented in the Doppler spectrum and hence needed for correct Doppler estimation.

The optimisation of the beam excitation coefficients of the antenna array is a second important task that can be performed with the Antenna Model. These excitation coefficients are complex values which are applied on the TRMs in order to steer the beam in the desired direction as well as to create an antenna pattern with an optimised gain, a desired pattern slope or suppressed side-lobes. With the optimisation process, an optimum set of excitation coefficients and hence an optimum performance for the full performance beams in terms of Noise Equivalent Sigma Zero (NESZ) and Total Ambiguity Ratio (TAR) are achieved.

Also, in case of contingences like TRM degradation or failures during the operational phase resulting in a degradation of the antenna patterns, the antenna excitation coefficients can be re-optimized to ensure the high performance.

The development and the establishment of an Antenna Model approach were driven by three main requirements.

- (i) The great number of more than 12 000 different beams to be calibrated.
- (ii) The tight accuracy requirement of an overall radiometric accuracy of better than 1.0 dB (1 sigma). This value was derived from the radiometric error budget calculated prior to the development of TerraSAR-X. All radiometric errors affecting the SAR acquisition were considered in this error budget. The main contributions are the accuracy of the internal calibration, the error of the antenna model, the mechanical and electrical antenna pattern variation, processing errors, the accuracy and stability of the measurement targets and atmospheric variations. In this budget, the requirement for the accuracy of the Antenna Model is to be better than ± 0.2 dB (peak-to-peak) for reproducing the pattern shape and predicting the gain offset between different beams. Another important reason for this number is that a deviation of more than 0.2 dB can visibly be recognized in overlaid or adjacent SAR images.
- (iii) The short duration of the commissioning phase of less than six months.

To ensure these requirements, several steps were realized.

- (i) As much effort as possible was moved from inorbit tasks to onground duties. This includes the accurate measurement of the embedded subarray patterns as well as the validation of the model onground before launch. The task was successfully performed by Astrium and DLR, and is described in more detail in Section 5.
- (ii) Different inorbit calibration techniques for Antenna Model verification were used. Therefore, inorbit verification was performed during the commissioning phase in the first months after launch.

The verification was divided into three main tasks:

- (a) measurements across the rainforest to verify the elevation pattern shape,
- (b) the use of ground receivers to verify the azimuth pattern and,
- (c) ScanSAR measurements over rainforest and over ground receivers to verify the prediction of the gain offset between the beams. This task is described in detail in Section 4.

- (iii) To ensure a short commissioning phase, the verified Antenna Model supported the absolute radiometric calibration which is the determination of the absolute calibration factor. With a verified Antenna Model, the absolute calibration factor of only one beam would have to be determined, which minimizes the effort for the absolute radiometric calibration significantly. A description of the absolute radiometric calibration would exceed the content of this paper and the interested reader is referred to [4, 5].

The described approach is summarized in Figure 2. Starting from the Antenna Model design, the model is validated onground first. After launch, the verification of the model is performed over distributed targets like rainforest and point targets like ground receivers. Hereby the actual state of the instrument and the TRMs is monitored simultaneously by applying the Internal Calibration facility and the so-called PN gating method in the instrument.

The Internal Calibration measures the actual state of the transmit and receive path within the radar instrument, which afterwards can be corrected during image processing. Therefore, it is performed at every beginning and end of an acquisition.

The PN-Gating method [6] is a novel approach to monitor the actual state of each individual TRM. It was demonstrated on TerraSAR-X for the first time inorbit. In contrast to the module stepping approach applied on Envisat/ASAR where each TRM was measured sequentially, the TRMs are characterised during quasinominal operation that means with all TRMs enabled. Hence, the TRMs are driven under most realistic conditions while they are characterised. This is realised by applying orthogonal PN- or Walsh-codes to the TRMs. The code consists of up to 512 code chips with one individual code at each TRM enabling the extraction of each individual TRM. The PN-Gating method is applied regularly to detect changes, drifts or failing TRMs. If the changes exceed a given limit, the antenna patterns have to be recalculated or even re-optimised.

By this Antenna Model sufficiently validated onground and verified by a limited number of a few selected beams really measured in flight, the thousands of reference patterns can be accurately derived.

4. Antenna Model Design

The Antenna Model itself mathematically calculates radiation patterns by the superposition of four inputs:

- (i) radiation patterns measured onground from the elements of the antenna, so-called embedded subarray patterns,
- (ii) beam excitation coefficients (amplitude and phase) of each individual transmit/receiver module (TRM),
- (iii) exact geometrical dimensions of the array antenna including the distances between the subarrays
- (iv) actual state of the SAR instrument like drifting and/or failed individual TRMs.

For active phased array antennas, the radiated pattern F_{Beam} is calculated by [3, 7]:

$$\begin{aligned} \bar{F}_{\text{Beam}}(\varepsilon, \alpha) = \sum_{m=0}^{M-1} \sum_{n=0}^{N-1} & \left(\bar{C}_{\text{SA},mn}(\varepsilon, \alpha) \cdot a_{mn} \cdot E_{\text{SA},mn} \right. \\ & \cdot e^{jksine \cos \alpha (-(N-1)/2+n)\Delta y} \\ & \left. \cdot e^{jk \cos \varepsilon \sin \alpha (-(M-1)/2+m)\Delta x} \right) \end{aligned} \quad (1)$$

with the desired elevation and azimuth angles ε and α , the amount of subarrays in N rows and M columns, the inter-subarray distances Δx (columns) and Δy (rows). The wave number k includes the centre frequency 9.65 GHz of the system by the relation of $k = 2\pi/\lambda$.

The embedded subarray patterns C_{SA} comprise the real measured radiation characteristics of the individual subarray elements. Therefore, the subarrays are embedded into the whole antenna and have to be given for each row, column, elevation and azimuth angle. The embedded pattern of one subarray mounted in the array antenna describes the radiation characteristic of this subarray. In this way, mutual coupling effects are included by the measurements. The antenna has a quite broad frequency bandwidth of 300 MHz, so that mismatch and gain are smooth over the frequency bandwidth. Therefore, only the embedded patterns at centre frequency are incorporated in the Antenna Model.

As input for the antenna model, all embedded subarrays of one panel were measured. The patterns of whole panels are very similar to each other, even for the ones at the edges. The measurement results showed that it is possible to use only the embedded patterns of one panel and substitute the others using their measured amplitude and phase offsets. These embedded patterns have to be known with a very high accuracy, as they are one main input of the model.

The commanded complex excitation coefficients are given by a . In case of TerraSAR-X, these coefficients are provided in form of amplitude and phase values row and column-wise. For each commandable beam, one set of values is put in a common table. This table is available onboard the satellite and can be updated if necessary, for example, in case of contingencies, as the onboard computer uses the table for each acquisition.

Finally, the error matrix E_{SA} describes drifting or failed antenna elements which are determined via the PN-Gating method using orthogonal code sequences applied to the TRMs of the instrument as described in Section 3.

To obtain the complete two-way antenna patterns, the equation is evaluated for transmit and receive individually.

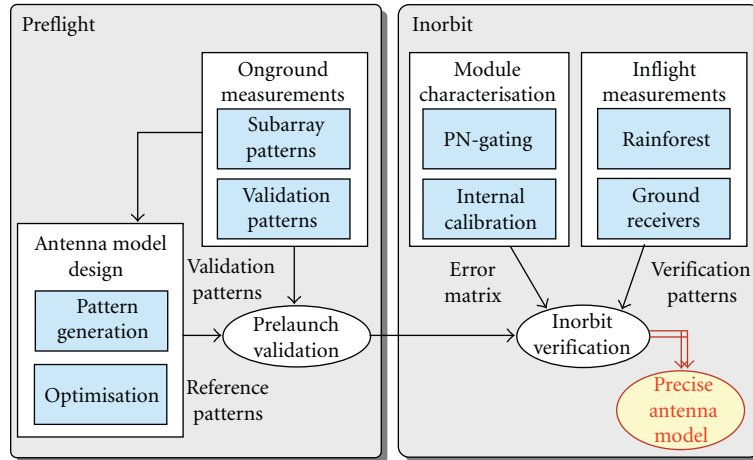


FIGURE 2: Antenna model verification approach.

Both, the excitation laws and the error matrix are different for transmit and receive. In case of the excitation coefficients, the differentiation allows greater flexibility for beam steering. On the side of the error matrix it is mandatory as the paths through the TRM are different, for transmit via the high power amplifier and in receive through the low noise amplifier.

For the TerraSAR-X SAR applications, cuts of the pattern in elevation (at $\alpha = 0$ deg) and azimuth ($\varepsilon = 0$ deg) are derived. These are saved into interface tables to be applied for image correction in the SAR processor.

The accuracy of the antenna model is on the one hand mainly determined by the accurately measured embedded subarray patterns and on the other hand by the stability of the instrument. This includes the accurate measurement of the error matrix via PN-Gating as well as the correction of internal variations by the Internal Calibration. To prove the accuracy, sensitive inorbit measurement methods are required as described below.

5. Prelaunch Validation

Knowing the design of the Antenna Model, at first an onground validation has been performed. The onground characterisation was realised in two stages. In a first step, the antenna was accurately measured in the Planar Near Field Scanner at and from Astrium GmbH, Germany. In the second step, the correct application of the conventions and input parameters was verified.

For the first step, two kinds of antenna patterns were determined in the Planar Near Field Scanner:

The embedded subarray patterns are required as a direct input into the Antenna Model. For comparison, the patterns of one complete panels or leaves (one third of the whole antenna) was measured.

Due to the dimensions of the whole antenna (4.8 m \times 0.7 m) and to enable the use of the available measurement chamber, the prelaunch validation was performed only up to

the stage of one leaf, for example, one third of the antenna or four panels in a column. To ensure a valid model even for the complete antenna, the accuracy of the antenna model was tracked through the whole built process of the antenna from individual subarray patterns over the patterns of one panel up to the patterns of the three leaves.

Of course, the measurement in an anechoic chamber is not exactly the same as if the antenna is mounted on the satellite. However, as there are no parts of the satellite structure rising into the near field of the SAR Antenna, the effects of the satellite and its mounting structure were expected to be small. On the other hand, the measurements on satellite level in orbit were expected to be better than the leaf-level measurements as three times more TRMs on the complete antenna provide better statistical distribution for the variation of the TRMs.

For the prelaunch validation, all patterns were measured for both polarisation and at five frequencies. After the measurement, the obtained near field results were transformed into the far field using a Fourier transform algorithm. Then, the antenna patterns generated with the Antenna Model using the embedded patterns were compared to the measured patterns of the complete panel and leaf, respectively. The results of this validation on leaf level exemplary for the centre leaf are depicted in Table 1. It can be seen that the deviation fulfils the required limit of ± 0.2 dB for all beams [8].

After the successful onground validation of the Antenna Model, also the correct application of the conventions in the antenna control unit was verified on satellite level. Here the complete antenna was mounted and connected to the satellite system. Especially the correct handling of the underlying inputs like antenna excitation coefficients, the correct numbering of the antenna elements and the correct steering angle application were successfully tested. Also, the correct update of all changeable antenna parameters like TRM enabling/disabling or update of the excitation coefficients table was verified.

The preflight validation proved a very stable and accurate instrument, which now had to be verified in orbit.

TABLE 1: The results of the prelaunch validation in elevation.

Beam	HH	VV
strip_003	+0.05 dB	+0.15 dB
strip_004	+0.10 dB	+0.08 dB
strip_005	+0.03 dB	+0.14 dB
strip_006	+0.08 dB	+0.08 dB
strip_007	+0.13 dB	+0.04 dB
strip_008	-0.06 dB	-0.15 dB
strip_009	-0.12 dB	+0.10 dB
strip_010	+0.10 dB	+0.17 dB
strip_011	+0.08 dB	+0.09 dB
strip_012	+0.09 dB	+0.05 dB
strip_013	+0.02 dB	+0.07 dB
strip_014	+0.11 dB	+0.08 dB

6. Inorbit Verification

The inorbit verification of the Antenna Model was performed in the commissioning phase during the first six month after launch. In contrast to the onground measurements, also the influence of the complete satellite structure is covered for azimuth and elevation patterns.

6.1. Antenna Model Verification in Elevation. To verify the Antenna Model in elevation, the simulated relative antenna patterns are compared with measured antenna patterns. The estimates are measured from SAR images acquired over rainforest in the Amazon basin, Brazil. The Amazon rainforest is a homogeneous scatterer [9] (see Figure 3(a)) and the pattern shape is clearly visible in the uncorrected SAR image data (compare Figure 1).

In the processing chain, the accurate position and geometry of the acquisition are determined and annotated after azimuth and range compressions. Then the antenna patterns mapped in the image data are corrected with the available modelled reference antenna patterns [10].

Thus, for pattern estimation, this pattern correction has to be reversed with the used reference patterns to obtain the original impact of the antenna characteristics on the image. Then, the image is freed from disturbances like rivers using an automatic masking algorithm. The radar image is denoted in beta nought β_0 where the backscatter depends on the incidence angle θ . For the comparison however, the gamma nought γ_0 has to be derived via sigma nought σ_0 using the formula [11]:

$$\gamma^0 = \frac{\sigma^0}{\cos(\theta)} = \beta^0 \cdot \tan(\theta). \quad (2)$$

Finally all azimuth lines are summed up and each pixel position is transformed as function of elevation angle resulting in a so-called Gamma Profile which is a vector of the mean antenna pattern over elevation angle.

For the Antenna Model verification, nominal Stripmap and ScanSAR acquisition were evaluated. The acquisitions had a bandwidth of 150 MHz and a duty cycle of 18%.

TABLE 2: Results of the elevation antenna model verification.

Beam	Polarisation	Max. deviation
strip_002	HH	+0.17 dB
strip_002	VV	-0.19 dB
strip_002	HV	+0.10 dB
strip_002	VH	-0.18 dB
strip_007	HH	+0.10 dB
strip_007	VV	+0.17 dB
strip_007	HV	+0.13 dB
strip_007	VH	+0.19 dB
strip_013	HH	+0.08 dB
strip_013	VV	+0.17 dB

As said before, to minimize the inorbit calibration effort, only few beams were selected for verification. These beams were in a further step also used for absolute calibration, that is, for the determination and verification of the absolute calibration factor.

An exemplary result of the Antenna Model in Elevation verification is depicted in Figure 3(b). The noisy ripple (in green) is the gamma profile, which now can be compared to the modelled reference pattern depicted in red.

The results show an excellent accordance between the simulated antenna pattern and the measured gamma profiles. This can be seen in Figure 3(c), where the deviation between the reference antenna pattern and the estimated pattern is depicted for the exemplary beam. Additionally, by fitting a blue curve into the profile, a noise-free picture is obtained.

Table 2 summarizes the measurements of the selected beams as well as the maximal deviation between measurement and reference patterns. Several other beams have been measured as well, showing similar performance. Hence, the deviation and consequently the accuracy of the Antenna Model are within ± 0.2 dB (peak-to-peak) for the pattern shape.

6.2. Antenna Model Verification in Azimuth. In the next step, the antenna model has to be verified also in flight direction. For this purpose, using ground receivers, the antenna can be determined during an overflight. As only the transmit-patterns can be measured with the ground receivers, the accuracy requirement with ± 0.1 dB (peak-to-peak) is half the one as for the two-way patterns. With ground receivers it is furthermore possible to verify the side-lobes being not possible over rainforest.

The verification of the antenna pattern in azimuth direction was performed for transmit pattern using the DLR ground receivers [12]. These receivers record the amplitude of the pulses transmitted by the SAR antenna as function of time and due to the flight movement, a cut through the antenna pattern is recorded. Transformed to the antenna azimuth angles and corrected by position information, the azimuth antenna pattern is obtained and can be compared to the modelled pattern. The measurements were performed for patterns over the whole specified angular range of the SAR

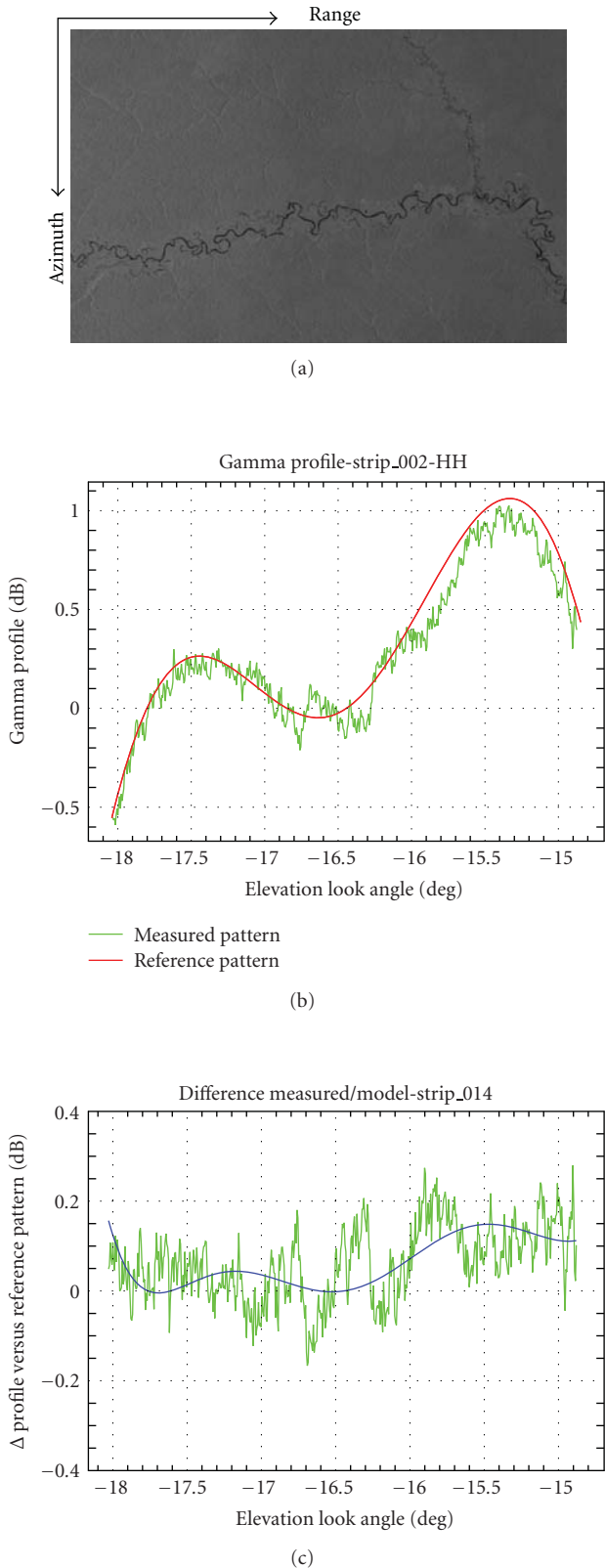


FIGURE 3: (a) Amazon rain forest scene used for antenna model verification. (b) Gamma profile of the antenna pattern extracted from rainforest (green curve) and reference pattern (red line) for comparison. (c) Deviation between gamma profile and reference pattern (green curve) and fit through the deviation (blue line).

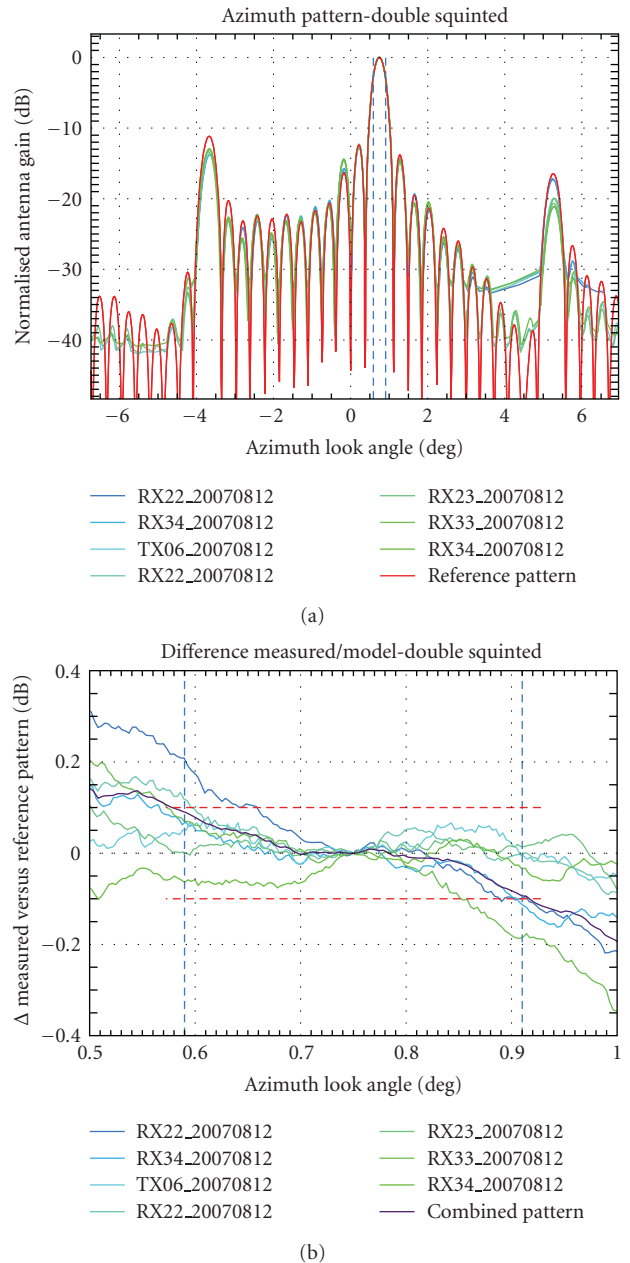


FIGURE 4: (a) Transmit patterns compared to a reference pattern, blue to green: measured profiles, red: reference patterns derived by the antenna model. (b) Deviation between measured and reference pattern.

antenna, that is, for low, mid and high incidence angles. Furthermore ground receivers were placed across each swath being measured at near, mid and far range.

Figure 4(a) shows the special case of a double squinted beam nominally only needed for high resolution spotlight acquisitions. In this case a beam steered to angles of $+0.75^\circ$ in azimuth and -16.5° in elevation which is at the specified limits for antenna steering. This beam was specially commanded to be fixed, as in nominal spotlight mode the beam would switch up to 123 times during one acquisition.

TABLE 3: Results of the azimuth antenna model verification.

Beam	Transmit polarisation	Max. deviation
strip_002	H	+0.09 dB
strip_002	V	+0.09 dB
strip_007	H	-0.08 dB
strip_007	V	-0.07 dB
strip_013	H	-0.07 dB
strip_013	V	-0.08 dB

The antenna patterns measured by ground receivers during one pass are depicted in green to blue and the corresponding reference pattern derived by the model is depicted in red. The resulting deviation between these measurements and the reference pattern are shown in Figure 4(b) by the purple line, whereby all measurements derived from the ground receiver deployed during one pass were averaged in order to reduce the error contribution of the ground receiver.

Table 3 summarizes the results for the selected beams of the azimuth verification. As for elevation, the Antenna Model verification shows extraordinary results, that is, the resulting deviation within the main beam and consequently the accuracy of the model is within the required ± 0.1 dB.

6.3. Verification of the Beam-to-Beam Gain Prediction. Besides the verification of the pattern shape, the capability of the Antenna Model to predict the gain offset between different beams is of great importance. First, this is required for the ScanSAR processing, where four different beams with different antenna gains are acquired, corrected with their corresponding pattern and combined into one image. Second, with an appropriate gain prediction, only one absolute calibration factor can be derived for the complete system and not all beams have to be measured during the absolute calibration [5].

The beam-to-beam gain prediction is verified evaluating ScanSAR data. In ScanSAR operation, the beam is switched sequentially from burst to burst between a set of four neighbouring swaths to get a broader swath width than for normal Stripmap acquisitions. By generating the unnormalised gamma profile for each of the four swaths, the relative gain deviation can be determined.

In order to obtain the beam-to-beam gain prediction over a wide range of elevation angle including the full performance range (between -15 deg and $+9$ deg antenna look angle), different sets of ScanSAR acquisitions were combined. The result is shown in Figure 5(a). Indeed, the images were acquired over different parts of the rainforest caused by switching the beam in ScanSAR operation. Thus, each illuminated part of the rainforest has different vegetation and consequently different backscatter. Consequently, each complete set of four beams was connected to its predecessor set within the overlapping region.

Figure 5(b) shows the deviation between the profiles measured and the corresponding reference pattern. Figure 5(c) emphasizes only the deviation between the overlapping regions of two neighbouring swaths. However, the

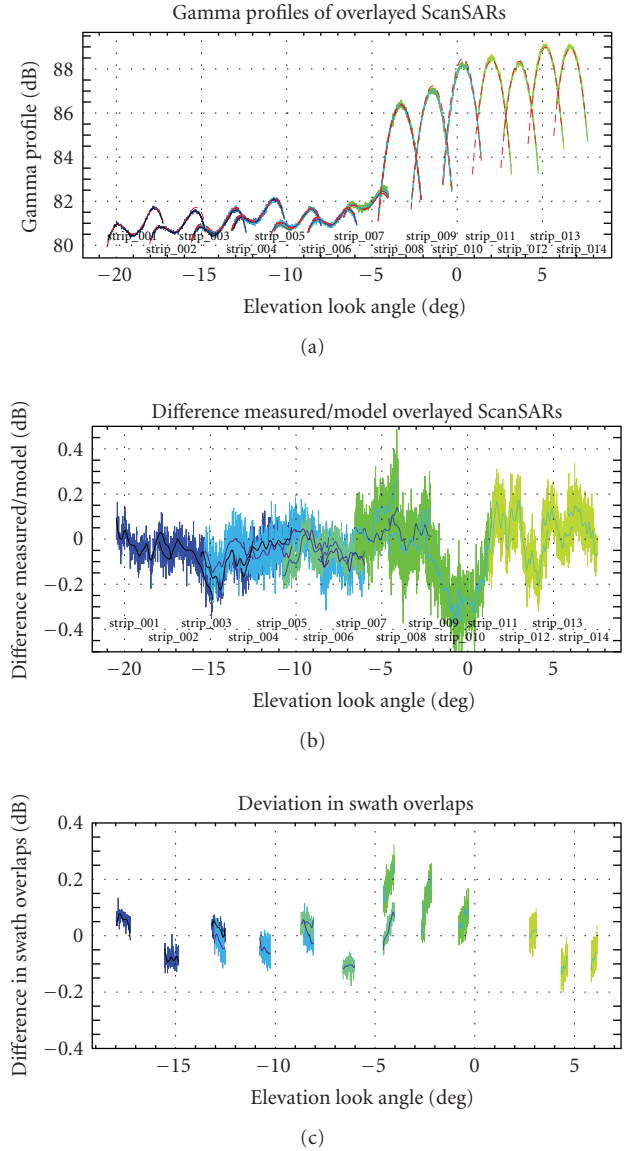


FIGURE 5: (a) Verification of the beam-to-beam gain prediction using ScanSAR images, blue to green: measured gamma profiles, red: reference patterns derived by the antenna model. (b) Deviation between gamma profile and the reference patterns remaining within the range of ± 0.2 dB. (c) Deviation within the overlapping areas of Figure 5(b).

results again have an excellent accuracy of below ± 0.2 dB peak-to-peak over the whole angular range and no drift is visible. The slight deviation at about 0 deg elevation angle in Figure 5(b) results from bad weather conditions disturbing the acquisition. Because illuminating an area of about $560\,000$ km² across the rainforest, nearly twice the area of Germany, it is natural to find individual regions with heavy rainfall rates, especially across the rainforest.

A second method to verify the beam-to-beam gain prediction was performed by deploying ground receivers in the overlapping regions of two neighbouring swaths and recording the transmit azimuth patterns. For this purpose

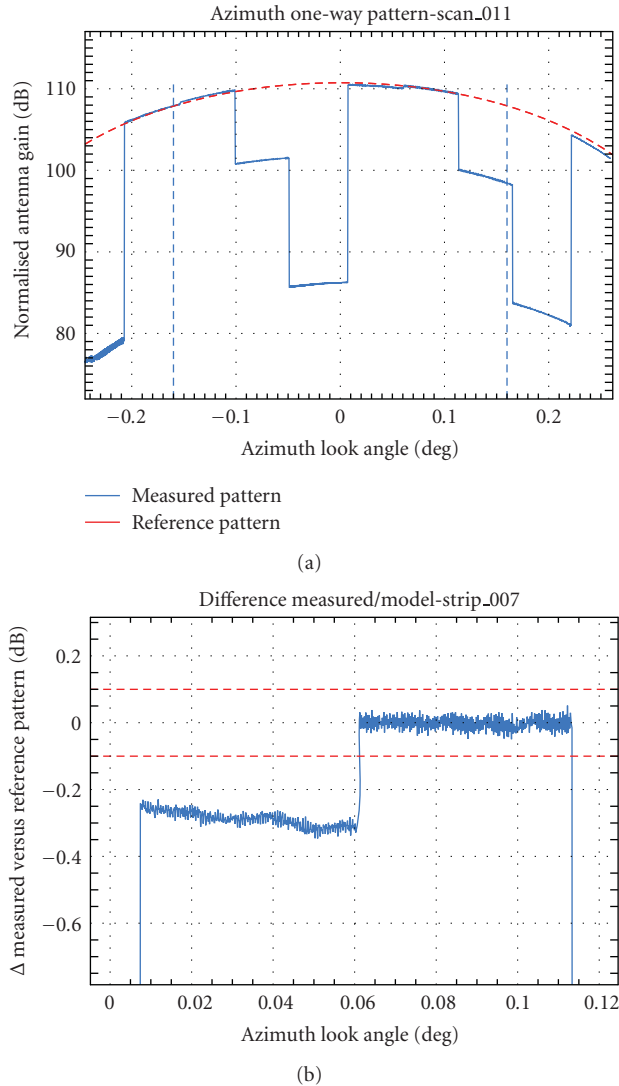


FIGURE 6: (a) Verification of the beam-to-beam-gain prediction using ground receivers. (b) Zoom into switching region between two swaths.

the instrument was operated again in ScanSAR mode and as shown in Figure 6(a) the switching of the instrument between the four beams during one pass is clearly visible by the received pulses. The deviation between the overlapping beams can be likewise compared with the Antenna Model. And even here, that is, measuring one-way patterns by ground receivers and the interrelated demand on higher accuracy (see above), the maximum deviation is within the required ± 0.1 dB peak-peak.

With the properly working Antenna Model, the absolute calibration factor required for deriving the radar backscatter coefficient of any target within an image, does not have to be measured for all relevant beams. It is measured only for one beam and verified for the same representative beams as used for the antenna model. By this approach it is possible to shorten the time and the effort extremely for the absolute radiometric calibration performed during the

commissioning phase of an SAR system. In case of TerraSAR-X with the verified Antenna Model, it was sufficient to measure only 3 of the 12 000 different beams: one with low, one with mid and one with high incidence angle. The measurement results show an absolute radiometric accuracy of 0.31 dB (1-sigma) [5].

7. Conclusion

The TerraSAR-X Antenna Model is utilised for generating the reference antenna patterns for processing and for beam optimisation. A high accuracy of the Antenna Model is achieved by accurately onground measured embedded sub-array patterns as well as a highly accurate internal calibration of the instrument. To ensure the specified product quality, its accuracy has been verified in orbit during the commissioning phase following the TerraSAR-X launch in June 2007. The results show the excellent accuracy of both, the whole TerraSAR-X system itself and the Antenna Model. The Antenna Model was verified on providing the reference antenna patterns with an accuracy of better than ± 0.2 dB (peak-to-peak) for image correction in elevation using Amazon rainforest. In azimuth, where transmit patterns were determined with ground receivers, an accuracy of ± 0.1 dB (peak-to-peak) was achieved. The prediction of the beam-to-beam gain offset could be verified with ± 0.2 dB (peak-to-peak) accuracy enabling accurate image referencing and a short commissioning phase.

The excellent results of TerraSAR-X show that the Antenna Model approach was successfully applied and the approach should be used for future system.

Acknowledgments

The authors would like to thank the whole TerraSAR-X team and especially to the HR calibration team for supporting the Antenna Model verification with an uncountable number of calibration campaigns and their unwearied effort at every possible weather and environmental conditions. Furthermore a special thank to the Astrium GmbH for performing the highly accurate embedded antenna pattern measurements and onground validation and developing the TerraSAR-X as such an highly accurate SAR system.

References

- [1] M. Zink and B. Rosich, "Antenna elevation pattern estimation from rain forest acquisitions," in *Proceedings of the Envisat Calibration Review (ECR '02)*, European Space Agency, Noordwijk, The Netherlands, September 2002.
- [2] S. Buckreuss, R. Werninghaus, and W. Pitz, "The German satellite mission TerraSAR-X," in *Proceedings of IEEE International Radar Conference (RADAR '08)*, pp. 1–5, Rome, Italy, May 2008.
- [3] B. Grafmüller, A. Herschlein, and C. Fischer, "The TerraSAR-X antenna system," in *Proceedings of IEEE International Radar Conference (RADAR '05)*, pp. 222–225, Washington, DC, USA, May 2005.

- [4] M. Schwerdt, D. Hounam, J. L. Álvarez-Pérez, and T. Molkenthin, "The calibration concept of TerraSAR-X: a multiple-mode, high-resolution SAR," *Canadian Journal of Remote Sensing*, vol. 31, no. 1, pp. 30–36, 2005.
- [5] M. Schwerdt, B. Bräutigam, M. Bachmann, B. Döring, D. Schrank, and J. H. Gonzalez, "Final results of the efficient TerraSAR-X calibration method," in *Proceedings of IEEE Radar Conference (RADAR '08)*, pp. 1–6, Rome, Italy, May 2008.
- [6] B. Bräutigam, M. Schwerdt, M. Bachmann, and M. Stangl, "Individual T/R module characterisation of the TerraSAR-X active phased array antenna by calibration pulse sequences with orthogonal codes," in *Proceedings of the 27th IEEE International Geoscience and Remote Sensing Symposium (IGARSS '07)*, pp. 5202–5205, Barcelona, Spain, June 2007.
- [7] C. A. Balanis, *Antenna Theory: Analysis and Design*, John Wiley & Sons, New York, NY, USA, 2nd edition, 1997.
- [8] M. Bachmann, M. Schwerdt, B. Bräutigam, B. Grafmüller, A. Herschlein, and J. L. Álvarez-Pérez, "The TerraSAR-X antenna model approach," in *Proceedings of the 2nd International ITG Conference on Antennas (INICA '07)*, pp. 139–142, Munich, Germany, March 2007.
- [9] A. P. Luscombe and A. Thompson, "RADARSAT-2 calibration: proposed targets and techniques," in *Proceedings of IEEE International Geoscience and Remote Sensing Symposium (IGARSS '01)*, vol. 1, pp. 496–498, Sydney, Australia, July 2001.
- [10] J. L. Álvarez-Pérez, M. Schwerdt, and M. Bachmann, "TerraSAR-X antenna pattern estimation by a complex treatment of rain forest measurements," in *Proceedings of IEEE International Geoscience and Remote Sensing Symposium (IGARSS '06)*, pp. 3857–3860, Denver, Colo, USA, July-August 2006.
- [11] J. E. Laycock and H. Laur, "ERS-1 SAR antenna pattern estimation," ES-TN-DPE-OM-JL01, iss. 1, rev. 1, September 1994, http://earth.esa.int/ers/instruments/sar/sar_AP_est.
- [12] B. Döring, M. Schwerdt, and R. Bauer, "TerraSAR-X calibration ground equipment," in *Proceedings of the Wave Propagation in Communication, Microwave Systems and Navigation (WFMN '07)*, pp. 91–96, Chemnitz, Germany, July 2007.

Research Article

Potential Benefits of Dynamic Beam Synthesis to Mobile Satellite Communication, Using the Inmarsat 4 Antenna Architecture as a Test Example

R. F. E. Guy

Department of Sensor Systems, BAE Systems ATC, West Hanningfield Road, Great Baddow, Chelmsford CM2 8HN, UK

Correspondence should be addressed to R. F. E. Guy, ron.guy@baesystems.com

Received 22 September 2008; Accepted 17 March 2009

Recommended by Giovanni Toso

Present mobile satellite communication systems use large antennas to provide multiple high-gain beams. Each beam covers a fixed geographic cell on the earth. Spatial frequency reuse is provided by synthesising beams with low-power levels over all cells operating at the same frequency. The performance needs for future systems are steadily increasing, leading to higher-gain requirements, which are met by using larger antennas with narrower beams. So the antenna pointing errors become a significant loss factor. An alternative approach is to abandon the use of fixed beams and dynamically synthesise the beams to optimise the antenna performance in real time. This both increases user gain and lowers cofrequency interference whilst also reducing the effects of pointing errors. Simulations, using the Inmarsat 4 antenna architecture as a test example, show that the spatial isolation performance can be significantly improved by using Dynamic Beam Synthesis.

Copyright © 2009 R. F. E. Guy. This is an open access article distributed under the Creative Commons Attribution License, which permits unrestricted use, distribution, and reproduction in any medium, provided the original work is properly cited.

1. Introduction

The fourth generation of Inmarsat satellites provides a good example of an advanced high-capacity, high-gain fixed beam/cell mobile communication system [1]. The L-band Mobile satellite system utilises a 9 m deployable reflector fed via a 120-element feed array. A digital signal processor (DSP) is used to produce many different beam types that cover the earth and provide different user services. The most demanding of these is the Personal Mobile Communication (PMC) service. This uses ~200 high-gain narrow spot beams to cover the earth. The beams provide spatial frequency reuse; so cocoloured beams are synthesised to have a high degree of isolation between them. The earth is covered by contiguous cells (nominally hexagonal, as viewed from the satellite) that are fixed with respect to geographic locations on the earth. The beams are changed throughout the day so that they remain aligned to these fixed geographic cells even though the satellite orbit is slightly inclined. Users are assigned to a beam that aligns with the geographic cell they occupy.

However, performance requirements for mobile satellite communication systems are steadily increasing, both in terms of higher antenna gain and frequency reuse capacity. In order to provide the edge of cell edge of coverage (EOC) directivity and the beam roll-off rate, required to achieve interbeam isolation, the beam size will need to decrease. So, many more beam/cells will be required to cover a given geographical area. This will lead to far larger reflectors and feed arrays with many more radiating elements. For conventional fixed beam/cell systems, the antenna pointing error is likely to become a dominant loss factor in the link budget. An alternative is to abandon the fixed beam/cell scheme and form beams that are optimised to individual user locations. This paper uses simulations of a “dynamic beam synthesis” (DBS) process to highlight the potential benefits of this approach.

2. Fixed Beam System

The Inmarsat 4 type of antenna system architecture is used as a baseline to compare the fixed beam/cell system to the

TABLE 1

Parameter	Value
Transmit	1525–1559 MHz
Receive	1626.5–1660.5 MHz
Polarisation	RHCP
Number of antennas	Single Tx/Rx array fed reflector
Antenna type	Offset-fed paraboloidal reflector
Diameter	9 metres
F/D	0.53
Feed	120 helical elements, array diameter = 2.2 metres
Feed position	In front of focal plane
Beamformer	Digital Signal Processor, (DSP) with $15 \times 8 \times 8$ multiport amplifier (MPA*) blocks on transmit
Beam alignment	Beams aligned with fixed geographic cells
Beam reconfiguration	Beams reconfigured throughout the day to compensate for orbit inclination
Frequency reuse	Spatial diversity provides frequency reuse between beams

*The MPA blocks are used to distribute power more uniformly over the transmit amplifiers and hence increase their efficiency.

alternative of dynamically synthesising the beams making use of the individual user locations. The following outlines the antenna system.

2.1. Frequency Reuse. Spatial frequency reuse allocates adjacent beams different frequencies but reuses the same frequency in more distant beams. To do this efficiently requires the use of a regular hexagonal grid of beams. Figure 1 shows 3, 4, and 7 colour schemes. Each colour represents a different frequency. The colouring principal can be extended to higher-colour schemes such as 9, 12, 13, 16, and 19. An interesting property is that the distance between common colour beam centres is the square root of the number of colours. This relationship also holds for a square lattice.

A typical PMC beamset, which was designed for 7 colour frequency reuse, is shown in Figure 2. This has 228 contiguous, high-gain beams (~ 38 dBi at edge of coverage). To achieve the isolation requirement the peak to edge gain variation of the beams is ~ 3 dB.

2.2. Future Trends. The trend for next generation satellites will be to increase the gain requirements. A 6 dB increase implies doubling the reflector diameter and quadrupling the number of feeds. There will also be pressure to increase the frequency reuse factor. Lowering the frequency colour scheme from 7 to 4 could require the peak to edge gain delta to increase by a further 1 to 2 dB. The exact figure is dependent on the isolation requirement.

2.3. Limitations of a Fixed Beam System. A fixed beam system is limited by the following factors.

- (i) Cells fixed at specific geographic location.
- (ii) Pointing errors are accounted for by expanding the geographic cells by the pointing error. This degrades both EOC gain and isolation.

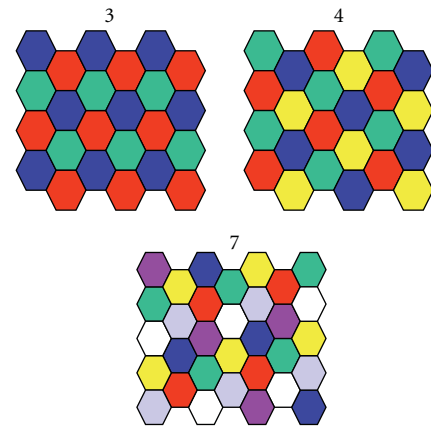


FIGURE 1: Frequency reuse schemes with 3, 4, and 7 colours.

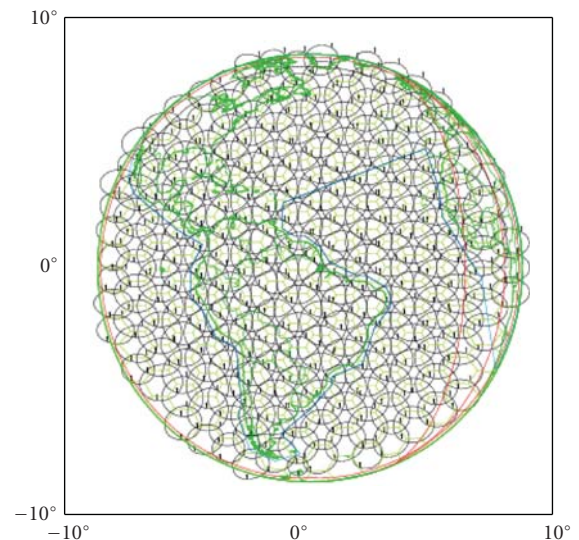


FIGURE 2: Example fixed beamset.

- (iii) Orbit inclination distorts the fixed cell grid, requiring resynthesis of the whole beamset and the use of new weights many times a day.
- (iv) The G/T figure of merit for the satellite is limited by what can be achieved at the worst point at the edge of cell grid, when distorted by the inclination and expanded by the pointing error. This is further reduced by other effects such as vector weight errors.
- (v) The EIRP figure of merit for the satellite is limited by the same effects.

2.4. *Consequences of Pointing Errors.* The following points highlight the effect of pointing error in a fixed beam system.

- (i) For the example beamset using a 7-colour reuse scheme, 0.1° pointing error gives ~ 0.6 dB loss of gain at EOC.
- (ii) For a scaled system with 6 dB more gain, 0.1° pointing error gives ~ 1.2 dB loss.
- (iii) For a scaled system with 6 dB more gain, using a 4-colour scheme, 0.1° pointing error gives ~ 2 dB loss.

Assuming the pointing error is not significantly reduced for the larger reflector diameters, then as the gain and frequency reuse factor is increased, still further, the pointing error will start to dominate the loss budget.

2.5. *Implications of Using a Fixed Beam System.* If a fixed beam system is used to meet future gain and isolation demands, the cell size must reduce, and both the reflector diameter and number of feed elements must increase. A 6 dB gain improvement requires doubling the reflector diameter and quadrupling the number of feeds.

If the reuse scheme falls from 7 to 4 colour, then the additional losses increase by ~ 3 dB requiring a ~ 9 dB improvement, which implies about three times the diameter reflector and eight times as many elements.

3. Dynamic Beam System

In a dynamic beam system the beams are not fixed. The beams are synthesised in “real time,” using the known user locations to both maximise individual user gain and minimise interference from other cofrequency users.

3.1. *The Synthesis Process.* The following outlines the dynamic beam synthesis process.

- (1) A fixed geographic cell lattice is used to assign frequencies to users, for example, using 7-colour reuse.
- (2) At any one time there are likely to be a number of users assigned the same frequency.
- (3) In any one cell only one user has the same frequency.
- (4) A new user requests a channel via a global beam, giving their location, (e.g., provided by a GPS

receiver). Their geographic location is used to assign an available channel frequency for that user cell.

- (5) All other users with the same frequency are identified.
- (6) The beams associated with every one of these users are resynthesised every time a new user is assigned an existing frequency.
- (7) Each beam is resynthesised to maximise power at the user location and minimise power at the other user locations.
- (8) The synthesis expands the user locations by the pointing error to provide coverage and isolation in the presence of pointing errors.
- (9) The pointing error allowance would be further expanded to provide extra margin to cope with vector weight errors, and satellite inclination change.
- (10) The weights would be resynthesised and updated on a periodic basis to cope with gross inclination changes.

3.2. *Simulation of the DBS Process.* The simulation program, MAXIM, has been written to simulate the dynamic beam synthesis process. It performs both the synthesis and the analysis to produce plots of directivity and isolation performance. The program works in the following order.

- (1) Reads secondary array fed reflector (AFR) element patterns.
- (2) Reads cell lattice coordinates and reuse colour scheme.
- (3) Chooses a far-field grid point.
- (4) Finds associated cell colour and finds all cocoloured cell coordinates.
- (5) Randomly assigns “N” other users in “N” different cocoloured cells at random points in each cell.
- (6) Synthesises ideal weights for each cocoloured user, using the inverse of the covariance matrix [2].
- (7) Calculates beams from the synthesised weights (this step can include vector weight errors if requested).
- (8) Calculates the directivity of the user with pointing errors.
- (9) Calculates the isolation of the user with pointing errors.
- (10) Repeats simulation “M” times and selects requested percentage confidence level performances.
- (11) Repeats simulation steps (3)–(10) for all grid points.
- (12) Outputs results.

3.3. *Simulation Results.* The DBS beams were synthesised to maximise power over the user and minimise power over cocoloured users. To illustrate this, the following example is used. A user is at $(0.08^\circ, 0.08^\circ)$, and seven other cocoloured user locations are chosen at random. The closest user is in the first cocoloured ring of cells surrounding the coverage

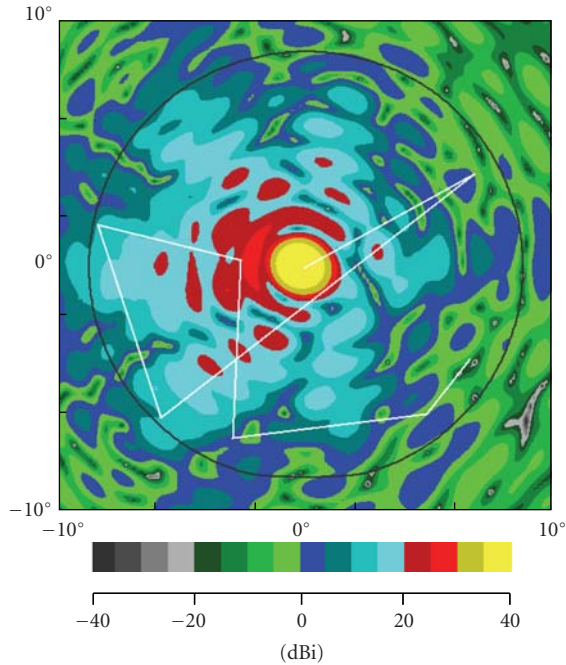


FIGURE 3: Beam prior to DBS.

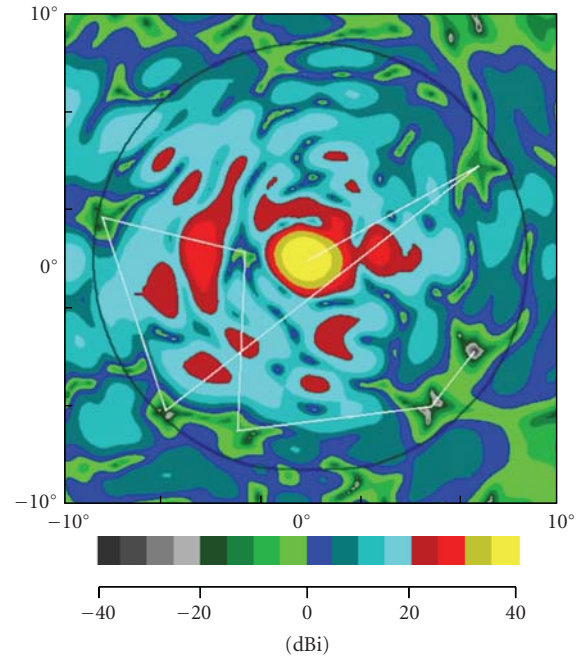


FIGURE 5: Synthesised beams with nulls, with errors.

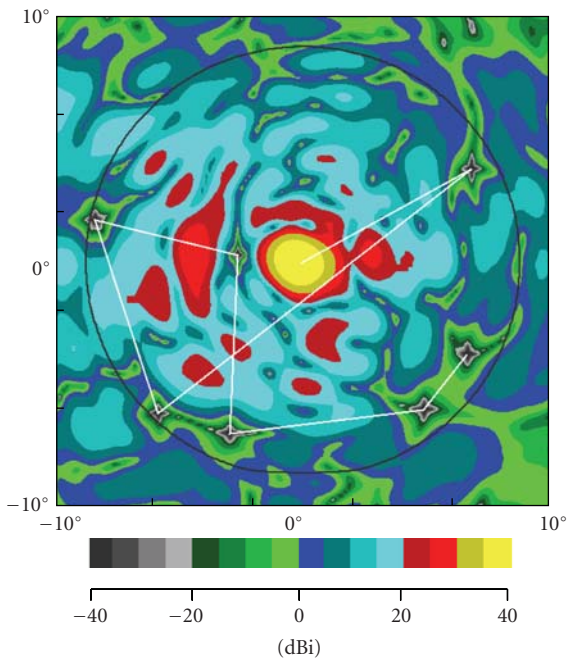


FIGURE 4: Synthesised beams with nulls, no errors.

cell. Figure 3 shows a maximum directivity beam for $(0.08^\circ, 0.08^\circ)$, and the locations of the other users are indicated by the vertices of the straight white lines. The beam peak is 43.5 dBi, and the level at the closest user is 25 dBi (i.e., 18.5 dB below the beam peak).

Figure 4 shows the synthesised beam with deep nulls over the other user locations. The nulls are below -50 dBi. The peak directivity has fallen by about 0.25 dB. Figure 5 shows

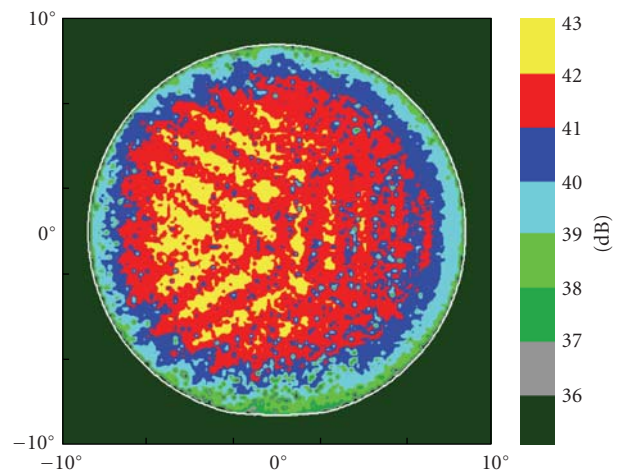


FIGURE 6: Minimum directivity of DBS beams biased for isolation, 7 colour, with errors, (scale 35 to 43 dB).

the effect of likely vector weight errors. The nulls have filled in; for example, the level of the closest user is -1 dBi (i.e., 26 dB lower than the maximum directivity case). All nulls remain below 0 dBi over an area encompassing the pointing error uncertainty margin and provide ~ 40 dB isolation.

A full simulation was carried out over the earth using five trials at each grid point. The worst values, for each grid point, of these five trials were selected. It included vector weight errors, as for the “fixed beamset”, and pointing errors of 0.16° . Satellite pointing error margin was 0.1° ; the additional 0.06° is equivalent to a user location error of 40 Km at the subsatellite point. GPS can give user location to tens of meters or better. The directivity levels are shown in Figure 6. The received isolation over the earth is shown in Figure 7.

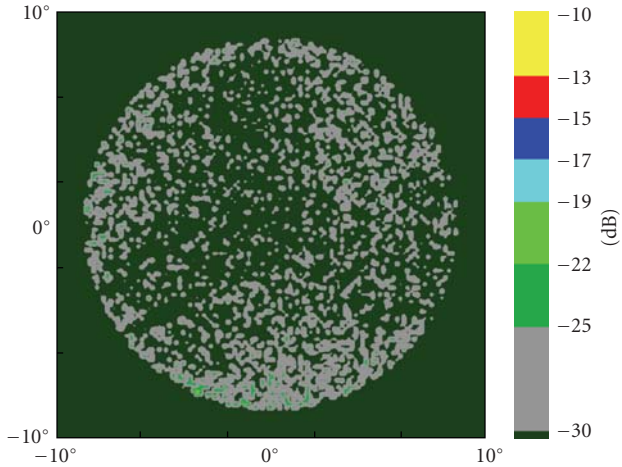


FIGURE 7: Minimum isolation of DBS beams biased for isolation, 7 colour, with errors, (scale -31 to -10 dB).

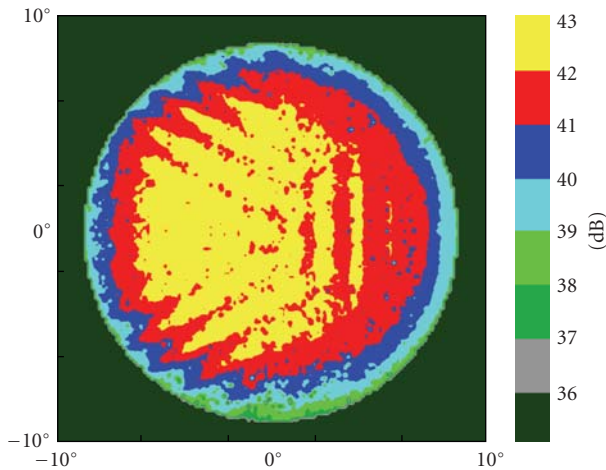


FIGURE 8: Minimum directivity of DBS beams, biased for gain, 7 colour, with errors, (scale 35 to 43 dBi).

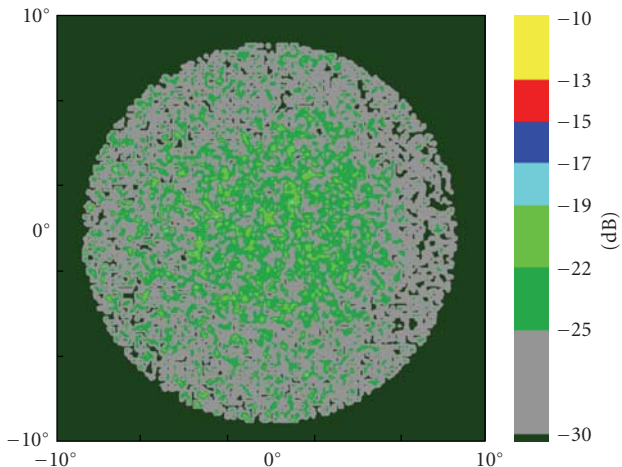


FIGURE 9: Minimum isolation of DBS beams, biased for gain, 7 colour, with errors, (scale -31 to -10 dB).

The received isolation was calculated as the ratio of the sum of the powers received from the cocoloured users to the power of the user. The results presented in this paper are for a 7-colour frequency reuse scheme, with eight cocoloured users.

The results show higher directivity levels than the fixed beamset. There are a few areas where the directivity was lower than before. This was due to the synthesis procedure achieving very low nulls at the expense of user directivity. Higher directivity levels can be achieved by relaxing the null depth. Figures 8 and 9 show the directivity and isolation when the synthesis is biased more towards directivity.

4. Conclusion

The “dynamic beam synthesis” (DBS) process has the potential to increase both the gain and isolation performance of multibeam, frequency reuse, and satellite communication systems. The simulations show that the isolation performance of dynamic beam synthesis can be an order of magnitude better than using the fixed beam case.

References

- [1] R. F. E. Guy, C. B. Wyllie, and J. R. Brain, “Synthesis of the Inmarsat 4 multibeam mobile antenna,” in *Proceedings of the 12th International Conference on Antennas and Propagation (ICAP '03)*, vol. 1, pp. 90–93, Exeter, UK, March–April 2003.
- [2] R. T. Compton, *Adaptive Antennas*, Prentice-Hall, Englewood Cliffs, NJ, USA, 1988.

Research Article

Planar C-Band Antenna with Electronically Controllable Switched Beams

Mariano Barba, Juan E. Page, and Jose A. Encinar

Departamento de Electromagnetismo y Teoría de Circuitos, Escuela Técnica Superior de Ingenieros de Telecomunicación, Universidad Politécnica de Madrid, Ciudad Universitaria, 28040 Madrid, Spain

Correspondence should be addressed to Mariano Barba, mbarba@etc.upm.es

Received 14 October 2008; Accepted 8 January 2009

Recommended by Giovanni Toso

The design, manufacturing, and measurements of a switchable-beam antenna at 3.5 GHz for WLL or Wimax base station antennas in planar technology are presented. This antenna performs a discrete beam scan of a 60° sector in azimuth and can be easily upgraded to 5 or more steps. The switching capabilities have been implemented by the inclusion of phase shifters based on PIN diodes in the feed network following a strategy that allows the reduction of the number of switches compared to a classic design. The measurements show that the design objectives have been achieved and encourage the application of the acquired experience in antennas for space applications, such as X-band SAR and Ku-band DBS.

Copyright © 2009 Mariano Barba et al. This is an open access article distributed under the Creative Commons Attribution License, which permits unrestricted use, distribution, and reproduction in any medium, provided the original work is properly cited.

1. Introduction

The well-known features of planar antennas are low profile, low mass, potential low cost, and ease of mounting; they make this antenna technology very attractive for many communications applications of both terrestrial and space systems. Moreover, for space applications, their planar geometry is very interesting because the simplifications that its geometry introduces in the packaging for the launching and deployment systems.

On the other hand, the well-established printed circuit technology and the consolidated market of planar microwave devices allow the introduction of nonlinear components, such as PIN diodes, varactor diodes, and MEMS, which can be used to reconfigure or reshape the beam by controlling or changing the RF signals. In this way, the added flexibility to the antenna can give an agile response to the continuous changing needs in communication systems. A good review of the advantages of reconfigurable antenna for mobile communication systems can be found in [1]; these advantages are very similar to fixed wireless services such as wireless local loop (WLL) or Worldwide Interoperability for Microwave Access (Wimax). The ideal situation would be that one where a complete pattern reconfiguration is attainable in the antenna according to the system needs, in

fact, this is achieved by using MIMO systems, however, they require many antennas, many antenna locations, and signal postprocessing. There is a very interesting way of developing agile antennas including partial and limited reconfigurability in just one single antenna by, as mentioned, the addition of controllable phase shifters in the antenna circuits at the RF level. Since base station antennas usually generate a pattern that covers a sector in azimuth with the appropriate beam shaping in elevation implemented by a linear array [2], the antenna can be designed to scan a sector typically covered by one passive antenna [3]. Alternatively, the antenna can be designed to switch the beam pointing direction to the area with a greater service demand. These solutions lead to electronically reconfigurable antennas at a moderate cost and complexity and very low power consumption. This concept of antenna reconfiguration is very suitable for space applications where switching, scanning, or reconfiguration of the beam is required to improve the performances of the system.

In this paper, a low-cost switchable antenna is proposed for base stations of WLL and Wimax systems in the 3.5 GHz band. The objective of this development was to obtain a low-cost low-complexity antenna covering a 60° sector with several switchable beams. A new topology is proposed for the beam switching, based on the implementation of 1 bit phase

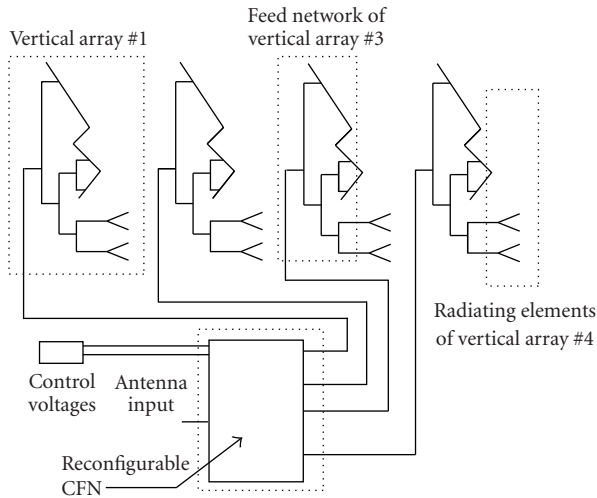


FIGURE 1: Antenna architecture.

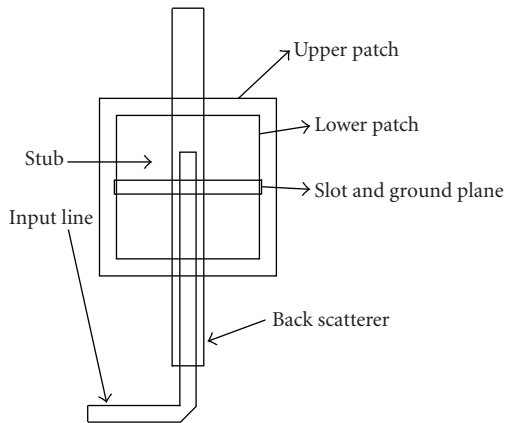


FIGURE 2: Radiating element. Top view and definition of conductors.

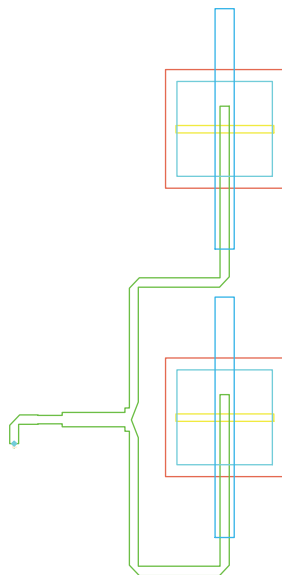


FIGURE 3: Vertical subarray topology.

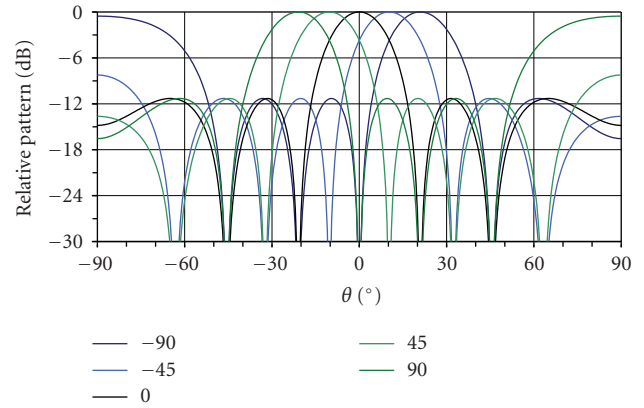


FIGURE 4: Five beams covering a 60° sector.

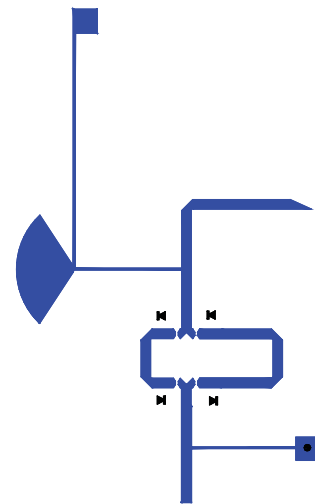


FIGURE 5: PIN diodes and microstrip delay lines phase shifter module.

shifters at each level of a conventional corporate feeding network. The distributed location of phase shifters in the feeding network yields a simplification of the antenna architecture. The concept of the proposed switchable antenna is demonstrated by the design, manufacture, and measurements of a prototype with three beams.

The development presented in this paper was focused on the scanning technology, circuits, and concepts to be applied to Wimax-WLL systems, but bearing in mind the use of the knowledge to develop switchable and reconfigurable antennas for other applications. In particular, the use of the concepts developed in this antenna for space systems is under consideration and most of the experience acquired with this development will be directly applied to other designs in progress for X-band SAR and Ku-band DBS applications.

2. Antenna Description

The antenna concept for the base station antenna with switchable beams addressed in this design is detailed in Figure 1. It is made up of a horizontal array of vertical

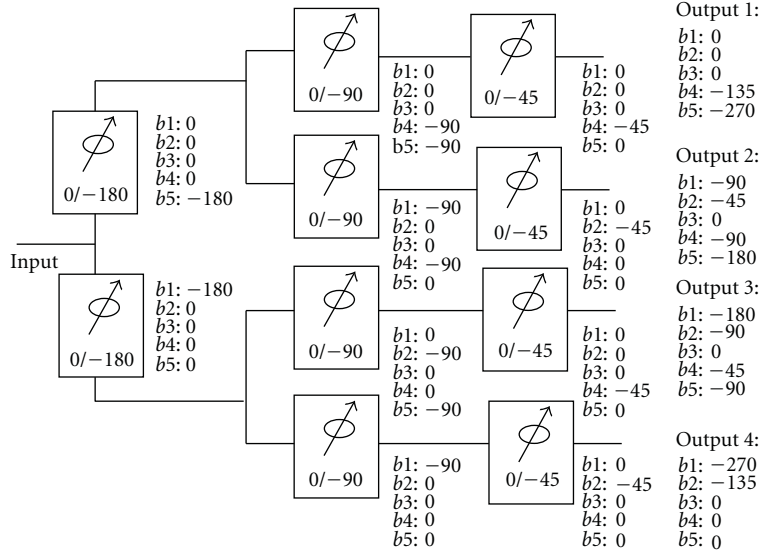


FIGURE 6: Phase shifter configuration and locations to obtain the desired beams.

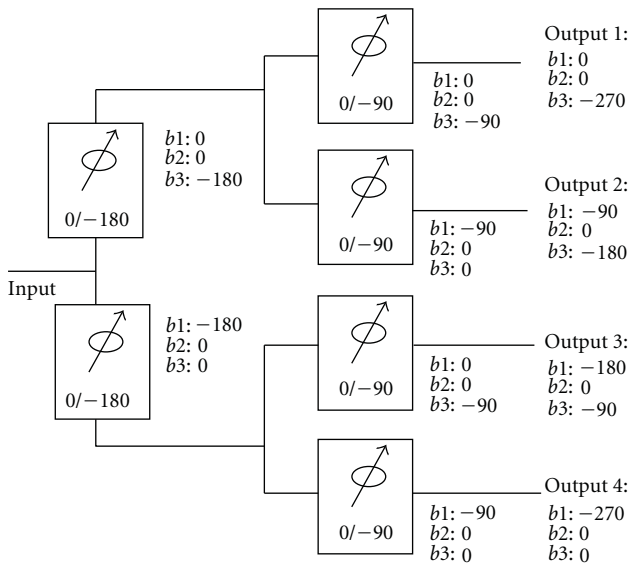


FIGURE 7: Phase shifter configuration to obtain 3 beams, the two extreme and the central.

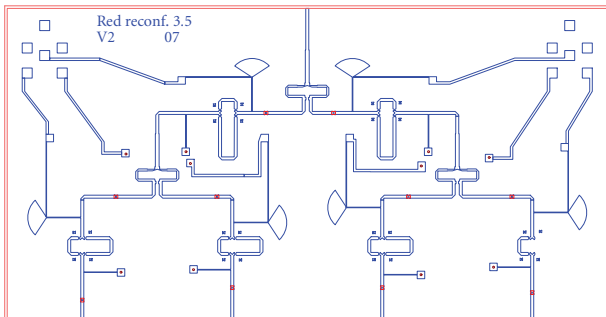


FIGURE 8: Drawing of the switchable feeding network.

subarrays. The vertical subarray produces the desired elevation pattern. For base station antennas, the requirements for the elevation patterns typically include shaping for upper lobe reduction, and often squared cosecant and null filling. According to these requirements and the gain specifications, these arrays have at least 8 elements, but sometimes up to 12 or 14 elements. In the antenna presented in this paper, the horizontal array has been implemented to produce the desirable beam scanning in azimuth by the inclusion of the proper electronically controllable feed network, which gives the different feed distributions needed. In this work, the main objective was to obtain the demonstrator of the switchable-beams antenna. Therefore the vertical array was obtained with just two radiating elements with equal amplitude and a phase shift to obtain a 2° degree tilt in the elevation pattern. The option for several elements in the vertical array is indicated by the saw lines in Figure 1. The reader is referred to [4, 5] for more discussions on the synthesis and the implementation of elevation beam-shaped patterns.

2.1. Radiating Elements. The radiating element is a dual-stacked patch coupled to a microstrip line through a slot. It has been designed to obtain the sufficient bandwidth and matching level for the required frequency band in the final antenna. Its design objectives, band from 3.3 GHz to 3.7 GHz, matching level better than -22 dB, have been established considering that this element has to be included in the array as its radiating element as well as considering the performance degradation that will be found in the prototypes as a result of the tolerance effects. This element is very similar to the one used in [3] for a lower frequency band. For reader convenience, their details and geometry are included in this paper; however, to focus this paper on the most relevant issues, the discussions about its design are avoided. Figure 2 shows the geometry including the

TABLE 1: Definition of the lay-up for the radiating element.

Description	Type	Dielectric layers		Conductors SIZE mm \times mm
		H mm	DK	
Upper patch	Conductor			19.83 \times 19.83
Upper substrate	Dielectric	12	1.6	
Lower patch	Conductor			24.64 \times 24.64
Lower substrate	Dielectric	6	1.6	
Ground plane	Conductor			Slot: 20.42 \times 1.55
RF substrate	Dielectric	0.5	3.2	
Microstrip, stub	Conductor			$w = 1.9$; stub = 4.73
Air		15		
Back scatterer	Conductor			4 \times 50
FR4	Dielectric	1.5	4.1	

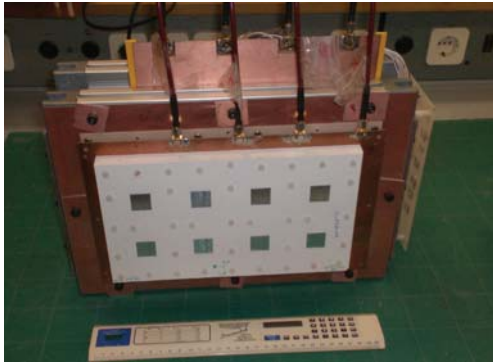


FIGURE 9: Phase antenna prototype. View of the radiating element and vertical subarray inputs.

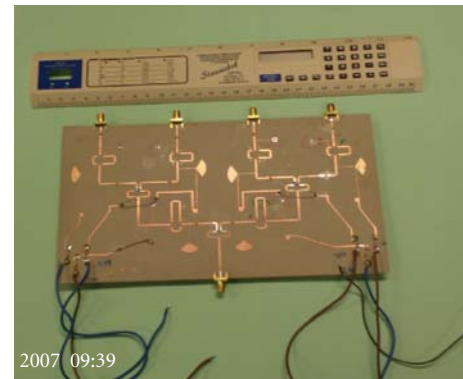


FIGURE 11: Prototype of feed network of the switchable antenna.

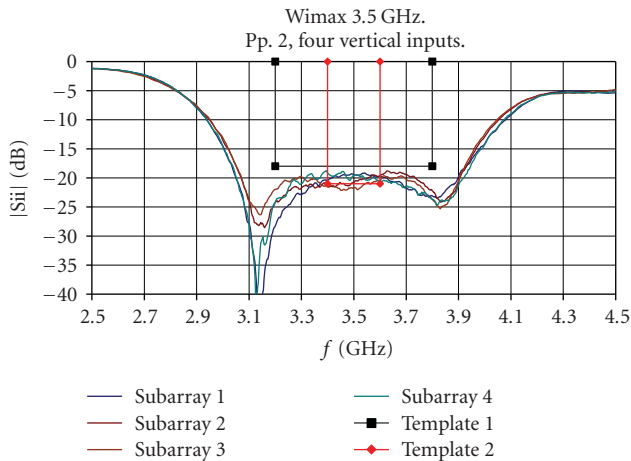


FIGURE 10: Antenna subarrays. Return losses for each input.

conductors of the radiating element and their description. In Table 1, the stack of the antenna and the parameters of the elements of the radiating element are listed.

The chosen separation distance for all of the radiating elements of both arrays is 60 mm (0.7λ). This value has been taken as the maximum distance between the elements, where

the disturbance introduced by the grating lobes level is not significant for the system requirements.

As has already been mentioned, the vertical array for this prototype consists of two elements fed with equal amplitude and with a phase shift that produces an elevation tilt of 2° . Figure 3 shows the arrangement of the vertical array for this prototype.

2.2. Feeding Network. The azimuth feed network has to provide switchable beams covering a sector of $\pm 30^\circ$. This can be done with an array of four elements, fed with equal amplitude and a progressive phase shift to tilt the pointing direction as desired. The desired coverage assuming a ripple of 2 dB can be obtained by 5 different beams pointing alternatively to -21° , -10.5° , 0° , 10.5° , and 21° , as shown in Figure 4. To obtain these beam inclinations and considering the separation between elements, the feed network should provide five different feed distributions with a progressive phase shift between adjacent elements of 90° , 45° , 0° , -45° , and -90° , respectively, and equal amplitude for all of them.

The feeding network has been designed and manufactured in microstrip technology. Although for this demonstrator, it is implemented in an independent board to allow all of the antenna components to be measured separately, however, in an industrial design, it can be integrated into the

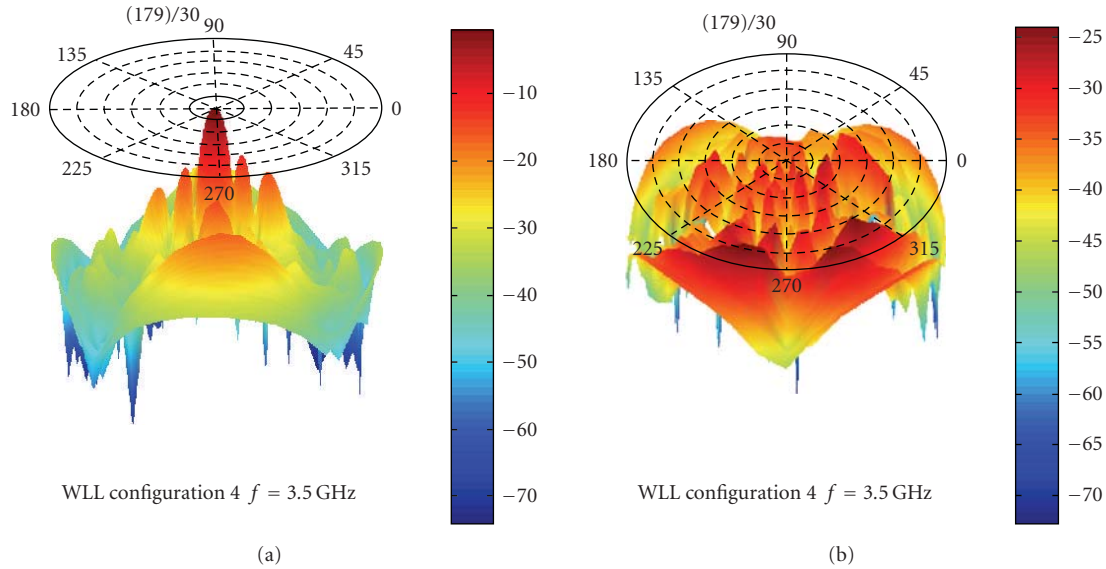


FIGURE 16: Pattern measurements. Three-dimensional pattern at 0° pointing direction. (a) Copolar patterns, and (b) cross-polar patterns.

same board where the input microstrip lines of the radiating element are located, thus reducing the size, cost, losses, and complexity. The amplitude distribution can be obtained through a corporate feed network with equal amplitude dividers.

The phase shifter can be implemented by microwave switches single-pole double-through (SPDT) and delay lines, having each phase shifter two switches and two delay lines with the proper difference of length to produce the desired phase shift at the centre frequency. In this design, the SPDT switches have been implemented using two PIN diodes, resulting in the phase shifter module shown in Figure 5. The selected diode for this application that, according to manufacturer specifications, can be used at higher frequencies is MACOM-MA4PBL027. It presents an equivalent series resistance in direct biasing of 3.5Ω and an equivalent reverse capacitance lower than 40 fF.

The simplest way to implement the feeding network using amplitude dividers and two-state phase shifters consists of, first, obtaining the four equal amplitude signals, and after that division and before the inputs of each subarray, including a set of phase shifters connected serially, in order to implement the required additional phase shift states. However, this structure can be simplified by taking advantage of the corporate structure by including the phase shifter for more significant shifting in the first branches of the feed network. In Figure 6, this concept to implement the phase shifting needed for this design is presented. This figure also shows the setting of each phase shifter to obtain the 5 beams.

In order to develop the prototype and to reduce the manufacturing costs, the number of beams for the demonstrator was reduced to three, considering the extreme phase shiftings (-90° , 0 , and $+90^\circ$). This option reduces the number of phase shifters and the manufacturing process, proves the concept keeping the most exigent beam tilts. Therefore, the

configuration taken for the 3-beam demonstrator is the one set out in Figure 7.

For the 0° beam pointing direction, only the situation with 0° phase shift has been indicated. However, it is clear that other configurations of the phase shifter positions lead to the equal phase distribution. Any setting of the phase shifters with equal phase shifting at each level leads to an equal phase distribution and therefore could be valid.

The drawings of the design of the 3-beam feed network are shown in Figure 8, where it can be seen how the 180° phase shifters are at one level of the corporate network and the 90° phase shifters at the element (subarray input) level. All of the elements of the network such as bends, dividers, and biasing stubs have been optimized to reach the best performances in the band of interest 3.3–3.7 GHz. Even with this careful design, there are some parasitic effects introduced by connections of the diodes to the lines and through the connections of the blocking capacitors. In some conditions, as discussed before, these effects will be added each to others and can mainly degenerate the signal at the outputs. To reduce this degradation it is essential to implement the amplitude division with Wilkinson dividers, whose topology can be easily seen in Figure 8. High-quality microwave with low-loss blocking capacitors are needed; in this design, ATC series 600 were used.

3. Prototypes and Measurements

3.1. Antenna Components. Figure 9 shows the front image of the manufactured prototype. The eight radiating elements corresponding to the four subarrays can clearly be seen. The inputs of the four subarrays are also seen, as well as the cables which connect the outputs of the feed network to these inputs. In an industrial model, as it has been mentioned, the cable will not be used, since the feed network and the

radiating element input lines can be integrated into the same board. However, at the prototype level they have been manufactured independently to allow the measurement of all of the elements and their validation.

The measured return losses at each subarray input are shown in Figure 10. It can be seen that their values are in range of 20 dB in the frequency of operation as it was expected from the simulations carried out during the design.

The manufactured prototype of the electronically controllable feeding network of the antenna is shown in Figure 11.

The set of measurements of the feed network is quite wide. The minimum needed are the reflection parameter and the transmission parameters (amplitude and phase) for the 3 feed distribution configurations. Because of space considerations, some of them are not included in this paper; the measured return losses are better of -15 dB and the amplitude of transmission is in the range of -9 dB, giving, therefore, an average losses of the network of 3 dB, where 1.5 dB are a result of the losses and another 1.5 to the RF microstrip lines.

In Figure 12, the output phases for the 3 configurations are shown. Figure 12(a) shows the measured output phases for the 0° phase shift configuration, showing that the four signals are in phase. Figures 12(b) and 12(c) show the measured output phases for the $+90^\circ$ and -90° progressive phase shifts. These measurements confirm that the feed network is working properly.

3.2. Complete Antenna. Figure 13 shows a photograph of the complete antenna after assembling all of the elements, including a simple but efficient switching control matrix, which allows the phase shifters to be biased at their proper position according to the desired phase shifting at each configuration.

Figure 14 shows the measurement of the return losses for the 3 pointing positions with two options for the 0° configuration. It can be seen that its value matches the typical specification for this type of antennas, -14 dB, which is equivalent to a VSWR of 1.5.

Figure 15 shows the azimuth cuts in a plane of 2° tilt for the 3 pointing directions of the far field measurements. It can be seen how beam switching is achieved as expected. As reference, the cross-polar measurement of the azimuth cut for the 0° beam pointing direction is also included. It can be observed that its maximum level is lower than 25 dB below the antenna gain.

For reference, the three-dimensional measurements for co- and cross-polar components normalized to the maximum of radiation for the 0° beam pointing direction are presented in Figure 16. The maximum level of cross-polar component in the range of the main lobe (from -15° to $+15^\circ$) is lower than 25 dB below the antenna gain.

4. Conclusions

This paper presents the design, manufacturing, and measurements of a switched-beam antenna at 3.5 GHz in planar

technology that demonstrate the suitability of scanning beam base station antennas for WLL and Wimax, where the beam scanning is achieved through the inclusion of phase shifters based on PIN diodes in the feed network, and where the strategy of phase shifter locations leads to a reduction in the number of components. The feasibility of this type of antenna for space applications is under consideration and the experience acquired with this development can be used for X-band SAR applications and Ku-band DBS.

Acknowledgment

This work has been supported by MEC, Spain, under Projects TEC2004-02155 and TEC2007-63650.

References

- [1] L. C. Godara, "Applications of antenna arrays to mobile communications—part I: performance improvement, feasibility, and system considerations," *Proceedings of the IEEE*, vol. 85, no. 7, pp. 1031–1060, 1997.
- [2] J. R. Sanford, J. F. Zürcher, and S. Robers, "Shaped beam patch arrays for mobile communication base station," *Microwave Engineering Europe*, pp. 31–33, June–July 1991.
- [3] ETSI, "Fixed radio systems; electronically steerable antennas, Multipoint (MP) antennas; Fixed Wireless Access (FWA) radio systems," Tech. Rep. TR101938 VI.2.1, ETSI, Sophia Antipolis, France, 2002.
- [4] M. Barba, J. E. Page, J. A. Encinar, and J. R. Montejo-Garai, "A switchable multiple beam antenna for GSM-UMTS base stations in planar technology," *IEEE Transactions on Antennas and Propagation*, vol. 54, no. 11, pp. 3087–3094, 2006.
- [5] E. Carrasco, M. Arrebola, J. A. Encinar, and M. Barba, "Demonstration of a shaped beam reflect array using aperture-coupled delay lines for LMDS central station antenna," *IEEE Transactions on Antennas and Propagation*, vol. 56, no. 10, pp. 3103–3111, 2008.

Research Article

Ku Band Hemispherical Fully Electronic Antenna for Aircraft in Flight Entertainment

Alfredo Catalani,¹ Franco Di Paolo,¹ Marzia Migliorelli,¹ Lino Russo,¹
Giovanni Toso,² and Piero Angeletti²

¹Antenna and Sub-Millimeter Wave Section, Space Engineering S.p.A., Via dei Berio 91, 00155 Roma, Italy

²Electromagnetics Division, TEC-EEA, European Space Agency, ESA ESTEC, Keplerlaan 1, PB 299,
2200 AG Noordwijk, The Netherlands

Correspondence should be addressed to Alfredo Catalani, alfredo.catalani@space.it

Received 30 September 2008; Revised 8 January 2009; Accepted 23 March 2009

Recommended by Stefano Selleri

The results obtained in the frame of the ESA activity “Advanced Antenna Concepts For Aircraft In Flight Entertainment” are presented. The aim of the activity consists in designing an active antenna able to guarantee the Ku band link between an aircraft and a geostationary satellite in order to provide in flight entertainment services. The transmit-receive antenna generates a single narrow beam to be steered electronically in a half sphere remaining compliant with respect to stringent requirements in terms of pattern shape, polarization alignment, EIRP, G/T, and using customized electronic devices. At the same time, the proposed solution should be competitive in terms of cost and complexity.

Copyright © 2009 Alfredo Catalani et al. This is an open access article distributed under the Creative Commons Attribution License, which permits unrestricted use, distribution, and reproduction in any medium, provided the original work is properly cited.

1. Introduction

Over the last few years the public's reliance on computer networks including, but not limited to, Internet has increased exponentially. Many people today use Internet for business and entertainment. Aeronautical broadband services provisioning by satellites are becoming a reality moving from an experimental base to an operational condition.

Aircrafts use antennas for transmitting and receiving communication signals. Key aspects to consider in the design of these antennas are the aerodynamic drag, the beam pointing capability, and the receive/transmit functionality.

Concerning the aerodynamic aspects, the antenna has to exhibit the minimum impact on the aircraft in order to reduce the extra fuel consumption due to the drag of the antenna installed on the fuselage. As a rule of thumb, the height of antennas on board large aircrafts and inclusive of the radome should not exceed 30/40 cm.

Concerning the beam pointing characteristics, to be operative both at equatorial routes as well as at the extreme latitudes required by polar routes, the preferred antenna

solution should exhibit wide-angle beam scanning capabilities.

The possible antenna architectures are based on fully mechanical [1], fully electronic [2], or “hybrid” (mechanical-electronic) solutions [3, 4].

Complexity and cost of the antenna are other key factors to consider together with ability to operate simultaneously in reception and in transmission.

The principal target, in terms of antenna characteristics, is the operation in the complete Ku Band (10.7/12.75 GHz in receive, 14.0/14.5 GHz in transmit) and the realignment of the polarization with respect to the satellite for both receive and transmit signals, with the capability to operate also with the circular polarization in receive signals.

The minimum antenna requirements in terms of operative Field of View, G/T, EIRP, and cross polar discrimination are reported in Table 1.

Regulatory aspects [5] are also considered: an antenna in transmission mode has to respect the applicable regulations for the EIRP antenna patterns expressed in terms of power per bandwidth as shown in Figure 1.

TABLE 1: Antenna performances requirements.

Requirements	Antenna
Radiation gain pattern over RF band	In agreement with (*)
Operative antenna field of view	$0^\circ < \varphi < 360^\circ$ $0^\circ < \theta < 90^\circ$
G/T over RF band, in the entire field of view and for every selectable polarization	$>8 \text{ dBK}^{-1}$
EIRP over RF band, in the entire field of view	$>43 \text{ dBW}$
Number of beams	1
Cross polarization discrimination (including pointing error)	$>15 \text{ dB}$

(*) Ref. [5]

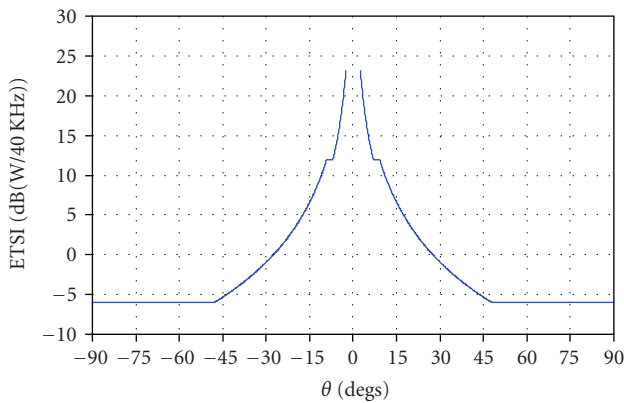


FIGURE 1: ETSI regulation mask [5].

2. Antenna Baseline Architecture

The proposed baseline antenna architecture is an evolution of the Hemi-Spherical Antenna Array shown in Figure 2.

This Antenna typology, due to its particular shape, once mounted on the aircraft is able to hold-on the appropriate link whatever the position of the airborne with respect to the satellite is.

In order to minimize the complexity of the antenna, the Hemi-Spherical continuous surface has been organized in flat facets. The icosahedron, a polyhedron with twenty equilateral triangles, has been selected to replace the sphere. Besides, a further division of each triangular face (obtained projecting the vertices of the triangles on the sphere) has been implemented. As a result of a dedicated optimization, the geodesic hemi-sphere with 40 facets shown in Figure 3 has been considered the geometrical candidate for the presented antenna. Each triangular face exhibits the same identical subarray; therefore the same number of radiating elements disposed on a triangular lattice.

The final optimized antenna is combining on the same aperture of the receive-transmit capabilities, exhibiting a diameter of 84 cm, a height of 39 cm, and a weight in the order of 90 Kg. The number of radiating elements is 1440 with an interspacing comparable to the wavelength at the Tx higher frequency.



FIGURE 2: Hemi-spherical array.

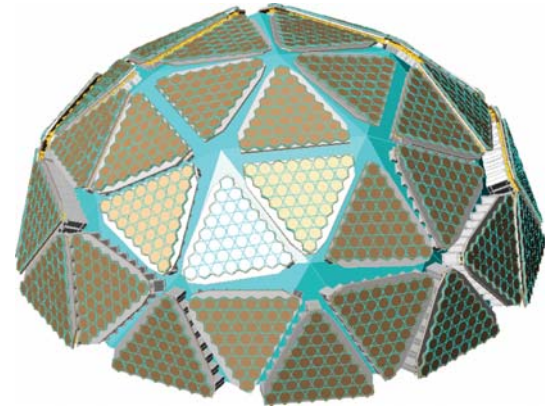


FIGURE 3: Faceted hemi-spherical antenna.

Each triangular subarray, indicated as *tile*, presents 36 radiating elements.

For a fixed beam direction only a sector composed by 14 tiles is active while all the other elements are turned off. All the radiating elements in the active sector are excited in order to generate an equal-phase wave front perpendicular to the desired beam direction.

The antenna block diagram, presented in Figure 4, is representative of the antenna electrical architecture.

The input/output ports are fed with the IF band signal, and they are converted in a Ku band signal by the up/down converter. Two dedicated beam forming networks 1 : 40 for the receive and the transmit mode are connected to the tiles, and the CPU controls a set of switches in order to involve the selected subarrays to form the antenna beam. Each tile is composed by the radiating elements and the transmit/receive modules, directly connected behind. The CPU controls the beam steering and the polarization alignment.

3. Antenna Description

The antenna works simultaneously in reception and transmission on the entire Ku band (10.7 GHz/12.75 GHz in Rx; 14.0 GHz/14.5 GHz in Tx). A deep investigation, optimization, and trade-off have been implemented in order to identify the wide-band radiating element.

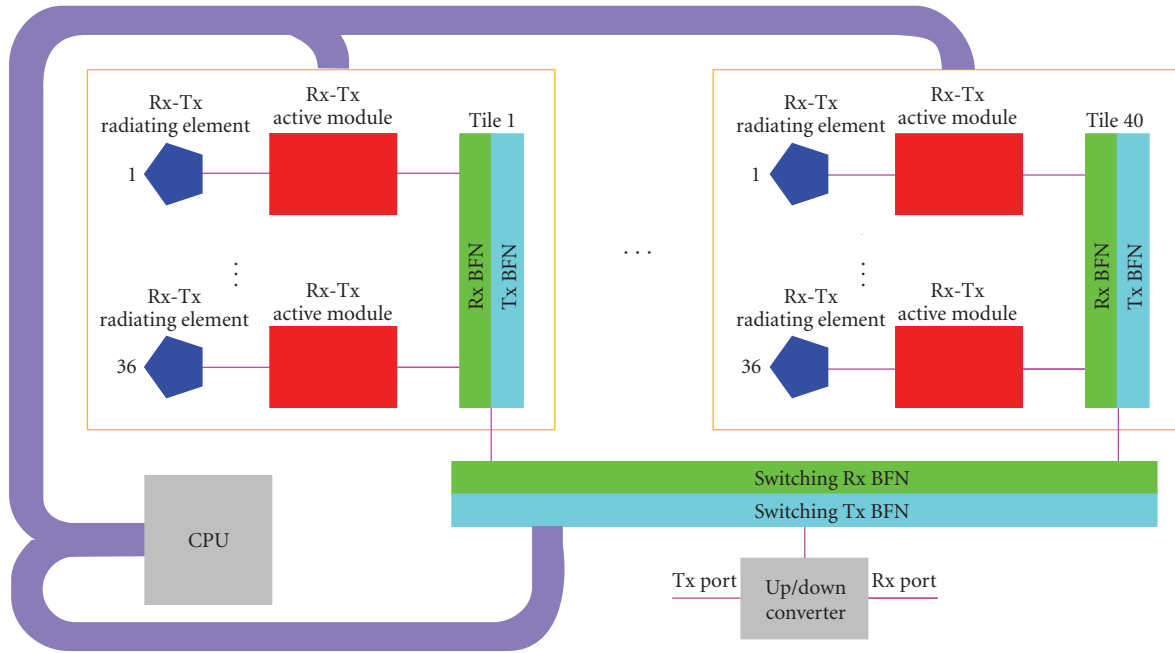


FIGURE 4: Hemi-spherical antenna block diagram.



FIGURE 5: Radiating element prototype.

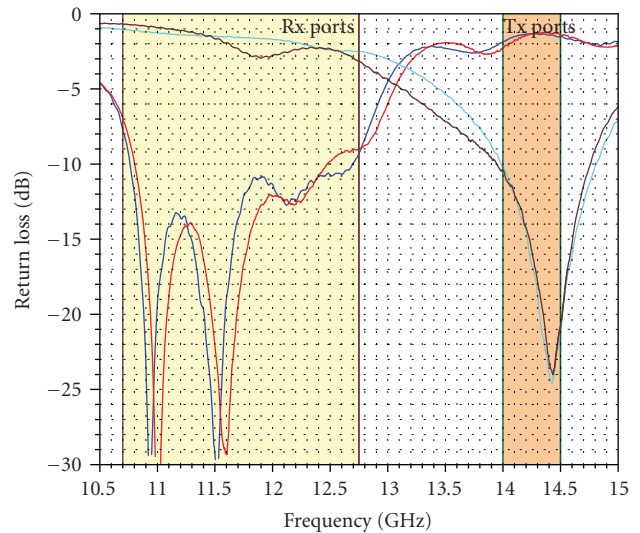


FIGURE 6: Measured radiating element return loss.

3.1. *Passive Radiating Module.* Two possible solutions are envisaged:

- (i) the first one is based on a wideband or dual band radiating element; in order to separate the receive signal from the transmit signal it is mandatory the use of a circulator or a diplexer;
- (ii) the second one is based on a self-diplexing radiating element; this element presents four physical ports (two for Rx, two for Tx). The self-diplexing element has the advantage to minimize the ohmic losses, therefore improving both the G/T and the EIRP.

The selected solution is based on a self-diplexing radiating element. It offers better electrical performances and permits reducing the manufacturing complexity.

A prototype of the realized radiating element is shown in Figure 5. The measured performances of the radiating elements in terms of Return Loss are reported in Figure 6. The isolation between the ports is better than 20 dB over the operative bands.

The radiation patterns of the radiating element at the center frequency in the receive and transmit band are shown in Figures 7 and 8.

3.2. *B. Tx/Rx Active Module.* Each radiating element presents an active circuitry directly connected to the output ports

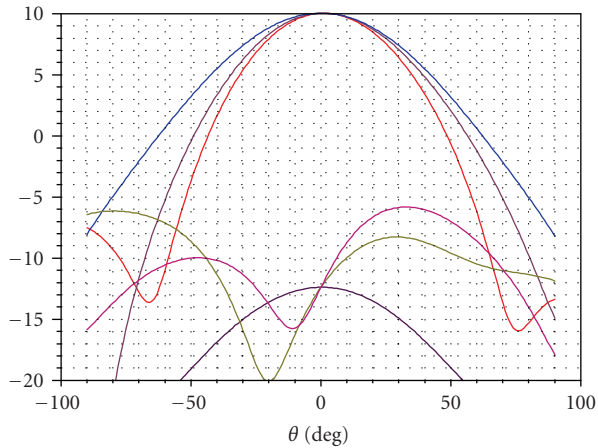


FIGURE 7: Simulated radiating pattern in receive.

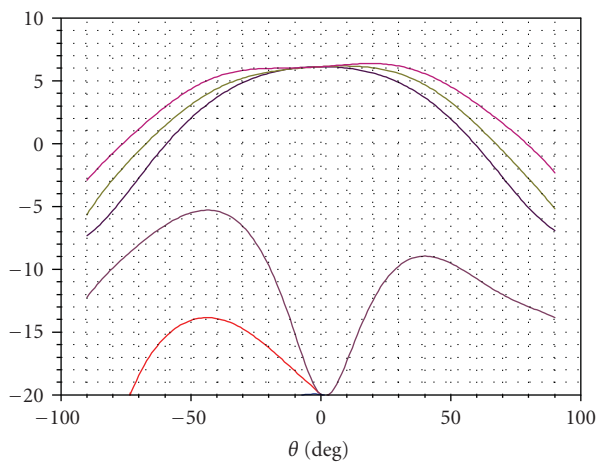


FIGURE 8: Simulated radiating pattern in transmit.

(Tx/Rx module). The Tx/Rx module is able to realign the linear polarization in receive and in transmit or, otherwise, it is able to generate a circular polarization [6]. The phase shifters used for the polarization control are able at the same time to form the antenna beam imposing the correct relative phase between the elements. The active modules are composed by the receive device and the transmit device (the assembled Tx/Rx device is shown in Figure 9).

The manufactured modules are presented in Figure 10: in particular the control board sides are shown.

Their dimensions are $20.6 \times 7 \times 37 \text{ mm}^3$, with a weight of 15 g.

As mentioned, each Tx/Rx Active Module is directly connected to the passive radiating elements (see Figure 9), and they are arranged in a triangular lattice with a number of 36 in order to compose the triangular subarray, that is, the tile of the Hemi-Spherical Antenna (Figure 11).

Two dedicated equal-amplitude and equal-phase beam forming networks combine the transmit and the receive signals coming from the active module (Figure 12).



FIGURE 9: Tx/Rx active module connected to the radiating element.

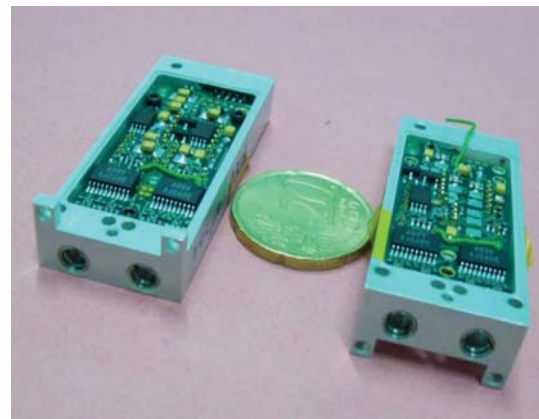


FIGURE 10: Tx and Rx active device—control board view.

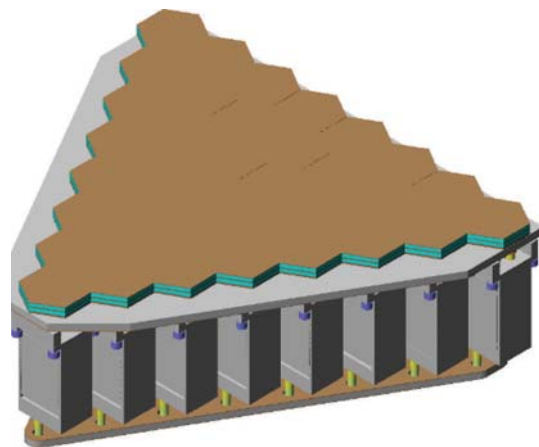


FIGURE 11: Tile of the hemi-spherical antenna.

Using the micro-coaxial cable, all the Rx and Tx ports behind the tiles are combined in two dedicated switching BFNs that are able to transmit and receive the signal of the selected tile. As mentioned, only a dedicated number of tiles, 14, are active instantaneously depending on the azimuth and elevation beam pointing. A micro-PC has controlled

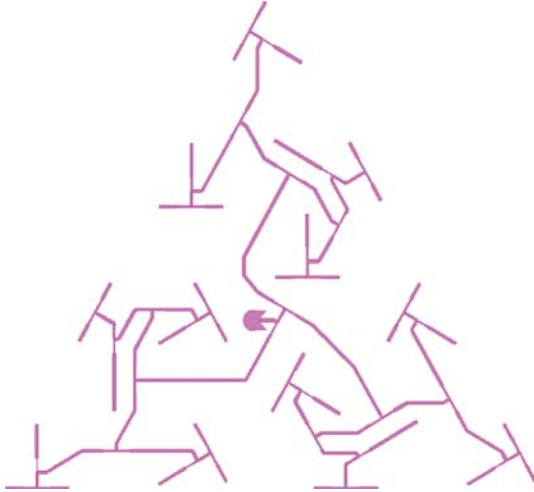


FIGURE 12: Receive BFN layout.

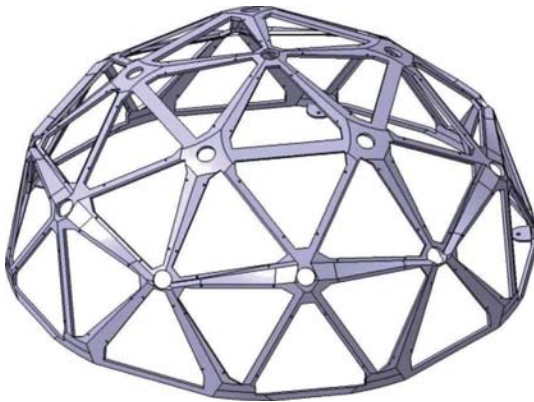


FIGURE 13: Antenna structure.

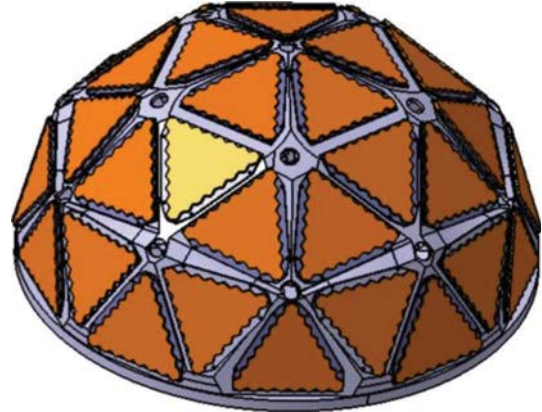


FIGURE 14: Assembled Hemi-Spherical antenna.

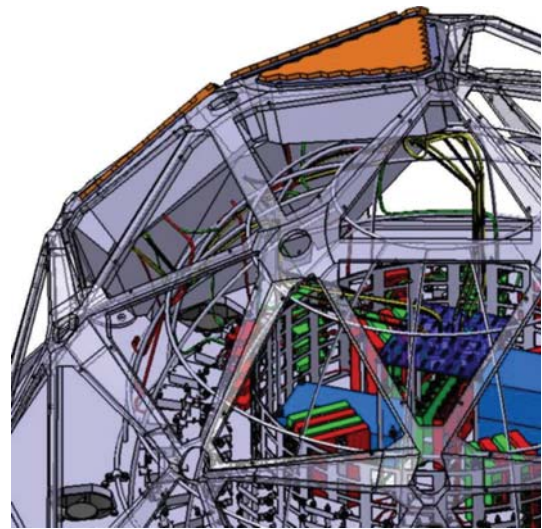


FIGURE 15: Cable routing of a part of the antenna.

all the active components taking into account the satellite position and the aircraft attitude. The beam forming network connecting the tiles is realized using commercial microwave components.

The tiles are positioned on the shell-shaped structure, shown in Figure 13, which can be manufactured by a casting process or by the assembly of simple part obtained by a numerical control machine.

The result of the assembled hemi-spherical antenna is presented in Figure 14. Some details of the inner part considering the cable routing between the tiles and the switching beam forming network are presented in Figure 15.

4. Antenna Performances

The tracking capability of the antenna permits to point the beam electronically in a hemi-spherical field of view (i.e., 360 degrees in azimuth and 90 degrees in elevation) with reduced degradations of the electrical performances,

guaranteeing a minimum G/T of 8 dB/K^{-1} and an EIRP of 43 dBW.

The results are obtained using the simulated pattern of an embedded radiating element. Moreover, in the optimization of the excitation coefficients, the realistic functionality of the Rx/Tx active module (combining the amplitude and phase of the two orthogonal polarization for each radiating element) has been taken into account.

The G/T is shown in Figure 16: as can be seen, the performances match the required 8 dB/K in the entire field of view. The obvious decreasing of performance at the lower pointing angles is due to different orientation angles of the tiles, involved in the beam forming, with respect to the horizon. The typical azimuth receive antenna pattern is shown in Figure 17.

In transmit all the active devices are able to work at the maximum power level, and the foreseen performance in term of EIRP is reported in Figure 18: the minimum guaranteed performance is in the order of 43 dBW over the complete antenna field of view.

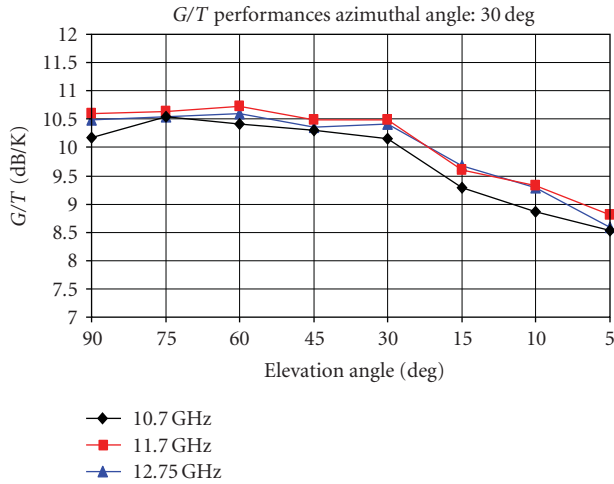


FIGURE 16: G/T versus elevation angle over the horizon.

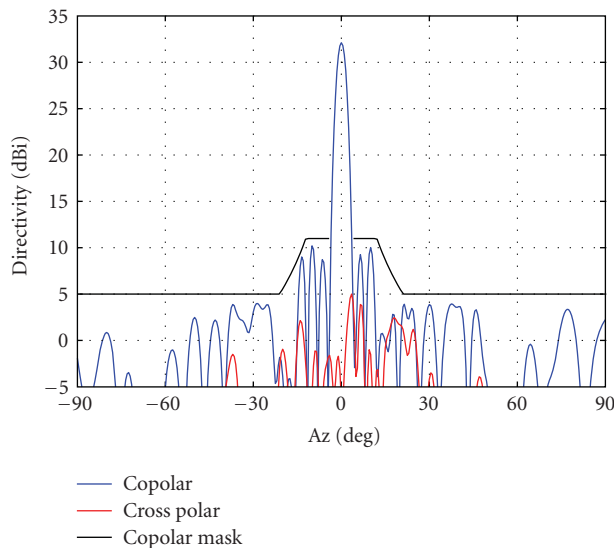


FIGURE 17: Azimuth Rx Antenna Pattern at 11.7 GHz, considering a 30° elevation pointing over the horizon.

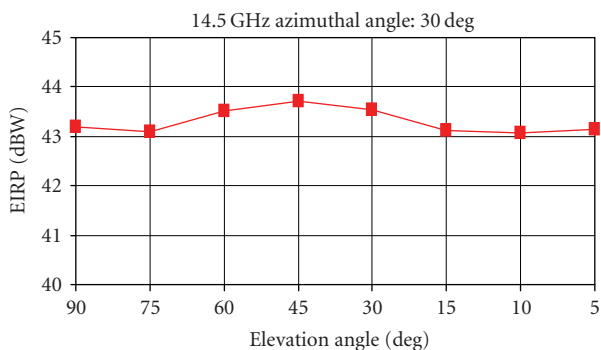


FIGURE 18: EIRP versus elevation angle over the horizon.

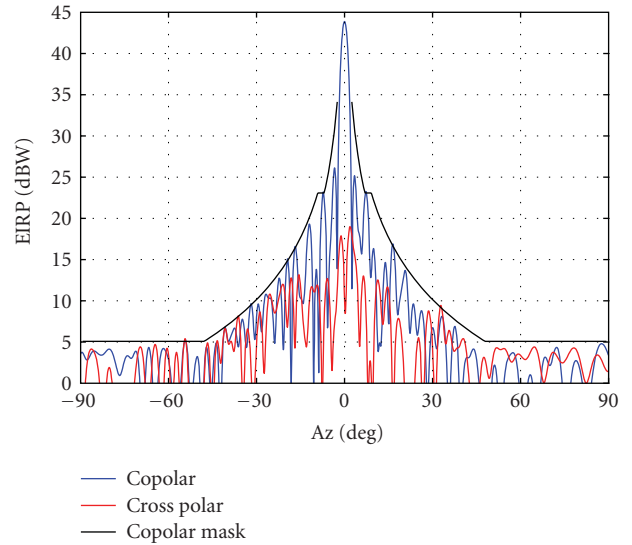


FIGURE 19: Typical Azimuth Tx Antenna Pattern at 14.25 GHz, 30° elevation pointing over the horizon.

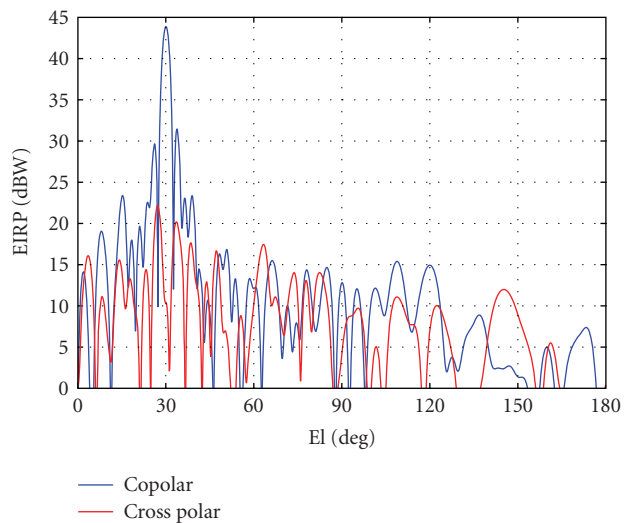


FIGURE 20: Typical Elevation Tx Antenna Pattern at 14.25 GHz, 30° elevation pointing over the horizon.

The antenna is also able to control the transmit antenna patterns side-lobe in order to respect the applicable regulatory recommendations such as ETSI in the European countries [5, 7] and the FCC in the United States.

The typical azimuth transmit antenna pattern is presented in Figure 19. The black line represents the mask that has been imposed in the optimization process (corresponding to the ETSI mask for 512 KHz bandwidth). Also the correspondent elevation transmit antenna pattern is shown in Figure 20.

5. Conclusion

In the paper the results of the activities carried out in the frame of the ESA Contract “Advanced Antenna Concepts For Aircraft In Flight Entertainment” have been presented.

The designed Ku band active antenna exhibits a compact size and the possibility of full beam pointing coverage. The antenna radiating element module is providing also polarization alignment capabilities in transmission and reception.

The antenna exhibits really good technical performances. The next activities will be focused on reducing dimension, cost, and complexity of the entire antenna in order to meet the severe expectation of a market product.

Acknowledgments

The authors acknowledge the colleagues R. Pasta and L. Flamini for UTRI; A. Toresin for Aeronavali; E. Limiti for the University of Roma Tor Vergata; S. Selleri for the University of Florence for their support and contribution in the activity.

References

- [1] G. Bellaveglia, L. Marcellini, A. Ferrarotti, S. Arenaccio, and R. Lo Forti, "Two-way low profile satellite antenna system for mobile applications," in *Proceedings of the 30th ESA Antenna Workshop on Antennas for Earth Observation, Science, Telecommunication and Navigation Space Missions*, Noordwijk, The Netherlands, May 2008.
- [2] C. O. Adler, A. D. Monk, D. N. Rasmussen, and M. J. Taylor, "Two-way airborne broadband communications using phased array antennas," in *Proceedings of IEEE Aerospace Conference*, vol. 2, pp. 925–932, Big Sky, Mont, USA, March 2003.
- [3] P. Halsema, B. Anderson, and J. Frisco, "Airborne DBS receive system," in *Proceedings of Antennas and Propagation Society International Symposium*, Montreal, Canada, July 1997.
- [4] M. Shelley, R. Pearson, and J. Vazquez, "Low profile, dual polarised antenna for aeronautical and land mobile satcom," in *Proceedings of the 4th Advanced Satellite Mobile Systems (ASMS '08)*, pp. 16–19, Bologna, Italy, August 2008.
- [5] ETSI EN 302 186 V1.1.1 (2004-01), "Satellite Earth Stations and Systems (SES); Harmonized EN for satellite mobile Aircraft Earth Stations (AESs) operating in the 11/12/14 GHz frequency bands covering essential requirements under article 3.2 of the R&TTE Directive".
- [6] "A system for electronically aligning the polarization of an antenna," Italian Patent no. IT/20.03.07/ ITA RM20070144, European Patent Appl. no./Patent no. 08425163.6 — 2220.
- [7] Recommendation ITU-R M.1643, "Technical and operational requirements for aircraft earth stations of aeronautical mobile-satellite service including those using fixed-satellite service network transponders in the band 14-14.5 GHz (Earth-to-space)," 2003.

Application Article

Flat Array Antennas for Ku-Band Mobile Satellite Terminals

Roberto Vincenti Gatti, Luca Marcaccioli, Elisa Sbarra, and Roberto Sorrentino

RF Microtech srl, a spin-off of the University of Perugia c/o DIEI, via G. Duranti 93, 06125 Perugia, Italy

Correspondence should be addressed to Roberto Vincenti Gatti, vincenti@rfmicrotech.com

Received 30 September 2008; Revised 9 January 2009; Accepted 17 February 2009

Recommended by Stefano Selleri

This work presents the advances in the development of two innovative flat array antennas for Ku-band mobile satellite terminals. The first antenna is specifically conceived for double-deck trains to allow a bi-directional high data rate satellite link. The available circular surface (diameter 80 cm) integrates both a transmitting and a receiving section, operating in orthogonal linear polarizations. The TX frequency range is fully covered while the RX bandwidth is around 1 GHz arbitrarily allocated on the DVB range depending on requirements. The beam is steered in elevation through a phased array architecture not employing costly phase shifters, while the steering in azimuth is mechanical. Active BFNs allow excellent performance in terms of EIRP and G/T, maintaining extremely low profile. High antenna efficiency and low fabrication cost are ensured by the employment of innovative SIW (Substrate Integrated Waveguide) structures. The second antenna, receiving-only, is designed for radio/video streaming services in mobile environment. Full DVB coverage is achieved thanks to cavity-backed patches operating in double linear polarization. Two independent broadband active BFNs allow simultaneous reception of both polarizations with full tracking capabilities and a squintless beam steering from 20° to 60° in elevation. A minimum gain of 20 dBi and $G/T > -3$ dB/K are achieved, while maintaining extremely compact size and flat profile. In the design of both antennas fabrication cost is considered as a driving factor, yet providing high performance with a flat profile and thus resulting in a great commercial potentiality.

Copyright © 2009 Roberto Vincenti Gatti et al. This is an open access article distributed under the Creative Commons Attribution License, which permits unrestricted use, distribution, and reproduction in any medium, provided the original work is properly cited.

1. Introduction

In the last few years an increasing interest has been addressed to many satellite services at Ku-band being proposed or already operative, ranging from digital radio and TV broadcast to broadband internet services. Potential applications and markets especially regard mobile environments (cars, trains, boats, airplanes), though some particular applications may also involve fixed users (e.g., flat wall-mounted antennas for digital TV and radio for environmental impact reduction).

The success of new services and the expansion of those already present depend to a great extent on the user terminal costs and performance and therefore on the employed antenna, which becomes a critical component of the whole system. Since most of the applications refer to mass consumer markets, the first driving factor for the antenna design and development is the fabrication cost, that must be maintained as low as possible. A compact size is then needed for an easy placement on mobile vehicles,

and for many applications a flat profile is mandatory to maintain aerodynamic properties of the vehicle as well as to allow the integration of the antenna itself. Finally high performance must be achieved in terms of EIRP and G/T in such a way as to ensure high data bit rate links, as well as the automatic beam steering to maintain the link in mobile environment. The most critical issue for an effective design achieving such stringent requirements is indeed the identification of the most suitable technology. The development of high-performance and low-cost critical components (e.g., LNAs, rotary joint, radiating element, etc.) is furthermore essential as well as the implementation of a cost-effective architecture for the BFN and control system. The major limiting factor for mobile terminal development is indeed represented by the beam steering approach and the number of electronic components employed. To that end RF Microtech has recently proposed [1] an alternative approach for beam steering, not employing phase shifters, based on a switched beam architecture to obtain electronic beam steering in the elevation plane, while mechanical



(a)



(b)

FIGURE 1: Typical scenarios of applications: (a) mobile vehicles such as cars, trains, boats, and trains; (b) example of strong environmental impact that could be reduced with the employment of flat wall-mounted antennas for DVB and radio reception.

beam steering is performed in the azimuthal plane. This approach allows a considerable reduction of the overall system complexity and fabrication costs being the BFN realized in microstrip technology in the form of a Rotman lens, still maintaining extremely high performance through the use of LNAs. The use of COTS in this case is the most convenient solution due to the extremely wide market of such components, already employed in all standard DVB receivers (LNB's for reflector antennas), making the cost of a single LNA as low as 2 €. None of the solutions present on the market or under development seem to retain all the required features, being either too costly or too bulky especially for what concerns the profile. In this work two innovative antenna systems for mobile satellite terminals at Ku-band are presented, retaining all the above mentioned characteristics. The constituting elements of such antennas

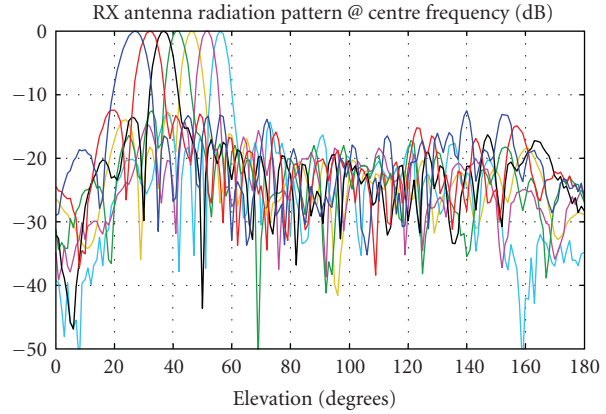
will be described in detail, and the achievable performance as well as the great potential of the proposed solutions will be illustrated.

2. Electronic Beam Scanning RX/TX Flat Antenna

The first antenna is specifically conceived for double-deck trains to allow a bidirectional high data rate satellite link, though with proper adjustments it could be also employed also in other kind of vehicles. The first and most important specification to be satisfied is the flat profile (<5 cm), together with a limited area (<80 cm) compliant with the roof of a double-deck train. The research group at the University of Perugia headed by professor Roberto Sorrentino is active in the field of flat beam scanning antennas since 2000.



(a)



(b)

FIGURE 2: SAET RX prototype antenna, 32×10 slotted waveguide array: (a) measurement setup; (b) measured radiation patterns.

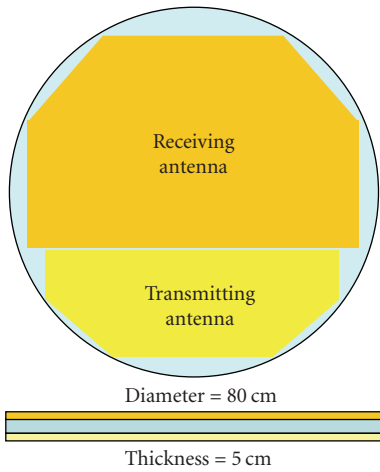


FIGURE 3: Final version size and geometry.



FIGURE 4: RX panel realized in SIW technology. The array is made of 32×32 slots, with a size of approximately 40×80 cm.

TABLE 1: Expected RX/TX antenna performance.

Parameter	Unit	TX section	RX section
Centre frequency	GHz	14.125	11.575
Bandwidth at VSWR<1.5	MHz	800	800
Polarization	—	Linear H	Linear V
Min gain (at 25° elev.)	dBi	31.2	31.8
Side lobe level	dB	-12	-12
Cross polarization	dB	-25	-25
Scan angles (elevation)	Degree	25° ÷ 50°	25° ÷ 50°
Scan angles (azimuth)	Degree	360°	360°
EIRP (ITU-R S.728.1)	dBW	32	—
G/T (at 25° elev)	dB/k	—	10
Size (D×H)	Cm	80 × 5	



FIGURE 5: Fabricated waveguide combining network.

This research activity has produced along the years a number of interesting and innovative solutions for mobile satellite terminal antennas operating up to Ka-band [2–7] and has spurred the development of a unique cad tool for the design of slotted waveguide technology [8]. In 2005 the University of Perugia was involved in ESA Project “Satellite Access for European Trains” (SAET, Contract N° 14272/00/NL/US) for a feasibility study of a bidirectional high-performance Ku-band flat antenna for mobile terminals to be placed on the roof of double deck trains [9]. In this framework the maximum achievable performance was assessed, and slotted

waveguide technology was identified as the most suitable technology for the realization of the flat array antenna. This result has been supported by the design, fabrication, and test of a proof-of-concept slotted waveguide array antenna. The tests have confirmed the validity of the electromagnetic modelling and the design tools as well as the feasibility of the proposed solution. The proof-of-concept antenna is represented by a dielectric-filled slotted waveguide array made of 32 waveguides with 10 slots each, and it is realized in aluminium. It has been designed and optimized to present the best performance in the scanning range from 30° to

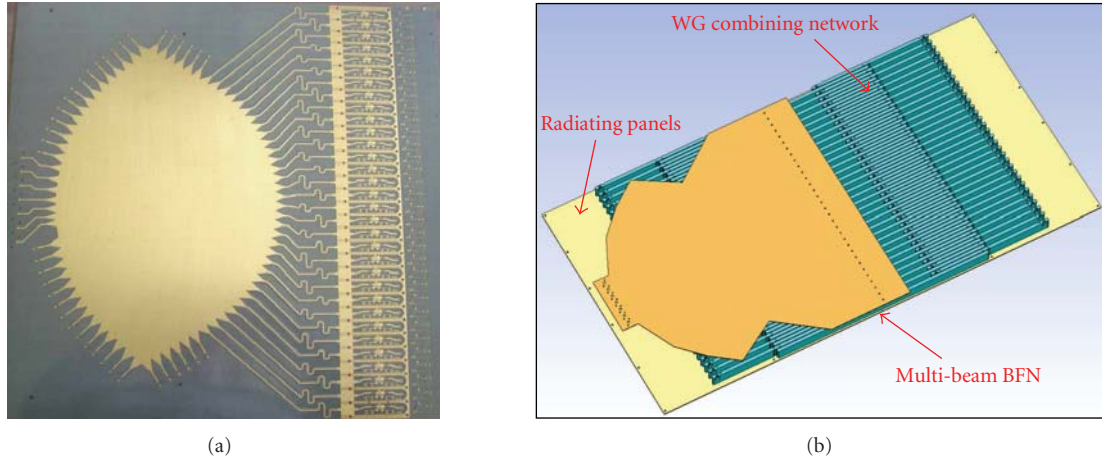
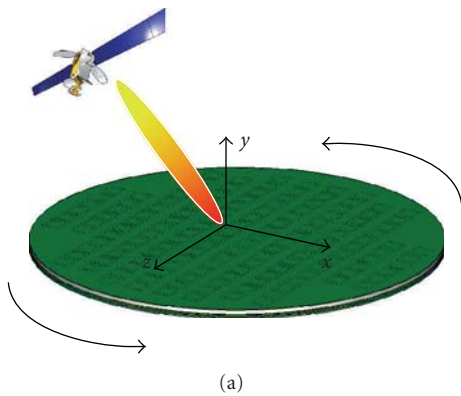


FIGURE 6: Fabricated active Rotman lens (a); schematic 3D view of the final antenna (b).



(a)

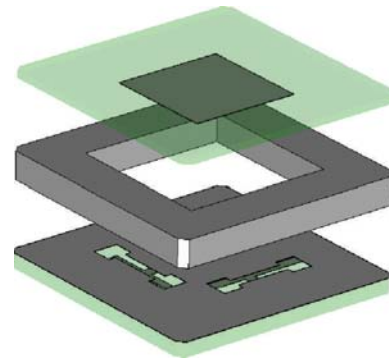
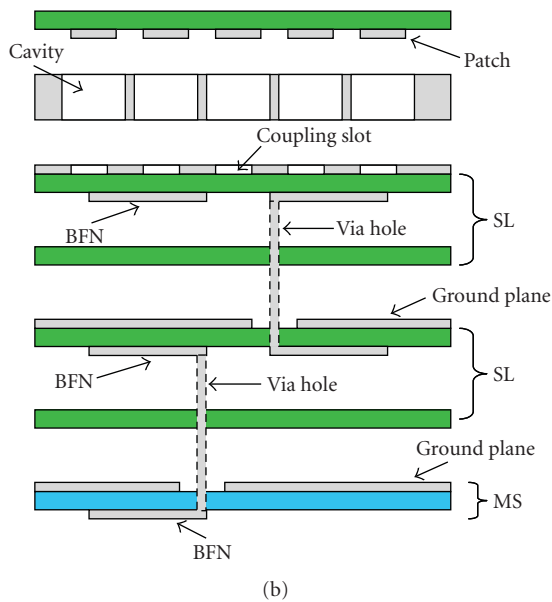


FIGURE 8: Dual polarization radiating element.



(b)

FIGURE 7: Antenna Architecture. BFN realized with two strip-line layers and a microstrip layer. Beam scanning is electronic in elevation and mechanical in azimuth.

50° in elevation (E-plane). Measured results confirm the high performance achievable with this technology, giving an overall antenna efficiency of about 80%.

With the conclusion of SAET Project, a self-financed R&D activity has been carried out aimed at the development of a ready-to-market product. To that purpose the spin-off company RF Microtech has been founded in 2007. What follows is the result of this activity. Table 1 shows the expected performance for the final antenna.

The final shape of the antenna will be circular (diameter 80 cm), as shown in Figure 3. A prototype antenna with the same performance of the final version but with a rectangular shape is now under construction. A picture of the RX panel is shown in Figure 4. The prototype antenna consists of two radiating panels for reception and transmission, respectively, each subdivided in four sections made of 32 centre-fed slotted waveguides with 8 slots each. Longitudinal slots are used for the receiving section while transverse slots are employed for the transmitting antenna. Substrate integrated waveguide (SIW) technology is employed, with strong impact on cost, ease of fabrication, thickness, and weight. Subarrays of the same line are fed in phase through the lowloss waveguide BFN shown in Figure 5, connected to a 32-way active Rotman lens realized in printed technology (see Figure 6) for

TABLE 2: Expected antenna performance.

Operative Frequency	10.7 ÷ 12.75 GHz
Polarization	Dual linear V/H
Scanning angle	Elevation: 20° ÷ 60° Azimuth: 0° ÷ 360°
3 dB beamwidth	>6° in azimuth >10° in elevation
Gain	>20 dBi
G/T	> -2 dB/°k
Thickness	<1 cm
Size	<30 cm
Estimated price (min 10.000 units)	<500 €

beam steering in elevation, while mechanical beam steering is performed in the azimuthal plane. The overall thickness is around 3 cm and total weight <20 kg. 12 dB-gain and 1 dB-NF LNAs covering the full DVB frequency range have been integrated in the RX section, while low-cost monolithic PA's are integrated in the TX printed circuit. The use of active BFNs allows high antenna efficiency and therefore high performance with a compact size and a low cost. Experimental results of the complete prototype are expected in the next few months.

3. Receiving-Only Broadband Dual Polarization Flat Antenna

The second antenna under development is a receiving-only circular array with full DVB frequency range coverage (10.7 ÷ 12.75 GHz) with simultaneous dual polarization. Main features are summarized in Table 2.

The antenna is fully realized in printed technology, the radiating element being a cavity-backed slot-fed patch antenna. Two parallel broad-band BFNs are employed, one for each polarization, realized with two strip-line layers and a microstrip layer where an active BFN, integrating LNAs at subarray level, is realized to allow electronic beam steering in the elevation plane. The overall architecture and the radiating element are shown in Figures 7 and 8. Full polarization tracking is possible, since the two orthogonal linear polarizations (V and H) are available at the same time. For the same reason a simultaneous double circular polarization is also possible (LHCP and RHCP) using simple passive circuitry. Two antennas with different diameters (22 cm and 30 cm) have been designed, employing 144 and 296 elements, respectively. The overall thickness is <1 cm. Beam steering is performed without the use of phase shifters and extremely low-cost active components are employed for the LNAs, thus resulting in a very competitive solution, potentially applicable also for larger diameters. The adopted beam steering architecture, together with the full DVB coverage, the simultaneous double polarization, and the low fabrication costs makes the proposed antenna system an attractive solution also as a flat wall-mount panel for fixed satellite terminals.

4. Conclusions

In this work two innovative products under development at RF Microtech have been presented. The proposed antenna systems include unique features which ensure a flat profile, reconfigurability, and high performance at a low cost. Prototypes of both solutions will be available for testing in the next few months.

Acknowledgments

The project of the receiving-only broadband dual-polarization flat antenna has been developed in the framework of two thesis works. The authors would like to thank Sonia Calzuola and Elisa Chiuppesi for their contribution.

References

- [1] R. Vincenti Gatti, L. Marcaccioli, E. Sbarra, and R. Sorrentino, "Flat array antennas for Ku-band mobile satellite terminals," in *Proceedings of the 30th ESA Antenna Workshop on Antennas for Earth Observation, Science, Telecommunications and Navigation Space Missions*, pp. 534–537, Noordwijk, The Netherlands, May 2008.
- [2] R. Vincenti Gatti, R. Sorrentino, and M. Dionigi, "Equivalent circuit of radiating longitudinal slots in dielectric filled rectangular waveguides obtained with FDTD method," in *Proceedings of IEEE MTT-S International Microwave Symposium Digest (MWSYM '02)*, vol. 2, pp. 871–874, Seattle, Wash, USA, June 2002.
- [3] R. Vincenti Gatti and R. Sorrentino, "A Ka-band active scanning array for mobile satellite terminals using slotted waveguide technology," in *Proceedings of the 25th ESA Antenna Workshop on Satellite Antenna Technology (ESTEC '02)*, Noordwijk, The Netherlands, September 2002.
- [4] R. Vincenti Gatti, R. Sorrentino, and M. Dionigi, "Fast and accurate analysis of scanning slotted waveguide arrays," in *Proceedings of the 32nd European Microwave Conference (EuMC '02)*, pp. 1–4, Milan, Italy, September 2002.
- [5] R. Vincenti Gatti and R. Sorrentino, "Low-cost flat-profile active scanning antenna for mobile satellite terminals in Ka-band," in *Proceedings of the 3rd ESA Workshop on Millimetre Wave Technology and Applications*, pp. 61–68, Espoo, Finland, May 2003.
- [6] R. Vincenti Gatti, L. Marcaccioli, and R. Sorrentino, "Design of slotted waveguide arrays with arbitrary complex slot voltage distribution," in *Proceedings of IEEE International Symposium on Antennas and Propagation Society (APS '04)*, vol. 3, pp. 3265–3268, Monterey, Calif, USA, June 2004.
- [7] R. Vincenti Gatti and R. Sorrentino, "A fast and accurate CAD tool for slotted waveguide arrays for radar applications," in *Proceedings of the 1st European Radar Conference (EuRAD '04)*, pp. 181–184, Amsterdam, The Netherlands, October 2004.
- [8] SWAN, <http://www.swan-soft.com/>.
- [9] R. Vincenti Gatti, R. Sorrentino, V. Schena, and G. Losquadro, "Flat-profile active scanning antenna for satellite terminals in Ku-band operating on new fast trains generation," in *Proceedings of the 28th ESA Antenna Workshop on Satellite Antenna Technology (ESTEC '05)*, Noordwijk, The Netherlands, May-June 2005.

Application Article

Low Profile, Dual-Polarised Antenna for Aeronautical and Land Mobile Satcom

Martin Shelley, Robert Pearson, and Javier Vazquez

Cobham Technical Services, Cleeve Road, Leatherhead, Surrey KT22 7SA, UK

Correspondence should be addressed to Martin Shelley, martin.shelley@cobham.com

Received 30 September 2008; Accepted 5 February 2009

Recommended by Stefano Selleri

High data rate communications on the move is fastly becoming a major application area for satellite systems using Ku- and higher frequency bands. The ground terminal antenna used in such systems has a profound impact on the system capabilities and is constrained in many often conflicting ways. While simple reflector systems offer the lowest cost solution, there is a widespread need for low profile antennas to minimize the antenna visual signature and to satisfy aesthetic and transportation requirements. It is often considered that the use of such antennas will compromise the system performance.

Copyright © 2009 Martin Shelley et al. This is an open access article distributed under the Creative Commons Attribution License, which permits unrestricted use, distribution, and reproduction in any medium, provided the original work is properly cited.

1. Introduction

In this paper, which is an extended version of a submission presented at the 4th Advanced Satellite Mobile Systems Conference, Bologna, August 26–28, 2008 [1], it will be shown that, in many scenarios, the use of low profile antenna solutions has operational as well as mechanical advantages. The paper will illustrate why this is the case and describe a unique low profile antenna solution that is being developed to make these advantages available to the system designer.

Agencies providing defense and emergency services are increasingly reliant on mobile communications. Travelling rapidly over large areas, mobile units require real-time, agile, communication systems for voice, data, images, and video. Airborne systems must operate in severe environmental conditions and meet demanding certification requirements; land systems must operate during all vehicle maneuvers, and should be unaffected by the type of terrain encountered. Installations on small business jets and UAVs, commercial and military aircraft, and a wide range of land vehicles including HMMWVs and SUVs, have to be very low profile to meet requirements for low drag, easy transportation and small visual signature.

A key requirement for satcom-on-the-move (SOTM) systems is to maximize the data throughput using an antenna with smallest aperture. Section 2 below shows that low

profile solutions have to potential to maximize data rates for many operational scenarios combining the clear physical advantages with significant system benefits.

Section 3 describes a new highly robust antenna system which has been developed, suitable for mounting on aeronautical and land vehicles, to capitalize on these benefits.

2. Benefits and Shortcomings of the Low Profile Antenna Solution

For any given two-way mobile communications system operating in Ku-Band, transmit requirements always dominate when sizing the mobile antenna and its associated power amplifier system. The aperture area of the antenna will determine its transmit gain. Regulations [2–5] will then limit the amount of power the user is allowed to radiate (defined in terms of EIRP/bandwidth), based on sidelobe templates defined to limit interference to adjacent satellites. This limit on the operation of the system will depend on the antenna aperture size and shape, and the relative locations of the user, and the satellite and the nearest neighboring satellites. Generally, the limit is only applied along the geostationary arc and antenna performance outside this region is unconstrained. Different operators apply different limits. Figure 1 shows some of the more common regulatory templates.

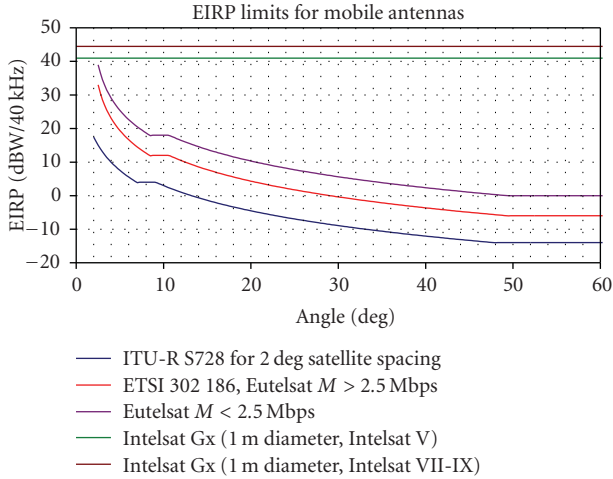


FIGURE 1: Typical transmit system regulatory templates.

Since the templates only apply close to the geostationary arc, a low profile antenna solution can have significant benefits when compared to an equivalent circular reflector in many situations.

Generally, unless the satellite and user have very different longitudes and/or the user is very close to the Equator, a mobile terminal will need to look in a southerly direction (if in the Northern Hemisphere) to form a link with a satellite in the geostationary arc. In this instance, the geostationary arc will be broadly aligned to the azimuth radiation pattern of the antenna, and in order to maximize the power that can be radiated, the antenna needs to have the largest possible aperture dimension in the azimuth plane. For a given aperture area, this is achieved best by using a low profile antenna.

However, if the user is close to the Equator and the satellite has an offset longitude, the geostationary arc is now broadly aligned to the elevation radiation pattern of the mobile antenna. In this instance, the performance of the low profile antenna will be compromised, as the beamwidth will be substantially larger than was previously the case, and the interference potential significantly greater. Taking a typical low profile antenna with a 900 mm azimuth aperture, Figure 2 shows how the EIRP must be backed off as the beamwidth increases.

An extensive study of this phenomenon has been carried out to assess how it impacts on the EIRP levels that can be radiated for different relative locations of the satellite and mobile. A comparison has been undertaken between the low profile solution, where the performance is location dependent, and a circular reflector with the same gain, where the performance is the same for all locations. A satellite is placed at an arbitrary location of 0 W. The coverage area where the satellite can be accessed is determined, and the beamwidth of the particular mobile antenna in the satellite look direction determined. This is then overlaid on the ITU-R S728 template and the maximum EIRP/Hz calculated. This was done for a low profile aperture with dimension

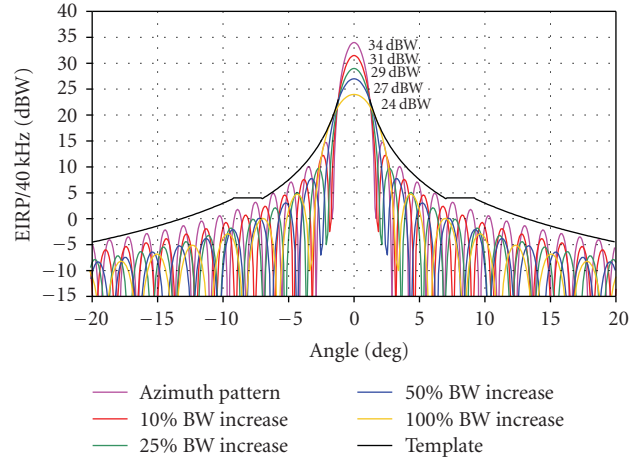


FIGURE 2: Impact of increasing beamwidth on EIRP.

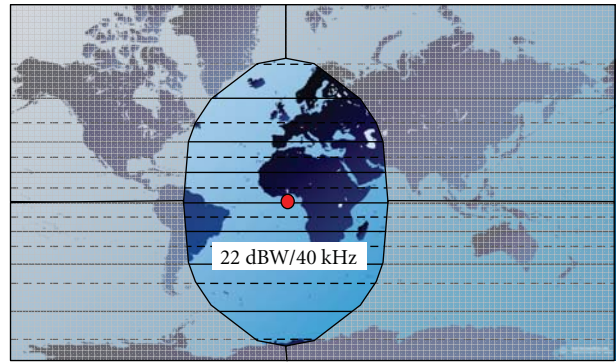


FIGURE 3: EIRP contours for a circular reflector.

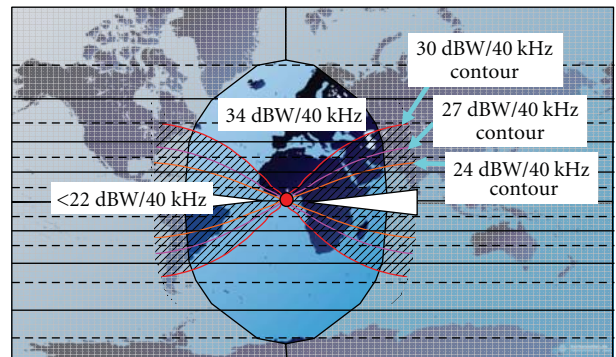


FIGURE 4: EIRP contours for a low profile antenna.

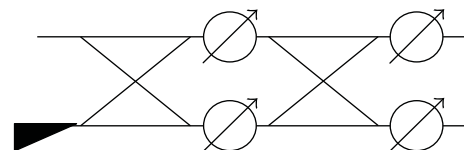


FIGURE 5: Polarisation control network.

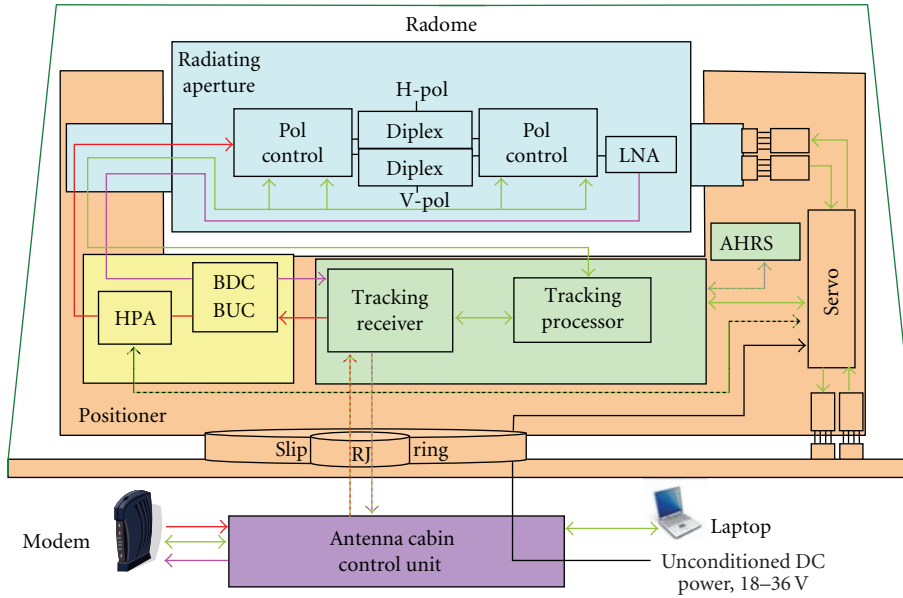


FIGURE 6: System block diagram.

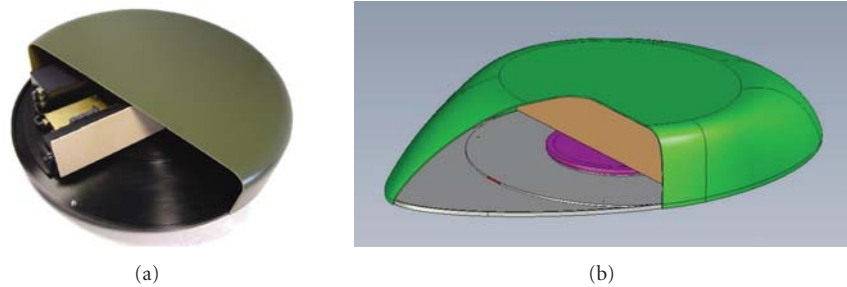


FIGURE 7: Antenna demonstrator.

900 mm × 150 mm and an equivalent 460 mm diameter circular reflector.

It is found that the low profile solution can provide up to 10 dB more EIRP/Hz (equivalent to a 10 × increase in data rate), over a large percentage of a typical coverage area and that its performance is only degraded with respect to the circular reflector in a small region along the equator at offset longitudes with respect to the satellite. This effect is illustrated in Figures 3 and 4, which shows the EIRP contours for both designs.

3. Spitfire Low Profile Antenna

The highly integrated SPITFIRE Ku-Band terminal includes a low profile aperture antenna, a positioner and servo controller, an autonomous tracking receiver, and an internal navigation unit. A low-noise amplifier, block up and down converters, and a high efficiency solid state power amplifier are also included, housed under a common radome above the deck. Key features of the design are

- (i) fully integrated antenna terminal, including radome and RF electronics,

- (ii) designed for commercial air transport and full MIL SPEC off-road applications,
- (iii) single, mechanically steered dual-polarised aperture providing a full band RX and TX air interface with zenith to horizon coverage,
- (iv) polarisation control function implemented in Ku-Band using unique low-loss components, including compensation for unavoidable radome depolarisation,
- (v) integrated onboard INS/GPS, providing low latency position and attitude data,
- (vi) simple L-band and power cable interface through the external vehicle skin. All control data sent via RF cables,
- (vii) small in-cabin control box, providing direct interface to different modems using RS422 or Ethernet, while also enabling control and monitoring of the system through a laptop computer.

Two versions of the antenna system are offered. The first is suited to the airborne environment, where shock

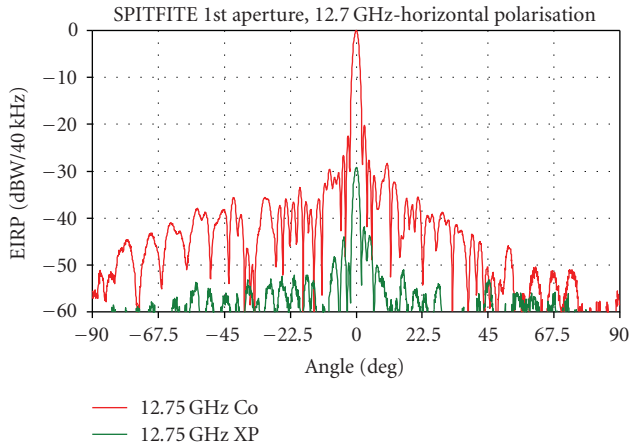


FIGURE 8: Typical measured RX band azimuth radiation pattern.

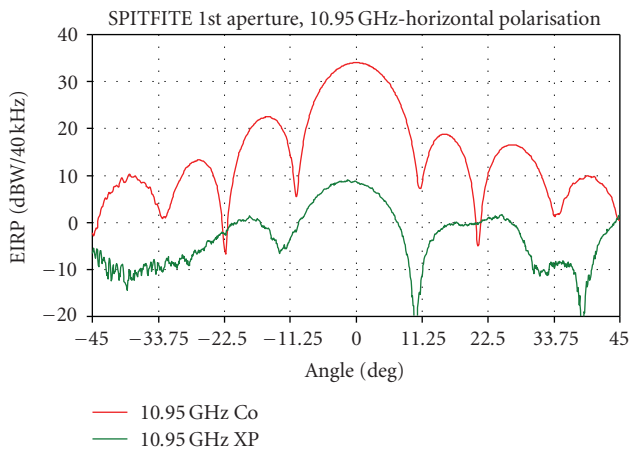


FIGURE 9: Typical measured RX band elevation radiation pattern.

and vibration levels are relatively low and vehicles dynamics benign. The second has a more robust positioner and larger motors which will allow it to operate in the much more demanding off-road scenario, where shock loads are much higher and there is a need to compensate for rapid vehicle attitude changes.

The array aperture is a hybrid construction, combining the benefits of low-loss waveguides with a compact printed circuit implementation where waveguides cannot be accommodated. The radiating elements are compact ridge waveguide horns, matched using an external impedance matching sheet. These are excited using balanced, printed probes formed as part of a stripline elevation power combining structure, configured to give low cross-polarisation. Azimuth beamforming is implemented in waveguide and includes integral diplexers, separating the TX and RX functions.

A waveguide hybrid network is used to control the polarisation, see Figure 5, using unique and patented mechanically adjusted noncontact waveguides [6].

The central phase shifters are adjusted to transfer the input energy between the upper and lower ports of the

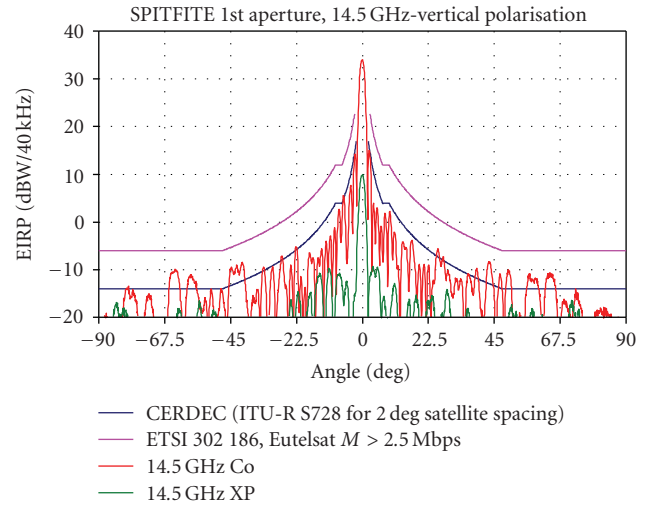


FIGURE 10: Typical measured TX band azimuth radiation pattern.

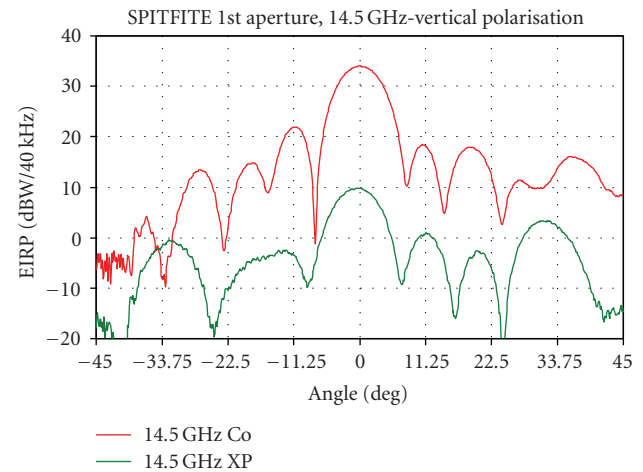


FIGURE 11: Typical measured TX band elevation radiation pattern.

antenna, which are connected to the vertically and horizontally polarised ports on the array face.

Additional phase shifters are provided on each output arm to compensate for radome phase imbalances which are unavoidable at scan angles close to the horizon using a low profile radome. These imbalances can otherwise degrade the cross-polar levels of the complete terminal from better than -25 dB to less than -15 dB.

The antenna system block diagram is shown in Figure 6. The complete antenna, including the land mobile radome, is some 200 mm tall and has a footprint of 965 mm diameter. The aeronautical version, with a teardrop radome, has a height of less than 250 mm and a footprint which is extended in the fore-aft direction to 1600 mm, to provide low drag. A photograph of a land mobile version of the antenna, with all the onboard equipment placed on the rotating platform, is shown in Figure 7. A CAD drawing of the aeronautical version, which is nearing completion, is also shown in the figure.

TABLE 1: Summary of antenna performance.

	TX	RX
Operating frequency band	13.75–14.5 GHz	10.95–12.75 GHz
Input return loss	10 dB minimum	10 dB minimum
G/T, 11.7 GHz	—	10.6 dB/K worst case
Gain, 14 GHz	32.2 dBi	—
Typical TX EIRP (meeting 25–25 log(θ) template)	34 dBW/40 kHz	—
Typical data rate capability	2 Mbps	20 Mbps
Polarisation	Single adjustable Linear	Single adjustable linear, orthogonal to transmit
Cross-polarisation on boresight, under all dynamic conditions	25 dB worst case	15 dB worst case

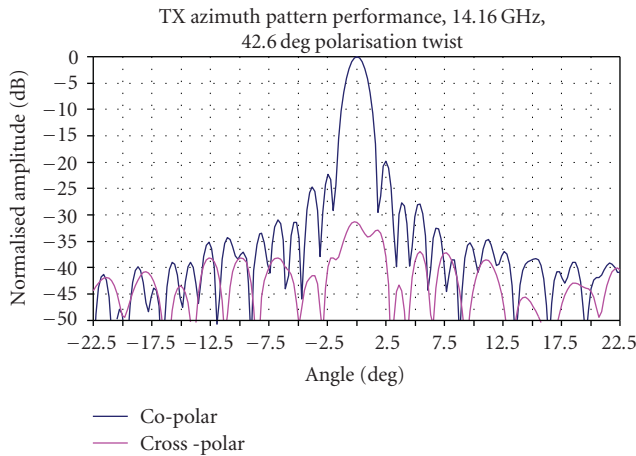


FIGURE 12: TX pattern with 42.6° polarization.

Typical azimuth and elevation radiation patterns of the aperture alone in the TX and RX bands are shown in Figures 8, 9, 10, and 11. These clearly show the excellent pattern and cross-polarization performance that has been achieved.

Both the radome and the polarisation control networks may degrade the antenna performance. The impact of both has been assessed in detail. The antenna has been configured to operate with a satellite at an offset longitude, where a polarization skew of about 45° is required. Figure 12 shows the TX pattern measured after polarization alignment has been undertaken.

The impact of the radome has been assessed by comparing azimuth patterns with and without the radome. Figure 13 shows a typical comparison in the TX band, where sidelobe control is particularly important. It can be seen that there is minimal degradation at all elevation angles, with some distortion close to the horizon (due to ground plane effects) and at zenith (due to direct reflections from the radome surface).

A summary of the antenna performance is provided in Table 1. On the receive side, the G/T is typically better than 11 dB/K, with a small reduction close to the horizon, where sky noise increases; radome losses are also slightly higher when the antenna looks through the highly curved section at about 10° elevation. On the transmit side, the gain is greater than 32 dBi, allowing the antenna to radiate an EIRP

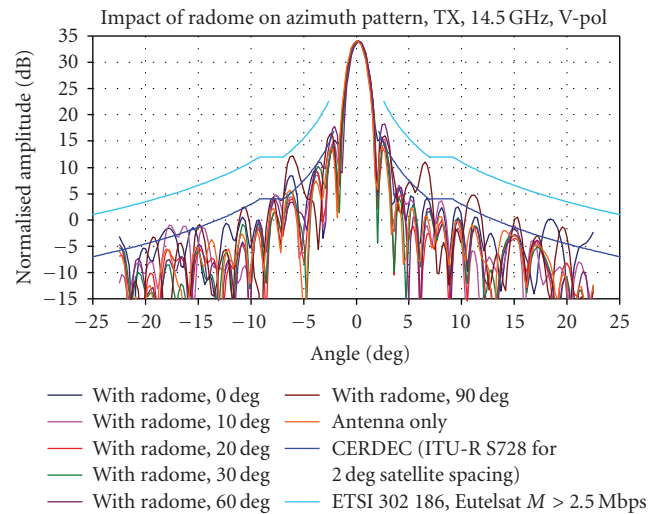


FIGURE 13: Impact of radome on azimuth patterns.

of typically 44 dBW using its internal 20 W amplifier. Cross-polarisation levels can be maintained below 25 dB using the polarization control networks.

4. Conclusions

In this paper, a key system benefit of using a low profile antenna in place of a circularly symmetrical reflector-based solution has been demonstrated. In most applications, the increased azimuth aperture provides significant additional protection to adjacent satellites and it is therefore possible to use the antenna to radiate much higher power than an equivalent circular reflector and hence makes it possible for a system to operate at a much higher data rate than one using a circular reflector.

The Ku-Band SPITFIRE antenna described allows these benefits to be realized in systems operating in the severe environments encountered onboard aircraft and on the battlefield. The antenna includes a highly integrated high performance aperture coupled to low-loss waveguide-based polarization control mechanisms, eliminating the need for complex electronic phase shifting components. The antenna includes all the tracking and steering components within the radome volume, creating a compact package that can easily be accommodated on a wide range of vehicle platforms.

The tracking and steering solution has been developed to support a range of other radiating apertures, including X-Band, Ka-Band, and Q-Band units and could be used in next generation systems employing multiband apertures.

Acknowledgments

The authors would like to acknowledge the support which has been given to the development of the SPITFIRE antenna system by the European Space Agency under its ARTES 4 program [7] and by Cobham PLC under its IRAD program. This paper is an extended version of a submission presented at the 4th Advanced Satellite Mobile Systems Conference in Bologna, August 26–28, 2008.

References

- [1] M. W. Shelley, R. A. Pearson, and J. Vasquez, "Low profile, dual polarised antenna for aeronautical and land mobile satcom," in *Proceedings of the 4th Advanced Satellite Mobile Systems Conference (ASMS '08)*, pp. 16–19, ERA Technology Ltd, Bologna, Italy, August 2008.
- [2] "RECOMMENDATION ITU-R S.728-1 Maximum permissible level of off-axis e.i.r.p. density from very small aperture terminals (VSATs)," International Telecommunications Union, October 1995.
- [3] ETSI 302 186 v1.1.1, "Satellite Earth Stations and Systems (SES); Harmonized EN for satellite mobile Aircraft Earth Stations (AESs) operating in the 11/12/14 GHz frequency bands covering essential requirements under article 3.2 of the R&TTE Directive," European Telecommunications Standards Institute, April 2004.
- [4] EESS 502 Issue 10 - Rev. 0, STANDARD M, "Minimum Technical and Operational Requirements for Earth Stations transmitting to a Eutelsat Transponder for Non-Standard Structured Types of SMS Transmissions," EUTELSAT SA, August 2006.
- [5] IESS-601 Rev 12. Standard G., "Performance Characteristics for Earth Stations accessing the Intelsat Space Segment for international and domestic services not covered by other Earth Station Standards," Intelsat, March 2005.
- [6] Waveguide, "Sanchez Fransisco Javier Vazquez; Pearson Robert A [GB]," ERA Patents Ltd, Patent no. WO03065497.
- [7] "Compact Ku-Band aeronautical antenna for commercial airliners," ESA Contract 20325/06/NL/US, <http://telecom.esa.int/telecom/www/object/index.cfm?fobjectid=28078>.